Radiative Transfer Notes

AT 622

Colorado State University

1992-2013

by **Graeme L. Stephens**

Be sure to give credit & proper attributions for these notes when necessary:

Graeme L. Stephens

Colorado State University

Fort Collins, CO

AT622 Section 1
Electromagnetic Radiation

The aim of this section is to introduce students to elementary concepts of radiometry and to describe some basic radiation laws relevant to the course.

1.1 Electromagnetic Radiation

Electromagnetic radiation from the sun is the principal source of energy that drives circulations in both the atmosphere and ocean. This radiation, in the form of a wave, is generated by oscillating (or, more generally, time varying) electric charges, which in turn generate an oscillating electric field. A characteristic of an oscillating electric field is that it produces an accompanying oscillating magnetic field that further produces an oscillating electric field. Therefore these fields, initiated by the oscillating charge, proceed outwards from the original charge, each creating the other. A visualization of such a propagating wave is given in Fig. 1.1. It was James C. Maxwell, who, more than a century ago, provided us with the theoretical synthesis of this phenomenon. Detailed account of this work can be found in most standard texts on electromagnetic radiation.

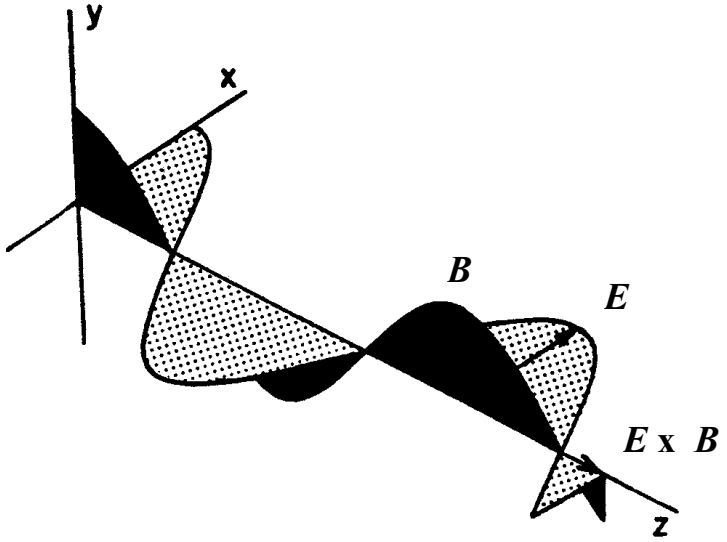

Fig. 1.1 Schematic view of a time-harmonic electromagnetic wave propagating along the z-axis. The oscillating electric E and magnetic B fields are shown. Note that the oscillations are in the x-y plane and perpendicular to the direction of propagation.

There are a number of basic properties that distinguish different electromagnetic (EM) waves. One is the rate of oscillation of the *E* and *B* fields (that is the frequency of the oscillation), the second is the amplitude of the wave (this defines the energy carried by the wave), and the third is the state of polarization of the wave. This third property is something we will not consider further in this course although it is fundamental to many topics relevant to remote sensing (and thus to AT652).

Electromagnetic theory predicts that the EM wave travels at a speed that depends on the medium through which it travels. This speed, *c*, can be related to the speed of propagation of light in a vacuum (namely c_0) by the formula:

$$c = \frac{c_0}{n}, \quad c_0 = 2.998 \times 10^8 \,\mathrm{ms}^{-1}$$

where n is the refractive index of the medium (more on this later). For most gases, the refractive index is close to unity especially at the wavelengths of interest to topics considered in these notes. For example, air at room temperature has n = 1.00029 over the visible spectrum (refer to Fig. 1.2).

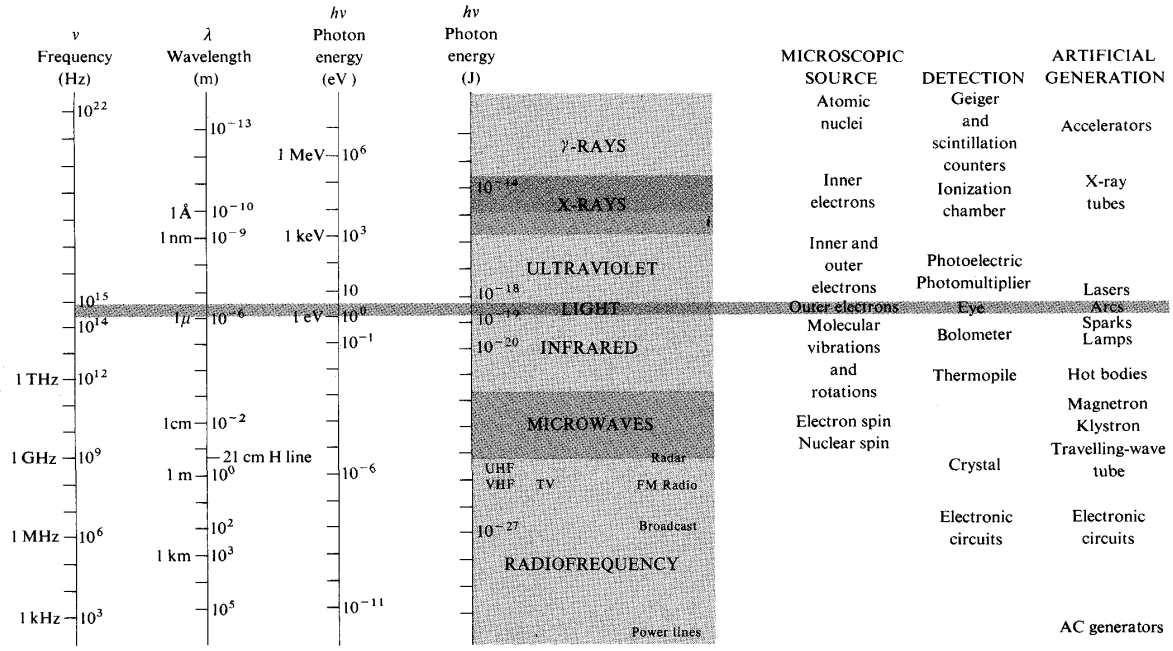

Fig 1.2. The electromagnetic-photon spectrum.

The wavelength of the EM wave depends upon the frequency of the oscillations. We shall denote this frequency (number of oscillations per second) by v, and it is related to c by

$$v = \frac{c}{\lambda}, \tag{1.1}$$

where λ is the wavelength of the wave. For example, red light with a wavelength of 0.7 micrometers (μm) corresponds to a frequency of 4.3 x 10^{14} oscillations per second, while violet light, at 0.4 μm, corresponds to 7.5 x 10^{14} oscillations per second. An alternate way of describing the frequency of radiation is in terms of *wavenumber*

$$\tilde{v} = \frac{1}{\lambda}, \tag{1.2}$$

which is a count of the number of wave crests or troughs in a given unit of length. For example, red light has 14,286 wave crests in a centimeter whereas 25,000 crests can be counted in a centimeter of violet light. Wavenumber is the measure often used by spectroscopists and others involved in experimental measurements of the interaction of radiation with matter.

Example 1.1: What is the frequency and wavenumber of 10 μm radiation?

$$\lambda = 10\ \mu\text{m} = 10\times10^{-6}\ \text{m}$$

$$\nu = \frac{c_o}{\lambda} = \frac{3\times10^{8}\ \text{m}\cdot\text{s}^{-1}}{10\times10^{-6}\ \text{m}} = 3\times10^{13}\ \text{Hz}$$

$$\tilde{\nu} = \frac{1}{10\times10^{-6}\ \text{m}} = 1000\ \text{cm}^{-1}$$

(a) Electromagnetic Spectrum

Even before Maxwell, the spectrum of electromagnetic radiation (that is the range of wavelengths or frequencies of the radiation) was known to extend beyond the visible (i.e., beyond those wavelengths detectable by the human eye). In fact, we now know that the visible portion of the spectrum, from 0.4 μm to 0.7 μm, is just a small part of a much broader spectrum of electromagnetic radiation. The character of the radiation and the way it interacts with matter is vastly different depending on the wavelength of the radiation. The radiation that is relevant to this course is shown in Fig. 1.3.

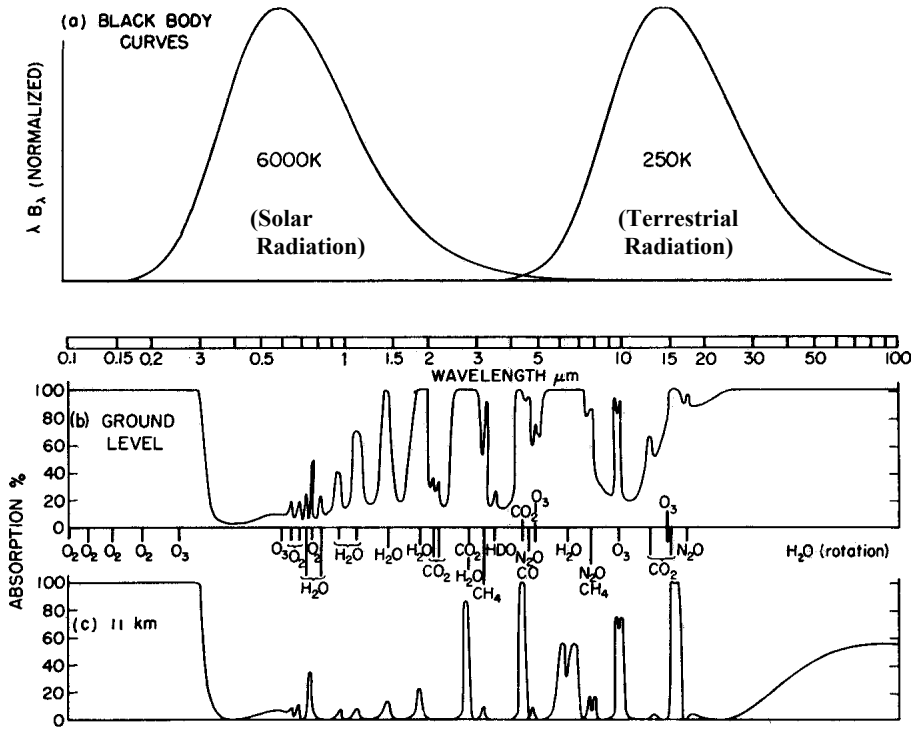

Fig. 1.3 Atmospheric absorptions. (a) Blackbody curves for 6000 K and 250 K. (b) Atmospheric absorption spectrum for a solar beam reaching ground level. (c) The same for a beam reaching the temperate tropopause. The axes are chosen so that areas in (a) are proportional to radiant energy. Integrated over the earth's surface and over all solid angles, the solar and terrestrial fluxes are equal to each other; consequently, the two blackbody curves are drawn with equal areas. Conditions are typical of mid-latitudes and for a solar elevation of 40° or for a diffuse stream of terrestrial radiation.

In the solar/terrestrial spectrum shown in Fig. 1.3, the frequency domains of greatest interest are the ultraviolet, visible, and infrared wavelengths. The ultraviolet frequencies range from the extreme ultraviolet (EUV) at 10 nm to the near ultraviolet (NUV) at 400 nm as shown.

Extreme Ultraviolet – EUV. The extreme ultraviolet, sometimes abbreviated XUV, is defined here as 10 nm to 100 nm. The division between the EUV and the FUV is frequently considered to be the ionization threshold for molecular oxygen at 102.8 nm. The EUV solar radiation is responsible for photoionization at ionospheric altitudes. The division between the EUV and the x-ray regions corresponds very roughly to the relative importance of interactions of the photons with valence shell and inner shell electrons, respectively.

Far Ultraviolet – FUV. This region extends from about the beginning of strong oxygen absorption to about the limit of availability of rugged window materials, the lithium fluoride transmission limit. The range as used here extends from 100 to 200 nm.

Middle Ultraviolet – MUV. The middle UV covers the region from 200 to 300 nm, which is approximately the region between the solar short wavelength limit at ground level and the onset of strong molecular oxygen absorption. Most solar radiation in this range is absorbed in the atmosphere by ozone.

Near Ultraviolet – NUV. This region covers wavelengths from 300-400 nm, and represents roughly the limits between the solar ultraviolet that reaches the surface of the earth and the limit of human vision in the visible.

The biomedical community uses a different convention:

UV-C	15-280 nm
UV-B	280-315 nm
UV-A	315-400 nm

UV-C is absorbed entirely in the upper atmosphere and is of practical significance to the biomedical community only in the sense that it is frequently used to sterilize surfaces and kill bacteria. UV-B is responsible for Vitamin-D production by the skin. Both UV-A and UV-B activate melanin in the skin, which is responsible for the darker appearance after exposure to the sun.

The infrared spectrum is occasionally divided into the near and far infrared.

Near Infrared. The portion of the spectrum beyond the visible (0.7 μm) where the amount of solar radiation is significant. Generally defined in the 0.7 μm to 2.5 μm range.

Far Infrared. The portion of the spectrum beyond near infrared where the Earth's radiation dominates. 2.5 μm to 1000 μm range.

Microwaves, while not contributing to the energy incident upon Earth or emitted from it, play an important role in remote sensing as well as communications. Figure 1.4 shows the allocation of the microwave spectrum to different users.

(b) The Mathematical Form of an EM Wave

The oscillatory E and B fields can be presented in a classical way as a harmonic oscillator of the form

$$E = E_0 \cos k(x - ct) \tag{1.3a}$$

where the quantity E_0 is the amplitude of the wave and, as we shall see later, the energy carried by the wave is related to the square of this amplitude and is the property of most interest and relevance to atmospheric sciences. The quantity $k(= 2\pi\tilde{\nu})$ is also referred to as wavenumber, but this should not prove to be a source of confusion as $\tilde{\nu}$ and k are used in different contexts; k generally applies to wave propagation, whereas $\tilde{\nu}$, is used, as in the previous section, to discriminate regions of the electromagnetic spectrum. Equation (1.3a) can also be written in the form

$$E = E_0 \cos(kx - \omega t) \tag{1.3b}$$

where $\omega = kc = 2\pi c/\lambda$ is the angular frequency of the wave and, according to Eqn. (1.1), $\omega = 2\pi\nu$.

The argument of the cosine function in Eqn. (1.3a) also has a particular meaning. It is represented by the function ϕ

$$\phi = k(x - ct) \tag{1.4}$$

and is referred to as the *phase of* the wave. A tidier expression for a harmonic oscillator is

$$E(x,t) = E_0 e^{ik(x-ct)}, \tag{1.5}$$

where it may be taken for granted that the real part of this expression represents the wave.

The general representation of the harmonic wave requires that the displacement E be specified at $x = 0$ and $t = 0$. We specify this initial displacement (initial since it is defined at $t = 0$) in terms of a constant phase, ϕ_0, at $x = 0$ and $t = 0$. For this general case,

$$\phi = \phi_0 + k(x-ct) \tag{1.6}$$

and

$$E(x,t) = E_0 e^{i\phi}. \tag{1.7}$$

Simple algebraic manipulations show that the square of the wave amplitude, given as

$$| E(x,t) |^2 = | E_0 |^2 , \tag{1.8}$$

is the same for all x and t since E_0 is a constant. The energy transferred by the wave, related to $| E_0 |^2$, does not vary along its path of propagation and is independent of our definition of ϕ_0. It is only the interaction of the wave with matter that alters the energy of the wave as it propagates. These interactions and the potential they offer for modulating the atmosphere is of interest to the atmospheric scientist.

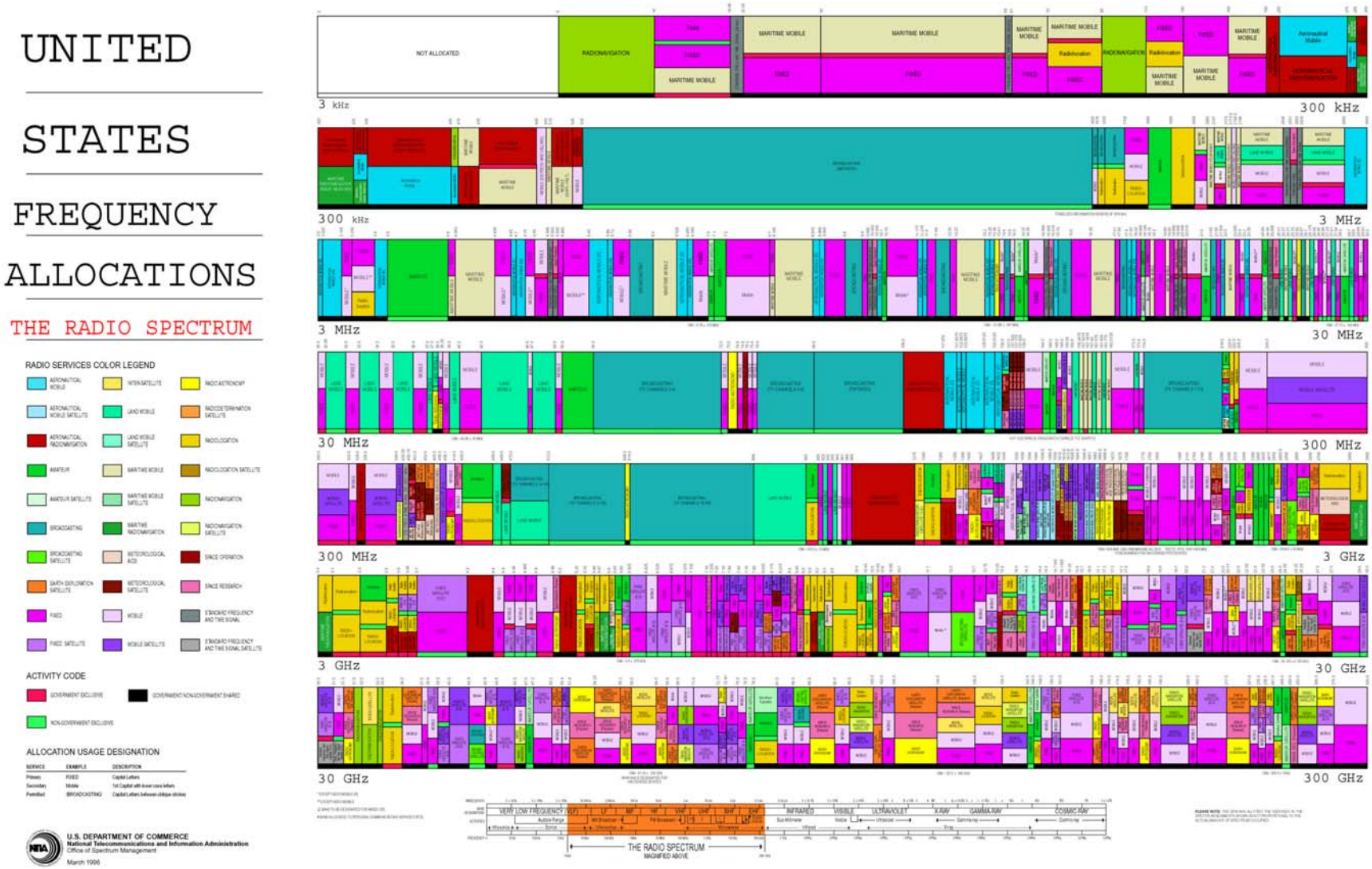

Fig. 1.4 Allocation of the microwave frequency spectrum. Details are available at: http://www.ntia.doc.gov/osmhome/allochrt.html.

1.2 Energy Carried by an EM Wave

An electromagnetic wave, traveling through space at the speed of light, carries electromagnetic energy, which is detected by sensors that respond to this energy. In the next section, we will discuss in a more geometrical way how we describe the flow of energy carried by an EM wave. But for now we will endeavor to see what defines this energy. Energy flows in the direction in which the wave advances and this direction of propagation is defined by the vector cross product of the electric and magnetic fields, $\vec{E}$ x $\vec{B}$. The energy per unit area per unit time flowing perpendicular into a surface in free space is given by the *Poynting vector* $\vec{S}$, where

$$\vec{S} = c^2 \varepsilon_0 \vec{E} \times \vec{B} \tag{1.9}$$

c is the speed of light and ε_0 is the vacuum permittivity (ε_0 = 8.85 x 10^{-12} F·m^{-1}). Energy per unit time is power, so the SI units of $\vec{S}$ are Wm^{-2}. At the frequencies of interest to the topics of this class, the fields $\vec{E}, \vec{B},$ and $\vec{S}$ oscillate at rapid rates. It thus remains impractical to measure instantaneous values of $\vec{S}$ directly. Rather, we measure its average magnitude, $< S >$, over some time interval that is a characteristic of the detector. This time averaged quantity is referred to as the radiant-flux density. Strictly speaking, the flux density emerging from the surface is known as the *exitance* and the flux density incident on the surface is called the *irradiance.* To avoid unnecessary complications with nomenclature, we refer to the flux density onto or from a surface as either irradiance or flux and use the symbol F to represent this quantity.

When the flow of light is nonparallel and when the detector collects the light confined to a range of directions, specified by a small element of solid angle $d\Omega$, then the quantity sensed is the *intensity,* defined *as* $< S > /d\Omega$ and has units of Wm^{-2}ster^{-1}. This quantity, referred to as a radiance, is used throughout and we will denote it by the symbol I (more about this below).

We can consider a more direct relationship between the energy carried by an electromagnetic wave and the amplitudes of the electric and magnetic fields by considering the simple case of a plane wave of the form

$$\vec{E} = E_0 \cos(kx - \omega t). \tag{1.10}$$

The magnetic field also has the form $\vec{B} = B_0 \cos(kx - \omega t)$ and therefore

$$S = c^2 \varepsilon_0 \vec{E} \times \vec{B} = c^2 \varepsilon_0 E_0 \cdot B_0 \cos^2(kx - \omega t). \tag{1.11}$$

Hence

$$< S > = c^2 \varepsilon_0 \left| E_0 \cdot B_0 \right| < \cos^2(kx - \omega t) >, \tag{1.12}$$

and the time average is calculated for an interval of length T according to

$$\left\langle \cos^2(kx - \omega t) \right\rangle = \frac{1}{T} \int_t^{t+T} \cos^2(kx - \omega t')dt' = \frac{1}{2} - \frac{1}{4\omega T} \left[\sin 2(kx - \omega(t+T)) - \sin 2(kx - \omega t) \right]. \tag{1.13}$$

When $T >> t$, $\omega T >> 1$ and $< \cos^2(kx - \omega t) > \rightarrow 1/2$. Since $E_0 = cB_0$,

$$F = < S > = \frac{c\varepsilon_0}{2} E_0^2 \tag{1.14}$$

or

$$F = c\varepsilon_0 < E^2 >, \tag{1.15}$$

where $< E^2 > = E_0/2$. It also follows that $I = < S > / d\Omega$.

Example 1.2: Consider the following problem: a plane, sinusoidal, linearly polarized electromagnetic wave of wavelength $\lambda = 5.0 \times 10^{-7}$ μm travels in a vacuum along the x axis. The average flux of the wave per unit area is 0.1 Wm^{-2} and the plane of vibration of the electric field is parallel to the y axis. Write the equations describing the electric and magnetic fields of the wave.

The solution is as follows: The wavenumber is $k = 2\pi/\lambda = 4\pi \times 10^6$ m^{-1}. Given the following,

$$c\varepsilon_0 = \frac{10^7}{4\pi c}$$

then the amplitude

$$E_0 = \sqrt{\frac{2 \times 0.1}{c\varepsilon_0}} = \sqrt{24\pi}$$

and the form of the E wave is

$$E_y(t) = \sqrt{24\pi} \cos 4\pi \times 10^6 (x - ct) \ \ [NC^{-1}]$$

and the magnetic field is governed by

$$B_z(t) = \frac{E_y(t)}{c} [T].$$

1.3 Momentum and Radiation Pressure

An electromagnetic wave, aside from carrying energy, also carries momentum. If an electromagnetic wave is absorbed or reflected by a material, it will impart momentum to the electrons in the material, which is subsequently transmitted to the lattice structure as a whole.

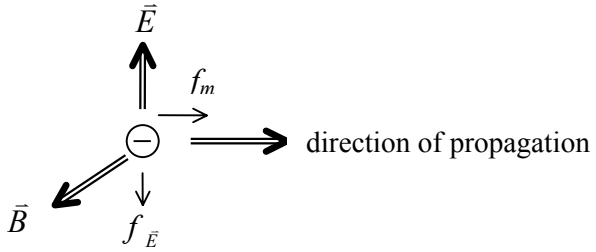

The electric field exerts a force $\vec{f}_E = q\vec{E}$, which drives an electron with a velocity $\vec{\mathrm{v}}_e$. (Note that the symbol $\vec{f}$ is used instead of F to distinguish it from the radiative flux F used throughout these notes). The magnetic field, in turn, exerts a force $f_m = q\vec{\mathrm{v}}_e \times \vec{B}$. Although f_E changes its direction as $\vec{E}$ varies, having the direction opposite to $\vec{E}$ at all times ($q < 0$), f_m is always in the direction of propagation since $\vec{\mathrm{v}}_e$ and $\vec{B}$ reverse directions simultaneously.

Thus the electron undergoes rapid oscillations in the direction of the $\vec{E}$ field, and a small increase in speed in the direction in which the light propagates. Because the time average of the transverse oscillations is zero, the net force on the electron is given by

$$< f > = q < \vec{\mathrm{v}}_e \times \vec{B} > = q\mathrm{v}_e B\hat{i} = \frac{q}{c} < \mathrm{v}_e E > \tag{1.16}$$

Power is the rate at which work is done $\frac{dW}{dt}$ and can be expressed (assuming constant forces) as

$$\vec{P} = \vec{\mathrm{v}} \cdot \vec{f} \tag{1.17}$$

$$\vec{P} = \vec{\mathrm{v}}_e \cdot (\vec{f}_E + \vec{f}_m) \tag{1.18}$$

$$= \vec{\mathrm{v}}_e \cdot (q\vec{E} + \vec{\mathrm{v}}_e \times \vec{B}) \tag{1.19}$$

$$= q < \mathrm{v}_e E > \tag{1.20}$$

Combining Eqn. (1.16) for the force, or the equivalent, for the rate of change of momentum with Eqn. (1.20), one obtains

$$< f > = \frac{P}{c} = \frac{< S > \cdot \mathrm{Area}}{c} \tag{1.21}$$

Finally, the radiation pressure, P, is given by $\frac{f}{\mathrm{Area}}$

$$\mathsf{P} = \frac{< f >}{\mathrm{Area}} = \frac{< S >}{c} \tag{1.22}$$

Equation (1.22) is appropriate if radiation is absorbed by the material. If a photon is perfectly reflected, the change in momentum is twice that computed here, and $\mathsf{P} = 2<S>/c$.

1.4 Problems

Problem 1.1

The wavelength of the radiation absorbed during a particular spectroscopic transition is observed to be 10 μm. Express this in frequency (Hz) and in wavenumber (cm^{-1}), and calculate the energy change during the transition in both joules per molecule and joules per mole. If the energy change were twice as large, what would be the wavelength of the corresponding radiation?

Problem 1.2

Electromagnetic radiation from the sun falls on top of the Earth's atmosphere at the rate of 1.37×10^{3} Wm^{-2}. Assuming this is to be plane wave radiation, estimate the magnitude of the electric and magnetic field amplitudes of the wave. The units of the electric field are m kg $s^{-2}Co^{-1}$ and the units of the magnetic field are kg $s^{-1}Co^{-1}$, which is also known as a telsa (T).

Problem 1.3

Assume that a 100 W lamp of 80% efficiency radiates all its energy isotropically. Compute the amplitude of both the electric and magnetic fields 2 m from the lamp.

Problem 1.4

The average power of a broadcasting station is 10^{5} W. Assume that the power is radiated uniformly over any hemisphere concentric with the station. For a point 10 km from the source, find the magnitude of the Poynting vector and the amplitudes of the electric and magnetic fields. Assume that at that distance the wave is plane.

Problem 1.5

A radar transmitter emits its energy within a cone having a solid angle of 10^{-2} sterad. At a distance of 10^{3} m from the transmitter the electric field has an amplitude of 10 Vm^{-1}. Find the amplitude of the magnetic field and the power of the transmitter.

Problem 1.6

Radio waves received by a radio set have an electric field of maximum amplitude equal to 10^{-1} Vm^{-1}. Assuming that the wave can be considered as plane, calculate: (a) the amplitude of the magnetic field, (b) the average intensity of the wave, and (c) the average energy density.

Assuming that the radio set is 1 km from the broadcasting station and that the station radiates energy isotropically, determine the power of the station.

AT622 Section 2
Elementary Concepts of Radiometry

The object of this section is to introduce the student to two radiometric concepts—intensity (radiance) and flux (irradiance). These concepts are largely geometrical in nature. Neither quantity varies as light propagates along.

2.1 Frame of Reference

Before considering how we might describe electromagnetic wave propagating in space in radiometric terms, it is necessary to consider ways of representing the geometry of the flow. We use a terrestrially based frame of reference such as a Cartesian coordinate system and select one of its axes to be anchored in some way according to some property of the terrestrial atmosphere.

$\hat{i}, \hat{j},$ and $\hat{k}$ are unit vectors that define three orthogonal axes. Examples of two sun-based frames of reference, where the x axis points to the sun (i.e., the azimuth angle is defined relative to the sun's azimuth), are shown in Fig. 2.1. A general reference point within a Cartesian frame of reference may be indicated by the position vector $\vec{r}$ such that

$$\vec{r} = (x, y, z),$$

where (x, y, z) defines the coordinates of the tip of this vector.

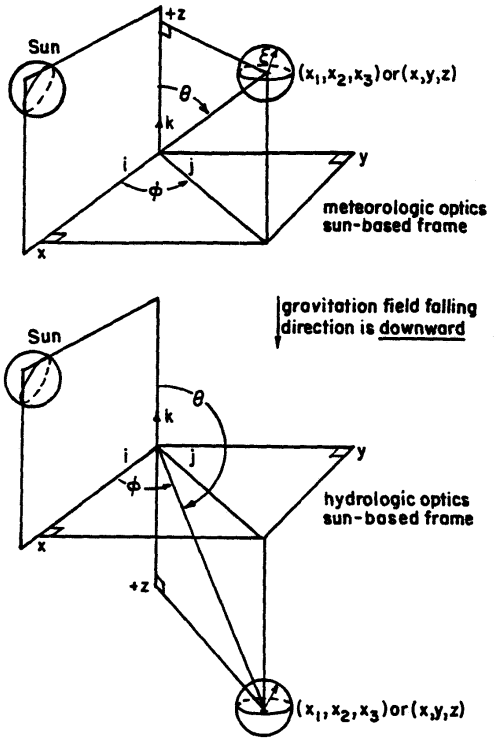

Fig. 2.1 Sun-based terrestrial frames of reference for meteorologic optics and hydrologic optics.

We define a direction vector in terms of a unit vector ($\vec{\xi}$) whose base is at the origin point and whose tip is the point (*a, b, c*) on the unit sphere that surrounds the origin. In this case, $\sqrt{a^2 + b^2 + c^2} = 1$. The unit direction vector may also be defined in terms of a general point (*x, y, z*) by

$$\vec{\xi} = \frac{\vec{r}}{|r|} = \frac{(x, y, z)}{(x^2 + y^2 + z^2)^{1/2}}.$$

A more trigonometrical interpretation of the direction vector follows by considering Fig. 2.2a. For a point (*a. b, c*) on the unit sphere, it follows that

$$a = \vec{r} \cdot \vec{i} = \cos\phi \sin\theta$$
$$b = \vec{r} \cdot \vec{j} = \sin\phi \sin\theta$$
$$c = \vec{r} \cdot \vec{k} = \cos\theta = \mu.$$

where θ is the zenith angle and ϕ is the azimuth angle. The latter, in this case, is measured positive counterclockwise from the *x* axis. Since $\vec{\xi}$ = (*a, b, c*), then

$$\vec{\xi} = (\cos\phi \sin\theta, \sin\phi \sin\theta, \cos\theta) \tag{2.1}$$

are the three components of the direction vector. We will also use $\mu = \cos\theta$ throughout these class notes.

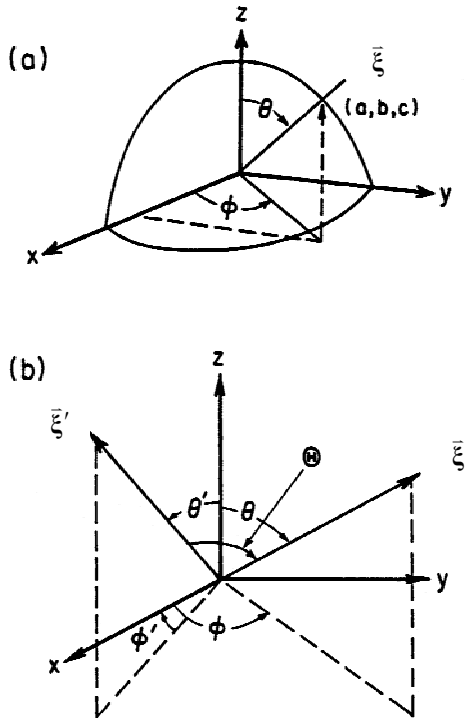

Fig. 2.2 (a) Angle and direction definitions defined with respect to a unit sphere. (b) Scattering geometry and the scattering angle on the unit sphere.

Example 2.1: Scattering angle

Many problems of interest require the definition of the angle formed between two directions. For example, the scattering angle Θ is the angle between the direction of incident radiation and the direction of the scattered radiation. If the former direction is $\vec{\xi}$ and the scattering direction is $\vec{\xi}'$ then

$$\cos\Theta = \vec{\xi}\cdot\vec{\xi}' .$$

We can schematically represent Θ and the two directions in question on a unit sphere (Fig. 2.2b). It follows from the above equation and Eqn. (2.1) that Θ can be stated in terms of two pairs of angles $\xi'(\mu', \phi')$ and $\xi(\mu, \phi)$

$$\cos\Theta = \mu\mu' + (1-\mu^2)^{1/2}(1-\mu'^2)^{1/2}\cos(\phi-\phi') .$$

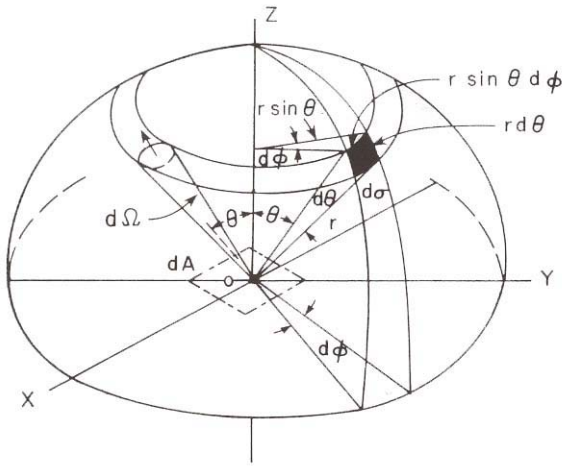

Fig. 2.3 Illustration of a solid angle and its representation in polar coordinates. Also shown is a pencil of radiation through an element of area dA in directions confined to an element of solid angle dΩ.

2.2 Solid Angle and Hemispheric Integrals

Many radiation problems, particularly those dealing with fluxes, require some type of integral over solid angle. A simple and convenient way to think about the solid angle is to imagine that a point source of light is located at the center of our unit sphere and that there exists a small hole of area A on its surface allowing light to flow through it. This light is contained in a small cone of directions, which is represented by the solid angle element Ω defined as

$$\Omega = \frac{A}{r^2} \tag{2.2}$$

With this definition, one can easily show that the solid angle with all directions around a sphere equals 4π. Referring to Fig. 2.3, one can write the differential area of the opening as

$$d\Omega = \sin\theta d\theta d\phi \,. \tag{2.3}$$

Integrating $d\Omega$ over the entire sphere

$$\Omega = \int_0^{2\pi} d\phi \int_0^{\pi} \sin\theta d\theta = 4\pi \tag{2.4}$$

yields the result we intuited earlier in Eqn. (2.2).

Suppose we now wish to integrate some function, like the intensity, over a complete hemisphere of directions. To fix ideas, consider the intensity $I(\theta,\phi)$ flowing to some point on a horizontal surface from the hemisphere above it. The hemispheric integral of this intensity is then

$$h = \int_0^{2\pi} d\phi \int_{90^\circ}^{0^\circ} I(\theta,\phi)\sin\theta d\theta = \int_0^{2\pi} d\phi \int_0^1 I(\mu,\phi) d\mu$$

An even more important quantity in radiation studies is the hemispheric flux F defined as

$$F = 2\pi \int_0^1 I(\mu,\phi)\mu d\mu \,.$$

Note how this quantity differs from h above through the appearance of the factor μ in the integrand. The hemispheric flux defined in this way is a measure of the energy flowing through a horizontal surface per unit area and per unit time (we will discuss this in a more formal way later). Recall from Section 1 that the intensity is a measure of the energy flowing though a surface normal to the flow per unit area, per unit time, and per unit solid angle. The cosine factor therefore accounts for the projection onto a horizontal surface of the area that is normal to the flow of photons.

Example 2.2: Solid angle

1) The solid angle of a spherical segment is

$$\Omega(D) = \int_{\theta_1}^{\theta_2} \sin\theta d\theta \int_0^{2\pi} d\phi = 2\pi[\cos\theta_1 - \cos\theta_2] \,.$$

2) The solid angle of a spherical cap defined by the angle θ is

$$\Omega(D) = \int_0^{2\pi} d\phi \int_0^{\theta} \sin\theta d\theta = 2\pi[1-\cos\theta]$$

For small θ, cos $\theta \rightarrow 1 - \theta^2/2 + \ldots$ and

$$\Omega(D) \approx \pi\theta^2 \,.$$

3) The solid angle of the sun is therefore

$$\Omega_\odot = \pi\theta_\odot^2$$

whereas we shall see later, $\theta_\odot \approx r_\odot / R_{S_E}$, and

$$\Omega_\odot = \pi\left(\frac{0.7\times10^6}{1.5\times10^8}\right)^2 \approx 0.684\times10^{-4} \quad \textit{steradian}$$

2.3 Basic Radiometric Concepts

Radiation is a way of transferring energy from one point to another and we now formalize a way of describing this flow. From Section 1 we learn how the energy of an EM wave is associated with the square of the amplitude of the *E* field. Now we consider the geometrical constructs of this flow of energy. These considerations are known as radiometry: **Radiation + Geometry.** Radiometry has almost become a discipline in itself—a large variety of terminologies and symbolisms exist. However, we need only consider one basic quantity from which others follow. Another point is that once we have established the nature of radiant energy, radiometry is by and large geometrical in nature.

The first basic quantity is the "radiant flux". The definition for "radiant flux" of monochromatic radiation is

$$P(v) = hv \times (n(v) \times c) \times dA \quad \text{W}(\mu\text{m})^{-1} \tag{2.5}$$

where *n(v) is* the phase space density = number of photons per unit frequency per unit volume; *hv is* the energy of each photon; and $n(v) \times c$ is therefore the number of photons per unit frequency crossing a unit area per unit time. Two quantities that follow from *P* are:

$F_v = P(v)/A$ for the area density of radiant flux [$\text{Wm}^{-2}\ \mu\text{m}^{-1}$]

which is strictly known as the flux density but we will call it flux (or irradiance and shortly dispense with the quantity *P*), and the monochromatic, or spectral intensity, or radiance

$I = P(v)/\Omega A$ [$\text{W m}^{-1}\text{sr}^{-1}\ \mu\text{m}^{-1}$] (radiance)

Example 2.3: Photon flow rate of Example 1.2

Here we estimate the rate of photon flow required to deliver a given amount of flux at a specific wavelength. We begin with Eqn. (2.5)

$$F_v = \frac{P(v)}{dA} = n(v) \times c \times hv\,,$$

such that

$$n(v) \cdot c = \frac{F_v}{hv}$$

For $F = 0.1\ \text{Wm}^{-2}$, $\lambda = 0.5\ \mu\text{m}$, $c = 3 \times 10^8$ m/s, and $h = 6.6 \times 10^{-34}$ Js, one obtains

$$n(s) \cdot c = \frac{0.1 \times 0.5 \times 10^{-6}}{6.6 \times 10^{-34} \times 3 \times 10^8} = 2.5 \times 10^{17}$$

photons of $\lambda = 0.5\ \mu\text{m}$ flow per sec through a unit area to produce 0.1 Watts of power per m^2.

There are only two ways that we need to visualize the flow of radiant energy (Fig. 2.4)—the first is as a function of direction and the second is as a function of space:

(1) For the first we imagine the radiant flux of energy *P(s)* passing through some area *dA* as in Fig. 2.4a.

(2) For the second depiction, radiant flux of energy *P(s)* passes through a single point *p* through a small set of directions *d*Ω.

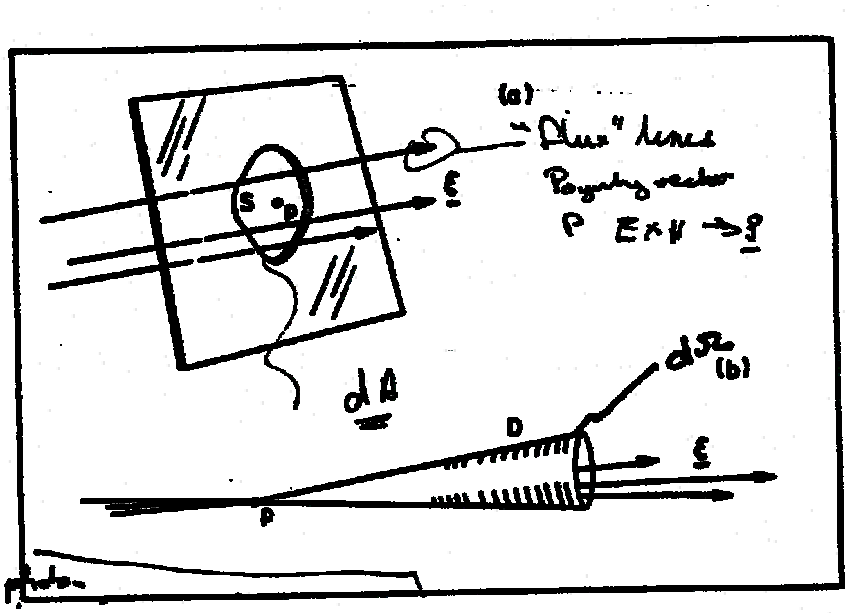

Fig. 2.4 (a) and (b) two hypothetical modes of flow of radiant energy.

(a) Spectral Intensity I

Unfortunately, the flows shown in 2.4a and b are not practical since these flow types are not measurable: an instrument detector can neither sense radiation at an infinitesimal point, since detectors have some characteristic area, nor can a detector measure purely parallel flow as they also have a characteristic angle. Consider a simple radiometer as shown in Fig. 2.5a. The detector subtends a solid angle

$$\Omega = a/\ell^{\,2}$$

where a is the area of the detector and ℓ is the length of the collimating tube. What is measured is then the quantity

$$I = \frac{P}{a \cdot d\Omega} \qquad [\mathrm{Wm^{-2}sr^{-1}}\mu\mathrm{m^{-1}}] \tag{2.6}$$

which we will refer to as either spectral radiance or spectral intensity. Radiance (intensity) is a fundamentally important quantity as it is directly measurable by instruments we call radiometers. The product of the area and solid angle $a\Omega$ is known as the 'throughput' T of the radiometer and the radiance is then P/T.

(b) Irradiance or Flux F

An even more important radiometric quantity, at least from the perspective of meteorology and climatology, is the quantity referred to as irradiance (or flux density or just flux, again remember that we will shortly dispense with *P* for the rest of this class). This quantity describes the total flow of radiant energy that flows onto or from a surface. For a general definition of this quantity, consider a surface of area *dA* and flow from two directions $\vec{\xi}_1$ and $\vec{\xi}_2$, which make angles θ_1, and θ_2 with respect to the normal $\vec{n}$ to *dA*. The radiances I_1, and I_2 define the radiation field along each direction. The flux onto *dA* is then

$$f(\vec{n}) = \frac{P}{dA} = I_1(\vec{\xi}_1)(\vec{\xi}_1 \cdot \vec{n} d\Omega_1) + I_2(\vec{\xi}_2)(\vec{\xi}_2 \cdot \vec{n} d\Omega_2) \qquad \mathrm{Wm^{-2}}\mu\mathrm{m^{-1}}$$

and in the limit that the number of sources → ∞, then

$$F(\vec{n}) = \int I(\vec{\xi}_i)\cos\theta d\Omega \tag{2.7}$$

where *F* is defined with respect to the normal $\vec{n}$ **(Note: it is only meaningful to talk of flux relative to the orientation of some surface...most of our interests are for horizontal surfaces and thus $\vec{n}$ represents either the zenith or nadir).** When the integration is carried out over the entire sphere of solid angles, this is the *net* flux that flows through the surface. It is more common to carry out this integral in two parts, one over a positive hemisphere (positive in the sense that $\vec{\xi} \cdot \vec{n} > 0$, see Fig 2.5a) and one over the corresponding negative hemisphere (Fig. 2.5b).

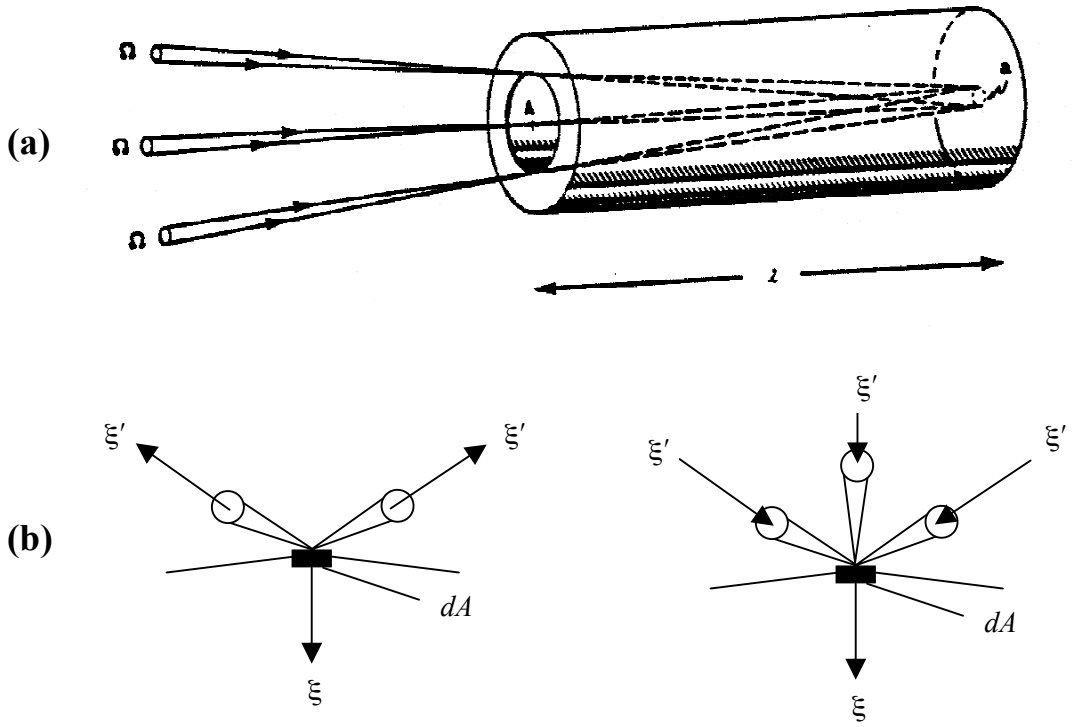

Fig. 2.5 (a) A simple radiometer and (b) hemisphere fluxes.

Example 2.4: Exploring the relation between radiance and flux

1) Consider the situation where radiation flows onto a surface defined by a discontinuity in refractive index. At the surface

$$\frac{P_1}{A_1} = F_1 = F_2 = \frac{P_2}{A_2}$$

Snell's law predicts that

$$m_1 \sin\theta_1 = m_2 \sin\theta_2 \qquad (\theta_1, \theta_2 \text{ are small by hypothesis})$$
$$m_1\theta_1 = m_2\theta_2$$

and it follows that

$$m_1^2 \Omega_1 = m_2^2 \Omega_2$$

where now we make use of our small cap approximation $\Omega = \pi\theta^2$. Since

$$\Omega_1 I_1 = F_1 = F_2 = \Omega_2 I_2$$

we obtain

$$\frac{I_1}{m_1^2} = \frac{I_2}{m_2^2}$$

Thus we take I/m^2 as the intensity when we are interested in propagation through an m varying media. The radiance from one m environment to another m environment thus needs to be adjusted by refractive index.

2) Hemispheric fluxes on a horizontal surface. The upward flux may be defined as

$$F^+ = \int_0^{2\pi} \int_0^{\pi/2} I(\theta,\phi) \cos\theta \sin\theta d\theta d\phi$$

and the downward flux is

$$F^- = \int_0^{2\pi} \int_{\pi/2}^{0} I(\theta,\phi) \cos\theta \sin\theta d\theta d\phi$$

and the net flux is $F = F^+ + F^-$. Often the limits of the θ integral for F^- are flipped, which in turn defines a positive F^- leading to an alternate definition $F = F^+ - F^-$. We will use this latter convention throughout. [Note also that the + sign on the upward flux means that the normal of the surface in question points upward along the vertical.]

Example 2.4: Continued.

3) Consider a special case of isotropic radiation (i.e., $I = I_0$ is constant), then it follows that

$$F^+ = \int_0^{2\pi} \int_0^{\pi/2} I_o \cos\theta \sin\theta d\theta d\phi = 2\pi I_o \int_0^1 \mu d\mu = \pi I_o$$

and also $F^- = \pi I_o$, *so* that $F^{net} = 0$. As much radiation flows onto the surface that leaves the surface.

4) Flux of an isotropic source on a vertical surface. Let us consider the surface in the y-z plane

$$\begin{aligned} F^{\pm} &= \int I(\xi)(\xi' \cdot \hat{i} d\Omega(\xi')) \\ &= I_o \int_{-\pi/2}^{\pi/2} \int_{\pi}^{0} \cos\theta \sin\theta d\theta d\phi = \pi I_o \end{aligned}$$

where we make use of Eqn. (2.1). Also take special note of the limits of the integration and the hemisphere these limits define.

5) The intensity and flux from the sun. We will see later how the sun radiates approximately as a blackbody of temperature $T_\odot = 5790$ K. This radiation is emitted isotropically from the sun with a broadband intensity (i.e., at an intensity that has been integrated over all wavelengths)

$$I_\odot = \frac{\sigma}{\pi} T_\odot^4 = 2 \times 10^7 \qquad [\mathrm{Wm^{-2}sr^{-1}}]$$

If we consider the geometry as shown, then the flux from the sun incident on a surface whose normal is along the direction from the point P on the earth's surface to the center of the sun is

$$\begin{aligned} F_\odot &= \int_{\Omega_\odot} I_\odot \cos\theta d\Omega \\ &= I_\odot \int_0^{2\pi} d\phi \int_0^{\theta_c} \sin\theta \cos\theta d\theta \\ &= I_\odot \pi [\sin^2 \theta_c] = I_\odot \pi \frac{r_\odot^2}{R^2} = I_\odot \Omega_\odot \\ &\approx 1380 \qquad [\mathrm{Wm^{-2}}] \end{aligned}$$

Example 2.5: The black of night: Olbers' paradox

An ancient astronomer, if asked why the night sky is black, probably would have answered that it was because the sun is absent. If we then ask why the stars don't take the place of the sun, then the likely answer is because the stars are of limited number and individually dim. This last argument has lost its force over the centuries and astronomers tell us that the number of stars occupying the night sky is tremendous indeed. We are left with a paradox of sorts—why is not the night sky as brilliant as the daytime sky filled with the light from an almost infinite number of stars. Olbers pondered this paradox and approached it with the following assumptions:

1. The universe is infinite in extent,
2. The stars are infinite in number, and
3. The stars are of uniform average brightness through all space.

He then considered space as divided into concentric shells about the observer that are large enough to be populated by stars. The amount of light that reaches us from each star (think of this as the product of $I_{\odot}\Omega_{\odot}$) varies inversely as the square of its distance from us. But as we look farther out in space the volume of the shell of space also expands (as the distance squared) in such a way that the increased number of stars in the farther shell cancels with the decreased brightness of these more distant stars.

Thus the crux of the paradox is—if the universe is infinite in extent and thus consists of an infinite number of shells, the stars of the universe, however dim they may individually be, ought to deliver an infinite amount of light to Earth. Somewhere in Olbers' paradox there is some mitigating circumstance or logical error. It is commonly thought that the failure of the above arguments occurs with assumption (3). We know that the stars of distant galaxies are receding and this movement caused a red-shift in the spectrum. With the expansion of the universe each succeeding shell delivers less light as it is subject to a successively greater red shift. Thus we receive only a finite amount of energy from the universe and the night sky is black.

2.4 Problems

Problem 2.1

Radiance of the moon and sun

(a) Calculate the solid angle subtended by the sun, and the solid angle subtended by the moon as seen from the center of the Earth.

(b) Calculate the radiance of the sun and the radiance of the moon as seen from the earth. Assume the following constants:

$$\text{SolarConstant} = 1367 \text{ Watts m}^{-2}$$

SunDiameter = 1.39 X 10^6 km
MoonDiameter = 3.48 X 10^3 km
Sun - EarthDistance = 1.49 X 10^8 km
Sun - MoonDistance = 1.49 X 10^8 km
Earth - MoonDistance = 3.8 X 10^5 km
Reflectivity of the Moon = 6.7%

Assume that the reflectance from the moon is isotropic (i.e., the moon's surface is said to be a Lambertian reflector).

Problem 2.2

A small perfectly black spherical satellite is in orbit around the earth at a height of 200 km. What solid angle does the earth subtend when viewed from the satellite? **Hint: Consider Fig. 2.6a and assume the Earth's radius to be 6370 km.**

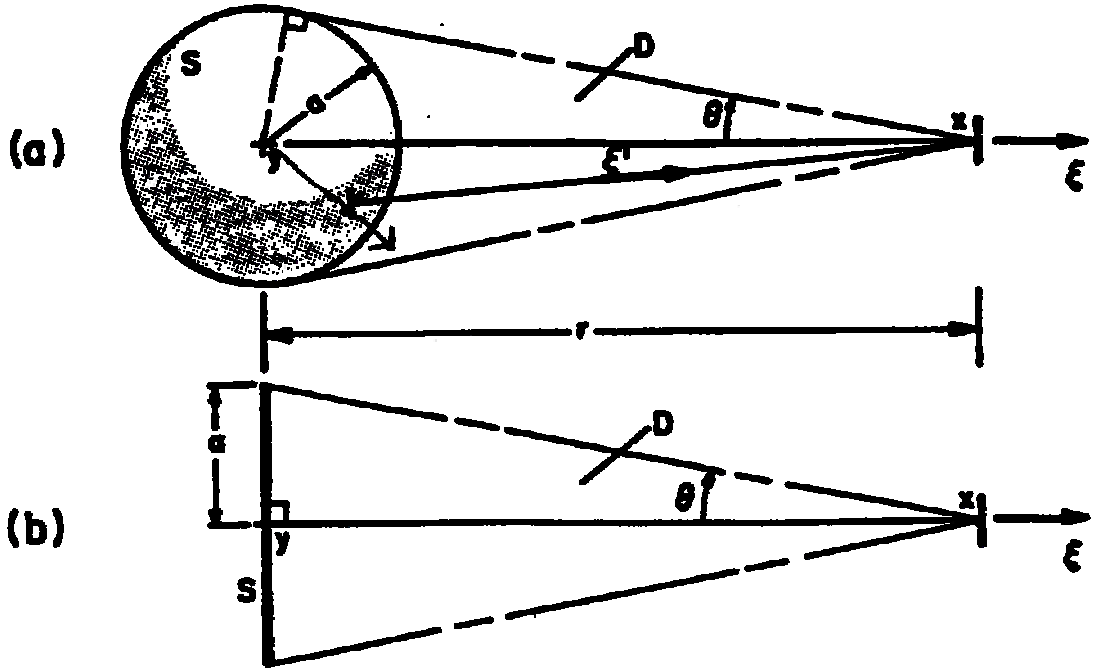

Fig. 2.6 Deriving the irradiance distance-law for spheres and disks.

Problem 2.3

Irradiance Distance Law for Spheres.

Consider a spherical surface S of radius a with uniform radiance distribution of magnitude I at each point. Suppose that S is viewed at a point x a distance r from the center y of S. The lines of sight lie in a vacuum and the background radiance of S is zero. See Fig. 2.6 (a). Derive the irradiance $F(x, \xi)$ at point x in terms of the given variables. Here ξ is the normal at x in the direction from y to x.

Problem 2.4

Irradiance Distance Law for Circular Disks

Refer to Fig. 2.6 (b). That figure depicts a circular disk of radius a of uniform surface intensity I at each point. The disk is viewed at point x on the perpendicular through the center y of S at a distance r from the center. The set D of the lines of sight from x to S lies in a vacuum and the background radiance of S is zero. What is the irradiance $F(x, \xi)$ at point x in terms of the given variables? Here ξ is the same as that in Eqn. (1.3). Compare your answer to that of problem 2.3 by determining the value of r (in units of radius α) such that the difference between the two irradiances is less than 1%.

Problem 2.5

If an incident azimuthally symmetric radiation field is described by $I(\theta) = I_o \tan\theta$, where θ is the zenith angle, briefly describe the visual appearance of such a field and derive an expression between F and I_o.

Problem 2.6

Solve the following:

(a) Using the cosine law and the definition of solid angle in the class notes, establish that the relationship between the hemispheric flux F on a horizontal surface and the intensity I flowing to that surface is

$$F = \int_0^{2\pi} \int_0^{\pi/2} I(\theta, \phi) \cos\theta \sin\theta d\theta d\phi$$

where θ is the zenith angle and ϕ is the azimuthal angle.

(b) Calculate this flux when the intensity field is uniform (isotropic) and flows through a set of directions defined by the angle θ centered on the normal to the horizontal plane. Derive this flux as a function of θ.

(c) Using your results of (b) above, show that the hemisphere flux is πI_o for an isotropic intensity field of magnitude I_o.

AT622 Section 3
Basic Laws

There are three stages in the life of a photon that interest us: first it is created, then it propagates through space, and finally it can be destroyed. The creation and destruction of a photon occurs through its interaction with matter. Here we consider the basic laws that characterize the creation of radiation by a process referred to as emission. Processes that destroy the photon, via absorption, are topics of later chapters.

3.1 Equilibrium Radiation and Kirchoff's Law

The generation of electromagnetic waves occurs as a general result of an accelerating electric charge. In general, any object is composed of a vast number of molecules that oscillate over a continuous range of frequencies and therefore emit radiation of all frequencies. However, this radiation is not emitted equally at all frequencies but is distributed in some way according to the emission spectrum, which, as we shall see, depends strongly on the temperature of the object.

The nature of the emission spectrum and its relationship to the temperature of the body loomed as a major challenge to physicists in the late nineteenth century. In fact, the relationship could not be accounted for using the principles of classical physics and its description marked one of the major turning points in the history of science. In attempting to formulate the description of the emission spectrum there emerged the hypothetical concept of a blackbody, which is a body whose surface absorbs all radiation incident upon it. It also follows that any two blackbodies at the same temperature emit precisely the same radiation and that a blackbody emits more radiation than any other type of object at the same temperature.

That it is more appropriate to view blackbody radiation as equilibrium radiation is evident by considering an isolated cavity with walls opaque to all radiation. The cavity walls constantly emit, absorb, and reflect radiation until a state of equilibrium is reached (i.e., until the temperature of the cavity walls no longer change in time). This equilibrium radiation fills the cavity uniformly and is just the same as the radiation emitted by a hypothetical blackbody at the same temperature of the cavity. To understand why this is so, imagine that a blackbody is placed in the cavity. This body absorbs the entire equilibrium radiation incident on its surface and, since the cavity is in a state of equilibrium, the radiation emitted by the object must be precisely that absorbed by it, which also happens to be the equilibrium radiation that fills the cavity. Therefore under the conditions of equilibrium, the ability of a body to radiate is closely related to its ability to absorb radiation. The mathematical formulation of this statement is known as Kirchoff's Law, which can be written as

$$E_\lambda(T) = \varepsilon_\lambda B_\lambda(T) \tag{3.1}$$

where E_λ *is* the emitted radiation and $B_\lambda(T)$ is the radiation of the hypothetical blackbody. E_λ *is* sometimes referred to as the spectral emissive power and the total emissive power is

$$E(T) = \int_0^\infty E_\lambda(T) d\lambda$$

The proportionality constant in Eqn. (3.1) is referred to as an emissivity, ε (sometimes also referred to as an absorption coefficient), which in this context varies between 0 and 1. If $\varepsilon_\lambda = 0$, then Eqn. (3.1) states that a body neither emits radiation at the given wavelength nor absorbs radiation at the same wavelength.

For $\varepsilon_\lambda = 1$ on the other hand, the emitted radiation is just blackbody radiation and the body absorbs all radiation incident upon it. As we shall see in following sections, the absorption coefficient contains information about the type of matter that emits radiation. The wavelength dependence of this coefficient varies dramatically according to the nature of the matter and the portion of the electromagnetic spectrum under consideration.

Table 3.1 Typical gray body emissivities and reflectivities for various 'opaque' surfaces. These quantities are averaged over respective terrestrial and solar emission spectra (later sections). Albedo (α) refers to the reflectivity of solar radiation. Because the sun and earth are not in thermal equilibrium, blackbody relationships between emission, absorption and reflection do not apply.

Type	**Albedo (α)**	**Emissivity (ε)**
Tropical forest	0.13	0.99
Woodland	0.14	0.98
Farmland/natural grassland	0.20	0.95
Semi-desert/stony desert	0.24	0.92
Dry sandy desert/salt pans	0.37	0.89
Water (0°-60°)[a]	<0.08	0.96
Water (60°-90°)[a]	<0.10	0.96
Sea ice	0.25-0.60	0.90
Snow-covered vegetation	0.20-0.80	0.88
Snow-covered ice	0.80	0.92

[a]The albedo of a water surface increases as the solar zenith angle increases. Ocean surface albedos are also increased by the occurrence of white caps on the waves.

Gray bodies: ε_λ is assumed constant and independent of λ.

It is through the statement of Kirchoff's Law that the whole point of blackbody radiation is relevant. All blackbodies at some temperature behave identically and the radiation emitted by such bodies at a given λ depends only on the temperature of the body. Thus the emission of radiation at some chosen wavelength is solely determined by the characteristics of the emitting matter (through a_λ) and temperature (through B_λ).

Example 3.1: Show that two blackbodies at the same temperature must emit the same radiation.

Proof of this lies in the second law of thermodynamics. In the case of two black surfaces *A* and *B* at the same temperature, suppose *A* radiates more energy than the other. Imagine placing these surfaces next to each other and allowing each to absorb the radiation from the other. Thus *B* must absorb more radiation than it emits, receiving more energy and becoming hotter. *A*, correspondingly becomes cooler. Thus the second law of thermodynamics is violated and our assumption that *A* radiates more than *B* is false.

3.2 Planck's Blackbody Function and Related Laws

The theoretical question of what form the wavelength distribution of the intensity of this cavity radiation takes and how this radiation in turn depends on the temperature of the walls of the cavity occupied the attention of many of the worlds leading physicists during the 1890's. It was Max Planck who provided us with the theoretical description of the blackbody radiation but in doing so he was forced to make an assumption that proved to be one of the most daring departures from the philosophies of physics at that time. He considered that each of the oscillators in the walls of the cavity could have only one of a discrete set of energies rather than the more conventional view that energy could assume any value above or equal to zero. The discrete energy level of the oscillator could then be represented in the form

$$E = nhv$$

where n is an integer, referred to as the quantum number, which defines the permitted number of discrete units of energy of the oscillator. The fundamental unit of energy turned out to be proportional to the frequency of the oscillator v where the proportionality constant h is known as Planck's constant. It is these discrete packets of quanta of energy that are emitted by the oscillators in the cavity walls after the oscillator undergoes a transition from one quantized energy state to another. On the basis of these arguments, Planck was able to demonstrate that the relationship,

$$B_\lambda(T) = \frac{2hc^2}{\lambda^5[e^{hc/K\lambda T} - 1]}, \tag{3.2a}$$

adequately describes blackbody radiation where K is Boltzman's constant and T is the absolute temperature of the cavity walls. It is also customary to introduce the constants

$$C_1 = 2\pi hc^2 = 3.7419 \times 10^{-16} \qquad \mathrm{Wm}^2$$

$$C_2 = \frac{hc}{\kappa} = 1.4413 \times 10^{-2} \quad \mathrm{m\,K}$$

in which case

$$B_\lambda(T) = \frac{C_1}{\pi\lambda^5[e^{C_2/\lambda T} - 1]}, \tag{3.2b}$$

where it is assumed for convenience that $c = c_o$.

The function defined by Eqn. (3.2) is known as Planck's function and is graphically portrayed in Fig. 3.1 for six different temperatures. These examples demonstrate a gross relationship that perhaps could have been anticipated. For example, consider an ordinary electrical element on a stove. On the highest and thus hottest setting the element glows brightest with a reddish hue (Fig. 3.1). When the electricity is turned off and the element is allowed to cool, the color of the element fades until its luminosity vanishes. But it is still radiating; a fact evident when a hand is placed above the cooling element. This simple experiment, known as Wein's displacement law, establishes a connection between the wavelength of maximum emission (λ_{max}) and the temperature of the radiator. This law is simply derived from

$$\frac{\partial B_\lambda}{\partial \lambda} = 0$$

from which it follows that

$$T\lambda_{max} = 2898 \text{ (}\mu\text{m °K)}. \tag{3.3}$$

Wein's displacement law is also graphically depicted on Fig. 3.1 as the diagonal line joining the maxima of the three Planck functions.

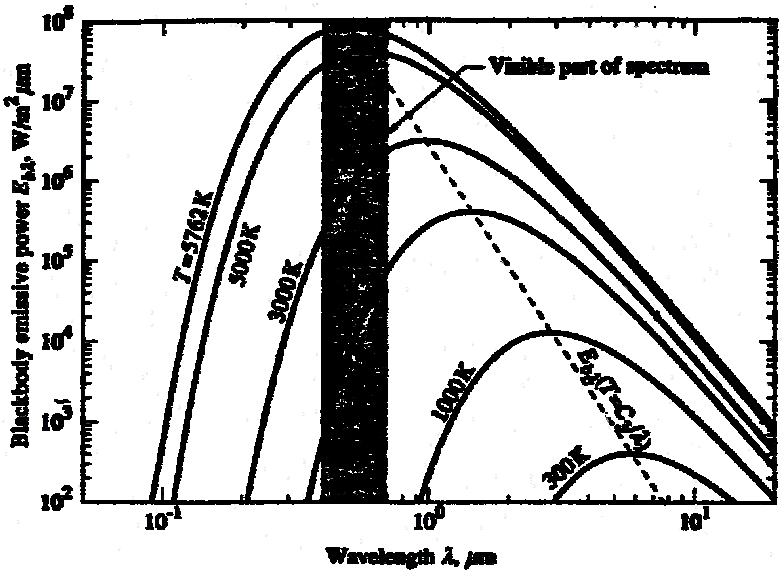

Fig. 3.1 Planck's blackbody flux curve at the three temperatures shown. The units of this function are Wm^{-2} μm^{-1}. The diagonal line intersecting the curves at their maxima depicts Wein's displacement law.

Example 3.2: What is the wavelength of the maximum emissive power of the sun? What is the corresponding wavelength of Earth? The temperature of the sun is approximately 5760K and it follows from Eqn. (3.3) that

$$\lambda_{\max} = \frac{2898}{5760} = 0.5 \text{ μm}$$

which roughly corresponds to the middle of the visible portion of the spectrum (Fig. 3.2a). Solar radiation is attenuated as it penetrates the atmosphere. Understanding this attenuation in some detail is one of the goals of this course.

Temperatures of emitters in the Earth's atmosphere vary. Assuming a value of 290K, it follows that

$$\lambda_{\max} = \frac{2898}{290} = 10 \quad \text{μm}$$

Example 3.2 Continued.

Figure 3.2a is an example of the emission spectrum at the top of the atmosphere measured at one location. This spectral emission does not follow the blackbody curve since it occurs through a kind of transfer from layer to layer in the atmosphere through a combination of absorption at low levels and emission at higher levels and at colder temperatures. The difference between the measured emission and that of a blackbody is crudely indicative of the absorption spectrum of the absorbing gases in the atmosphere. The transfer of radiation and a detailed understanding of the absorption spectrum are topics that we will return to later.

(a)

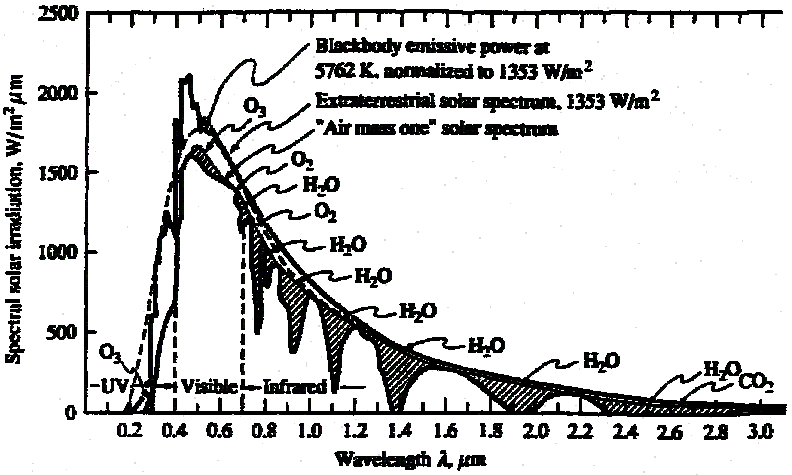

(b)

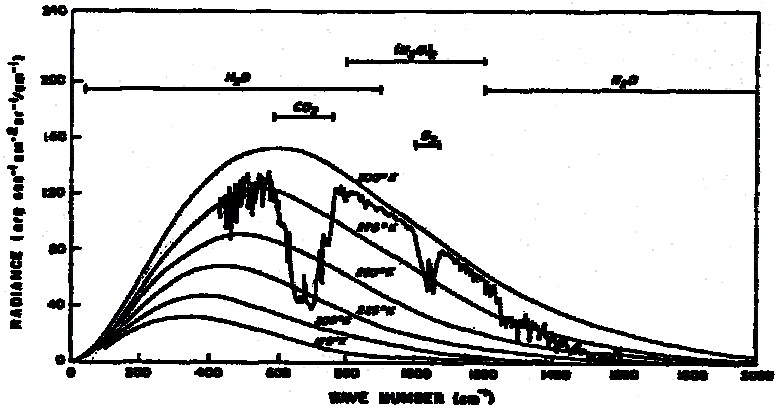

Fig. 3.2 *(a) Solar irradiation measured at the top of the Earth's atmosphere compared to that of a 5760K blackbody normalized to 1353 Wm^{-2} (the reason for this will be discussed later). Also shown in a schematic way is the irradiance at the surface under 'typical' clear sky conditions. (b) The spectrum of infrared radiation emitted to space from Earth as measured by an instrument on an orbiting satellite. This spectrum corresponds to clear sky conditions over the Saharan desert.*

There follows from Eqn. (3.2) two important limits of the Planck function. The first of these limits is referred to as Wein's distribution and applies to $\lambda \rightarrow 0$

$$B_\lambda = B_{\tilde{\nu}} = 2hc^2 \frac{1}{\lambda^5} e^{-hc/K\lambda T} \tag{3.4}$$

whereas the longer wavelength limit, $\lambda \rightarrow \infty$ is referred to as the Rayleigh-Jeans distribution, and is expressed by

$$B_\lambda = B_{\tilde{\nu}} = 2cKT \frac{1}{\lambda^4} \tag{3.5}$$

This long wave limit has a direct application to passive microwave remote sensing problems. At these wavelengths, the emission by the earth's atmosphere is directly proportional to temperature and intensity and temperature can be treated as mutually equivalent. We refer to the intensity expressed in units of temperature as the brightness temperature, which is the temperature that is required to match that measured intensity to the Planck blackbody function. For microwave radiation, this is simply obtained from Eqn. (3.5). At other wavelengths, the brightness temperature is obtained by inverting either Eqn. (3.2) or Eqn. (3.4).

3.3 Total Blackbody Emissive Power

An obvious characteristic of blackbody radiation is that the hotter the object, the greater the total amount of radiation is emitted from a given surface area. This is just a statement of Stefan-Boltzmann's law, which can be simply derived by integrating B_λ over the entire wavelength domain according to

$$B(T) = \int_0^\infty B_\lambda(T) d\lambda = \frac{C_1 T^4}{\pi} \int_0^\infty \frac{d(\lambda T)}{(\lambda T^5)\left[\exp^{C_2/\lambda T} - 1\right]} = \left[\frac{C_1}{\pi C_2^4} \int_0^\infty \frac{y^3 dy}{e^y - 1}\right] T^4$$

where $y = C_2/\lambda T$. The integral in this expression is $\pi^4/15$ and the constant

$$\sigma = \frac{\pi^4 C_1}{15 C_2^4} = 5.67 \times 10^{-8} \qquad \text{Wm}^{-2}\text{K}^{-4}$$

is the Stefan-Boltzmann constant. The total blackbody emission (intensity) thus follows

$$B(T) = \frac{\sigma}{\pi} T^4 \tag{3.6a}$$

where the reason for the appearance of the π factor arises from the properties of isotropic radiation. The hemispheric blackbody flux is thus

$$\pi B(T) = \sigma T^4 \tag{3.6b}$$

As an example, the radiation emitted from a 6000 K blackbody, for instance, is 160,000 times that emitted from a 300 K blackbody.

It is often convenient to use the Planck function defined in terms of wavenumber rather than wavelength. The relationship between these two forms is obtained from the simple requirements that the integrated energies must be an expression of Stefan-Boltzman's law. Thus

$$B_\lambda(T)d\lambda = -B_{\tilde{\nu}}(T)d\tilde{\nu}$$

and, with Eqn. (3.2a) together with the definition of $\tilde{\nu}$, it follows that

$$B_{\tilde{\nu}}(T) = \frac{2hc^2\tilde{\nu}^3}{e^{ch\tilde{\nu}/KT} - 1} \tag{3.7}$$

Many problems in atmospheric radiation require the Planck function integrated over some finitely wide spectral region, say between λ_1, and λ_2. Then

$$\int_{\lambda_1}^{\lambda_2} B_\lambda(T)d\lambda = \left[\frac{C_1}{\pi C_2^4}\int_{y_2}^{y_1}\frac{y^3dy}{e^y - 1}\right]T^4$$

cannot be evaluated analytically. The fraction of blackbody radiation between 0 and λ_1, namely

$$f(\lambda_1 T) = \frac{\int_0^{\lambda_1} B_\lambda(T)d\lambda}{\int_0^{\infty} B_\lambda(T)d\lambda} = \frac{15}{\pi^4}\int_{y_1}^{\infty}\frac{y^3dy}{e^y - 1}$$

can be evaluated numerically or using precomputed look-up tables. The spectrally integrated blackbody radiation then becomes

$$\int_{\lambda_1}^{\lambda_2} B_\lambda(T)d\lambda = \left[f(\lambda_2 T) - f(\lambda_1 T)\right]\frac{\sigma}{\pi}T^4 \tag{3.8}$$

and a program that calculates the factor in parentheses is supplied in Appendix 3A.

Example 3.3: What fraction of the total solar emission occurs at wavelengths longer than 0.7 μm?

Making use of the above mentioned program

```
program test
W2=4
W1=0.7
T=5800
frac=PLANCK(W1,W2,T)
write(*,*) 'fraction=' , frac
end
```

Distribution of the solar constant in various wavelength bands.

Band	Wavelength Interval (nm)	Irradiance (W m^{-2})	Fraction of E_s (percent)[a]
Ultraviolet and beyond	< 350	62	4.5
Near ultraviolet	350-400	57	4.2
Visible	400-700	522	38.2
Near infrared	700-1000	309	22.6
Infrared and beyond	> 1000	417	30.5
Total		1367	100.0

[a]Percentages computed from data in Thekaekara (1976).

3.4 Problems

Problem 3.1

Assuming that the normal body temperature is 37 °C, what would the emittance (i.e., how much radiation is emitted) by the body if:

(a) The body was a perfect blackbody?
(b) The body was gray with 90% absorption?

What is the wavelength of maximum emission?

Problem 3.2

Consider a room with a fireplace, which has an opening of 1 m^2. The opening is composed of 10% flame, 30% logs and 60% walls. The flames have an emittance of 0.5, while the walls and logs are black. Assume the respective temperatures of the flames to be 2000 K, of the logs, 1000 K, and of the walls, 500 K, and that only radiation energy escapes into the room. What is the total radiant power escaping the fireplace from each source and the wavelength of maximum emission from each? Explain the effect of placing a glass plate over the opening if the glass has the property of

$$\text{transmittance} = 1, \text{absorptance} = 0; \ 0 \le \lambda \le 3\mu$$

$$\text{transmittance} = 0, \text{absorptance} = 1; \ \lambda > 3\mu$$

Problem 3.3

There are two approximate forms of Planck's Law. The first is known as Wien's Law.

$$B_\lambda = c_1 \lambda^{-5} e^{-(c_2/\lambda T)} .$$

This expression is valid for very small values of λT. What would be the numerical value of T for which less than a 1% error would be incurred at 1 μm using the above approximation?

A second simiplification is the Rayleigh-Jeans approximation often applied to microwave wavelengths.

$$B_\lambda = c_2 \lambda^{-4} T$$

Derive the above expression from Planck's Law and define the 1% error threshold in terms of T and λ = 500 μm.

Problem 3.4

Convert the wavelength form of Planck's Law to the wavenumber form given below:

$$\mathcal{B}_\nu = \frac{c_1 \tilde{\nu}^3}{e^{c_2 \tilde{\nu}/T} - 1} \qquad \text{where: } \tilde{\nu} = \frac{1}{\lambda}; \quad d\tilde{\nu} = -\frac{1}{\lambda^2} d\lambda$$

Problem 3.5

Show that the maximum intensity of the Planck's function is proportional to the fifth power of the temperature. Comment.

APPENDIX 3A

```
FUNCTION PLANCK(Wl,W2,T)
C
C  Use an approximate integral scheme to evaluate the integral
C  of Planck's Law. W1 and W2 define the upper and lower wavelength extent of
C  the band in micron and T is temperature in K.
C  Output is in units of W sq m per ster (radiance units)
C  Ref:
C
       WVN1=1./(Wl*I.E-4)
       WVN2=1./(W2*1.E-4)
       X1=1.43868*WVN1/T
       X2=1.43868*WVN2/T
C
C  CALCULATE THE MEAN PLANCK FUNCTION
C
C
       PLANCK=ABS(PL(X1)-PL(X2))*SIGMAP*T**4
       write(*,*) X1,X2,WVN1,WVN2,T
       PLANCK=ABS(PL(X1)-PL(X2))
C
       RETURN
       END
 ---------------------------------------------------------------------
C
FUNCTION PL(X)
C
       INTEGER MM
       PI=3.1415926
       PL=0.0
       IF (X.GT.2.5) THEN
       DO 101 MM=1,50
       M=FLOAT(MM)
       TERM=EXP(-M*X)*(((M*X+3.)*M*X+6.)*M*X+6.)*15.0/(PI*M)**4
       PL=PL+TERM
       IF (ABS(TERM/PL).LT.1.0E-5) RETURN
101    CONTINUE
       ELSE
       PL=1.0-15.0/PI**4*x**3*
      $(1./3.-X/8.+X**2/60.-X**4/5040.+X**6/272160.-X**8/13305600.)
       ENDIF
       RETURN
       END
```

AT622 Section 4
Elementary Radiative Transfer

The aim of this section is to acquaint students with simple, basic concepts of radiative transfer as it applies to both a sourceless atmosphere and an atmosphere that contains general or arbitrary sources of radiation. The equation derived will be applied to study radiative transfer in an absorbing atmosphere in the context of infrared transfer in a clear atmosphere. Thus we begin to learn how these transfer processes shape the thermal structure of the atmosphere.

4.1 Extinction

The propagation of radiation through attenuating material undergoes changes as a result of radiative processes that take place in the medium. Extinction is one of the elementary processes affecting this transfer and it is defined as follows. The change in intensity dI_v on propagating along a path of length ds (Fig. 4.1) is empirically related to the incident intensity of the radiation via *Lambert's law of extinction*

$$dI_v = -\sigma_{ext} I_v ds \tag{4.1}$$

where σ_{ext} *is* the proportionality constant known as the extinction coefficient. This extinction may occur as a result of scattering by particles or molecules in the atmosphere, by absorption by particles and molecules in the atmosphere or by a combination of both (although the molecules that scatter radiation are, on the whole, different from the molecules that absorb radiation—The reason for this will become apparent later). Thus we can write

$$\sigma_{ext} = \sigma_{sca} + \sigma_{abs}$$

where examination of Eqn. (4.1) reveals that the quantity

$$d\tau = \sigma_{ext} ds$$

is unitless. This is a fundamental quantity known as the *optical path* and when the path is vertical, it is the *optical depth.* We will see later that there are different ways of measuring σ_{ext} and thus different complementary measures of path length ds.

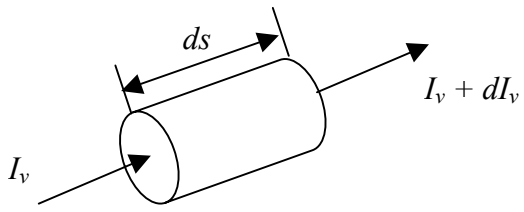

Fig. 4.1 The law of extinction.

Equation (4.1) may be readily cast into a radiative transfer equation

$$\frac{dI_v}{ds} = -\sigma_{ext,v} I_v \ , \tag{4.2}$$

which has a solution of the form

$$I_v(s'') = I_v(s')\exp(-\tau_v), \tag{4.3}$$

where $\tau_v = \int_{s'}^{s''} \sigma_{ext,v}(s)ds$ *is* the optical thickness. This solution, referred to as *Beer's law,* serves as the basis for many remote sensing applications and is a good approximation to the measurements of sunlight in the clear and relatively clean atmosphere. For example, consider the measurement of direct sunlight. If the sun is inclined at an angle $\theta_\odot$ from the vertical (the solar zenith angle), then Eqn. (4.3) becomes

$$I_v(\tau_v^*) = I_v(\tau_v = 0)\exp(-\tau_v^* / \cos\theta_\odot), \tag{4.4}$$

where τ_v^* is the optical depth. The logarithmic form of Eqn. (4.4) is

$$\ln I_v(\tau_v^*) = \ln I_v(\tau_v = 0) - \tau_v^* / \cos\theta_\odot \, . \tag{4.5}$$

Figure 4.2 is an example of this type of relationship derived from radiometer (pyrheliometer) measurements obtained at the Manua Loa Observatory. The data are from a spectral radiometer pointed towards the sun and measurements are recorded as the sun moves across the sky throughout the course of a day. If the logarithms of these measured intensities are plotted as a function of $\sec\theta_\odot$ then the optical depth τ_v^* is the slope of the line and the incident intensity $I_v(\tau_\lambda = 0)$ is given by the intercept determined by extrapolating $\sec\theta_\odot$ to zero. From this diagram we see how the clear sky measurements of solar fluxes at the wavelengths of the filters used is very closely represented by Lamberts law.

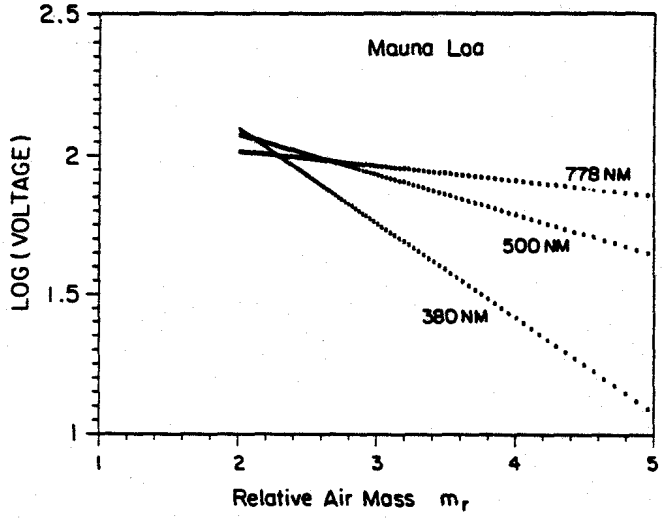

Fig. 4.2 An example of a Lambertian plot: the logarithm of solar intensity is plotted as a function of optical air mass for clear, stable atmospheric conditions.

Example 4.1 Extinction—it's black and white.

The experimenter who observes that extinction has taken place by measuring radiation at two levels in the atmosphere cannot determine if the radiation is decreased because it is absorbed or decreased because it is scattered. A simple illustration of this elementary point is well described by Bohren (1987) and is highlighted in Fig. 4.3. One cannot distinguish between the images of two water-filled glass petri dishes projected on a screen yet their darkness arises from different mechanisms. Light incident on the inky water is attenuated mainly by absorption, whereas light incident on the milky water is mostly scattered. It is only by looking at the dishes that this difference between them becomes apparent. An important scattering parameter that helps quantify these differences is the *single scattering albedo* $\tilde{\omega}_o$. This parameter is the ratio of the amount of scattering that attenuates the light to the total extinction (absorption *plus* scattering). For the milky water we might infer that $\tilde{\omega}_o \approx 1$ since light is primarily scattered in all directions from the dish. On the other hand, $\tilde{\omega}_o \approx 0$ for inky water little light is scattered and most of the extinction occurs through absorption. We will see later how the parameter $\tilde{\omega}_o$ is fundamental to problems of multiple scattering and thus for understanding how radiation is transferred from layer to layer in clouds.

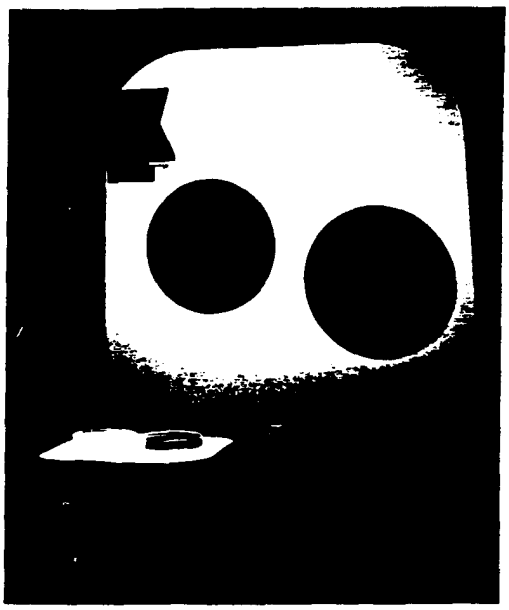

Fig. 4.3. The images of two water-filled glass beakers projected on a screen are identical yet their darkness (extinction) arises from different mechanisms. Light incident on the inky water is attenuated mainly by absorption, whereas light incident on the milky water is attenuated mostly by scattering. It is only by looking at the beakers that this difference becomes apparent.

4.2 Adding Sources of Radiation

Example 4.1 illustrates how multiple scattering confuses the interactions between radiation and the atmosphere. For example, photons originally scattered away from the viewing direction can reappear, and scattering can also cause photons to arrive having been incident from some other direction. Multiple scattering acts as a kind of source of radiation (this is sometimes referred to as virtual emission).

Whether it is real emission (governed by Kirchoff's law, Section 1) or virtual emission that contributes to a beam as it traverses a path of length *ds,* the increased intensity may be expressed as

$$dI_\nu = \sigma_{ext,\nu} J_\nu ds, \tag{4.6}$$

which defines the *source function* J_ν. When this emission takes place in the lower atmosphere where thermodynamic equilibrium occurs, $J_\nu = \mathcal{B}_\nu$.

The net change in radiation along a path element, *ds,* due to the combination of emission and extinction is

$$dI_\lambda = dI_\lambda(\text{emission}) + dI_\lambda(\text{extinction}). \tag{4.7}$$

and with the combination of Eqns. (4.1) and (4.6) we obtain

$$\frac{dI_\nu}{ds} = -\sigma_{ext,\nu}[I_\nu - J_\nu], \tag{4.8a}$$

4.3 A Radiative Transfer Equation for Absorption/Emission

In many problems of infrared radiative transfer that interest the atmospheric scientist it is reasonable to neglect scattering so we can substitute σ_{abs} for σ_{ext}. Then substituting Eqns. (4.1) and (4.6) in Eqn. (4.7), we obtain the following transfer equation

$$\frac{dI_\nu}{ds} = -\sigma_{abs,\nu}[I_\nu - \mathcal{B}_\nu], \tag{4.8b}$$

which is the mathematical relationship describing how radiation is transferred from one layer to another layer as a result of absorption and emission. The amount of radiation leaving the end of the path is a function of the distribution of absorber along the path (we will see that this is implied in $\sigma_{abs,\nu}$) and the distribution of temperature (through the presence $\mathcal{B}_\nu$).

In general, the interactions between radiation and the gases of the atmosphere are weak enough that the photon mean free path exceeds the mean free path of molecules. Hence, the radiative transfer in the atmosphere tends to be nonlocal requiring integration of processes along the path. To derive this integral form of the radiative transfer equation, we first make use of the definition, $d\tau_\nu(s) = -\sigma_{abs,\nu}(s)ds,$ for an element of the optical thickness (the reason for the negative sign in this definition of optical thickness becomes evident below) and then multiply each side of Eqn. (4.8b) by the factor $\exp(-\tau_\nu(s))$. Combining terms, we obtain

$$\frac{dI_\nu e^{-\tau_\nu(s)}}{d\tau_\nu} = -\mathcal{B}_\nu e^{-\tau_\nu(s)}. \tag{4.9}$$

Consider a general path extending from some point $s = s'$ to an end point $s = s''$. Then simple integration of Eqn. (4.9) from $\tau(s')$ to $\tau(s'')$ yields

$$I(s'')e^{-\tau_\nu(s'')} - I(s')e^{-\tau_\nu(s')} = \int_{\tau(s')}^{\tau(s'')} \mathcal{B}[\tau(s)]e^{-\tau(s)}d\tau(s)$$

which, on rearrangement, gives

$$I(s'') = I(s')e^{-[\tau(s')-\tau(s'')]} + \int_{\tau(s')}^{\tau(s'')} \mathcal{B}[\tau(s)e^{-[\tau(s)-\tau(s'')]}d\tau(s) \tag{4.10}$$

where the frequency dependence of all factors (we could have equally used wavelength rather than frequency here) in Eqn. (4.10) is taken to be understood. The first term on the right-hand side of this equation represents the radiation, originally incident at s', that is transmitted to s''. We will refer to this as the surface term. The integral term represents the emitted radiation that accumulates along the path and transmitted to s''.

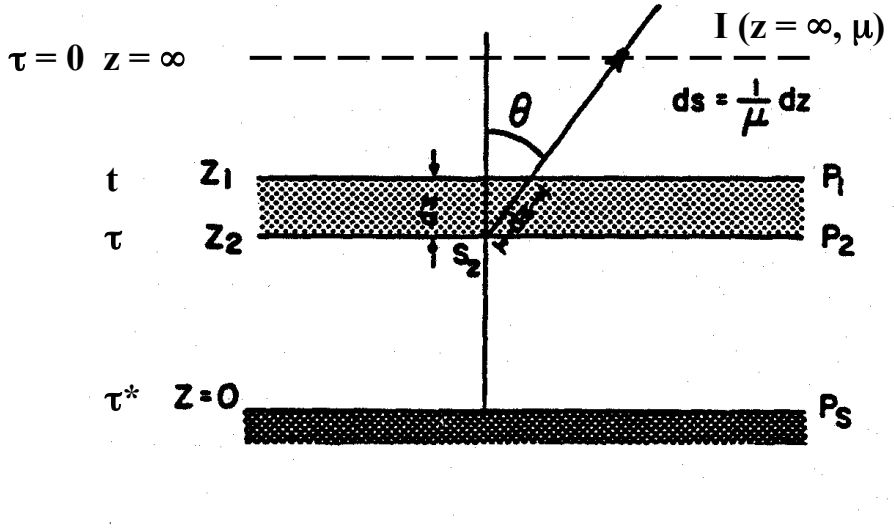

Fig. 4.4 The geometric setting for the integral transfer equation in a plane parallel vertically stratified atmosphere.

When Eqn. (4.10) *is* applied to the atmosphere (Fig. 4.4), it is customary, but not necessarily realistic, to assume that the atmosphere is plane parallel and horizontally homogeneous. For such a stratified atmosphere, the integral equation can be expressed in terms of optical depth $\tau(z)$ (rather than optical thickness $\tau(s)$). It is conventional to define the optical depth such that $\tau = 0$ at the top of the atmosphere and $\tau = \tau^*$ at the surface.[1] For slant paths, the expression relating optical depth to optical path is

$$\tau(s) = \tau(z)/\cos\theta.$$

[1] The convention that τ increases downward from the top of the atmosphere has roots in the traditional astrophysics literature on radiative transfer where τ is taken to increase along the direction of sunlight entering the atmosphere. Optical depth increases in the oppposite sense to z and hence the negative sign in its definition.

producing

$$I(\tau,+\mu) = I(\tau^*,-\mu)e^{-(\tau^*-\tau)/\mu} + \int_{\tau}^{\tau^*} \mathcal{B}(t)e^{-(t-\tau)/\mu}\frac{dt}{\mu} \tag{4.11a}$$

for $0 < \mu < 1$, which defines radiation that upwells from the atmosphere, and

$$I(\tau,-\mu) = I(0,-\mu)e^{-\tau/|\mu|} + \int_{0}^{\tau} \mathcal{B}(t)e^{-(\tau-t)/|\mu|}\frac{dt}{|\mu|} \tag{4.11b}$$

for $0 > \mu > -1$ for downwelling radiation.

Figure 4.5 is an example of a measured intensity spectrum obtained from an interferometer instrument flown on Nimbus 4. Superimposed on the measurements are the blackbody curves for selected temperatures. Also highlighted are spectral positions of the absorption bands of the predominant absorbing gases. This diagram more clearly shows how emissions from different levels in the atmosphere (and therefore at different temperatures) combine to produce the observed spectra. For instance, emission in the central portions of the 9.6 μm ozone band occurs at temperatures below about 250 K, and emission in the 15 μm CO_2 band varies throughout the atmosphere according to the spectral position relative to the band center. For both O_3 and CO_2, the increase in emitted radiation in the strongest part of the center of the absorption band occurs higher up in the atmosphere than in the neighboring spectral regions and is an indication of the increase in temperature with increasing altitude in the stratosphere. Also noteworthy is the water vapor emission that is confined to the lower atmosphere (emission by the vibration and rotation bands is broadly characterized by the 275 K blackbody curve for this example). An important spectral region is the atmospheric window between about 800 cm^{-1} and 1200 cm^{-1} in which the atmosphere is almost transparent (except for the ozone band) and the emission originates from levels close to the surface.

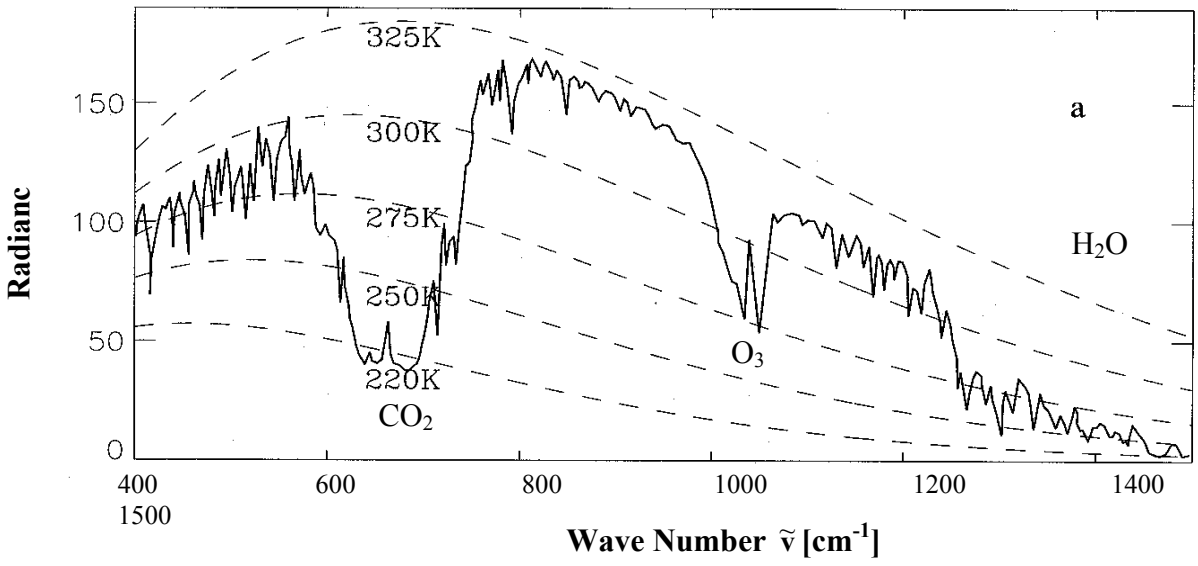

Fig. 4.5 Earth's emission spectrum seen at the top of the atmosphere.

Example 4.2: Radiative transfer in an isothermal atmosphere

Consider a simple demonstration of Eqn. (4.11): Isothermal atmosphere

- an isothermal atmosphere, $\mathcal{B}(t) = \mathcal{B}$. Thus

$$I(\tau^*, \mu) = \mathcal{B}(1 - e^{-\tau^*/\mu}).$$

This leads to limb brightening for downwelling radiation at $\tau = \tau^*$ and isotropic fields for the upwelling intensity at $\tau = 0$ since

$$I(0, \mu) = \mathcal{B}e^{-\tau^*\mu} + \mathcal{B}(1 - e^{-\tau^*/\mu}) = \mathcal{B}\ .$$

- For the nonisothermal problem, the solutions for the intensities and fluxes become much more complex. For illustrative purposes, assume the Planck function to be linear in optical depth. Let $\mathcal{B}_o$ and $\mathcal{B}^*$ be the Planck functions at the top ($\tau = 0$) and bottom of the atmosphere, respectively. It is easily shown that

$$I(\tau^*, \mu) = \mathcal{B}_o(1 - e^{-\tau^*/\mu}) + (\mathcal{B}^* - \mathcal{B}_o)\left(1 - \frac{\mu}{\tau^*}\left(1 - e^{\tau^*/\mu}\right)\right)$$

(Limb Brightening)

$$I(0, \mu) = \mathcal{B}^* e^{-\tau^*/\mu} + \mathcal{B}^*(1 - e^{\tau^*/\mu}) - (\mathcal{B}^* - \mathcal{B}_o)(1 - e^{-\tau^*/\mu})$$

(Limb Darkening)

when $\mathcal{B}(\tau) = \mathcal{B}_o + (\mathcal{B}^* - \mathcal{B}_o)\tau/\tau^*$. Generally the angular variation of upwelled radiation is less marked than that of downwelled radiation.

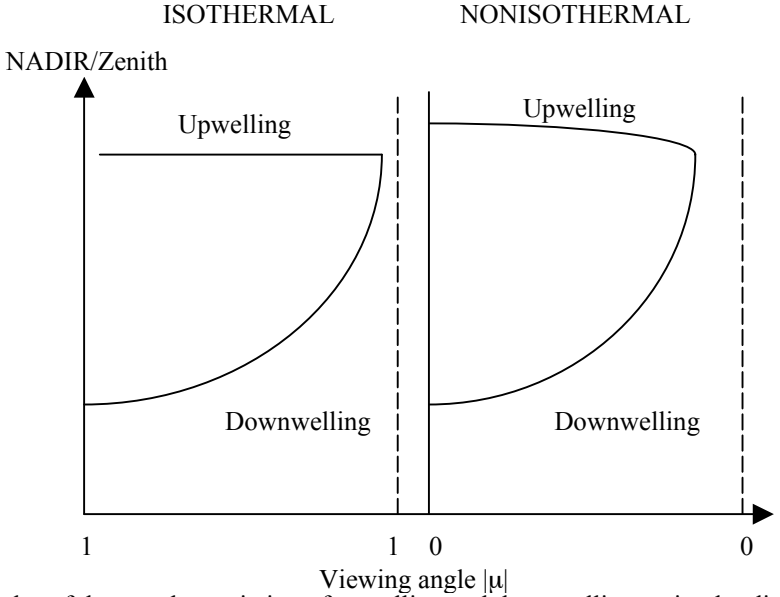

Examples of the angular variation of upwelling and downwelling emitted radiation.

Example 4.3: The exponential integral, flux equation and diffusivity

We adopt the transfer equations above to obtain fluxes. We choose to demonstrate this using Eqn. (4.11a), which is integrated as follows:

$$2\pi\int_0^1 I(\tau,+\mu)\mu d\mu = 2\pi\int_0^1 I(\tau^*,\mu)e^{-(\tau^*-\tau)/\mu}\mu d\mu +$$
$$2\pi\int_0^1 d\mu\int_\tau^{\tau^*}\mathcal{B}(t)e^{-(t-\tau)/\mu}dt$$

which becomes

$$F^+(\tau) = \pi I_s\int_0^1 e^{-(\tau^*-\tau)/\mu}\mu d\mu + 2\int_\tau^{\tau^*}\pi\mathcal{B}(t)\int_0^1 e^{-(t-\tau)/\mu}d\mu dt$$

where the surface radiation is taken to be isotropic. Introducing the exponential integral function

$$E_n(x) = \int_1^\infty e^{-xt}\frac{dt}{t^n} = \int_0^1 \mu^{n-2}e^{-x/\mu}d\mu$$

then the flux equation becomes

$$F^+(\tau) = \pi I_s 2E_3(\tau^*-\tau) + 2\int_\tau^{\tau^*}\pi\mathcal{B}(t)E_2(t-\tau)dt$$

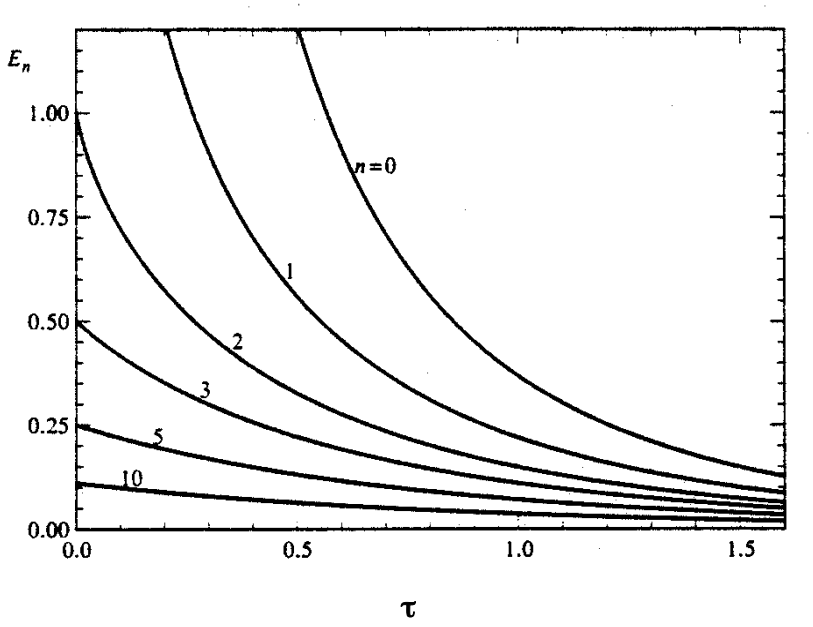

General behavior of the exponential integral. Shows also that $2E_3(x) \approx \exp(-\beta x)$ where $\beta = 1.66$ and is known as the diffusivity factor. We return to this factor and its interpretation later, but note that it represents a transmission function for flux.

4.5 Problems

The attached diagram presents the emission spectrum measured by an interferometer on a satellite viewing Earth.

(1) Identify major absorption features in the spectrum.
(2) What conditions (clear sky or cloudy, dry or moist atmosphere) do you think are applicable to measured spectrum?
(3) Draw a schematic of the **difference** in the emission spectrum before and after a CO_2 doubling has occurred. Consider only clear sky conditions and the following two scenarios:

   a. CO_2 doubling with fixed absolute humidity
   b. CO_2 doubling with fixed relative humidity

   Briefly discuss the different spectra highlighting key features as they relate to a CO_2 increase (you may wish to draw these spectra as applied to global mean conditions).

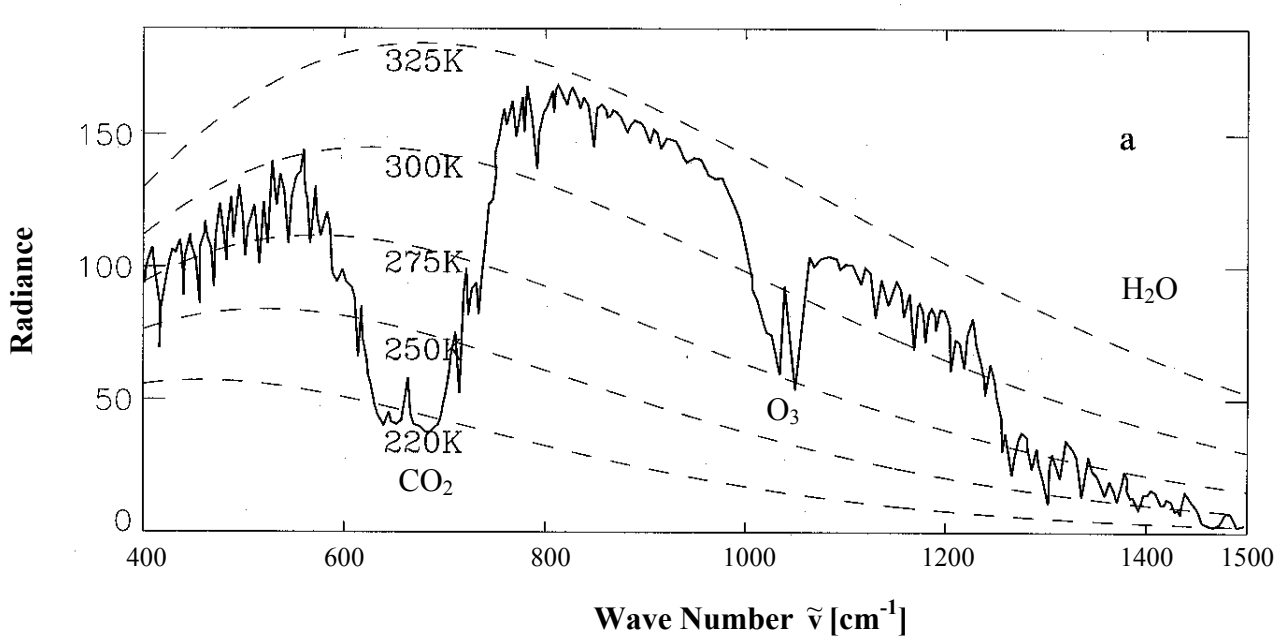

Earth's emission spectrum seen at the top of the atmosphere.

AT622 Section 5
The Sun

The main aim here is to acquaint the student with basic radiative properties of the sun and the factors that govern the disposition of solar radiation received at Earth.

5.1 The Solar Atmosphere

The sun is an entirely gaseous star composed of hydrogen (75%) and helium (25%). It is approximately 4.6 billion years old and located approximately 1.5 x 10^8 km from the Earth. It accounts for virtually all energy received by Earth and is responsible for circulation of the Earth's atmosphere and oceans. The solar atmosphere is portrayed in Fig. 5.1. The bulk of the electromagnetic radiation emitted from the sun and received at Earth arises from the vicinity of the photosphere.

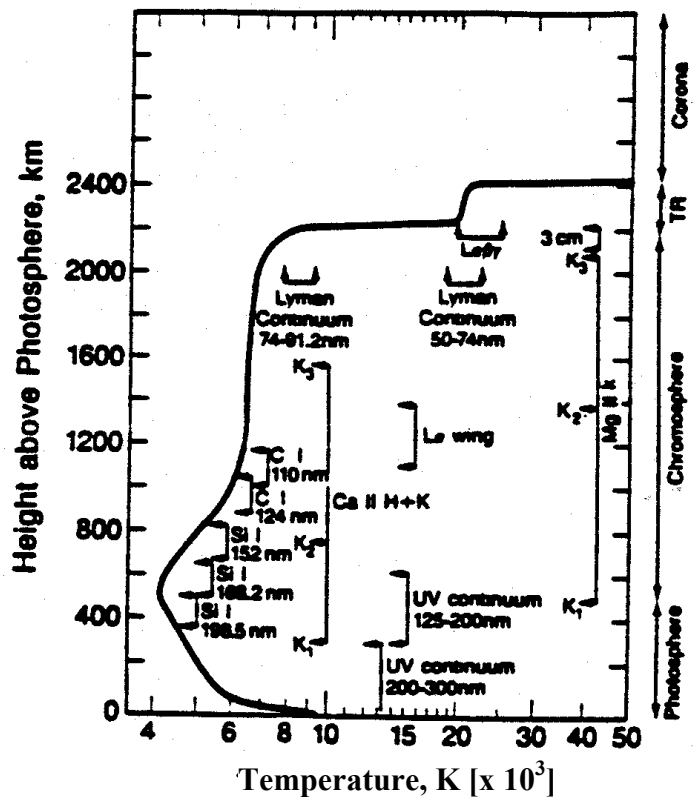

Fig. 5.1 A schematic cross section of the solar atmosphere.

The sun's emission is much like that of Earth in that it is a result of superimposing emissions from several regions within its own atmosphere. The emission from the sun is entirely analogous to the Earth's emission spectrum already shown previously where radiation arises from different levels according to the wavelength of the emission. Absorption/emission is stronger at shorter and longer wavelengths (Fig. 5.2a and c) of the solar spectrum where absorption within the atmosphere is largest (Fig. 5.2b) observe greater variability in emission due to solar activity. The emission at these extreme wavelengths originates in the rarefied corona at temperatures exceeding 10^6 K.

The intensity of solar radiation from the UV to far infrared approximately follows the 5785 K blackbody curve (Fig. 5.2a,b). The emissions at wavelengths shorter than 0.1 μm and longer than 1 cm are coronal, and highly variable. These emissions are related to measures of the solar activity, such as the sunspot number (Fig. 5.3a and b and see further discussion later). The spectrally integrated or total irradiance (i.e., the area under the curve) is a quantity that is most important for various atmospheric science applications. This irradiance measured at the top of the Earth's atmosphere under certain fixed conditions is paradoxically termed the solar constant.

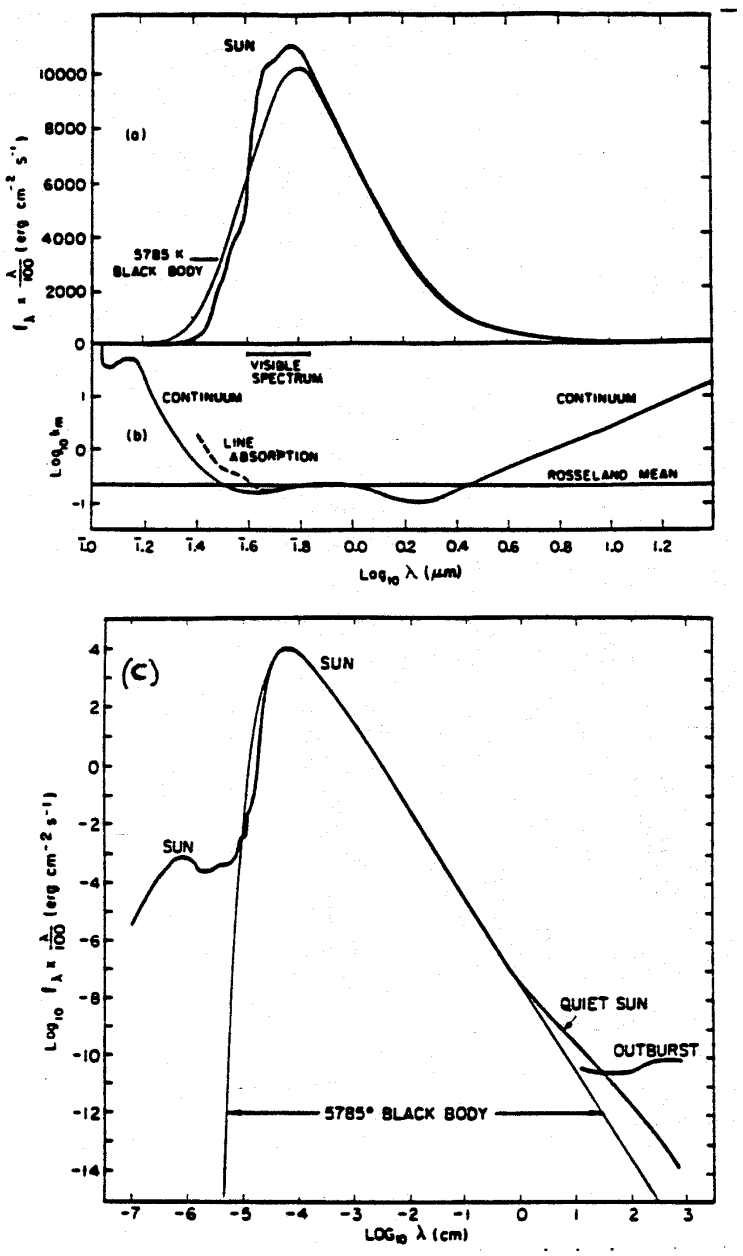

Fig. 5.2 Spectrum of solar emission and photospheric absorption. (a) Solar spectrum compared to that of a 5784 K blackbody. The method of plotting gives areas ($f_\lambda \lambda d \log_{10}\lambda/100$) proportional to energy flow ($f_\lambda d\lambda$). (b) Mass absorption coefficient for the photosphere at a temperature of 5785 K. After Allen (1958). (c) The solar irradiance.

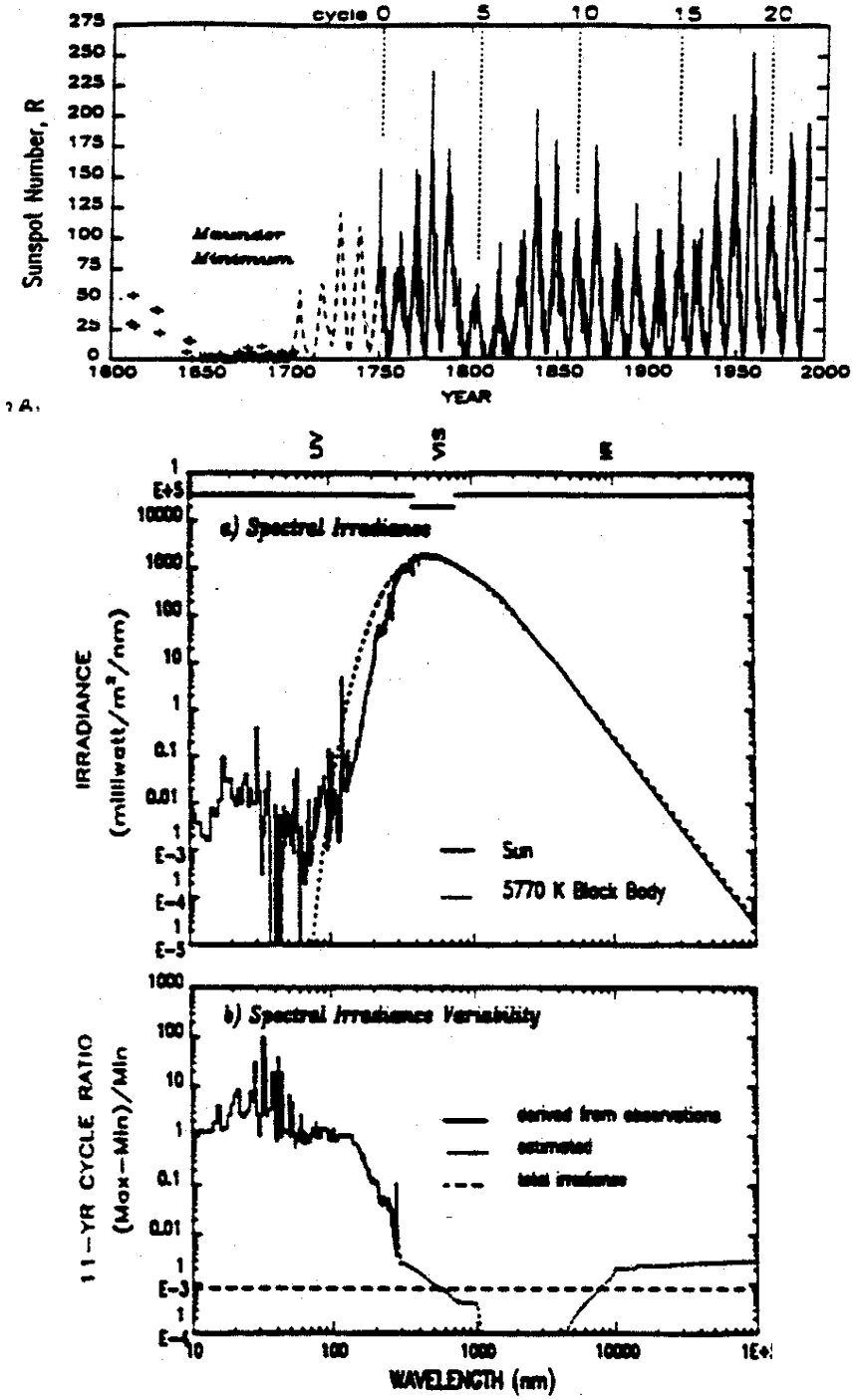

Fig. 5.3 Solar activity as defined by the sunspot number (a) undergoes a distinct cycle, which affects the radiant output (b).

5.2 The Solar Constant

According to our understanding of blackbody emission, a 5785 K hot body like the sun emits substantially more than a 288 K blackbody (in fact $(5785/288)^4 \approx 163{,}000$ times more). How can the Earth be in a state of radiative equilibrium: an observed equilibrium established by a balance between incoming solar and emitted longwave radiation? The answer simply lies in the dilution of the sun's radiation as it radiates out from the sun and reaches Earth.

We calculate the effect of this dilution as follows. The spectrally integrated radiation emitted by the sun and received at the top of the Earth's atmosphere is

$$Q_{\odot} = \int_0^{\infty} F_{\odot,\lambda} d\lambda \approx \frac{\sigma T_{\odot}^4}{\pi} \Omega_{\odot} \approx 1370 \text{ Wm}^{-2} \tag{5.1}$$

which, when calculated assuming the mean sun-Earth distance, is termed the *solar constant* and hereafter is denoted as $Q_{\odot}$ - **Note that by definition, the solar constant does not vary with the position of** the **Earth relative to the sun.** The *spectral* flux, defined by substituting B_{λ} for $\sigma T_{\odot}^4 / \pi$ in Eqn. (5. 1) will be referred to as the 'spectral solar constant' $F_{\odot,\lambda}$. $Q_{\odot}$ was traditionally difficult to measure but recent instrumentation flown on satellites offer clear evidence of its variability and the magnitude of this variability.

Example 5.1: Overlapping solar and terrestrial radiation

Using both the Planck routine program, developed in Section 3, determine the fraction of the total solar radiation that falls at wavelengths below 4 μm and the fraction of radiation emitted by a 288 K blackbody at wavelengths longer than 4 μm.

```
program test
    W2=200
    W1=4
    T=288
    frac=PLANCK(W1,W2,T)
    write(*,*)'fraction=' , frac
    end
```

Output, fraction =0.998

```
program sun
    W1=0.2
    W2=4
    T= 5785
    frac= PLANCK(W1,W2,T)
    write(*,*)'fraction=' , frac
    end
```

Output, fraction =0.992

This exercise illustrates an important practical point in atmospheric physics in that only 0.8% of the total extra-terrestrial solar flux resides in wavelengths longer than 4 μm (it is actually even less than this as the energy blow of 0.2 μm is excluded in function solar). On the other hand, only about 0.2% of the total IR radiation from a 288 K blackbody resides in wavelengths shorter than 4 μm. Thus from a total energetics point of view, solar and terrestrial radiation can be treated independently due to the combination of both the dependence of blackbody radiation with temperature and the dilution of the sun's radiation as it flows to Earth.

5.3 The Solar Insolation

We will refer to the solar flux incident on a horizontal plane as solar insolation. At the top of the atmosphere, this insolation depends on the latitude, season and time of day as is expressed in the relationship

$$F_\lambda = F_{\odot,\lambda}\left(\frac{\overline{R}_{s-E}}{R_{s-E}}\right)^2 \cos\theta_\odot \tag{5.2}$$

which is the insolation at any given instant of time. $R_{s\text{-}E}$ is the sun-Earth distance at the time of observation, $\overline{R}_{s-E}$ is the mean sun Earth distance and $\theta_\odot$ is the solar zenith angle (i.e., the angle between the local normal to Earth's surface and a line at the Earth's surface to the sun). According to this expression we acknowledge that the insolation received at the top of the atmosphere depends on

- Variations of sun-Earth distance, which in turn depends on variations in the eccentricity of the orbit of the planet around the sun.

- The sun's elevation (through $\theta_\odot$, which is influenced by astronomical factors as we will soon see). The dependence of insolation on these orbital properties was recognized by Milankovitz in his proposition that variations in these properties is the cause for ice ages on Earth.

5.4 Orbital Influence on the Insolation

Figure 5.4 illustrates the general characteristics of the Earth's orbit about the sun. The sun is situated at the focus of an ellipse and the changing Earth-sun distance as the Earth orbits around the sun, determined by the eccentricity of the orbit, creates asymmetries in solar insolation. The four reference points on this orbit, labeled 1 - 4, are the cardinal points that are used to delineate Earth's seasons.

(a) Eccentricity

The eccentricity defines the flatness of the orbital ellipse. For Mercury and Pluto, $e \sim 0.2$ and these planets are substantially closer to the sun at perihelion than at aphelion. For earth, $e \sim 0.017$ and Mars $e \sim 0.093$. In the simplest climatological sense, the summers of the southern hemisphere are hotter and winters are colder based on proximity to the sun (e.g., the Martian northern polar cap persists through summer but the southern hemisphere cap disappears).

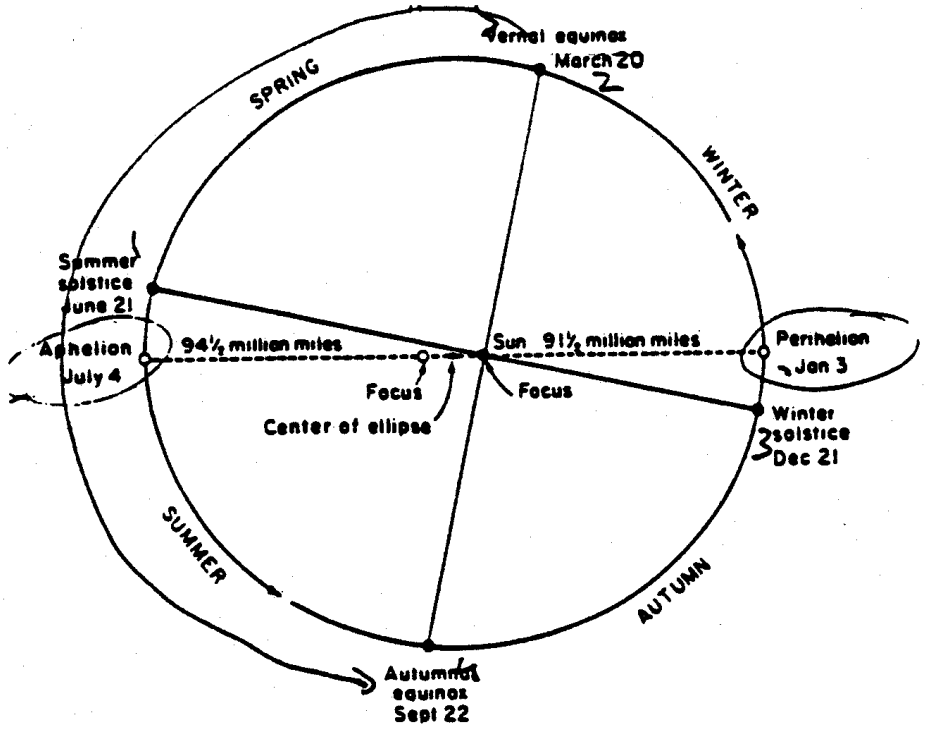

Fig. 5.4 *Dates of equinox and solstice. At the equinoxes, the Earth's axis is pointed at right angles to the sun, and day and night are of equal length all over the globe. At the summer solstice, the North Pole is tipped in the direction of the sun and the northern hemisphere has the longest day of the year. At the winter solstice, the North Pole is tipped away from the sun, and the northern hemisphere has the shortest day of the year.*

Example 5.2: The Effect of eccentricity on solar radiation received on Earth

At perihelion, $R_{s-E} / \overline{R}_{s_E} = 0.983$ and the flux received at the top of the atmosphere is

$$F_{\odot} = Q_{\odot}\left(\frac{\overline{R}_{s_E}}{R_{s-E}}\right)^2 = 1370 \times 1.035 = 1419$$

and at aphelion, $R_{s-E} / \overline{R}_{s_E} = 1.017$ leading to

$$F_{\odot} = Q_{\odot}\left(\frac{\overline{R}_{s_E}}{R_{s-E}}\right)^2 = 1370 \times 0.967 = 1325$$

Thus the amplitude of the variation of the solar insolation at the top of the atmosphere is 93 Wm^{-2}.

(b) Solar Zenith Angle (also see Sellers, Physical Climatology, p. 13-28)

The other principal factor that defines the solar insolation received by a horizontal surface at the top of the atmosphere is the solar zenith angle $\theta_\odot$.

$$\cos \theta_\odot = \sin \phi \sin \delta + \cos \phi \cos \delta \cos h \tag{5.3}$$

where ϕ is the latitude, δ is the declination and h is the hour angle.

The declination, δ, is defined as the angle formed between the equator and plane of orbit. This parameter has a substantial impact on how the solar radiation is distributed over the globe and thus on how and why seasons occur on Earth (Figs. 5.5a, b, c).

$$\delta \approx -23°27' \times \cos\left[\frac{360}{360.25} \times (JD + 9)\right]$$

where *JD* is Julian Day.

The hour angle, h, is defined by ±15° each hour before or after solar noon. Account must be taken for all observers not at an integral meridian.

> Denver is located at 105°W, or exactly 7 hours before GMT. Local noon occurs at 12:00. Salt Lake City is 7° further west but in the same time zone. At 12:00, the hour angle is therefore +7°, while at 1:00 p.m. the hour angle is -8°.

(c) Solar Azimuth Angle

The solar azimuth angle is given by

$$\sin \xi = \frac{\cos \delta \sin h}{\sin \theta_\odot}$$

where ξ is referenced to the south. $\xi > 0$ is eastward and $\xi < 0$ is westward.

The mean total daily insolation is also a quantity of some interest in climatological studies

$F = Q_\odot \times$ fractional day length $\times \cos \bar{\theta}_\odot$

Fractional day length is determined as $2H$, and

$$\cos \bar{\theta}_\odot = \int_{\text{day length}} \cos \theta_\odot dt \Big/ \int dt$$

Values are tabulated in Table 5.1 and shown graphically in Figs. 5.5b and c. As we shall see, the product of the fractional day length by $\cos \theta_\odot = 1/4$ on the global average.

Figure 5.6a shows the distribution of daily insolation as a function of latitude and month. Of note are

- locations of maximum and minimum values and the relation of these to astronomical factors
- latitudes of smallest and largest seasonal variations
- asymmetrical hemispheric distribution, and
- typical values of the insolation at low, middle, and high latitudes.

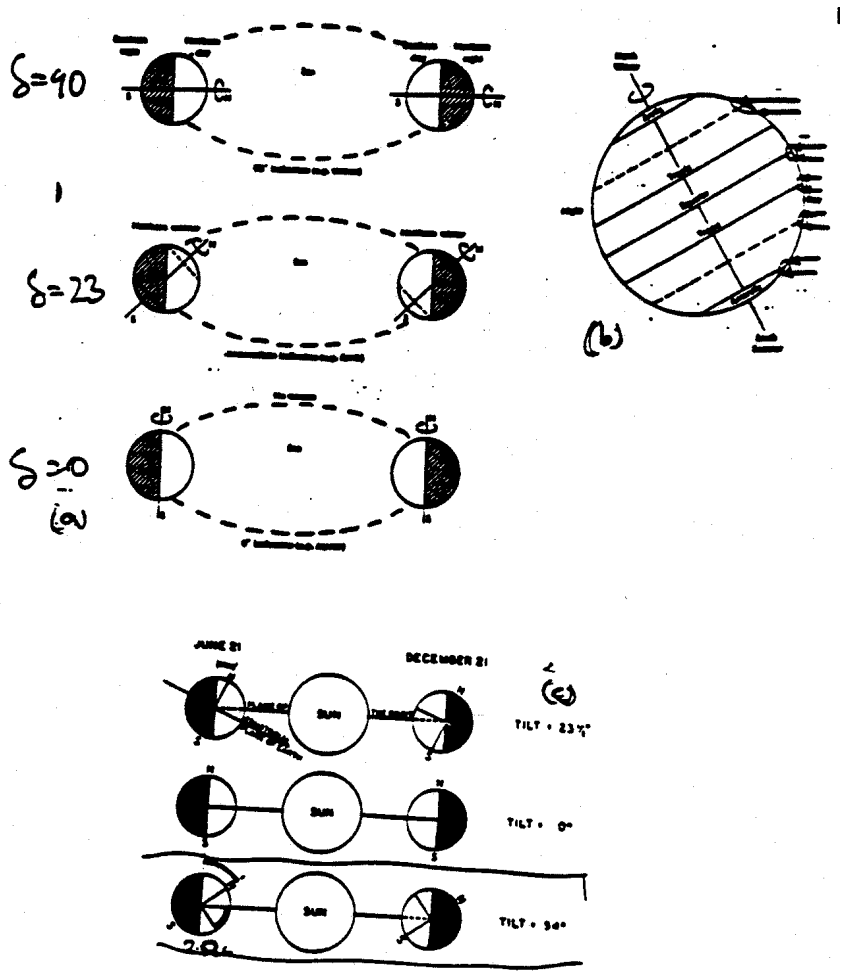

Fig. 5.5 *(a) How seasonal variations depend on the angle between the equator and the plane of the orbit. If a planet had exactly 90° inclination, it would be impossible to draw an analogy with terrestrial north and south poles. The labels in the top panel would then be arbitrary. (b) Incident solar radiation at a solstice. A beam of sunlight is spread over a larger area of ground at high latitudes, where the sun is close to the horizon, than at low latitudes where the sun is almost overhead. The day is longer than the night in the summer hemisphere whereas the night is longer than the day in the winter hemisphere. Both effects are important in determining the incident solar radiation. (c) The effect of axial tilt on the distribution of sunlight. When the tilt is decreased from its present value of 23½°, the polar regions receive less sunlight than they do today. When the tilt is increased, polar regions receive more sunlight. The possible limits of these effects (never actually achieved) would be a tilt of 0°, when the poles would receive no sunlight: and 54°, when all points on the earth would receive the same amount of sunlight annually.*

*Table 5.1 The seasonal and latitudinal distributions of the length of the daytime given in parts of 24 hours and those of the weighted mean values of cos $\bar{\theta}_{\odot}$ (see Table 6 of Manabe and Moller, 1961: On the radiative equilibrium and heat balance of the atmosphere, Mon. Wea. Rev., **8a,** 503-532.)*

°Lat	Fractional length of daytime				Cos $\theta_{\odot}$			
	Apr.	July	Oct.	Jan.	Apr.	July	Oct.	Jan.
5	.508	.517	.500	.496	.625	.587	.614	.591
15	.521	.537	.492	.471	.618	.601	.579	.549
25	.533	.562	.483	.450	.599	.593	.524	.474
35	.546	.596	.471	.421	.558	.567	.458	.393
45	.562	.637	.454	.362	.501	.521	.379	.317
55	.596	.708	.437	.321	.423	.453	.282	.203
65	.629	.837	.404	.208	.345	.369	.176	.106
75	.750	1.000	.329	---	.241	.311	.071	---
85	1.000	1.000	---	---	.168	.318	---	---

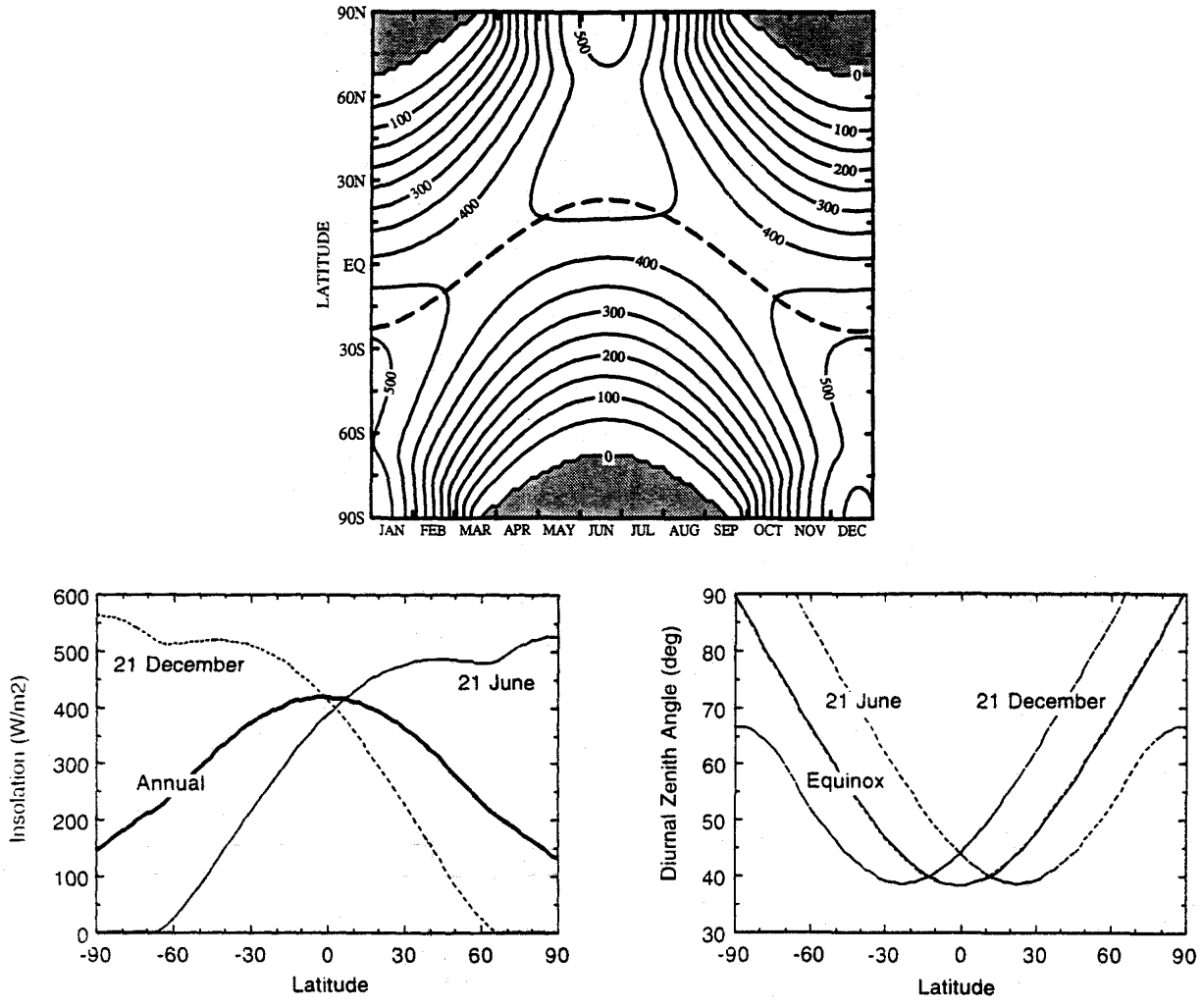

Fig. 5.6 The daily variation of the solar radiation at the top of the atmosphere as a function of latitude. The units are Wm^{-2}.

Example 5.3: Some properties of the solar zenith angle

Some examples:

- Poles: cos θ, sin ϕ, and cos $\theta_\odot$ = sin δ, 90 - $\theta_\odot$ = δ = constant, where 90 - $\theta_\odot$ is the elevation angle. Thus the sun circles the pole and is never higher than 23.5° and transition from day to night occurs at equinoxes ($\delta = 0$).

- Solar noon: cos h = 1, $\theta_\odot = \phi - \delta$. Note since –23.5° < δ < 23.5° only for $\phi <$ |23.5°| can the sun be directly overhead.

- Sunrise and sunset: $h = H$ (half day length), cos $\theta_\odot$ = 0 and it follows that cos H = - tan ϕ tan δ, H = 6 hours when tan ϕ (equator) or tan δ = 0 (equinoxes).

Convenient formulae for the declination δ and the ratio $(\bar{R}_{s_E} / R_{s-E})^2$ are

$$\delta = \sum_0^3 a_n \cos m\psi_n + b_n \sin m\psi_n$$

and

$$\left(\frac{\bar{R}_{s_E}}{R_{s-E}} \right)^2 = \sum_0^3 c_n \cos m\psi_n + d_n \sin m\psi_n$$

where

$$\psi_n = \frac{2\pi \, \text{day}_n}{365}$$

where the day number day$_n$ ranges from 0 on January 1 to 364 on December 31.

n	a_n	b_n
0	0.006918	
1	-0.399912	0.070257
2	-0.006758	0.000907
3	-0.002697	0.001480

n	c_n	d_n
0	1.000110	
1	0.034221	0.001280
2	0.000719	0.000077

Example 5.4: Example use of a sun-path diagram:

The solar zenith angle can also be calculated graphically using sun path diagrams such as shown below for the latitude of 41°N. This diagram is a convenient graphical way of representing Eqn. (5.3).

Example Sept. 21, at 9 a.m., azimuth = 122°; $\theta_{\odot}$ ~ 57° (elevation angle 33°)

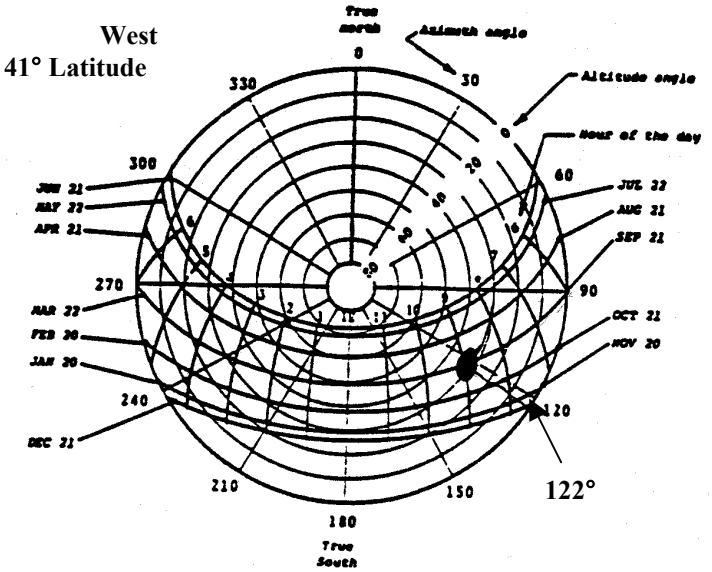

An example of a sun path diagram for a latitude near that of Ft. Collins.

5.4 Variability of Solar Flux Outside the Atmosphere

There are two main causes for the variability of $Q_{\odot}$, and these manifest themselves in very different ways over an enormous range of time scales. The first has to do with changes in the radiation output of the sun itself and the second has to do with changes in astronomical factors that influence how this output is received at Earth.

(a) The Flickering Sun

(Reference: Foukal: The Variable Sun, Scientific American, Feb, 1990). The emission from the sun varies in time. Large changes in coronal activity are well established giving rise to changes in coronal UV emission and microwave/radiowave emissions. This variable output was indicated previously in Fig. 5.2b. However, the greater part of the solar emission comes from the photosphere where the magnitude of the variability is much less. The shorter term variabilities of solar output (order of 0.2%) over time scales of weeks is thought to be caused by passage of

- sunspots (dark spots on 'surface' of the sun) across disc

- faculae (bright spots) associated with the sun's magnetic activity that accompanies sunspots.

Long-term variability can also be identified with the solar cycle. The output decreased by about 0.1% between the peak in 1981 and its minima in mid 1986 (Fig. 5.7a). The sun grew more luminous as the sunspots grew larger—area covered by bright faculae outweighs the increase in area by dark sunspots.

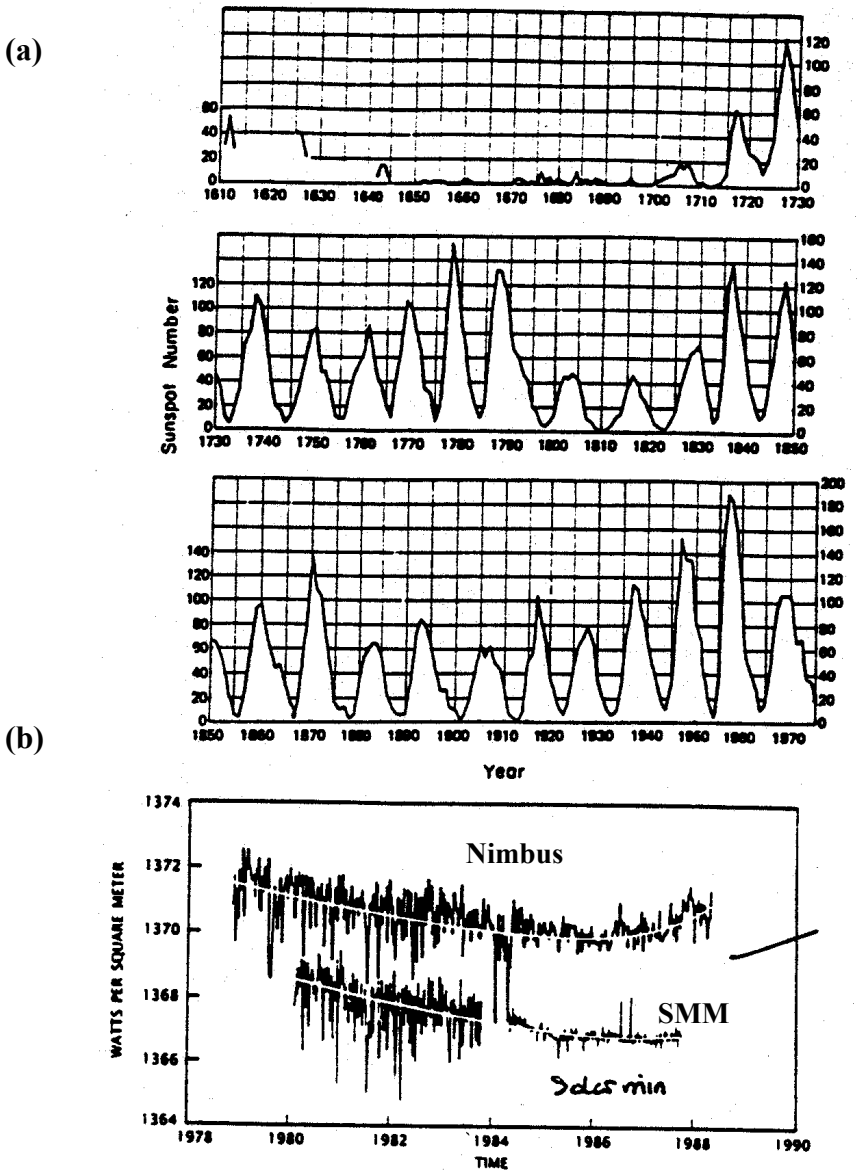

Fig. 5.7 *(a) Flickering of the sun was recorded by radiometers on two satellites, Nimbus 7 (blue) and Solar Maximum Mission (red). Short-term decreases in solar output produced the sharp spikes in the SMM data, and most of those seen in the Nimbus 7 data, which also included some instrument noise. On the average (yellow line) the sun shone brightest at the time of maximum sunspot activity. Apparently the greater number of bright faculae at maximum activity outweighed the effect of dark spots. (b) Solar cycle manifests itself in the changing number of spots on the sun's visible surface (left). The dearth of spots between about 1645 and 1715, known as the Maunder minimum, appears to coincide with an era of unusually cold weather.*

(b) Astronomy

The three main astronomical factors that govern the radiation received on a flat surface, namely δ, orbital eccentricity and axial precession all vary in a regular manner as shown in Fig. 5.8a and b. Vernekar (1972: Long period global variations of incoming solar radiation, *Meteorological Monographs,* **12**, No. 24) shows how the solar irradiance varies in time and as a function of latitude. An example is given in Fig. 5.9a. The upper panel shows the changes in the radiation for the NH winter and the lower for the SH winter. The main point is that the distribution of irradiance is altered significantly but the global and annual average is not (units quoted are in Ly day^{-1}, compare these numbers with those presented in Fig. 5.6 to gain some idea of the percentage change in $Q_{\odot}$. The characteristics of the variabilities in the astronomical factors appear in climate records (Fig. 5.9b). Another reference of relevance is that of Berger (1987: Long-Term variations of Daily insolation and quaternary climatic changes, *J Atmos. Sci.*, **35**, 2362-2367).

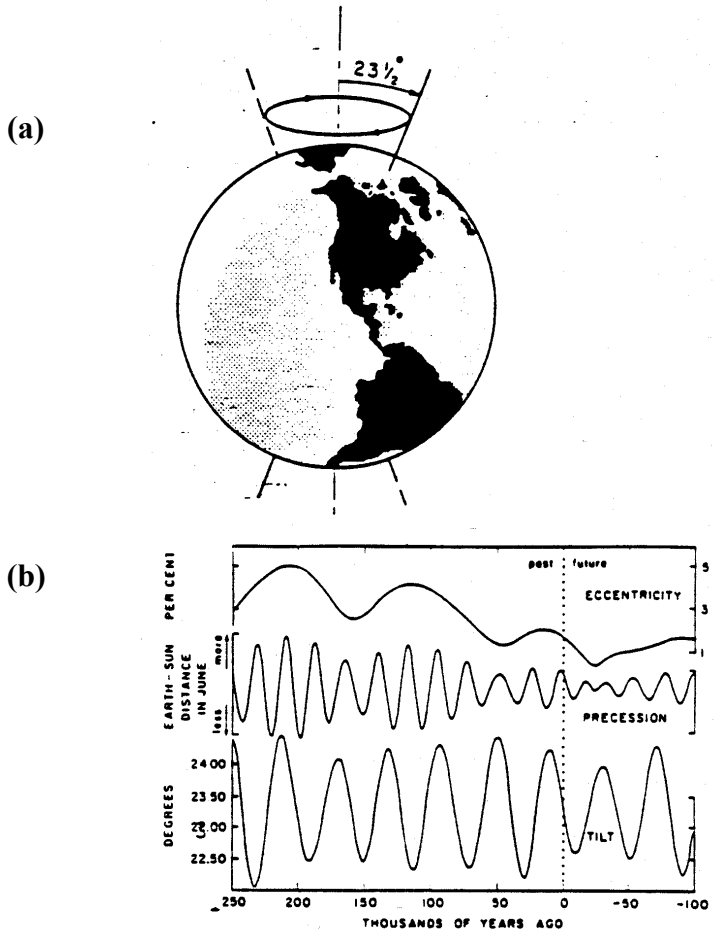

Fig. 5.8 *(a) Precession of the earth. Owing to the gravitational pull of the sun and moon on the equatorial bulge of the earth, its axis of rotation moves slowly around a circular path and completes one revolution every 26,000 years. Independently of this cycle of axial precession, the tilt of the earth's axis (measured from the vertical) varies about 1.5° on either side of its average angle of 23.5°. (b) Changes in eccentricity, tilt, and precession. Planetary movements give rise to variations in the gravitational field, which in turn cause changes in the geometry of the Earth's orbit. These changes can be calculated for past and future times. (Data from A Berger.)*

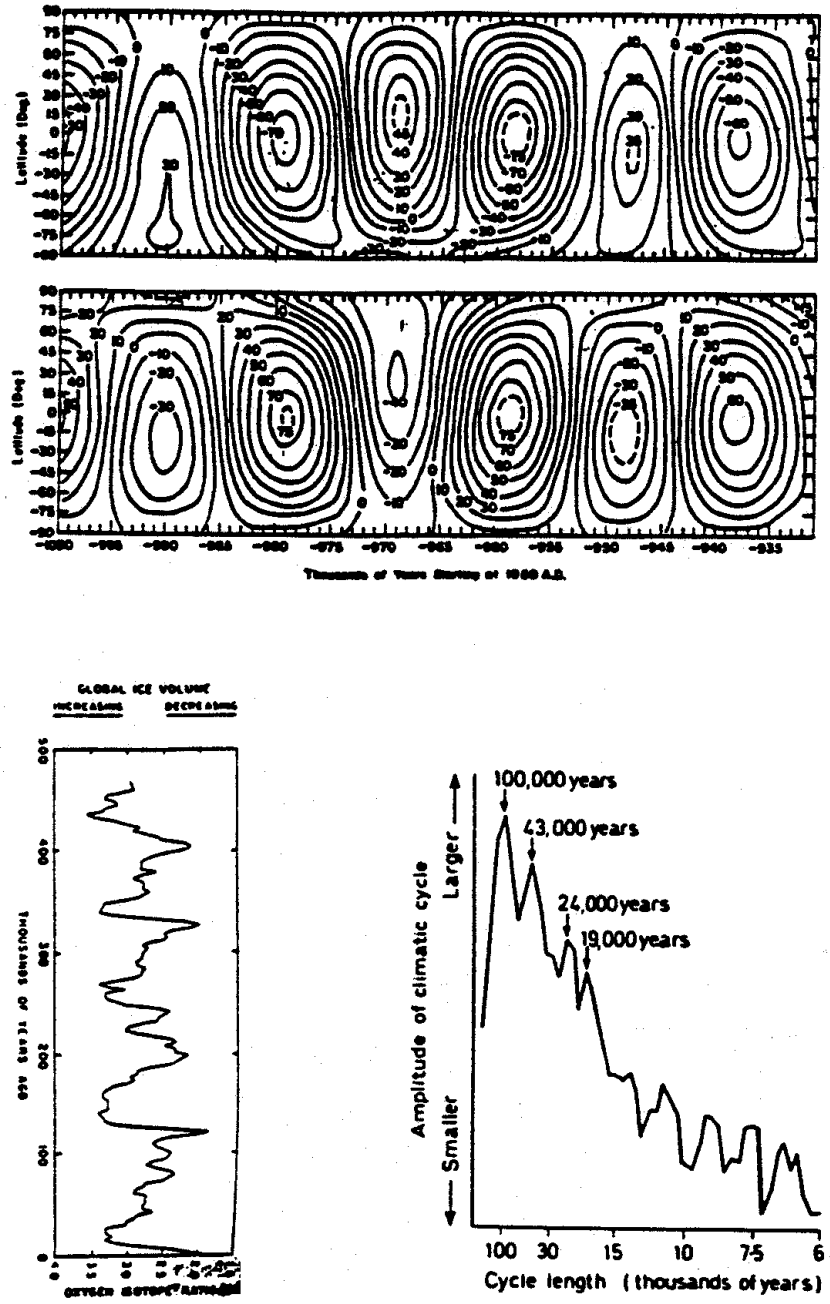

Fig. 5.9 *(a) Variation in $\Delta Q_{\odot}$ (ly day^{-1} as a function of latitude and time measured from 1950 AD). (b) Time series of isotopic measurements (these reflect global ice volume) from two Indian Ocean cores (upper panel) and the spectrum of this variation showing the imprint of different climatic cycles in the isotopic record—these seem to support predictions of the Milankovitch theory. (Data from J.D. Hays et al. 1976.)*

5.6 Problems

Problem 5.1

Given the following characteristics for Mars and Jupiter:

Sun Diameter = 1,390,600 km
Mars Diameter = 6860 km
Jupiter Diameter = 143,600 km
Sun—Mars Distance = 228 X 10^6 km
Sun—Jupiter Distance = 778 X 10^6 km
Mars Albedo = 16%
Jupiter Albedo = 73%
Solar Output = 6.2 kw cm^{-2}

Calculate for each planet

(a) Solar Constant
(b) Equivalent Blackbody Temperature
(c) Wavelength of Maximum Emission
(d) Solid Angle Subtended by the Sun

Problem 5.2

Calculate the radiative equilibrium planetary temperatures for earth assuming albedos of 0.2, 0.3, 0.4, and 0.5.

Problem 5.3

Calculate the net longwave power per unit area gain/loss of a grass surface at 2°C when under a clear sky with an effective temperature of -30°C, and when under a tree with an effective temperature of 5°C.

Problem 5.4

Find the wavelength at which the incoming solar irradiance at the top of the earth's atmosphere is equal to the outgoing terrestrial irradiance. Assume the sun and earth to be emitting as blackbodies at 6000°K and 255°K, respectively.

Problem 5.5

Show that for an isothermal, surface-atmosphere system the upward infrared irradiance is invariant with height.

Problem 5.6

(a) Derive a relationship between solar irradiance and the distance (d) between the sun and the observation. (Assume $R._{sun} << d$).
(b) Does the radiance obey the same relationship?

Problem 5.7

If the average output of the sun is 6.2 kw cm^{-2}, the radius of the sun is 0. 71 X 10^6 km, the distance of the sun from the earth is 150 X 10^6 km, and the radius of the earth is 6.37 X 10^3 km, what is the total amount of energy intercepted by the earth?

Problem 5.8

Calculate the solar zenith angle and azimuth angle for the following dates, locations, times:

Date	Latitude	Longitude	Time
1 Jan.	0°	20° W	1200 GMT
22 Mar.	30° N	180° W	1800 GMT
1 July	45° S	90° W	0900 Local sun time
1 Nov.	60° S	35° E	1000 Local sun time
1 Dec.	75° N	45° W	0600 Local sun time

Note: Reference your azimuth angle from the south such that east of south is negative and west of south is positive.

Problem 5.9

(a) Derive a simple expression for the elevation angle of the sun at local noon as a function of date and latitude.
(b) Derive an expression for time of sunrise as a function of date and latitude.

Problem 5.10

Calculate the azimuth angle of sunrise at 40° N on June 21. Sketch the sun-earth geometry and interpret your results.

Problem 5.11

(a) The eccentricity of the earth's orbit is 0.01673. What would be the percentage variation in the irradiance at the top of the atmosphere due to this eccentricity from time of apogee to time of perigee?
(b) On which dates would you observe these min max values?

Problem 5.12

An aircraft is being used to measure the surface albedo for a certain region. The downward irradiance is measured with a pyranometer to be 750 Wm^{-2} and the upward irradiance is measured to be 250 Wm^{-2}. The angle of attack (angle between the horizontal and the plane of the wing) is known to be 4°. If the plane is flying due west at latitude 0° on Julian day 80, at 1500 local solar time, and assuming that the total radiation striking the upward looking sensor is 40% direct and 60% pure diffuse, calculate the albedo of the underlying target.

Problem 5.13

In Table 5.1 the latitudinal distribution of both the fractional day length and mean cosine of the solar zenith angle are listed for the Northern Hemisphere. Calculate the matching values of these quantities for the June 21 solstice for the Southern Hemisphere using the equivalent 9 (Southern) latitudes. Use these values to provide the latitudinal distribution of the daily solar insolation for this date and compare your results with those of Figure 5.6a of your notes.

AT622 Section 6
The Earth

This section provides students with an understanding of the radiative budget of the Earth and seeks to put this budget in the context of the total energy budget of the planet thus placing the topic of atmospheric radiation in a broader context.

KEY REFERENCES

Barkstrom, B., 1984: The earth radiation budget experiment (ERBE), *Bull. Amer. Met. Soc.*, **11**, 1170-1185.

Kiehl, J. T. and K. E. Trenberth, 1997: Earth's annual global mean energy budget, *Bull. Amer. Met. Soc.*, **78**, 197-208.

Ramanathan, 1987: Role of earth radiation budget studies on climate and general circulation research, *JGR*, **92**, 4075 - 4095.

Ramanathan, Barkstrom and Harrison, 1989: Climate and the earth's radiation budget, *Physics Today*, 22-37.

Stephens, Campbell and Vonder Haar, 1981: Earth radiation budgets, *JGR*, **86**, 9739 - 9760.

6.1 The Earth's Radiation Budget

A fundamental property of the Earth's climate system is the radiative budget defined as

$$F_{net} = \frac{Q_\odot}{4}(1-\alpha) - F_\infty \tag{6.1}$$

referred to as the Earth's Radiation Budget (ERB). In this definition, F_{net} is the net radiation imbalance at the top of the atmosphere, $Q_\odot$ is the solar constant (remember where the factor of 4 comes from?), α is the albedo of the planet and F_∞ is the outgoing emitted longwave radiation. We believe that on the annual and global mean the planet as a whole is in radiative equilibrium (an assertion supported by satellite measurements—at least to the accuracy of the measurements), thus $F_{net} = 0$ and

$$\frac{Q_\odot}{4}(1-\overline{\alpha}) = \overline{F}_\infty \tag{6.2}$$

where the overbar emphasizes the global-annual average of the specified quantities.

(a) The Planetary Temperature

It is sometimes convenient to consider F_∞ in terms of an equivalent blackbody emission (of course it is not purely blackbody as we have already seen). If we write $\overline{F}_\infty = \sigma T_p^4$, then this balance can be written as

$$\underbrace{\frac{Q_\odot}{4}(1-\alpha)}_{\text{absorbed solar energy}} = \underbrace{\sigma T_p^4}_{\text{emitted energy}} \tag{6.3}$$

It follows from this balance that

$$T_p = \left(\frac{Q_\odot (1-\alpha)}{4\sigma} \right)^{1/4} \tag{6.4}$$

where $Q_\odot$ depends on the sun-earth distance. Figure 6.1 graphically presents Eqn. (6.4) and Table 6.1 provides values of various quantities that help define the radiative equilibrium for various planets. Note for example that T_p for Venus is similar to that of Earth even though $Q_\odot$ is almost twice as large.

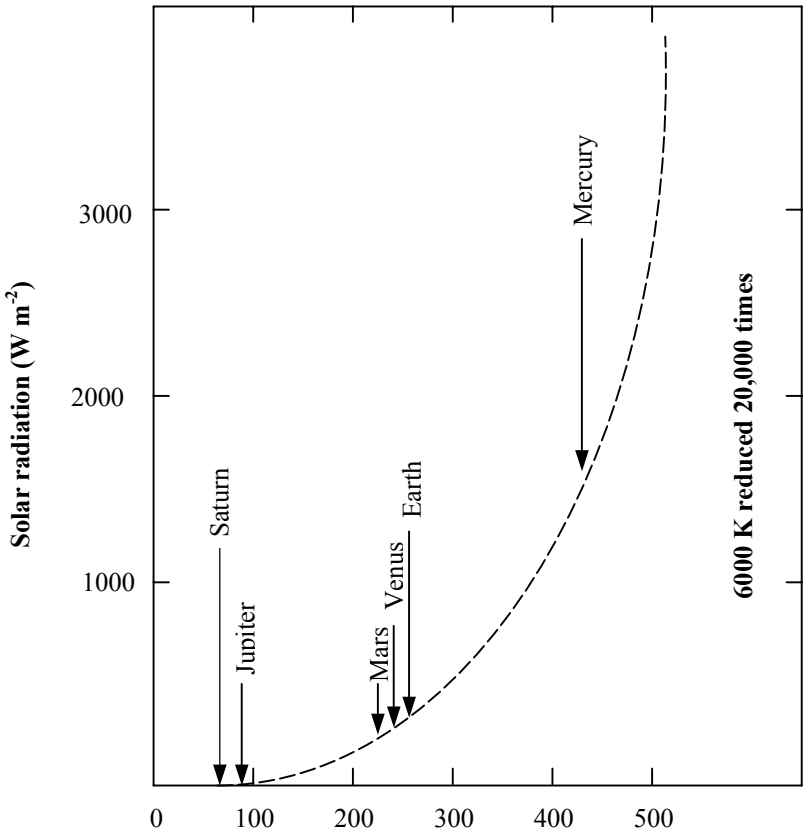

Fig. 6.1 The Stephan-Boltzmann law equates the emitted heat radiation to 5.67 × 10^{-5} × (temperature)^4. Effective temperatures of the sun and planets are shown in Table 6.1.

The value of T_p for Earth is 253 K, which is much too cold to be representative of the globally averaged surface temperature of 288 K (actually, T_p = 253 K is approximately the mean temperature of the 500 mb surface). The reason for the difference between the surface and planetary temperatures is that the Earth's atmosphere itself emits radiation. For temperatures typical of Earth, this emission occurs mainly in the infrared region of the electromagnetic spectrum with a peak wavelength around 10 μm (Section 3). The difference between T_p and the observed surface temperature, T_s, is therefore a measure of strength of the greenhouse effect.

Table 6.1 Effective temperatures of the sun and planets.

Planet	Distance from sun (10^4 km)	Flux of solar radiation (10^4 erg cm^{-3} sec^{-1})	Albedo	T_p
Mercury	58	9.2	0.058	442
Venus	108	2.6	0.71	244
Earth	150	1.4	0.33	253
Mars	228	0.60	0.17	216
Jupiter	778	0.049	0.73	87
Saturn	1430	0.015	0.76	63
Uranus	2870	0.0037	0.93	33
Neptune	4500	0.0015	0.84	32
Pluto	5900	0.00089	0.14	43

(b) The Evolutionary Theory of Planetary Atmospheres

In essence, the Earth's atmosphere is fairly transparent to solar radiation but opaque (except for the window region) to infrared radiation. Thus the surface is warmed by sunlight and maintained by radiation from the atmosphere. This produces an increase in surface temperature over the planetary temperature and is a phenomenon understood to be the greenhouse effect. This effect is obviously very different from planet to planet as a comparison between T_p and T_s, for the planets listed in Table 6.1. Of some interest to our overall understanding of the present state of the Earth's climate is how the Earth's atmosphere evolved with water vapor and CO_2 being released into the atmosphere. This sort of understanding is also important to the assessment of how our present climate might change with changing concentrations of these gases.

One hypothesis for the evolution of the climates of the three inner planets of the solar system is graphically portrayed in Fig. 6.2. The proposed evolution of the surface temperature of Venus, Earth, and Mars is shown as a function of the amount of water vapor in the atmosphere. This figure suggests that as water accumulates in the atmosphere, owing to the greenhouse effect, the surface temperature rises. It is thought that as more water vapor is added in the atmosphere of Venus, the temperature increases creating a runaway feedback (the so called **runaway greenhouse effect**). The atmosphere of Venus presently contains little water vapor. This is explained under the runaway hypothesis by requiring most of the water vapor to have reached the upper atmosphere where it photodissociated and ultimately escaped. The present strength of the greenhouse on Venus is maintained by the clouds and large abundance of CO_2. Both Earth and Mars are said to experience a **truncated greenhouse effect** such that increases in vapor are met with water phase changes.

In summary:

- MERCURY: all outgassed gases are stripped. No atmosphere.
- VENUS: sufficiently massive that important gases do not escape. Close enough to the sun that water phase transitions are not reached and an unbuffered runaway system is set up.
- EARTH: Particular T_p allows encounter of the H_2O phase transitions near the triple point. Thus Earth's climate is buffered by these phase changes, i.e., continued outgassing condenses into oceans and clouds or sublimes; partial pressure of gas cannot increase and feedback on the greenhouse effect is much weaker than it is (hypothesized) for Venus.
- MARS: Low T_p forces encounter with ice/vapor transition. Mars' climate is buffered as any H_2O outgassing sublimes to ice preventing further increases of gas partial pressure.

The present state of the atmospheres of Venus and Earth, in this view, is therefore largely a result of the proximity of the planet to the sun.

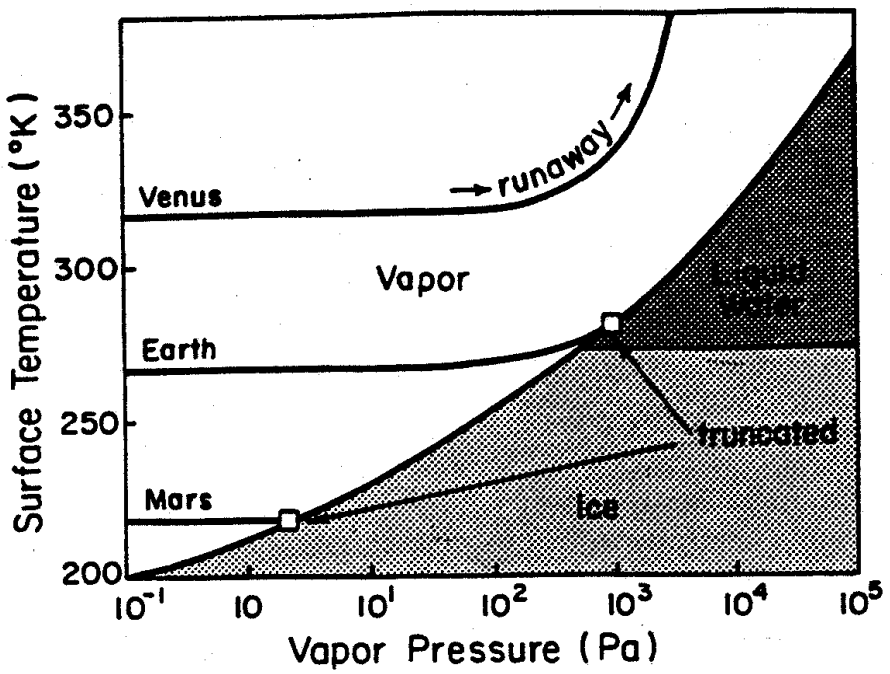

Fig. 6.2 *The runaway greenhouse effect. The solid lines show how surface temperatures increase, due to the greenhouse effect, as water vapor accumulates in the atmospheres of the inner planets. On Mars and on Earth the increase is halted when the water vapor pressure is equal to the saturated vapor pressure (shown as the dark curve) and freezing or condensation occurs. Temperatures are higher on Venus because Venus is closer to the sun and saturation is never achieved. The temperature runs away. Note that the temperatures on the left-hand axis are not the same for Earth and Venus as the effective temperatures in Table 6.1. They differ because a different albedo has been used. (After S. I. Rasool and C. DeBergh, 1970) Source: (G. & W.).*

6.2 Gray Body Transfer: The Role of Radiation on the Temperature Structure of the Atmosphere

It is instructive to study the role of infrared radiation in a simple climate model, in which the rather drastic assumption is made that the optical depth is independent of frequency. This is known as the "gray" approximation. To this end, we will consider the concept of gray body radiative transfer and further introduce the notion of radiative equilibrium—a notion that we will return to later.

In dealing with gray body transfer, let us begin with a monochromatic RTE

$$\mu \frac{dI(\tau,\mu)}{d\tau} = I(\tau,\mu) - B(T) \tag{6.5a}$$

$$-\mu \frac{dI(\tau,-\mu)}{d\tau} = I(\tau,-\mu) - B(T) \tag{6.5b}$$

Example 6.1: An estimate of the gray-body optical depth

The spectral optical depth is a complex function of wavelength and several ways of spectrally averaging τ exist. The approach used here is one appropriate to the radiative equilibrium arguments introduced to arrive at Eqn. (6.11) and follows from the following flux-mean mass absorption coefficient (Mihalas, 1978)

$$k_f = F_\infty^{-1} \int k_f F_{\infty,\lambda} d\lambda .$$

The contribution to τ by water vapor, carbon dioxide and other minor greenhouse gases present in the Earth's atmosphere obtained using k_f in Eqn. (6.6), is shown below. The spectral absorption data used to derive k_f are those tabulated by Rothman (1981). The total gray body optical depth derived from these data is $\tau = 3.9$ corresponding to $w = 28$ kg m^{-2}, which is close to the global mean values of w. The value $\tau = 3.9$ is larger than the value of the optical depth derived from later considerations. This highlights the ambiguity of the quantitative meaning of τ and to understand the value it is necessary to understand how it is derived. The advantage of the flux-weighted value is that it allows us to estimate τ from spectral integration and thus the contributions by individual gases. These contributions clearly emphasize the dominance of water vapor to the total gray body optical depth for the global mean conditions considered.

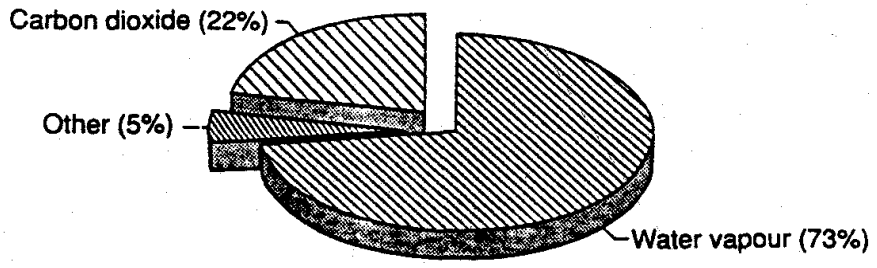

A pie diagram showing the percentage of the gray body optical depth due to water vapor and other greenhouse gases in the Earth's atmosphere based on typical mean global concentrations of these gases.

where I is the intensity, $\mu = \cos\theta$ where θ is the angle of the beam from the zenith. The optical depth is defined as

$$\tau = \int_z^\infty k \rho_a dz \qquad (6.6)$$

where k *is* the mass absorption coefficient, ρ_a is the density of the absorbing gas, and z is the lowest end point of the path. It is simple to cast these equations into equations for (see box below) upward (F^+) and downward (F^-) hemispheric fluxes,

$$\frac{dF^+}{d\tilde{\tau}} = F^+ - \pi B, \tag{6.7a}$$

$$-\frac{dF^-}{d\tilde{\tau}} = F^- - \pi B, \tag{6.7b}$$

where

$$\tilde{\tau} = \frac{3}{2}\tau .$$

We now introduce the gray body assumption, which means if we take $\tilde{\tau}$ to be independent of wavelength (we know that it is not), then we can treat the fluxes in Eqns. (6.7a and b) as broadband quantities and replace πB with σT^4. The factor of 3/2 is a form of *diffusivity factor* and its interpretation follows from the considerations discussed below.

Let us introduce the notion of radiative equilibrium, which for our purpose means that at the top of the atmosphere

$$F^+(\tilde{\tau} = 0) = \frac{Q_\odot}{4}(1-\alpha) = F_\infty \tag{6.8a}$$

where $Q_\odot$ is the global-annual mean incoming solar radiation at the top of the atmosphere and α is the planetary albedo **(note:** these are all broadband quantities). Radiative equilibrium also implies that throughout the atmosphere (why??)

$$F_{net} = F^+(\tilde{\tau}) - F^-(\tilde{\tau}) = const \tag{6.8b}$$

(we are also assuming that no solar radiation is absorbed in the atmosphere). Given this condition, it follows from Eqn. (6.7a) that

$$F^+(\tilde{\tau}) + F^-(\tilde{\tau}) = 2\pi B(\tilde{\tau})$$

and further from (6.8b) that

$$F^+(\tilde{\tau}) + F^-(\tilde{\tau}) = F_{net}\tilde{\tau} + C .$$

On combining these equations we obtain

$$B(\tilde{\tau}) = \frac{F_{net}}{2\pi}(\tilde{\tau} + 1) .$$

Example 6.2: A further derivation of the flux equations

It is a relatively simple matter to convert Eqns. (6.5a and b) into flux equations if we define a direction $\bar{\mu}$ such that the flux

$$F^+ = 2\pi\int_0^{+1} I(\mu)\mu d\mu = \pi I(\bar{\mu}).$$

Thus it is straightforward to write down the RTE at $\mu = \bar{\mu}$. By multiplying each side of this equation by a factor of π we arrive at Eqns. (6.7a and b) with $\bar{\mu}$ = 2/3.

The solution to these equations follows by first differencing these equations to yield

$$\frac{dF_{net}}{d\tilde{\tau}} = (F^+ + F^-) - 2\pi B \qquad (6.9a)$$

(remember F_{net} = (F^+ - F^-)) and summing the equations to obtain

$$\frac{d(F^+ + F^-)}{d\tilde{\tau}} = F_{net} \qquad (6.9b)$$

which provides two equations for the two unknowns F_{net} and (F^+ + F^-). We will now explore these solutions given an additional assumption about radiative equilibrium.

At the top of the atmosphere, we have $\tilde{\tau}$ = 0 and F^- = 0, so that $F_{net} = F_\infty$ and $C = F_{net}$. Further, under the gray body assumption

$$\sigma T^4(\tilde{\tau}) = \frac{F_\infty}{2}(\tilde{\tau} + 1) \qquad (6.10a)$$

At the bottom of the atmosphere, where $\tilde{\tau} = \tilde{\tau}_s$, we have $F^+ = \sigma T_s^4$ and it follows that

$$\sigma T_s^4 - F^-(\tilde{\tau}_s) = F_\infty$$

$$\sigma T_s^4 + F^-(\tilde{\tau}_s) = F_\infty(\tilde{\tau}_s + 1)$$

and that

$$\sigma T_s^4 = \frac{F_\infty}{2}[2 + \tilde{\tau}_s] \qquad (6.10b)$$

$$F_g^- = F^-(\tilde{\tau}_s) = \frac{F_\infty}{2}\tilde{\tau}_s \tag{6.10c}$$

at the surface.

Example 6.3: Skin temperatures and temperature discontinuities

The solutions represented by Eqns. (6.10a) and (6.10b) provide rather interesting insights into the temperature profiles that are predicted by these equations. One of the results of this model is an estimate of the 'skin' temperature, which we think of as a measure of the stratospheric temperature. We obtain this using Eqn. (6.10a) with $\tilde{\tau} = 0$

$$\sigma T^4(\tilde{\tau} = 0) = \frac{F_\infty}{2}$$

and with $F_\infty \approx 235$ Wm^{-2}, it follows that this temperature is T_{skin} = [117.5/5.68 × 10^{-8}]$^{0.25}$ = 213 K.

The solutions in Eqns. (6.10a) and (6.10b) predict a discontinuity between the surface temperature T_s and the air temperature just above the ground $T(\tilde{\tau}_s)$. Differencing these equations and with $\tilde{\tau} = \tilde{\tau}_s$,

$$\sigma T_s^4 - \sigma T^4(\tilde{\tau}_s) = \frac{F_\infty}{2}.$$

The results of the model are presented in Fig. 6.3a, showing the profiles of upward and downward fluxes and the profile of the temperature that is contained in the profile of flux πB. Highlighted are the skin temperatures and the discontinuity at the surface. At first sight, the model does not seem to bear any resemblance to the real temperature profile. This is because the coordinate τ is not an easy coordinate to interpret. Let us suppose that τ is largely defined by water vapor and that

$$\rho(\mathrm{H_2O}) = \rho_0 e^{-z/H_{\omega v}}$$

where $H_{\omega v} \approx 2$ km. To simplify matters, we assume that τ varies with z in the same way $\rho(\mathrm{H_20})$ varies with z

$$\tau = \tau_s e^{-z/2} \tag{6.11}$$

and

$$\sigma T^4(z) = \frac{F_\infty}{2}\left[1 + \frac{3}{2}\tau * e^{-z/2}\right]$$

The profile of temperature with height equivalent to Fig. 6.3a is presented in Fig. 6.3b. For comparison, the profile defined by a 6 K km^{-1} lapse rate is presented. We note that the radiative equilibrium profile is

unstable throughout most of the atmosphere, at least to where the 6 K km^{-1} profile cuts the radiative equilibrium profile. This radiative equilibrium profile is unstable w.r.t. vertical motion and is destroyed by convection, which we may think of in this simple model as producing the constant lapse rate profile. Where the latter intersects the radiative equilibrium profile at about 10 km is where this simple model predicts the position of the tropopause.

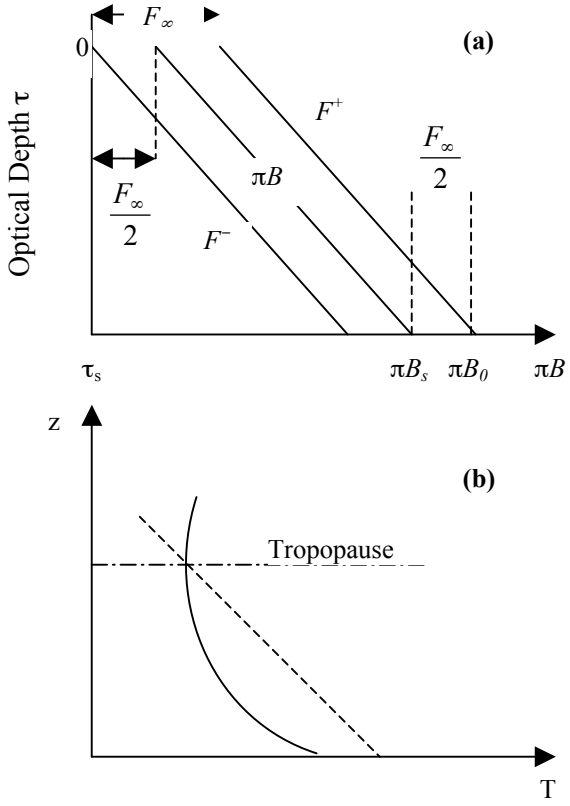

Fig. 6.3 (a) The flux profiles and blackbody function predicted by the simple gray body model as a function of optical depth. (b) The radiative equilibrium temperature profile as a function of altitude predicted by the flux model and assuming the profile of optical depth in Eqn. (6.11).

6.3 The Greenhouse Effect and Water Vapor Feedback

Theories of the evolution of the atmosphere of Venus are a subject of some debate. Conjectures other than the runaway greenhouse-hydrodynamic loss hypothesis have been forwarded to explain the present climate of Venus. A contrary view is that the atmosphere of Venus never contained water vapor at the levels required for the runaway hypothesis and that most of the planet's water remains fixed in its interior (Kaula 1990). Whether this runaway greenhouse model proposed for Venus actually occurred or not is not the issue here. The runaway hypothesis serves to illustrate a feedback between water vapor, the greenhouse effect, and the surface temperature of the planet—a feedback that is also thought to occur on Earth although on a much more limited scale (Manabe and Wetherald 1967). In fact, it is the water vapor feedback in present day climate models that contributes the major portion of the global warming predicted for increasing concentrations of atmospheric CO_2.

Figure 6.4a provides a schematic depiction of how this water vapor feedback is thought to take place under the influence of increasing concentrations of carbon dioxide. As the sea surface temperature warms

from the rising levels of CO_2, increased evaporation of water from the oceans leads to an enhanced water vapor content of the atmosphere (Fig. 6.4a), which further warms the oceans. The total warming calculated by a typical climate model is also given in Fig 6.4a as is the amount of warming calculated for a doubling of CO_2 without any water vapor feedback. While these results apply to a specific climate model (Manabe and Wetherald 1967), most models give similar responses and half of the projected observations, like those shown in Fig. 6.4b, suggest that a kind of thermodynamic equilibrium exists between the sea surface temperature and water vapor content in a manner closely resembling the Clausius-Clapeyron relation.[1]

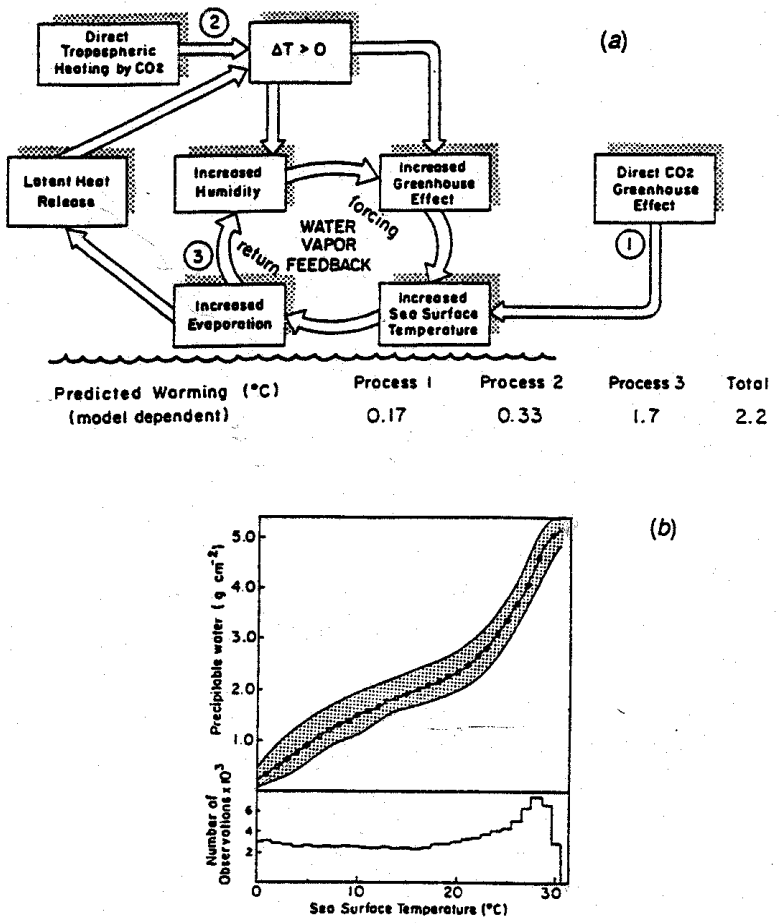

Fig. 6.4 *(a) An illustration of the water vapor feedback as it is thought to occur on Earth when triggered by a small warming induced by increasing atmospheric CO_2. The water vapor feedback is thought to account for more than half of the final warming simulated by present day climate models (adapted from Ramananthan, Manabe and Wetherald, 1967). (b) A necessary condition for the existence of water vapor feedback on Earth. Water vapor exists in equilibrium with the oceans in a way that is related to the sea surface temperature largely through the Clausius-Clapeyron relationship. The curve shown is established from thousands of observations of water vapor over the world's oceans (Stephens, 1990).*

[1] Other views have been expressed that the positive feedback does not operate to the extent predicted in current climate models. For further discussion see S. H. Schneider, 1990: The global warming debate heats up: an analysis and perspective, *Bull. Amer. Meteor. Soc.*, **71**, 1292-1304.

Unlike Venus, however, the water vapor feedback loop on Earth is interfered with by condensation of vapor into clouds, which in turn imparts a substantial influence of their own on the greenhouse effect. The actual way this interference by clouds takes place and the specific connection between water vapor, cloudiness, and the greenhouse effect on Earth are still not well understood, poorly observed, and largely unexplored.

(a) A simple Estimate of the Water Vapor Feedback

We can devise a simple way of estimating the strength of this feedback. Consider our energy budget and suppose we can seek to determine the magnitude of the perturbation of temperature ΔT_s due to a small change $\Delta Q_\odot$ in solar flux. It follows then that:

$$4\sigma T_p^3 \Delta T_p = \frac{\Delta Q_\odot}{4}(1-\alpha) = \Delta F_\infty \tag{6.12}$$

and then

$$\Delta T = \Delta F_\infty \left(\frac{T_{eq}}{4F_\infty} \right) = 0.63 \text{ K} \tag{6.13}$$

But this sensitivity does not take water vapor and its feedback into account. One way to think of the feedback is to consider Fig. 6.5 and

$$F_\infty = A + BT_s \tag{6.14}$$

where $A \approx 203.3$ W m^{-2} and B ≈ 2.09 W m^{-2} ° C^{-1}. It follows then that**:**

$$\Delta T = \frac{\Delta F}{B} = \frac{0.01(A+BT)}{B} \approx 1.12°\text{C} \tag{6.15}$$

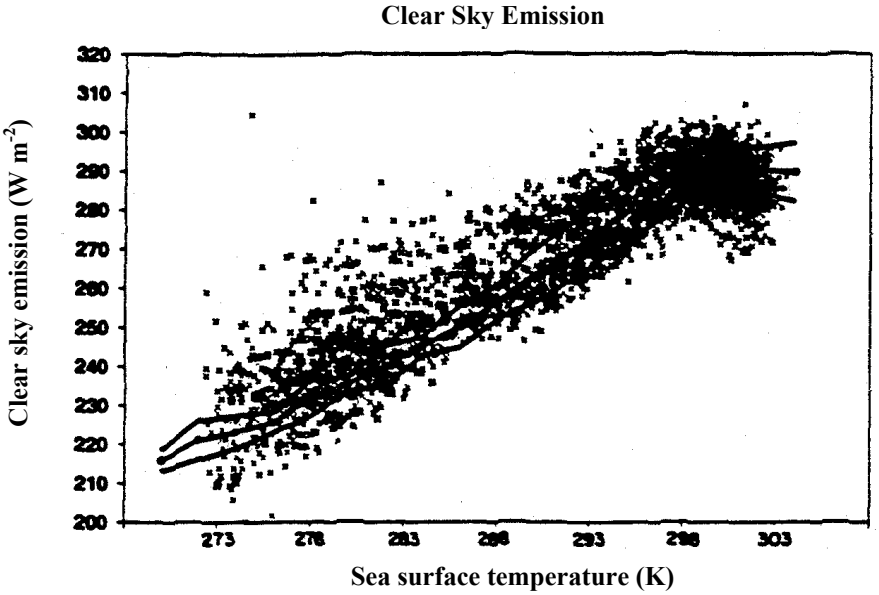

Fig. 6.5 The longwave flux emitted to space at different locations on Earth as a function of the surface temperature measured at that location (Stephens et al., 1993).

Thus the presence of an atmosphere (chiefly water vapor), which is modeled via the Budyko relationship (IR emission varies with T_s by a factor less than a T^4), increases the sensitivity of 'climate' to solar forcing by approximately a factor of two.

(b) Studying the Greenhouse Effect and Water Vapor Feedback from Space

It is not possible, in principle, to observe the direct effects of feedbacks occurring in the climate system since we observe the collections of responses. We can, however, observe key components of these feedbacks. First, let us introduce a measure of the greenhouse effect. Perhaps the simplest way is to use the difference between the mean radiating temperature of the planet and the surface temperature (Kondratyev and Moskalenko, 1984; Stephens and Tjemkes, 1992). However, the relationship between this temperature difference and the concentration of emitting species cannot be simply and conveniently defined. We will make use of our relationship in Eqn. (6.10b) and define a greenhouse parameter as

$$G = \frac{\sigma T_s^4}{F_\infty} = 0.5(\tilde{\tau}_s + 2) \tag{6.16}$$

or more generally

$$G = \frac{\sigma T_s^4}{F_\infty} = a + b\tau_s \tag{6.17}$$

where from Eqns. (6.8) and (6.10a), a = 1 and b = 3/4. This definition identifies the gray body optical depth as the key parameter in defining the strength of the greenhouse.

Let us simply assume that in the case of water vapor, the gray body optical depth is

$$\tau_s = \int k_f \rho_a dz \approx k_f w. \tag{6.18}$$

This assumption, together with Eqn. (6.17) then leads to the following (e.g., Stephens and Greenwald, 1991b)

$$G = a + cw\ . \tag{6.19}$$

The advantage of this relationship is that all factors in Eqn. (6.19) are independently observed over the global oceans, primarily from satellites. For example, the SST can be obtained from independent analyses of blended ship, buoy, and satellite data (e.g., Reynolds, 1984). The OLR available from ERBE data and w follow from microwave measurements. The annual, January and July monthly mean values of G derived in this way are plotted against corresponding mean values of w in Fig. 6.6. The solid line through the scatter of annual mean points depicts the average of these points and the slope parameter c = 0.00634 (kg m^{-2})$^{-1}$, which is estimated via a least squares fit of the data (shown as the solid line in Fig 6.6), is a measure of how the greenhouse effect changes for given changes in w and is potentially important in the analyses of water vapor feedback.

The relationship in Eqn. (6.19) may be explored using data over the Earth's oceans where suitable global measures of the SST, F_∞ and w are available from existing satellite observations. Since the relationship between w and SST is well defined, it is also possible to consider G as a function of SST. An example of this kind of relationship derived from satellite data is taken from Webb et al. (1994) and shown in Fig. 6.6a for July 1988 and Fig. 6.6b for January 1989. When plotted in this way with the

relationships for each hemisphere indicated by the different symbols, a dramatic seasonal branching of the relation between *G* and SST emerges. Webb et al. (1993) identify this as largely due to a seasonal effect associated with changes in the vertical profile of atmospheric temperature in the middle latitudes.

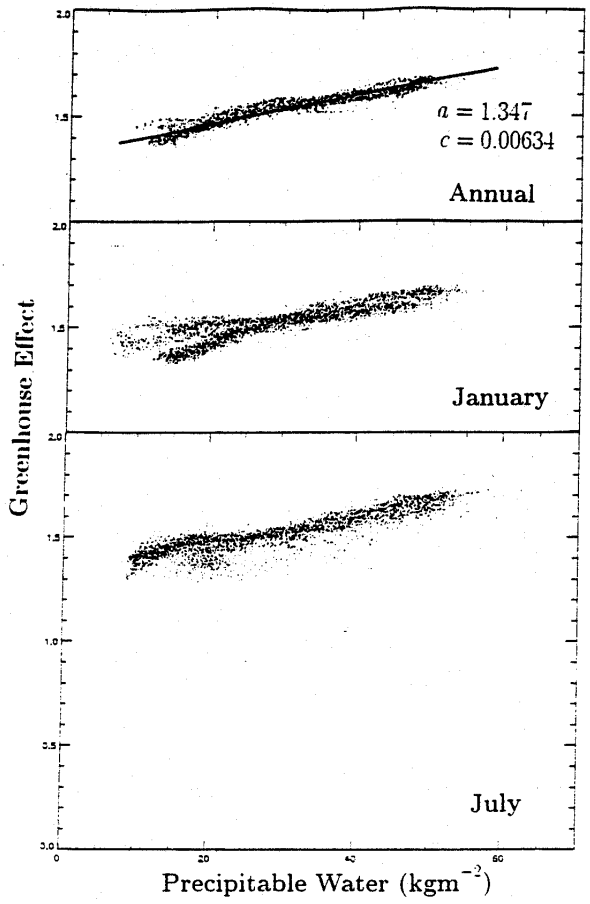

Fig. 6.6 The correlation of G with w based on annual mean (upper panel), 1989 January mean (middle panel), and 1988 July mean data (lower panel). The unit of c is (kgm^{-2})$^{-1}$.

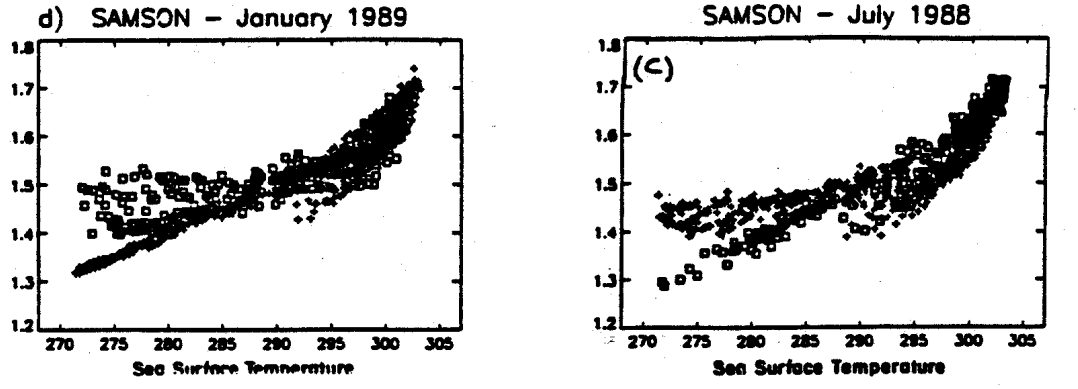

Fig. 6.7 The greenhouse effect as a function of SST with the relationships derived from hemispheric data separated for clarity.

Example 6.4: Another estimate of the gray body optical depth

We can use Eqn. (6.17), together with the data listed on Table 6.1 to arrive at an estimate of τ_s for Earth and Venus. For Venus

$$\left(\frac{750}{244}\right)^4 = \frac{3\tau_s}{4} + 1$$

or $\tau_s = 117$. For Earth,

$$\left(\frac{288}{253}\right)^4 = \frac{3\tau_s}{4} + 1$$

or $\tau_s = 0.9$. The parameter τ_s is therefore a direct measure of the strength of the greenhouse effect.

Physical properties of the three inner planets of the solar system

Planet	Distance from sun (10^6 km)	Solar constant (W m^2)	Albedo	T_e (K)	T_s (K)	τ_F^*
Venus	108	2620	0.71	244	750	117
Earth	150	1367	0.31	253	288	0.9
Mars	228	593	0.17	216	220	~ 0

6.4 Post Satellite View of the ERB

Figure 6.8 shows the globally and monthly averaged components of the ERB derived from measurements made on satellites (these are from a composite of various pre-ERBE satellite measurements). Figure 6.9 shows the net flux separated by winter and summer hemispheres. These diagrams highlight the annual cycle in F_{net}, α, and F_∞. Some notable points:

- Upper panel: planetary albedo - note the maximum during NH winter months. This is associated with illumination of snow covered land surfaces.
- Middle panel: maximum emission NH summer related to heating of land masses.
- Lower panel: net flux maximum in SH summer (perihelion) and minimum during NH summer (aphelion). Sun-Earth distance effects on solar insolation produce an annual cycle ~26 W m^{-2} compared to 22 W m^{-2} observed. (Note offset in observations about ~9 W m^{-2}.)

Zonally averaged profiles of the three components are shown in Fig. 6.10a, b and c. Emitted flux distributions show a bimodal distribution with a minimum about the equator (due to deep, cold convection) and maximum in subtropics (clear sky). Albedo increases poleward due to increasing reflectivity of clouds and other reflecting surfaces as the solar elevation decreases. Note areas shaded show both the surplus of net flux and deficit of net flux in the Polar Regions, implying a transport of energy out of the equatorial regions toward the poles (see §6.6). This is the fundamental drive of the atmosphere and oceanic circulations.

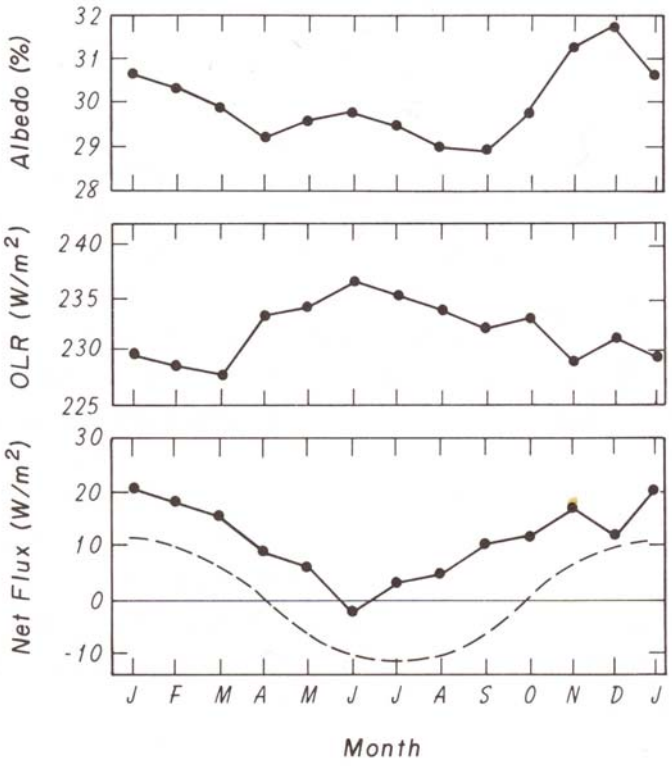

Fig. 6.8 Annual variation of the global albedo, emitted longwave flux and net flux. Also shown in the dashed line is the monthly deviation from the annual mean insolation using a solar constant of 1376 W m^{-2} (after Stephens, et al., 1981).

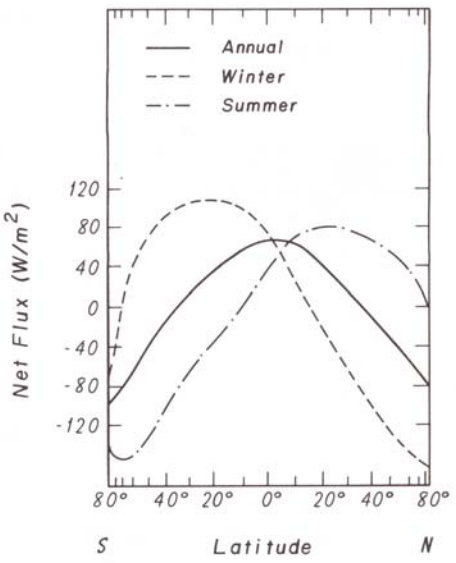

Fig. 6.9 Latitudinal distribution of the annual, winter (December, January, and February), and summer (June, July, and August) net fluxes (after Stephens, et al., 1981, with modifications).

Figs. 6.10a and b show regional distributions of net flux and albedo. These show significant longitudinal variations (e.g., along the equator). The east-west variations in the individual components is as large as the north-south variations. The hot spot of the globe is the maritime continent.

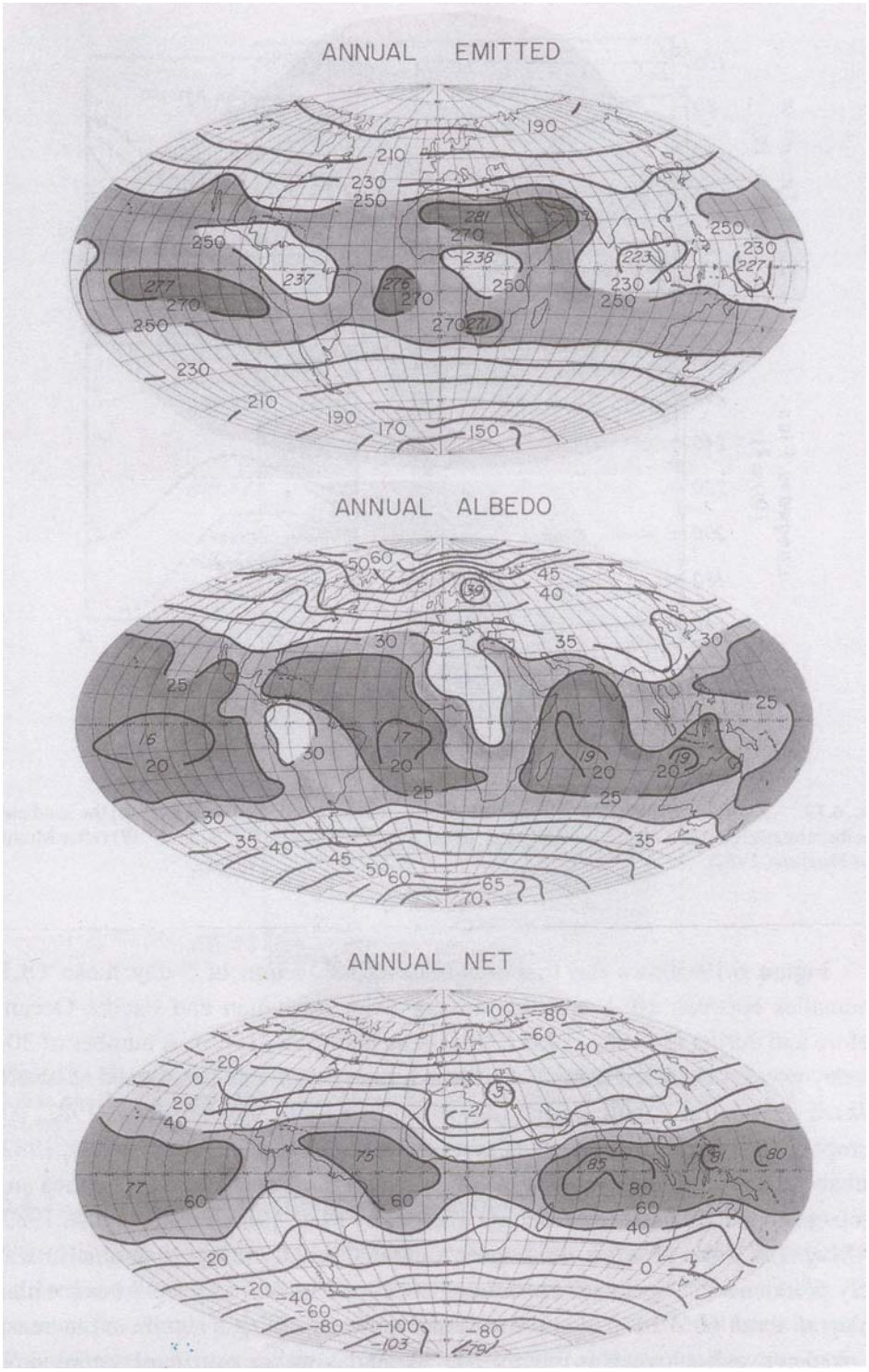

Fig. 6.10 Mean annual infrared flux (W m^{-2}), planetary albedo (%), and net flux (W m^{-2}) (after Stephens, et al., 1981).

6.5 The Energy Budget of Earth

So far we have considered only the part of the budget that applies to the top of the atmosphere. The ERB is also the planetary energy budget since the only exchanges of energy between earth and space take place via radiation. We now examine this energy balance in more detail.

(a) Annual-Global Mean Energy Balance

The annual and globally averaged radiative balance of the atmosphere, unlike for the ERB, is not zero but distinctly negative: *LW* balance = $G - (E + M) - (F + K)$ = -174 W m^{-2} and *SW* balance = $A - D - B$ = 68 W m^{-2}. That is the atmosphere constantly loses energy via radiation by an amount –174 + 68 = -106 W m^{-2} and the earth's surface gains energy by the same amount to balance this loss. Heating of the lower boundary of a fluid while cooling its interior is the classical mechanism for inducing convective instability and turbulence. Turbulent heat transfer (S = 16 W m^{-2}) and condensation of water (the excess of condensation over evaporation—in the form of precipitation falling to the ground, H = 90 W m^{-2}) make up the radiative deficit. The combination of these non-radiative processes is loosely called convective heat transport and the balanced state of the atmosphere is termed at radiative-convective equilibrium.

The surface budget is made up of a balance between net solar radiation at the ground (B = 169 W m^{-2}) plus the net longwave budget at the ground ($E + M – G$ = 63 W m^{-2}) and the heat transferred to the atmosphere via sensible heating (S) and latent heating (H). While the global average shows the transfer of energy ($H + L$) from the surface to the atmosphere, there are times and places where the transfer is in the other direction.

Representations of this budget have varied in detail over the years since the original version of Dines (1917), which is reproduced in Fig. 6.11a. For instance, the planetary albedo, estimated by Dines to be 50%, has been considerably revised to the value of D/A = 30%, largely because of modern satellite ERB measurements. One issue of concern to Dines at the time of his study was the precise value of the Stefan-Boltzmann constant.

(b) Schematic View of IR Radiative Transfer in the Atmosphere

An important observation noted above is that the atmosphere loses IR radiation by the amount of -174 W m^{-2}. This gives rise to an overall atmospheric cooling (to be discussed later). This is a result of longwave radiative transfer in the atmosphere. Longwave radiation is absorbed, emitted and to a much lesser extent scattered from layer to layer in the atmosphere thus creating a transfer problem of some complexity. The chief absorbers of this radiation are:

- Trace gases - CO_2, H_2O and O_3 (these absorptions are quantized processes, which produce discrete absorption "lines". The absorptions occur through quantization of rotation and vibration of the molecular bands and is discussed in more detail in the next chapter).
- Cloud droplets and crystals.
- Aerosol (such as dust, soot, etc.).

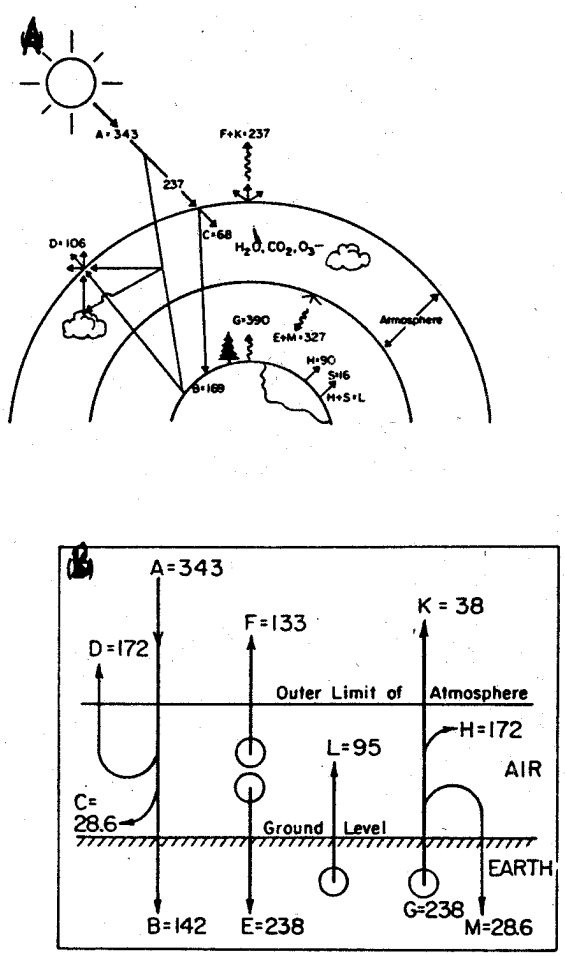

Fig. 6.11 (a) The modern view of the energy budget (Stephens and Tsay, 1991). (b) Original view of the energy budget of the planet as envisaged by Dines (1917).

Figure 6.12a provides a schematic of the longwave flux measured at the ground. This flux is a result of radiative transport processes in the terrestrial atmosphere. Of particular importance to the energy budget of the Earth-atmosphere system is the so called "atmospheric window", which is fairly transparent to radiation processes in the clear atmosphere but this is "filled in" by cloud. Figure 6.12b provides an example (the reverse of Fig. 6.12a) of radiation emitted by Earth and other planets. The radiation is expressed as an equivalent temperature, which is the spectral equivalent of T_p. It is this kind of measurement that enables us to deduce the composition of planetary atmospheres via remote sensing.

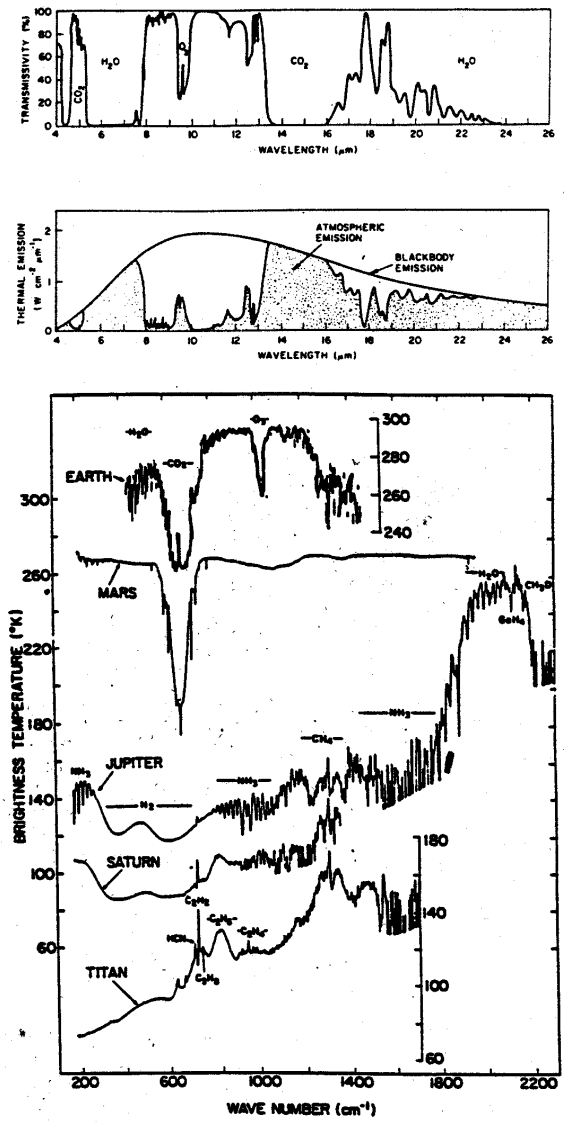

Fig. 6.12 (a) The emission from a clear sky (solid curve) and a cloudy sky (dashed curve) measured by a hypothetical radiometer on the ground. (b) A low-resolution depiction of the absorption by the main greenhouse gases of the Earth's atmosphere (upper part of (b)) spectra of IR emission, plotted as brightness temperatures, for four planets and Titan (Hanel, 1983).

6.6 The Meridional Transport of Heat by the Planet

(a) Observations

The profound role of the general circulation on temperature is illustrated by reference to Fig. 6.13. Without horizontal transport of heat, the temperature of each latitude would be governed by radiative equilibrium alone. In this case, summers in mid-latitudes would be warmer than without transport, and winters much colder. Heat is transported by the atmosphere and oceans out of the equatorial regions and subtropics to the Polar Regions where it is mixed mechanically to produce more moderate temperatures at higher latitudes

(Additional reference, Oort and Vonder Haar, 1976: On the observed annual cycle in the ocean-atmosphere heat balance over the Northern Hemisphere, *J. Phys. Ocean.,* **6**, 781-800.)

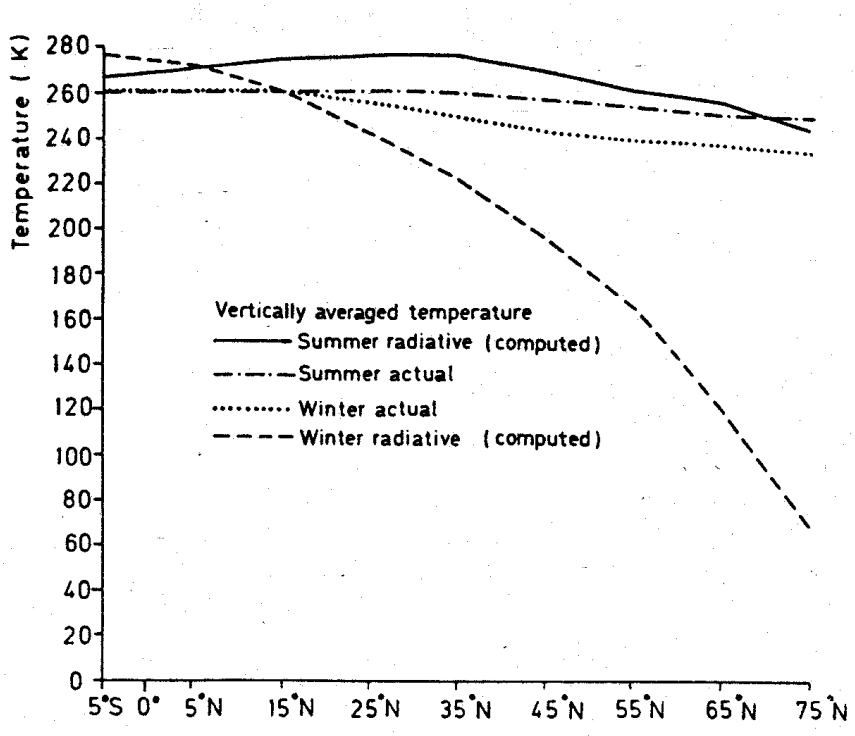

Fig. 6.13 Comparison of theoretically derived radiative equilibrium and observed vertically averaged temperature profiles for the summer and winter.

We can calculate this total transport required from simple principles of energy conservation. Consider the 'system' as in Fig. 6.14 that loses (or gains) energy through its upper boundary and transports energy across its lateral boundaries. The rate at which energy changes inside this system is

$$\frac{\partial E}{\partial t} = F_{net} - div\mathbf{T}_{\mathbf{A}} - div\mathbf{T}_{\mathbf{o}} \tag{6.20}$$

where

- F_{net} = net radiation input into the top of the atmosphere (e.g., Fig. 6.15)
- $div\mathbf{T}_{\mathbf{A}}$ = divergence of energy from the atmosphere due to atmospheric transports
- $div\mathbf{T}_{\mathbf{o}}$ = divergence of energy from the ocean due to oceanic transports.

$\partial E/\partial t$ is the energy gained by the "system" which is then stored in the atmosphere and ocean, i.e.,

$$\frac{\partial E}{\partial t} = S_A + S_o + S_L + S_I \tag{6.21}$$

where S_A, S_o, S_L, and S_I are energy storage terms associated with the atmosphere, ocean, land, and ice, respectively.

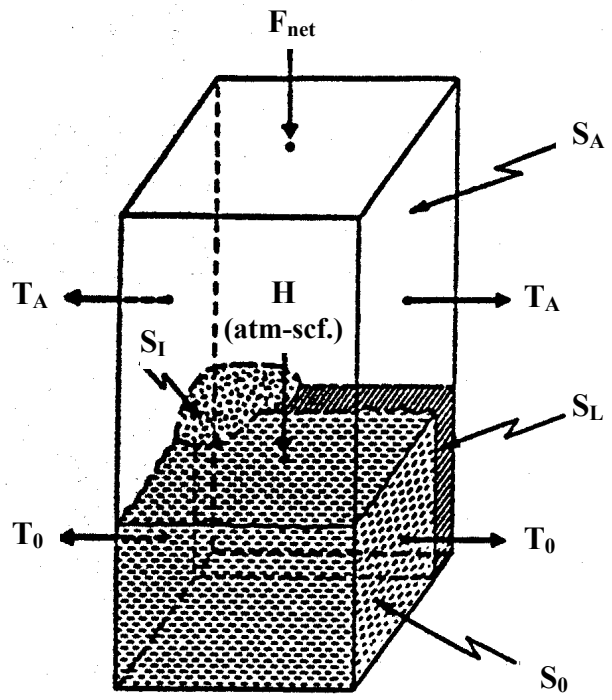

Fig. 6.14 Schematic diagram of the different terms in the earth's energy balance (Oort and Vonder Haar, 1976).

Figures 6.15a and b provide zonally averaged estimates of heat storage by the atmosphere and oceans, respectively (i.e., of S_A and S_o) as a function of time year. The atmosphere storage plays only a minor role in the energy budget. This storage occurs by incoming solar energy, which is used to increase internal energy (temperature), and the specific humidity (i.e., latent energy). The maximum storage occurs around May and maximum depletion is around September. By contrast, the storage of energy by the oceans plays a far more formidable role in the time varying energy budget of the climate system. This reaches a maximum in excess of 100 W m^{-2} at about 40°N. Most of the storage occurs east of North America in the Gulf and east of Japan. The land and ice storage terms are smaller although estimates of S_I are poorly based.

On the annually averaged basis, we consider each latitude zone to be in steady state, i.e.,

$$\left\langle \frac{\partial E}{\partial t} \right\rangle = 0 \tag{6.22}$$

where < > is an annual average.

Thus,

$$\langle F_{net} \rangle = \langle divT_a \rangle + \langle divT_o \rangle \tag{6.23}$$

or

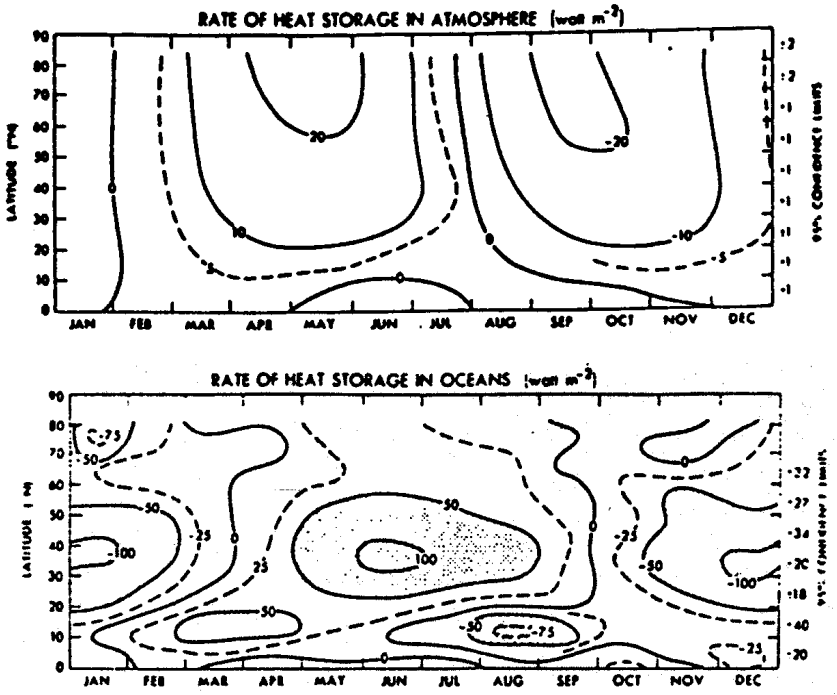

Fig. 6.15 (a) Rate of heat storage in the atmosphere (S_A) based on radiosonde data as a function of latitude and month of the year. Units are in W m^{-2}. (b) Rate of heat storage in the oceans (S_o) based on hydrographic stations, MBT and XBT data as a function of latitude and month of the year. Units are in W m^{-2}. To obtain typical oceanic values divide by the percentage of the horizontal area covered by oceans (factor = 0.61 for the Northern Hemisphere as a whole).

$$\left\langle F_{net}(\phi)\right\rangle = \frac{1}{a}\frac{\partial T}{\partial \phi} \tag{6.24}$$

where a is the mean radius of the earth and ϕ is latitude and T is the combined oceanic and atmospheric transport. We can numerically integrate Eqn. (6.24) to obtain the transport required to balance the net radiation deficits (e.g., Carrissimo et al., 1985: Estimating the meridional energy transports in the atmosphere and oceans, *J. Phys. Ocean,* **15**, 82-91). For example, integration of Eqn. (6.24) over the polar cap (Fig. 6.16a) yields

$$T(\phi) = T_a(\phi) + T_o(\phi) = 2\pi a^2 \int_{\pi/2}^{\phi} \left\langle F_{net}\right\rangle(\phi')\cos\phi' d\phi' \qquad \text{(W)} \tag{6.25}$$

The total transport is estimated this way using satellite data for F_{net}. The meridional energy transports by the atmosphere may be obtained from analysis of conventional meteorological data (e.g., Oort and Vonder Haar). The ocean transports (Fig. 6.16b) can be derived as a residual.

An alternate way of estimating the heat transport by the Earth's oceans is to consider the average form of the terrestrial branch of the energy balance, i.e.,

$$\left\langle F_{net-surf}\right\rangle = \left\langle div\mathbf{T_o}\right\rangle \tag{6.26}$$

where, on an annual average basis, the storage terms are zero. The estimate of the oceanic energy transport derived according to this balance is also depicted in Fig. 6.16b (after Sellers). The significant discrepancy between the two estimates has been a topic of debate for some time.

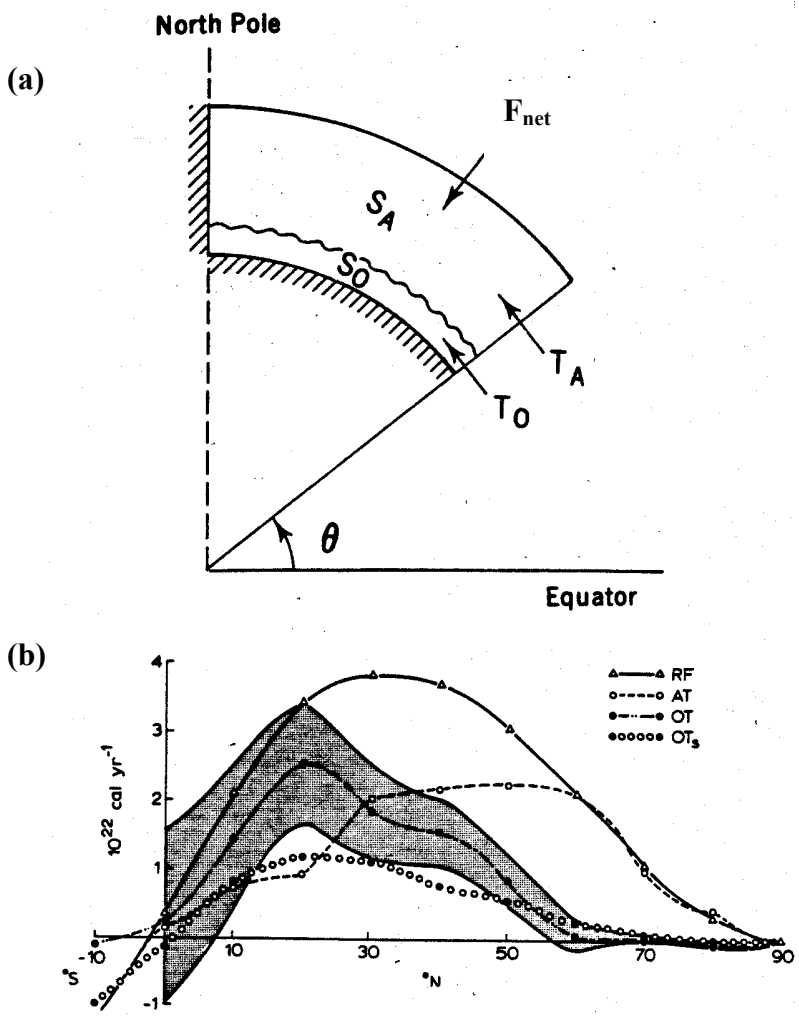

Fig. 6.16 (a) Principle of integration over the polar cap. (b) Variation of net energy transport with latitude over the northern hemisphere: RF = total required energy transport inferred from satellite measurements; AT = measured energy transport by the atmosphere; OT = oceanic energy transport derived from RF and AT; OT_s = oceanic energy transport according to Sellers (1965). Uncertainty in the OT values is denoted by the shading. Minus values indicate net transport to the south (after Vonder Haar and Oort, 1973).

The heat flux distribution around the oceans, based on a similar analysis of the surface budget, is depicted in Fig. 6.17a. The fascinating aspect of the analysis portrayed in this diagram is the consistent northward transport depicted for the entire Atlantic Ocean. However, we should view this analysis as being somewhat speculative given the comparisons of Fig. 6.17a and b. The only real convincing estimate of heat transport of the oceans is from direct estimates from measurements conducted in the ocean. Figure 6.17b shows the results of these kinds of estimates in limited portions of the ocean. The two estimates of Fig. 6.17a and b are broadly similar but differ in important detail.

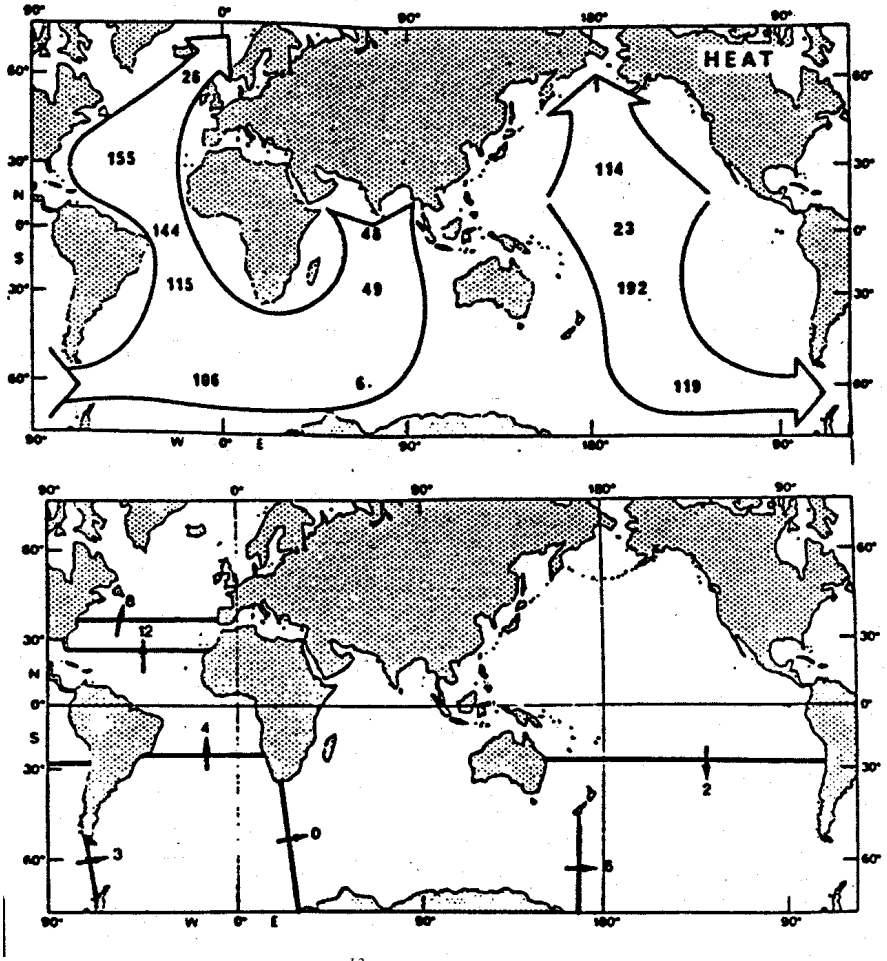

Fig. 6.17 *(a) The circulations of heat (10^{13} W) around the world ocean, as deduced by Strommel (1979) and Baumgartner and Reichel (1975) from the global patterns of energy. (b) The circulation of heat 10^{14} W in the world ocean deduced from oceanographic measurements at a few trans-ocean sections (Bryden 1982).*

(b) Model Comparisons with Observation

(ref Glecker et al., 1995: Cloud radiative effects on implied energy transports as simulated by AGCMs, *Geophys. Res. Letters*, **7**, 791-794.)

Recent model comparisons have revealed how radiation processes in clouds in different AGCMs lead to an unacceptable large spread in the implied meridional transport. Figure 6.18a shows T_{O+A} inferred from TOA net radiation as observed from ERBE and derived from ERB simulations from models. Figure 6.18b is the atmospheric component of this total transport as deduced from observations (Oort), analyses (Trenberth/Savijarvi) and derived from models. Figure 6.18c shows the zonal average net surface energy flux as simulated from models and as derived from observations (complete with error estimates on the latter). Various observational estimates of T_o are given in Fig. 6.18d and these are contrasted with model deduced transports on Fig. 6.18e also derived from model surface fluxes. The spread in these results and the difference from 'observations' was attributed by Glecker et al. to model differences in treatment of the radiative effects of clouds (Fig. 6.18f). The quantity shown in Fig. 6.18f is the quantity C_{SW} introduced in the next section. When the combined transport of Fig. 6.18a and the atmospheric transports of each model (Fig. 6.18b) are used, the residual ocean transport of Fig. 6.18g is obtained. Together Fig. 6.18f and g

suggest that the implied energy transport in the oceans is not correct largely as a result of poorly represented cloud-radiation processes.

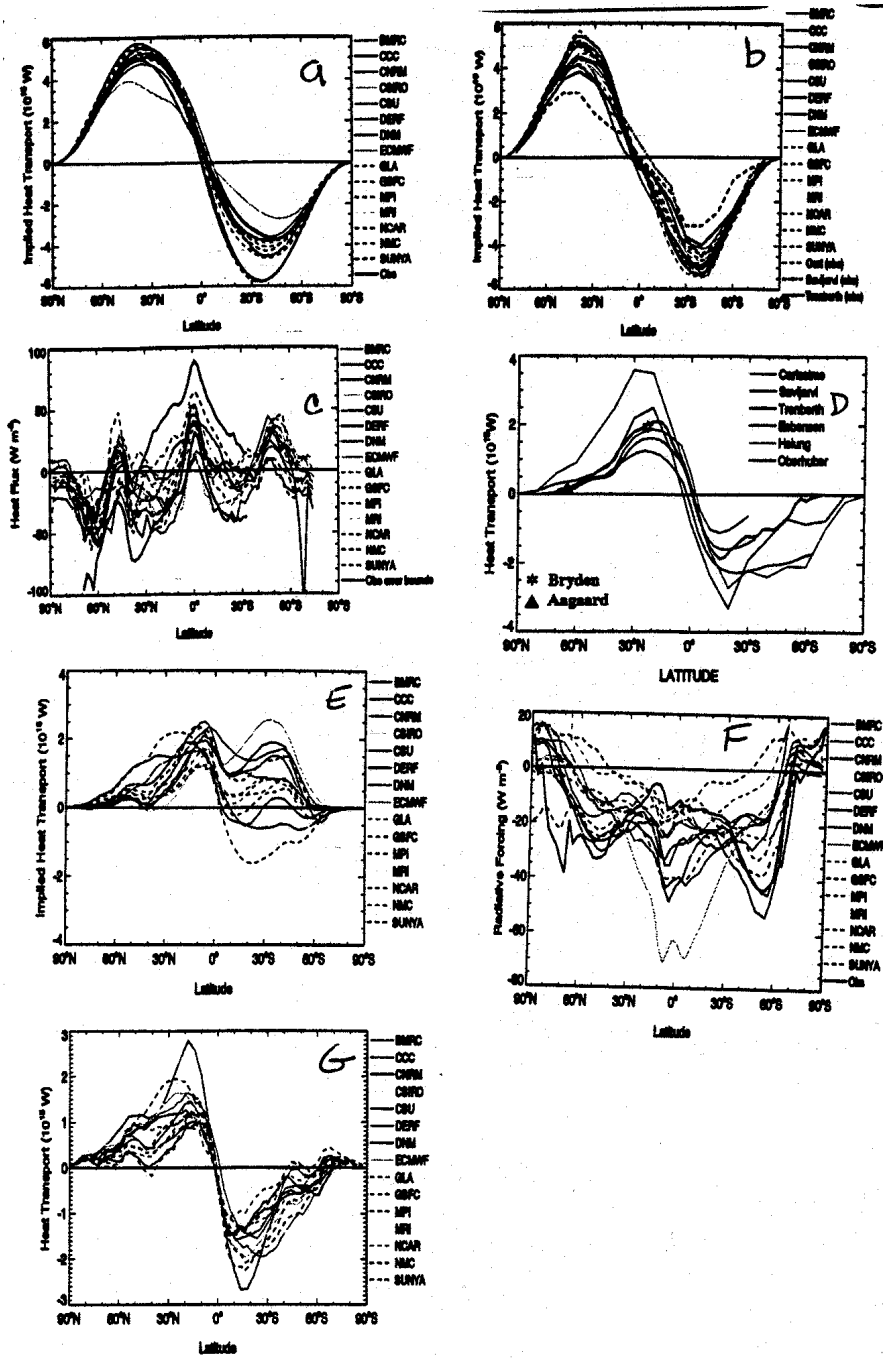

Fig. 6.18 *(a) Annual mean northward meridional energy transport of oceans plus atmosphere. (b) Annual mean northward meridional energy transport of the atmosphere. (c) Net ocean surface heat flux, (d) Observed annual mean northward meridional energy transport of the ocean. (e) Annual mean northward meridional energy transport of the ocean derived from model surface fluxes. (f) Zonal, annual average net TOA cloud flux differences as defined in the next section. (g) Annual mean northward meridional energy transport of the ocean derived from model atmospheric transport and observed TOA ERB.*

6.7 Problems

Problem 6.1

Suppose that a cloud layer whose temperature is 7°C moves over a snow surface whose temperature is 0°C. What is the maximum rate of melting of the snow that could be supported by net LW radiation convergence at the surface if the absorptance of the cloud is 1.0 and of the snow is 0.95?

Problem 6.2

If one assumes that the planetary albedo of the earth is 30%; that the atmosphere transmits all SW radiation; and that the atmosphere acts as a single isothermal layer that absorbs all longwave radiation falling on it, find the radiative equilibrium temperatures of the atmosphere and the earth's surface.

Problem 6.3

A so-called greenhouse is depicted below. Assume a solar zenith angle θ, that the top of the house transmits all SW radiation and has an infrared emittance ε_{TOP}. The ground absorbs all LW radiation and has an albedo ρ_{grnd}. Assuming radiative equilibrium, derive an expression relating the temperature of the ground to the emittance of the roof and the solar zenith angle. Derive a second expression for the equilibrium temperature of the roof as a function of the ground temperature if $\varepsilon_{TOP} = 1$ and $\rho_{grnd} = 0.2$.

Problem 6.4

If the average surface temperature of the earth is 288° and the average albedo of the earth and atmosphere for solar radiation is 30%, find the "effective absorptance" of the atmosphere for longwave radiation.

AT622 Section 7
Earth's Radiation Budget

Here we examine the effects of the atmosphere and clouds on the Earth's radiation budget (ERB). While the notions described deal with the simpler aspects of these effects and are heavily based on TOA observations, the material presented provides important insight into atmospheric radiation. More detailed and rigorous understanding will come when the topics of this section are revisited in later sections in the context of radiative transfer.

7.1 The ERB Measured From Space: An Overview of the ERBE

The history of the ERB measurements closely parallels the overall space effort within the United States and other countries of the world. A reference that details the history of the ERB observation is that of House et al., 1986: History of satellite missions and measurements of the earth radiation budget (1957-1984), *Revs. Geophys,* **24***, 357-377*. Discussion of pre-satellite ERB studies is provided by Hunt, 1986 (same issue of *Rev. Geophys*.). Table 7.1 provides a convenient overview of this history. The first-generation instruments were narrow spectral channel scanning radiometers. These provided spectral radiance measurements for limited ranges of angle. Models of the angular distribution of radiance were required to convert these to flux (via bi-directional models). The second-generation instruments were flat

Table 7.1: Historical Overview.

Satellite Mission	Launch Date	Altitude Range (km)	Inclination Angle (deg.)	Orbit Time	Lifetime(s)	Contributions
First-Generation Missions						
Explorer 7	Oct. 13, 1959	550-1,100	51	Drifter	7 months	First dedicated satellite providing usable ERB data
TIROS 2	Nov. 23, 1960	717-837	48	Drifter	1-5 months	First scanning radiometer with five SW/LW channels
TIROS 7	June 19, 1963	713-743	58	drifter	12 months	Provided 1 year of radiation balance observations
Second-Generation Missions						
Research/ESSA	1960s	≈ 1,500	102	0900/1500	3-15 months	Global data sets from WFOV nonscanning radiometers
Nimbus 3	Apr. 14, 1969	1,100	99	Noon	1 year	Detailed global radiation balance for 1 year
NOAA NOAA-N/NOAA	1970s 1978-1981	≈ 1,500 ≈ 840	102 99	0900 1500/0730	Years Years	Combined data sets provided 10 years of observations
Third-Generation Mission						
Nimbus 7 ERB	Oct. 1978 To the present	950	99	noon	6+ years	Total and spectral solar monitoring; bi-directional reflectance and directional albedo models
Geostationary Missions						
GOES-E/W (75°-135°)	1970s/1980s	36,000	0	24 hours	Years	Diurnal variations of SW/LW exitances and cloud distributions: satellite mission simulations
METEOSAT ½ (0° longitude)	1977/1982	36,000	0	24 hours	Years	

plate broadband instruments that measured a quantity more closely resembling the hemispheric flux (Fig. 7.1) although some deconvolution is required to obtain fluxes. The third generation instrument suite

includes wide field of view, broadband instruments, and narrow field of view scanning instruments. One advantage of the latter is the spatial resolution.

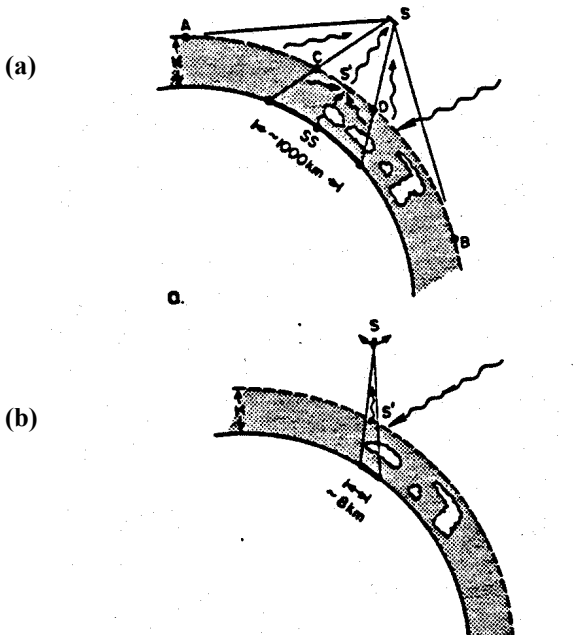

Fig. 7.1 (a) Flat plate instrument versus (b) Scanners.

One of the significant problems of the early studies is the lack of sampling of the diurnal variations. Single satellite missions cannot provide enough observations to pull out the seasonal and diurnal variability at scales varying from the global scale to the synoptic scale to the more localized regional scale. ERBE proposed a three-satellite strategy for sampling the globe (Fig. 7.2a and b) involving two polar orbiters and the ERBS at a 57° inclined orbit. The resulting sampling is given in Fig. 7.2a.

The ERBE instruments are built in two packages: a scanner package and a nonscanner package. The scanner contains three scanning radiometers and capabilities for onboard calibration. The scanner (Fig. 7.3a) consists of a shortwave, longwave, and total radiometer mounted in a single scan head to receive radiation from the same FOV (usually scans across the track). The nonscanner (Fig. 7.3b) contains a total wide FOV (WFOV- view of the entire earth disc) radiometer and a shortwave radiometer. There are also medium FOV radiometers (MFOV) and an active cavity radiometer to measure solar output.

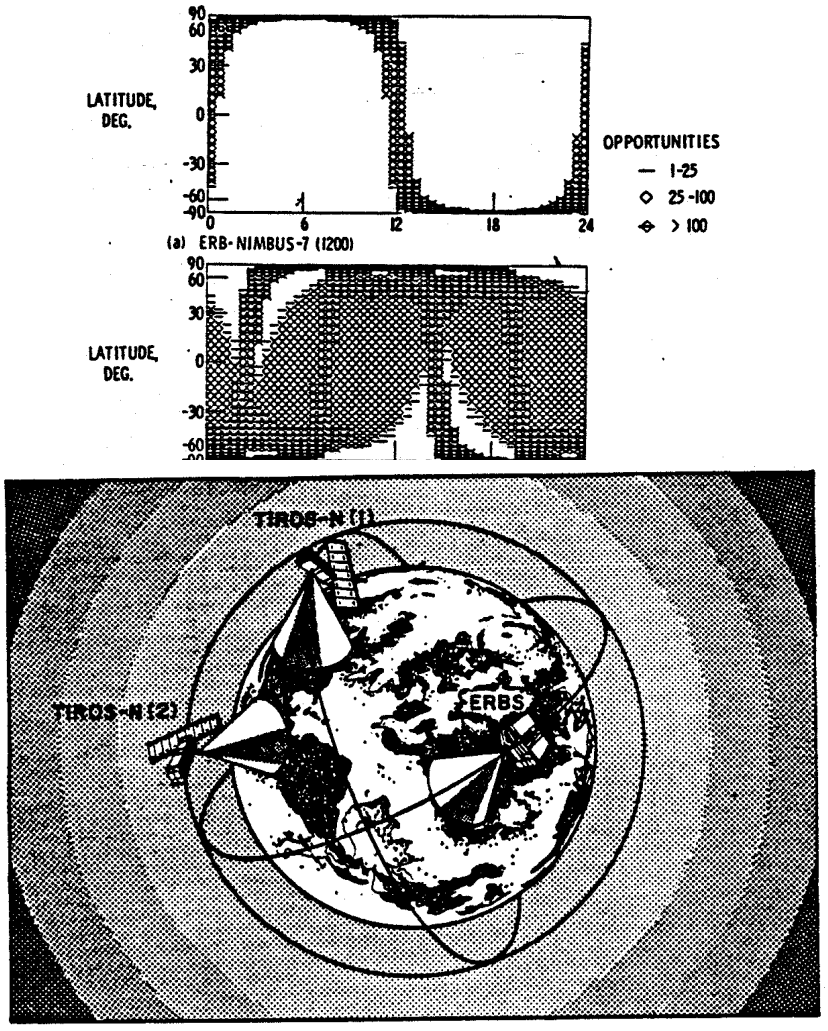

Fig. 7.2 (a) Local time coverage of Nimbus 7 satellites upper and the three satellites combined (lower). (b) The three satellite orbit configurations.

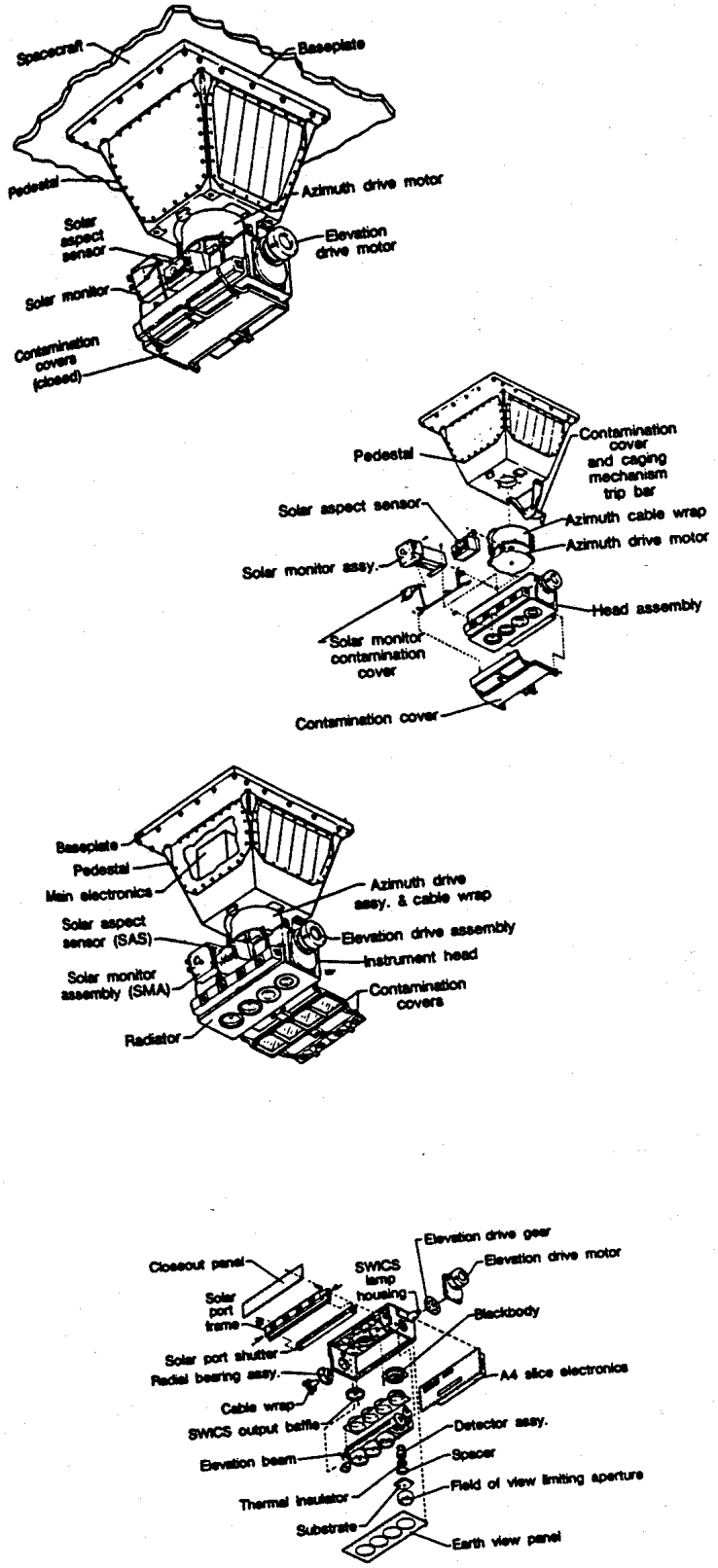

Fig. 7.3 (a) Scanning radiometer. (b) Nonscanning radiometer.

7.2 Satellite Classification of Clouds

Clouds provide a first-order effect on the radiative budgets and water exchanges in the atmosphere. They also play a fundamental role in studies of climate and climatic change. Several attempts have been made to classify the global distribution of clouds based on measurements obtained from radiometers flown on satellites. Two examples of these radiometric classifications of clouds will now be discussed.

(a) Emission Classification in the Split Window

Inoue (1989) developed a simple way to classify clouds according to the difference in their emission properties at 11 and 12 μm. As mentioned earlier, $\Delta T = T_{10.8} - T_{12}$ is a good indicator of the opacity of clouds. Thick clouds, radiating approximately like a blackbody, possess small values of ΔT whereas thin clouds exhibit more variable values of ΔT as described earlier in a way that depends on particle size and other factors.

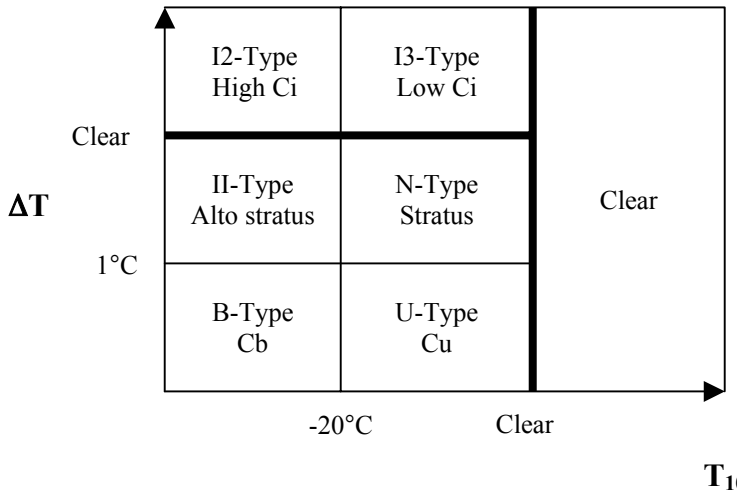

Fig. 7.4 An example of a cloud-type classification diagram introduced by Inoue (1989).

Inoue's classification scheme is based on threshold analyses of the T - ΔT diagram like that shown in the example shown in Fig. 7.4. Two threshold values of ΔT can be identified, one at ΔT = 1 K corresponding to optically thick clouds and another to a slightly larger value corresponding to the clear sky value of ΔT. Two threshold values of the brightness temperature $T_{10.8}$ are also introduced in the Inoue scheme; one is the high cloud threshold, which is set at -20°C, and the other corresponds to clear sky temperatures. Data representing different cloud types fall in the different classification boxes. For example, cumulonimbus clouds are thick, possess ΔTs less than 1 K, and are cold. These fall in the type B category. Low level cumulus and stratocumulus clouds fall into Inoue's category U. Thin cirrus clouds are characterized by values of ΔT that exceed the clear sky threshold value and fall in categories 12 and 13 for thick and thin clouds, respectively. Stratus clouds have opacities between cirrus and cumulus clouds, and fall into categories II and N.

(b) The International Satellite Cloud Climatology Project (ISCCP)

ISCCP formerly began in 1983 with the collection of the first internationally coordinated satellite intensity data. The original plan called for this collection for only a five-year period but the ISCCP extended this collection to 1995. This program was the first of its kind involving routine collection of

operational satellite data. Many key problems needed attention including lack of global converge and cross calibration of satellite radiometers. These issues are addressed elsewhere.

The cloud detection scheme used in ISCCP is different from the emission scheme highlighted above as it uses both visible reflection information as well as emitted radiation. The detection approach examines all of the data for one month to collect statistics on the space/time variations of the VIS and IR intensities. The key assumptions used in the analysis are that the intensities in clear scenes are less variable than those in cloudy scenes and that it is the clear scenes that compose the darker and warmer parts of the VIS and IR intensity distributions, respectively. Estimates of the clear sky values of VIS and IR intensities for each location and time are made and composited into maps (these are referred to as the "clear sky composites"). This approach is novel in two respects. First, all of the complicated tests usually used to detect cloudiness directly, many of which were first proposed by other investigators, are used here to identify clear scenes. The use of time variations at one location to identify clear scenes also differs from many other methods.

The differences between the intensities measured and the estimated clear sky intensities are compared to the uncertainties in estimating the clear intensities. If the differences are larger than this uncertainty and in the "cloudy direction" at either wavelength (colder IR or brighter VIS), then the pixel is labeled cloudy. Once each pixel is classified as clear or cloudy, the measured intensities are compared to radiative transfer model calculations that include the effects of the atmosphere, surface and clouds. The intensity data are then converted into two-cloud properties—the "visible" optical thickness (defined at 0.6 μm) and a cloud-top pressure. The optical thickness parameter determines the amount and angular distribution of sunlight reflected by the cloud layer (the full effects of multiple scattering are included in the model and we will examine the form of this model later)—the cloud-top pressure is supposed to account for cloud emissivities less than 1. At night, when only IR intensities are measured, no cloud optical thickness is reported and IR variations are associated with the cloud-top brightness temperature.

Thus, the ISCCP clouds are categorized in terms of cloud-top pressure and optical-depth properties as schematically shown in Fig. 7.5a. A second category group, based on a combination of those in Fig 7.5a, is given in Fig 7.5b. Two examples of the two-dimensional categories as defined in Fig. 7.5a for July 1983 are presented in Figs 7.5c and d for two different latitude zones. Maps of the categories introduced in 7.5b are shown later in Fig. 7.9. In the subtropics during winter (Fig. 7.5c), the predominant cloud type has low tops and relatively low optical depths (probably associated with highly broken cloud). The tropical distribution is more complicated showing a prevalence of high, optically thick clouds and low, relatively thin clouds associated with highly broken low-level clouds.

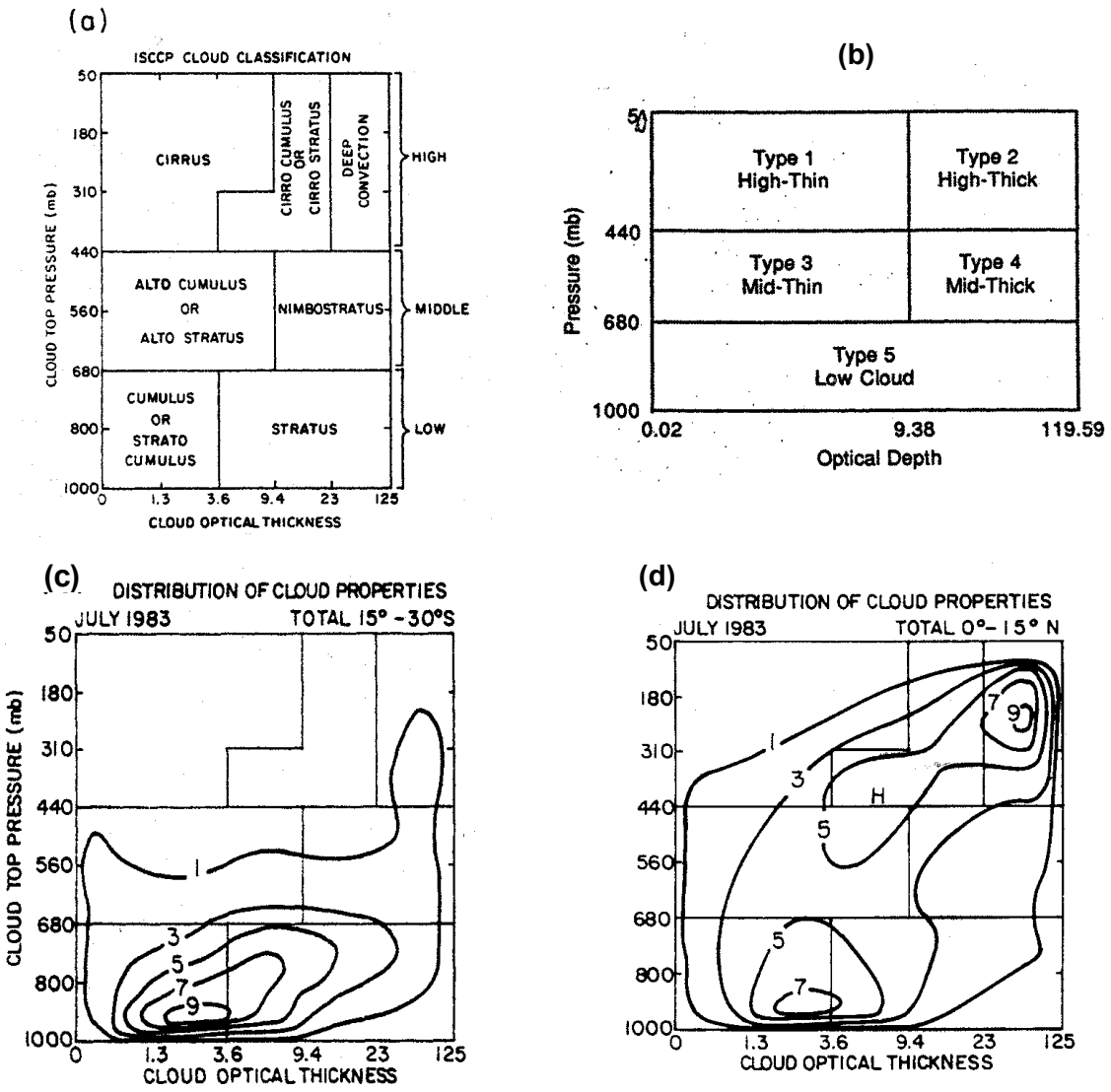

Fig. 7.5 (a) Radiometric classification of cloudy pixels in terms of optical thickness and cloud-top pressure. (b) A second category group based on a combination of those in (a). (c) The frequency distribution of cloud optical thickness and cloud-top pressure for July 1983 for the southern subtropics and (d) the northern tropics (from Rossow and Shiffer, 1991).

7.3 The Effects of Clouds on the ERB: The Idea of Cloud Radiative Effect

Our every day experience tells us that clouds are white and reflect significant amounts of solar radiation. Conversely, clouds are dark at infrared wavelengths, strongly absorbing and hence also strongly emissive. These characteristics are used to detect clouds in the ISCCP algorithm. What we will learn in later sections is that the ability of clouds to reflect solar radiation is related to their ability to emit radiation in a complex manner. When viewed from the top of the atmosphere, clouds produce a curious impact on radiative transfer, on the one hand increasing (solar) radiation leaving the planet, yet on the other hand inhibiting the emission of (infrared) radiation to space by absorbing radiation emitted from below and replacing it with a reduced amount of radiation emitted by the colder cloud particles

themselves. These two competing processes produce a net effect that is in somewhat delicate balance—a balance that depends on height, thickness, amount of clouds, and even on the size of the particles in the cloud that governs the ability of cloud particles to scatter and absorb radiation.

Example 7.1: Golden Arches

One of the advantages of satellites as observational platforms of clouds is their ability to record patterns and structures of clouds over wide ranges of space and time. A method that exploits this particular advantage, as well as using the properties of cloud emission, is the spatial coherence technique introduced by Coakley and Bretherton (1983). The idea behind the approach is portrayed in the upper panel in Fig. 7.6. It schematically shows a group of 2 x 2 neighboring pixels of 11 μm radiances expressed in this specific example as brightness temperature. These pixels are processed to provide the average 11 μm brightness temperature of the group and the standard deviation about this average. The latter is a measure of the texture of the image on the scale of the pixel array chosen. These two pixel group quantities are then plotted on a scatter diagram in the fashion given by Fig. 7.6. The satellite data used to construct this scatter plot are the 11 μm radiances obtained with the NOAA-9 overpass at 2242 GMT on July 7 obtained from the AVHRR viewing marine stratus clouds off the west coast of California (Coakley, 1991).

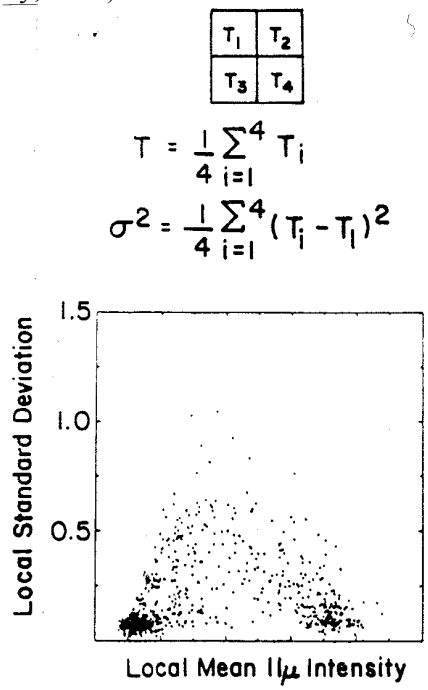

Fig. 7.6 A schematic demonstration of the method of spatial coherence (upper panel) as it might be applied to brightness temperatures. Spatial coherence analysis of 11 μm intensities for a (250 km)^2 region over stratus clouds off the west coast of California. Each point represents values for a 4 x 4 array of (1 km)^2 AVHRR pixels (Coakley, 1991).

Example 7.1: Continued.

The scatter of points on the diagram resembles an arch. The feet of the arch contain important information about those regions of the image that are relatively homogeneous across the group of neighboring pixels. One foot is associated with the relatively clear sky portion of the scene and the other to the pixel groups that are completely filled by a cloud with the same temperature. This provides a way of discriminating clear sky brightness temperatures from partially cloudy skies (T_{broken}) and from the brightness temperature (T_{cld}) of a homogeneous layered cloud. For the case shown, only two effectively homogeneous surfaces exist, one is the clear sky background and the other is that of the solid cloud portions of the image. The point in the arch corresponds to a partially filled pixel group of cloud cover N. This approach relies on the statistical nature of the observations that can be used to identify both T_{clr} and T_{cld}.

We consider and refer to the two largely compensating effects as follows:

- The albedo effect—clouds reduce the net solar input into the planet by reflecting more solar radiation to space. This is also sometimes referred to as a cooling potential of the planet.
- The 'greenhouse' effect—clouds reduce the longwave output by effectively raising the level of emission to levels specified by colder temperatures.

A graphic example of these two processes, manifested in the ERB, is shown in Fig. 7.7 in which the annual cycle of the ERB quantities of α, F_{∞}, and F_{net} are presented for a region of the Asian monsoon. What is remarkable is how nearly complete is the cancellation of these opposite effects. The fundamental question is do these effects cancel globally or does one component dominate over the other?

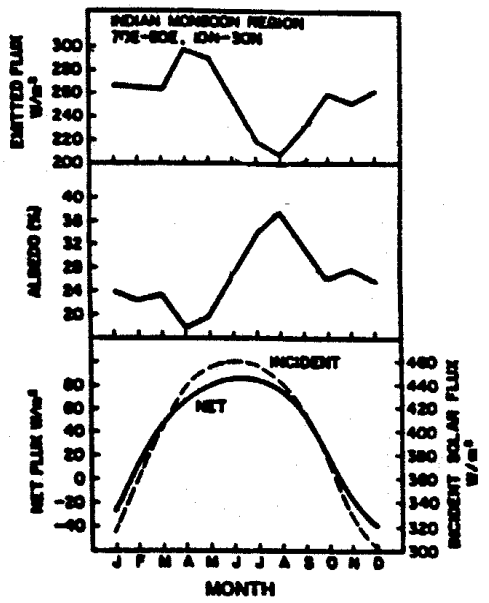

Fig. 7.7 The annual cycles of α, F_{∞}, and F_{net} for the Asian monsoon region indicated.

(a) The Cloud Radiative Effect

One way of studying these compensating radiative processes on the ERB is in terms of a comparison between the TOA fluxes in cloudy portions of the atmosphere to equivalent fluxes in clear skies. Flux difference quantities derived in this way are often mistakenly thought of as the measure of a forcing applied to the Earth-atmosphere system by radiative processes of clouds. As we will see it is not, but these quantities do serve as a useful and helpful diagnostic of the effects of clouds on the ERB. Unfortunately, these diagnostics do not provide the insight needed to determine just what properties of clouds govern these effects although we will hint at these governing properties here and return to these later.

The flux difference quantities are introduced as follows. Suppose for the moment the shortwave component of the reflected radiation can be written as

$$F_s\,(\text{observed}) = F_s\,(\text{clear})\,(1 - N) + NF_s\,(\text{cloudy}) \tag{7.1}$$

where N = cloud amount, F_s (clear) is the radiation reflected by the clear sky portion of the atmosphere and F_s (cloudy) is that flux associated with reflection from the cloudy skies. It should be stressed that we use Eqn. (7.1) only to fix ideas as a relationship such as this and has no theoretical basis. Ignoring this with rearrangement

$$\begin{aligned} F_s\,(\text{observed}) &= F_{clear} + N\overbrace{(F_{cloudy} - F_{clear})}^{-C_{SW}} \\ C_{SW} &= F_s\,(\text{clear}) - F_s\,(\text{observed}) < 0 \end{aligned} \tag{7.2}$$

The quantity C_{SW} refers to the specific contribution to the ERB by reflection from clouds. It can be derived independent of the dubious assumptions of Eqn. (7.1) provided we know the clear sky flux. In going from Eqn. (7.1) to Eqn. (7.2) we can think of C_{SW} as containing a factor due to how much cloud exists (i.e., N) and a factor that defines how readily clouds reflect sunlight when they exist. The flux quantity C_{SW} is negative by convention since clouds increase the reflection to space relative to clear skies.

Using entirely similar arguments

$$C_{LW} = F_\infty\,(\text{clear}) - F_\infty\,(\text{observed}) > 0 \tag{7.3}$$

is the effect of clouds on the longwave component. As noted, this component generally exceeds zero as a result of reduced emission from colder clouds. The net effect of clouds is

$$C_{net} = C_{SW} + C_{LW} \tag{7.4}$$

(b) ERBE Results of Cloud Effects

Once clear sky fluxes are derived, then C_{SW} and C_{LW} readily follow. Examples of these flux difference quantities are shown in Fig. 7.8. Monthly average fluxes derived from ERBE are composited together to produce JJA and DJF maps of C_{LW}, C_{SW}, and C_{net}. Features of most relevance to note are:

- Longwave cloud forcing is a measure of the reduction by clouds of the longwave radiation emitted to space; hence it is a measure of the greenhouse effect of clouds. Clouds reduce emission to space because at their bases they absorb radiation emitted by the warmer surface and at their tops they emit to space at colder temperatures. Deep cold clouds such as occur as part of the monsoon cloud systems over the Indian Ocean and Indonesia have the largest greenhouse effect.

- Because clouds reflect more shortwave solar radiation than the adjacent clear skies, the shortwave forcing is negative—a 'cooling' effect. Surprisingly, the magnitude of this effect is almost precisely as large as the longwave forcing over the tropical cloud systems, and is even larger than the longwave effect over the mid- and high-latitude oceans in the summer hemisphere.
- The net cloud radiative forcing (shown as the bottom panel) is the sum of longwave and shortwave cloud forcing. The averages range from -100 to –140 W m^{-2} (dark blue) to 10-40 W m^{-2} (red). The net globally averaged effect is largely negative; hence clouds overall act to cool the planet (see Tables 7.2 and 7.3). The strongest cooling is caused by the persistent maritime stratus off the west coast of continents and storm-track clouds in the summer hemisphere over the mid- and high-latitude Atlantic and Pacific Oceans.

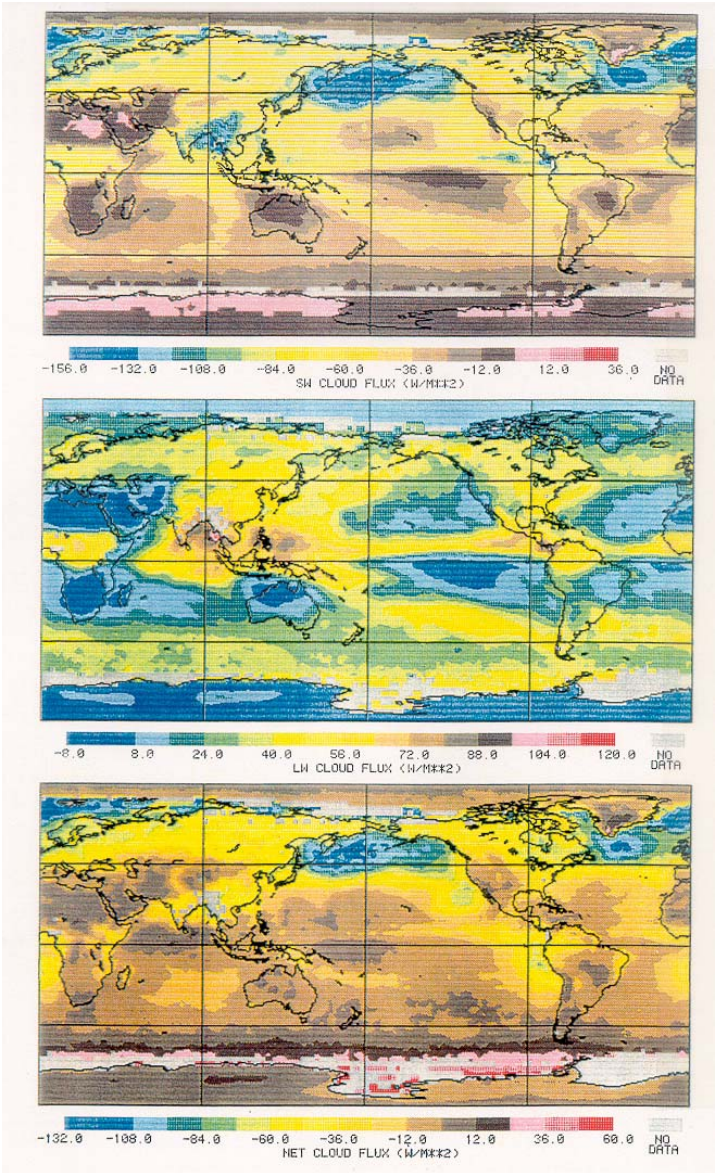

Fig. 7.8 Cloud radiative forcing for JJA 1985 (scales expressed in W m^{-2}).

Because the effects of clouds on C_{LW} and C_{SW} are largely reciprocal, processes that affect one component by a disproportionate amount offers greatest potential for significantly influencing the ERB and thus the Earth's climate. We will study some of these processes later in this course and return to this reciprocity in Section 7.6.

Table 7.2 Nimbus 7 cloud short, long, and net radiative forcing (W m^{-2}). ERBE estimates are in parentheses for middle month of the three-month cycle.

	C_{SW}	C_{LW}	C_{net}
JJA	-42.1 (-46.4)	24.4 (30)	-17.6 (-16.4)
SON	-44.0 (-45.2)	24.5 (32)	-19.4 (-17.4)
DJF	-44.6 (-44.6	22.2 (30.6)	-22.4 (-21.3)
MAM	-44.7 (-44.7)	25.2 (31.3)	-19.5 (-13.2)

Table 7.3 Contributions to flux effects by type.

	Type 1 high, thin		Type 2 high, thick		Type 3 mid, thin		Type 4 mid, thick		Type 5 low		
	JJA	DJF	JJA	DJF	JJA	DJF	JJA	DJF	JJA	DJF	Sum Average
Ni	10.2	10.0	8.5	8.8	10.7	10.7	6.5	8.2	27.2	25.9	63.3
OLF	6.5	6.3	8.4	8.8	4.8	4.9	2.4	2.4	3.5	3.5	25.8
Albedo	1.2	1.1	4.1	4.2	1.1	1.0	2.7	3.0	5.8	5.6	14.9
Net	2.4	2.3	-6.4	-7.5	1.4	0.8	-6.6	-8.5	-15.1	-18.2	-27.6

7.4 Classification of Cloud Effects in Terms of Cloud Type

Ockert-Bell and D. L. Hartmann (OBH), 1992: The effect of cloud type on earth's energy balance: results for selected regions, *JGR*, **86**, 9739-9760.

In this study, the effects of different cloud types, as defined by ISCCP are regressed with ERBE data. For convenience, a reduced cloud category was introduced (Fig. 7.5b) and the 1985/86 DJF and 1986 JJA distributions are also shown in Figs. 7.9a and b for reference. High cloud types occur preferentially where convection occurs in the tropics and in mid-latitude storm tracks. High thick clouds occur over a smaller portion of these areas than high thin clouds. Low clouds appear to be predominantly oceanic and most abundant in the eastern subtropical oceans where the SST is relatively low and the mean vertical motion is downward. Total cloud cover is greatest over the high-latitude ocean where stratus regimes are well developed and in regions of intense tropical convection.

To isolate the contribution of each cloud type to the TOA ERB cloud flux effect, OBH uses a simple regression analysis of the form

$$R = a_0 + \sum_{i=1}^{5} a_i N_i \tag{7.5}$$

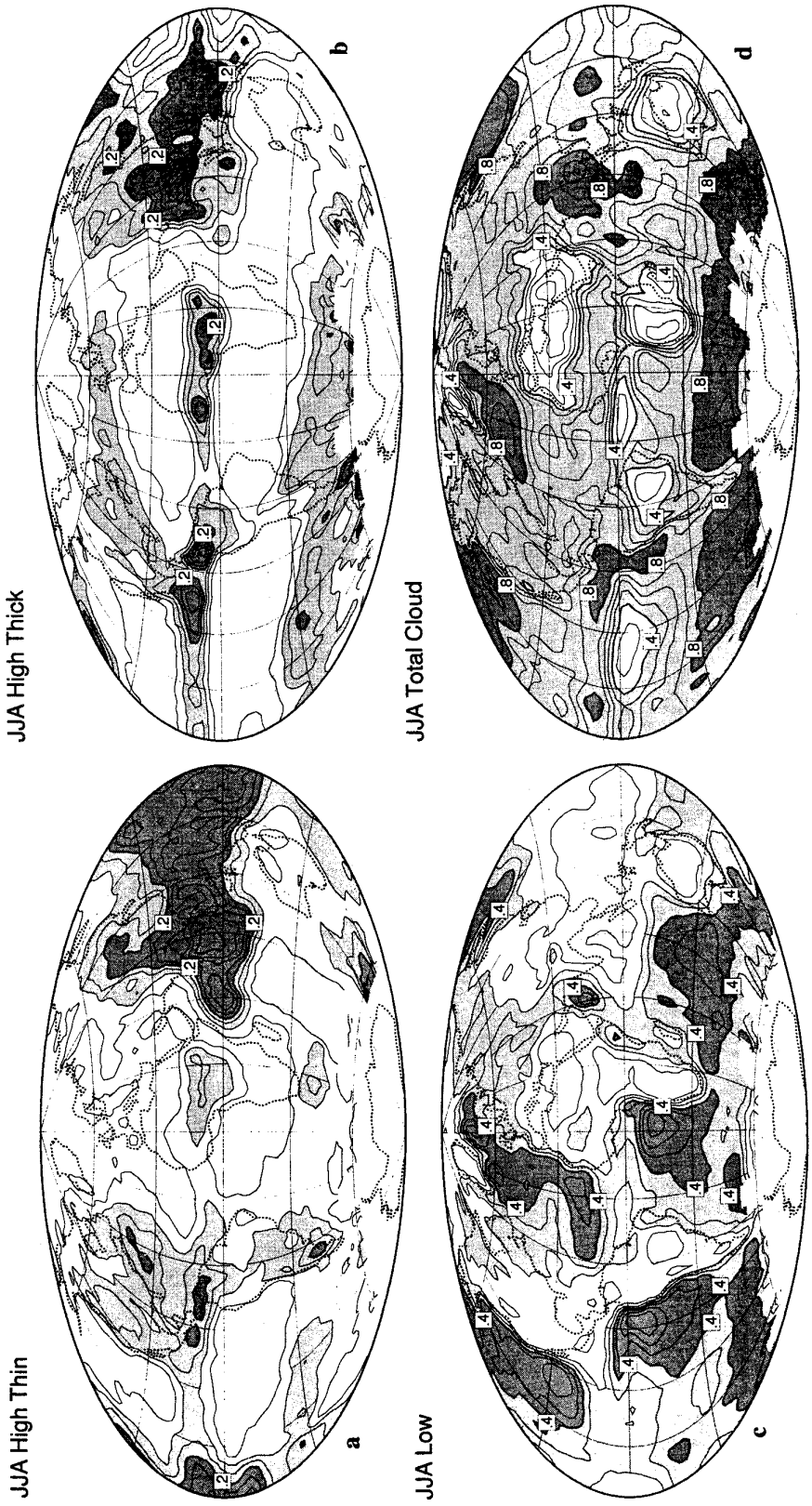

Fig. 7.9a Geographic distributions of the cloud fraction as given by the categories of Fig. 7.5b for the JJA season of 1996. Missing values occur where insolation is small.

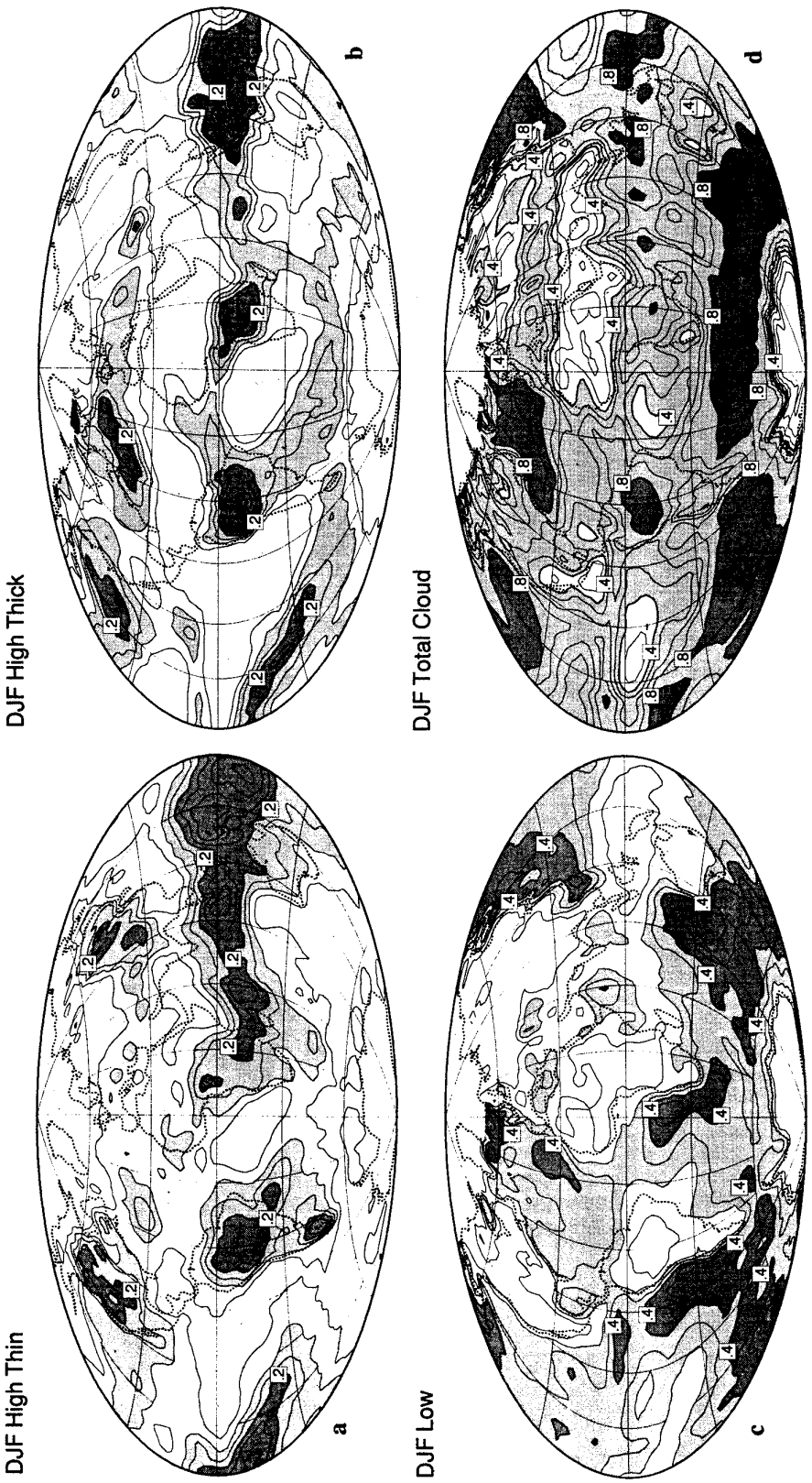

Fig. 7.9b As in (a) but for DJF 1995/1996.

where R is the relevant flux quantity of interest (the net flux, OLR or albedo), N_i is the fractional cloud coverage by type i and a_i is the coefficient of the regression. If this regression approximates the effect of cloud on radiation, its interpretation is as follows

$$R = R_{clear} + \sum_{i=1}^{5} \Delta R_i N_i \tag{7.6}$$

where $R_{clear} = a_0$ is the radiation flux in the absence of clouds and ΔR_i is the change in radiation associated with overcast cloud of type i. This interpretation does depend on how well the data fit this equation (e.g., if the scene is overcast most of the time it will be difficult to deduce the intercept a_0).

Figure 7.10a, b and c shows zonal average values of the OLR flux difference, the shortwave flux differences, and the net flux difference derived as the sum for all cloud types (i.e., the curves labeled ISCCP are the summation terms of Eqn. (7.6)) compared to the flux differences formed from ERBE data. ERBE values suffer in regions where persistent overcast conditions prevail and the differences between the two estimates tend to be greatest in these regions, particularly poleward of 60°S.

The contributions by cloud type are more easily seen in Fig 7.11a, b and c. From these diagrams we note:

- Highest clouds contribute most to the longwave flux effect (type 1 and 2 of Fig. 7.5b) although middle and low clouds contribute in high latitudes.
- The largest effect on shortwave fluxes comes from thicker high clouds in the tropics and low clouds in mid-to-high latitudes. Optically thin clouds (type 1 and 3) contribute little.
- The largest contributions to the net flux difference are provided by low clouds especially through their effect on solar radiation in the summer hemisphere.

The flux differences by type are given in Table 7.3. The longwave effect is about 26 W m^{-2}, some 5 W m^{-2} lower than the ERBE value of 31 W m^{-2}. The albedo effect is about 15% for both ISCCP and ERBE but the net flux of -27 W m^{-2} is more negative than the ERBE value by approximately 10 W m^{-2}.

7.5 Other Relations

(a) SST

The C_{LW} provides a direct measure of the reduction of longwave radiation by absorption and emission of clouds in the atmosphere relative to clear skies. Figure 7.12a presents 12 months of C_{LW} derived from ERBE data as a function of SST and compares the same flux quantity derived from the CSU GCM. The general behavior of C_{LW} with SST appears to show two distinct regimes of behavior; in one regime, C_{LW} decreases over much of the SST range varying from values of 40 W m^{-2} at $T_s \approx 273$ K to about 0-10 W m^{-2} at $T_s \approx 300$ K. The second regime occurs over water warmer than about 300 K, where C_{LW} dramatically increases to values near 80 W m^{-2}. This behavior is partly indicative of the increased cloudiness both equatorward and poleward of the subtropics, which are indicated on this diagram by the minimum in C_{LW}, and partly a result of the changing macroscopic properties of clouds in these regions where cold deep clouds prevail over the warmer equatorial regions and give rise to the largest values in C_{LW}. The comparison between the simulated relationship and that observed suggests that these two regimes are actually well simulated by the model although the magnitudes of C_{LW} over the warm ocean regime are larger than observed and slightly smaller than observed over colder waters. Two possible sources for the discrepancy over the warmest SSTs may be related to specific assumptions in the model

regarding how clouds are treated. The assumption that anvil clouds radiate as a blackbody together with the assumption that clouds completely fill the grid box will exaggerate the model values of C_{LW} over the warm SST regions.

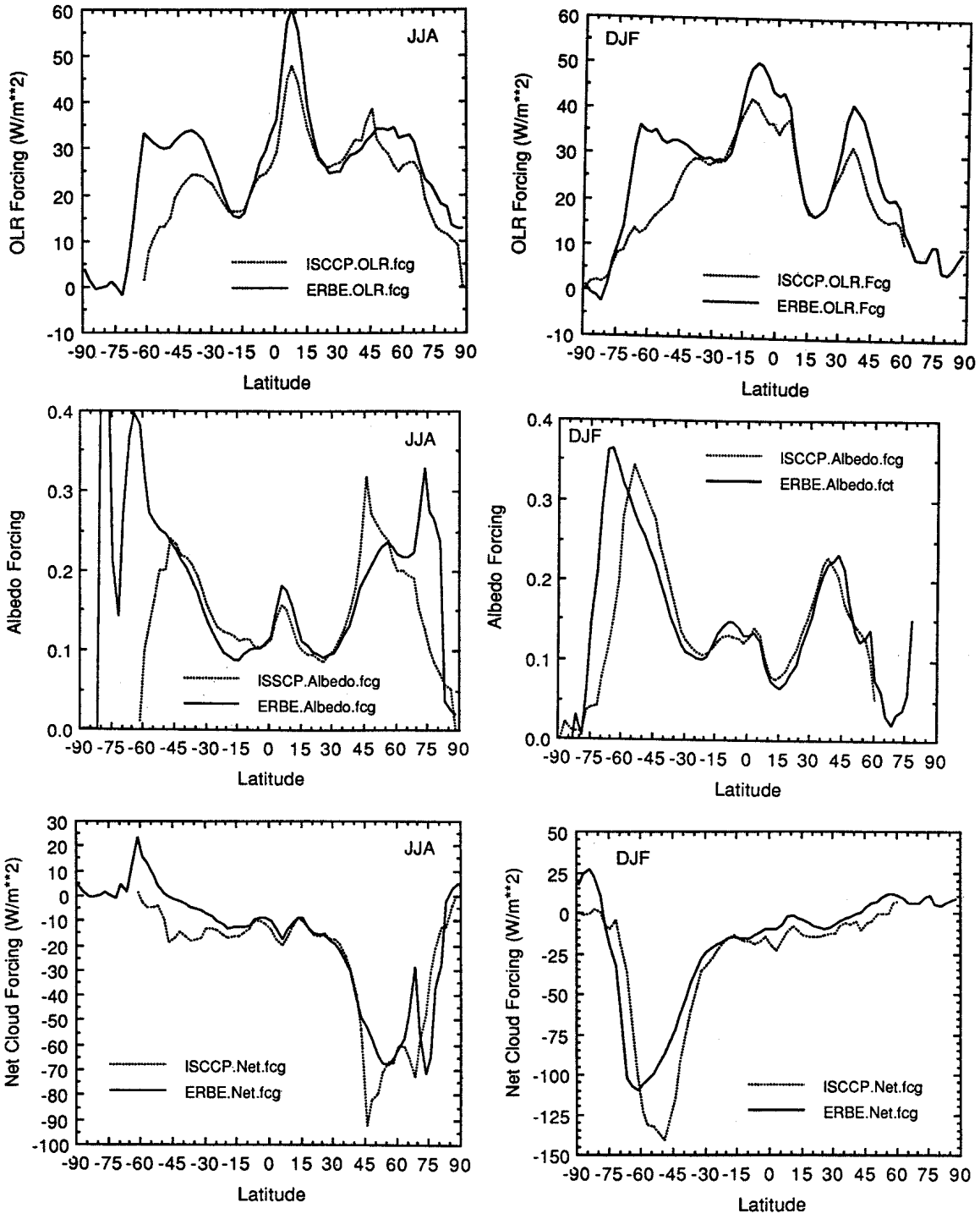

Fig. 7.10 Zonally averaged C_{LW}, C_{SW}, C_{net} derived from the ERBE-ISCCP regression and compared to ERBE quantities.

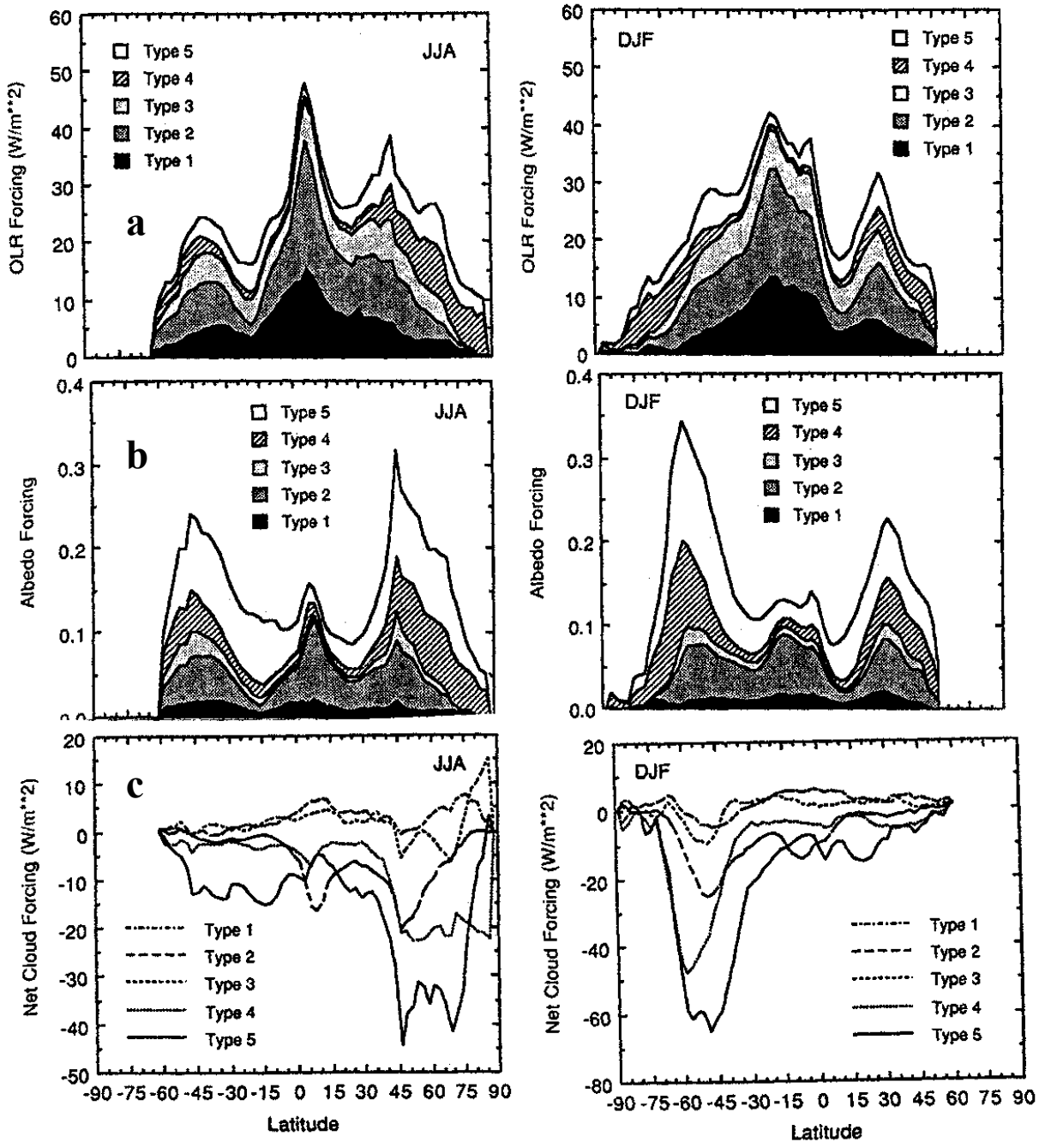

Fig. 7.11 Zonally averaged cloud radiative OLR (a) by cloud category and albedo difference (b), and (c) net flux differences.

Figures 7.12b shows the January and July values of C_{SW} as a function of SST. Values for each hemisphere are shown separately to highlight the complicated variation of C_{SW} with SST. The solar fluxes reflected by the summer hemisphere clouds vary with SST in a way that resembles the two regimes noted for C_{LW}, except that C_{SW} increases from about -150 W m^{-2} for the colder SST's (and thus at higher latitudes) due to the reflection from the summertime clouds located in the mid- to high-latitude storm tracks. C_{SW} increases to near zero over the subtropics, followed by a sharp decrease associated with the

bright clouds of the warmer equatorial oceans. The behavior of C_{SW} in the winter hemisphere poleward of the subtropics differs from that just described for the summer hemisphere. In the former case, the variation of C_{SW} with SST is a result of the product of two factors that have opposing variations with latitude; one is the decreasing insolation and the other is the increasing albedo with increasing latitude. The latter, in turn, is a result of both increasing cloudiness poleward of the subtropics and the decreasing solar elevation with increasing latitude. Both factors contribute to an increase in the albedo, of cloud from the subtropics to mid-latitudes as we show below. The two factors, that of an increased albedo and that of a decreasing solar flux, combine to produce a variation in C_{SW} that starts near zero for clouds at high latitudes and decreases to a minimum of -50 W m^{-2} at approximately T_s = 293 K, followed by an increase towards zero and then a rapid fall off with increasing SST, similar to that noted for the summer hemisphere.

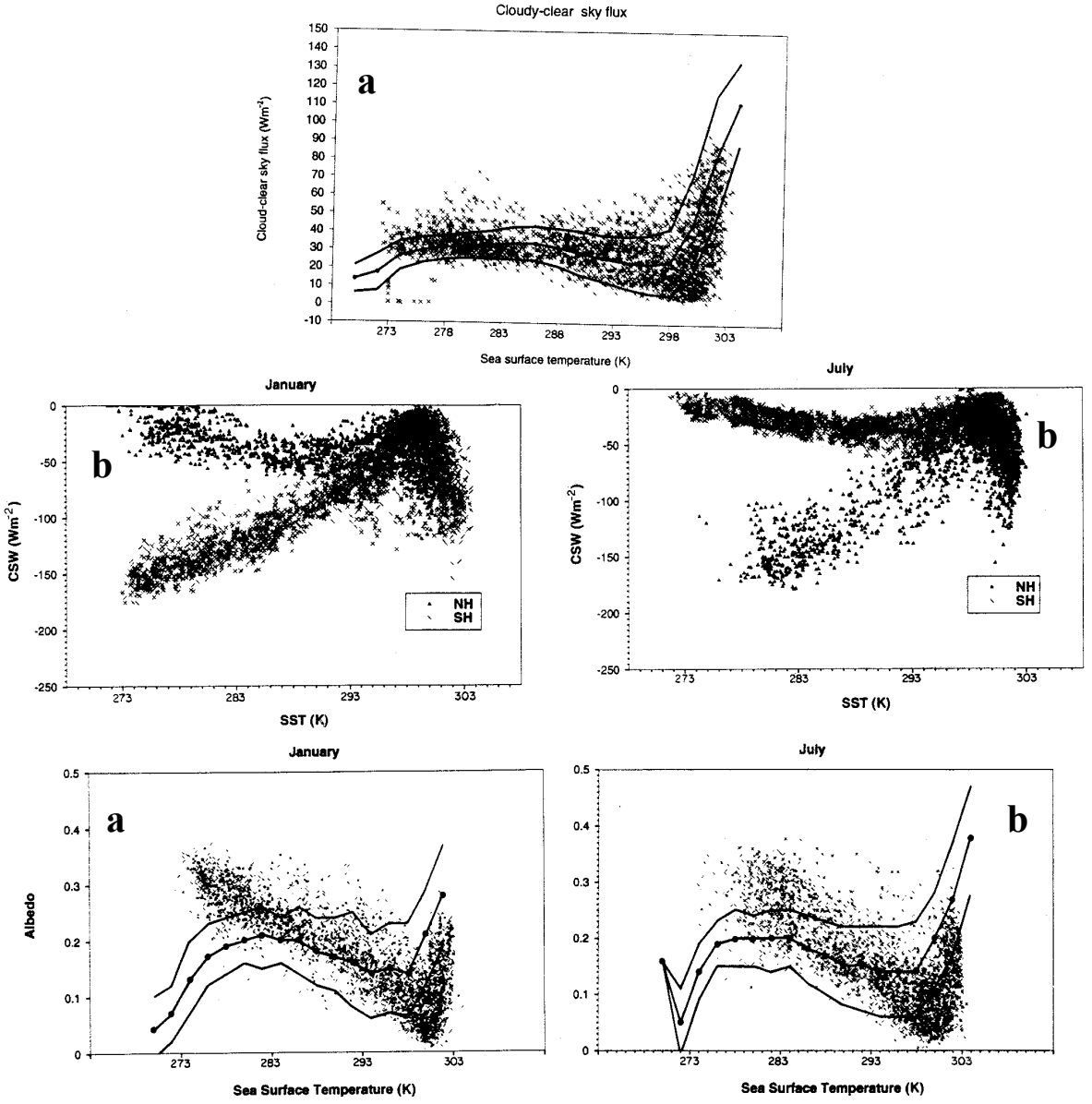

Fig. 7.12 (a) C_{LW} as a function of SST. (b) January and July C_{SW} as a function of SST. (c) Same as for (b) but albedo ($\Delta\alpha = 4C_{SW}/Q_{\odot}$) as a function of SST. Lines indicate CSU GCM model results.

Figure 7.12c presents January and July values of $\Delta\alpha$ as a function of SST. The remarkable feature of these diagrams is how the different hemispheric behavior of C_{SW} maps onto one broad and apparently well-defined relationship. The albedo parameter $\Delta\alpha$ has a minimum over the subtropics where there is a minimum in cloudiness and increases both equatorward and poleward of these clear sky regions. The SST-$\Delta\alpha$ relationships obtained from the GCM are also given on these diagrams for comparison. The model behavior of $\Delta\alpha$ with SST broadly follows the observed behavior, although there are significant differences between the two sets of data. The cloud albedo predicted by the model exceeds that observed in the equatorial warm ocean regions but is much too low for the mid-latitude clouds over regions characterized by $T_s < 285$ K. These features may be due to poorly modeled cloud amount, poorly specified cloud albedo, or a combination of both (note that $\Delta\alpha$ is a hybrid of both factors). Comparisons conducted by Harshvardhan et al. (1989) between the total cloudiness of the model versus the ISCCP total cloudiness reveals that the model tends to overpredict cloudiness in the subtropics (hence the larger values of $\Delta\alpha$ at temperatures near 300 K), slightly underpredicts the total cloudiness in the equatorial regions and greatly overestimates the cloudiness in the summer mid-latitudes. This suggests modeling problems both with the parameterization of cloud albedo in the equatorial region and with estimating the effect of cloud amount on the subtropics and higher latitudes on albedo.

(b) Relation to Liquid Water

We will learn later the importance of the cloud water (and ice path) to the bulk radiative effects in clouds. In fact, it is shown that the liquid and ice water paths are directly related to the cloud optical depth. Global cloud liquid water information is presently derived from the microwave radiance data obtained from the SSMI operational instrument (e.g., Greenwald et al., 1993). From these data, we hope to establish a better understanding of the links between liquid water path, temperature and radiative properties of clouds. For example, Fig. 7.13a presents the results of the correlation between LWP and atmospheric temperature much in the way cloud optical depth and temperature were correlated in the study of Tselioudis et al. (1992). Figure 7.13a presents the parameter

$$f = \frac{d \ln W}{T} \tag{7.7}$$

derived from gridded LWP data. The clouds used to define this parameter correspond to ISCCP defined low clouds and the liquid water is correlated with the mean temperature of the surface—680 hPa layer, which crudely approximates the cloud temperature. These data apply to the region from 60°N to 60°S and show that in the warmest regions of the globe a decrease in W is correlated with an increase of temperature. This result is similar to the optical depth sensitivities deduced by Tselioudis et al. (1992) who argue that specific regional changes in the optical depth-temperature correlation is more complex than one simply defined by thermodynamical considerations.

The relationship between LWP and cloud albedo can be examined using global SSM/I information and cloud albedo available from ERBE. While this is an important task, it has been difficult to find enough coincident data to carry out correlations between albedo and LWP—a problem that will be rectified with the launch of NASA's Tropical Rainfall Measurement Mission (TRMM) in 1997. Nevertheless a limited match of SSM/I and ERBE was presented in the study of Greenwald et al. (1995) in which the albedo of low overcast clouds as determined by ISCCP is presented as a function of LWP (Fig. 7.13b). The curves shown represent relations derived from theory assuming different values of r_e. Possible reasons for differences between theory and observation as shown need to be explored and explanations vary from biases introduced in sampling the different data to macroscopic effects that dramatically alter the intrinsic relationship between albedo and LWP.

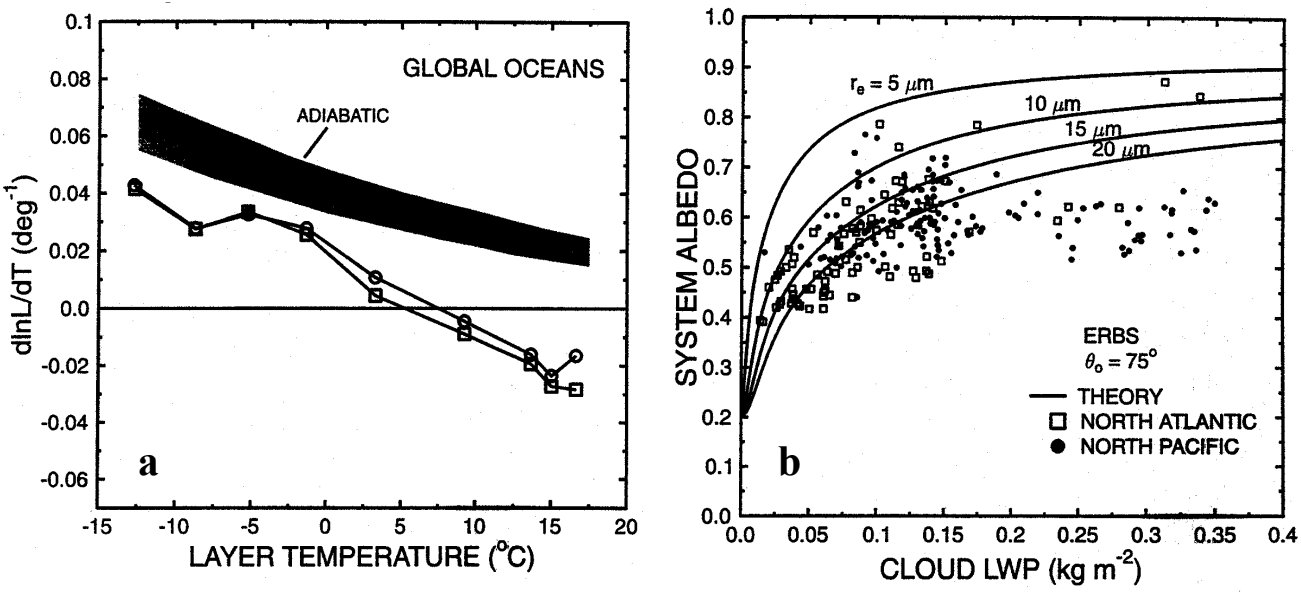

Fig. 7.13 (a) Global observations between f versus temperature (C) of the atmospheric layer between the surface and 680 hPa. Observations using composite ISCCP and microwave liquid water are given by symbols and the light shading indicates the range of the relationship derived from adiabatic assumptions for clouds of varying thickness and height. (b) Scatter diagram of the instantaneous albedo measurements from ERBs at a solar zenith angle of 75 ° versus coincident SSM/I LWP data for low clouds over the Northern Pacific and Atlantic during June and July 1988. Also shown are relationships based on parameterized theory for different values of r_e (Greenwald et al., 1995).

(c) Net Radiation and Reciprocity

One of the curiosities of the flux difference analyses post ERBE is the near reciprocity between longwave and shortwave effects over the tropics. We can begin to explore this reciprocity in the following way. Consider the following

$$\frac{dC_{net}}{d\mathcal{W}} = \frac{dC_{SW}}{d\mathcal{W}} + \frac{dC_{LW}}{d\mathcal{W}} \tag{7.8}$$

where $\mathcal{W}$ is some unspecified cloud parameter. To help fix ideas, we might think of $\mathcal{W}$ as the cloud liquid water path W or cloud fraction N or some combination of these such that some given increase in this parameter leads to more negative values of C_{SW} and larger values of C_{LW}. For example, Fig. 7.14a presents a scatter plot of C_{net} as a function of satellite liquid water path for the mid-latitudes and tropics.

The results for the two regions appear to be fundamentally different with an apparent change in sign if rearrange Eqn. (7.8) to obtain

$$C_f = \frac{dC_{net}}{dC_{LW}} = \frac{dC_{SW}}{dC_{LW}} + 1. \tag{7.9}$$

In this expression, dC_{SW}/dC_{LW} is the change in C_{SW} with respect to C_{LW}. Over ocean regions it is reasonable to suppose that these changes arise primarily from large-scale changes in cloudiness and

perhaps large-scale changes in cloud water. The interpretation of the right-hand side of Eqn. (7.9) is as follows,

$$C_f = \begin{cases} > 0 & \text{greenhouse effect dominates,} \\ 0 & \text{greenhouse and albedo effects cancel,} \\ < 0 & \text{albedo effect dominates.} \end{cases}$$

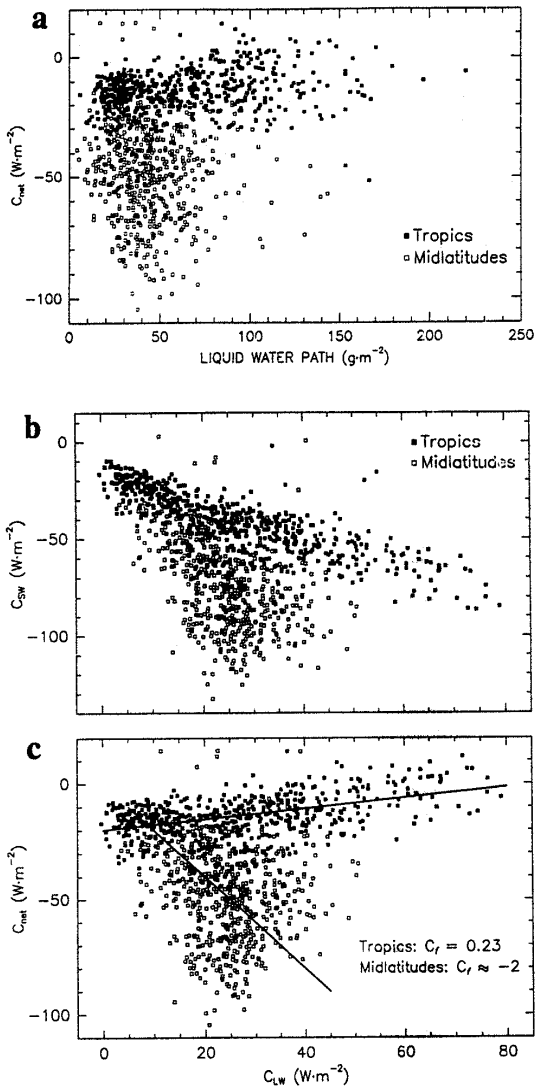

Fig. 7.14 (a) Scatter diagram of an annual composite of C_{net} versus W for the tropics (filled squares) and mid latitudes (open squares) using the Nimbus-7 ERB flux data. (b) Scatter diagram of C_{SW} versus C_{LW} for the tropics (filled squares) and mid latitudes (open squares) using the Nimbus-7 ERB flux data. The negative correlation indicates the general reciprocoal influence of clouds on the shortwave and longwave components of the ERB. (c) Scatter diagram of C_{net} and C_{LW} for the same data used in (a). The slope of a linear correlation between these flux quantities defines C_f and estimates of C_f are given.

An estimate of C_f may be obtained from plots of C_{net} and C_{LW} data presented in the manner shown in Figs. 7.14b and c. The negative correlation of C_{SW} and C_{LW} is indicative of the reciprocity of cloud effects on the ERB. The results indicate that a given change in C_{LW} (the greenhouse effect) is associated with a change in C_{SW} (the albedo effect) that is smaller for tropical clouds than observed for mid-latitude clouds. From the slope of the relationship between C_{net} and C_{LW} of Fig. 7.14c we deduce a value of C_f and therefore establish the combined impact of the greenhouse and albedo effects of clouds on the net radiation budget. We estimate $C_f = 0.23$ for tropical clouds, indicating that a change in the greenhouse effect is more dominant than the compensating change in albedo effect although the results are scattered and shows largely a reciprocity. On the other hand, $C_f \approx -2$ for mid-latitude clouds, which implies that the albedo changes dominate the net radiation balance. The result of Fig. 7.14c is consistent with the notion that the differences in the response of the ERB to tropical clouds versus mid-latitude clouds relates to the differences in the ERB attributed to large-scale changes in cloud liquid water. The greenhouse changes associated with changes in LWP cannot be completely neglected as previous cloud water feedback studies have assumed (e.g., Sommerville and Remer, 1984; Paltridge, 1980, and others).

7.6 Clouds and the Surface and Atmospheric Budget

Although the net radiative effect of clouds at the top of the atmosphere is small throughout most of the low latitudes (e.g., 7.15a and b), the partitioning of this effect between the atmosphere and the surface is both large in magnitude and opposite of sign. This is evident in the model results presented in Figs. 7.15c and d which show the distributions of the net flux differences within the atmosphere (this will be referred to as the atmospheric cloud radiative forcing, ACRF) and at the surface (the surface cloud radiative forcing) for the same GCM climate model simulations used to produce the TOA distributions presented in Fig. 7.15b. These simulations show how clouds radiatively heat the atmospheric column (relative to the clear sky) and how this heating is largely compensated by a cooling at the surface (e.g., Slingo and Slingo, 1988). The heating of the atmosphere by clouds is important for a number of reasons. The location of the maximum heating of the ACRF coincides with the maximum of deep convection and convective heating. The coupling of these different forms of heating and feedbacks between them are mentioned in more detail below.

Estimating the proportional effect of clouds on the radiative balance of the atmosphere and surface is crucial for understanding links between clouds and other components of the climate system. For instance, both the heating of the atmosphere and the cooling at the Earth's surface (specifically the ocean) by clouds are key elements of hypothesized cloud-climate feedback mechanisms (Randall et al., 1989; Ramanathan and Collins, 1992). Unfortunately, there are no measurements to confirm model simulations of the partitioning of the cloud radiative forcing between the atmosphere and the surface and it is clear that more detailed information about the surface radiation budget is required to do this.

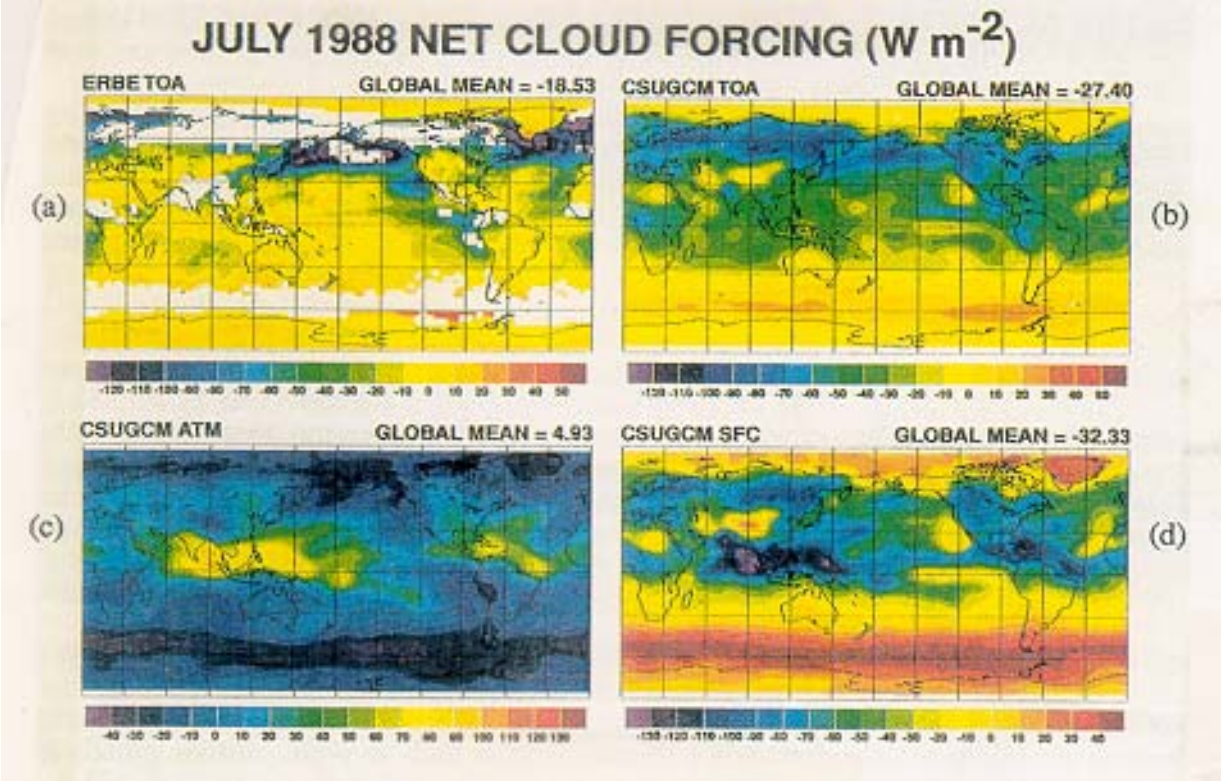

Fig. 7.15 Net cloud-radiative forcing for July 1988 (all numbers are in W m^{-2}). (a) The TOA forcing derived from ERBE. (b) A GCM model comparison. (c) The forcing derived from model simulations for the atmosphere, and (d) surface.

AT622 Section 8
Elementary Molecular Spectroscopy

The aim of this section is to build up some understanding of how gases absorb, why only certain gases absorb and what dictates where they absorb in the atmospheric absorption spectrum.

References
Chapter 3: Remote Sensing Notes
Chapters 3, 4, and 5: Goody and Yung
Selected reference cited in notes.

8.1 Atomic Absorption

In 1752 Thomas Melville studied the color of flames using a prism and found that the spectrum is not continuous like the spectrum of the sun or the radiation emitted by a blackbody. From this historical perspective we learned that the interaction of radiation with certain gases produce not a continuous spectrum like the emission spectrum but a discrete spectrum.

The realization that the bright line spectra of vaporized elements match the dark lines in the solar spectra (Fig. 8.1) was the key to understanding the quantum nature of matter. The basic explanation was forwarded by Bohr who perceived an orbital model of atoms (Fig. 8.2). Electrons falling from one level to a lower level give rise to emission of photons

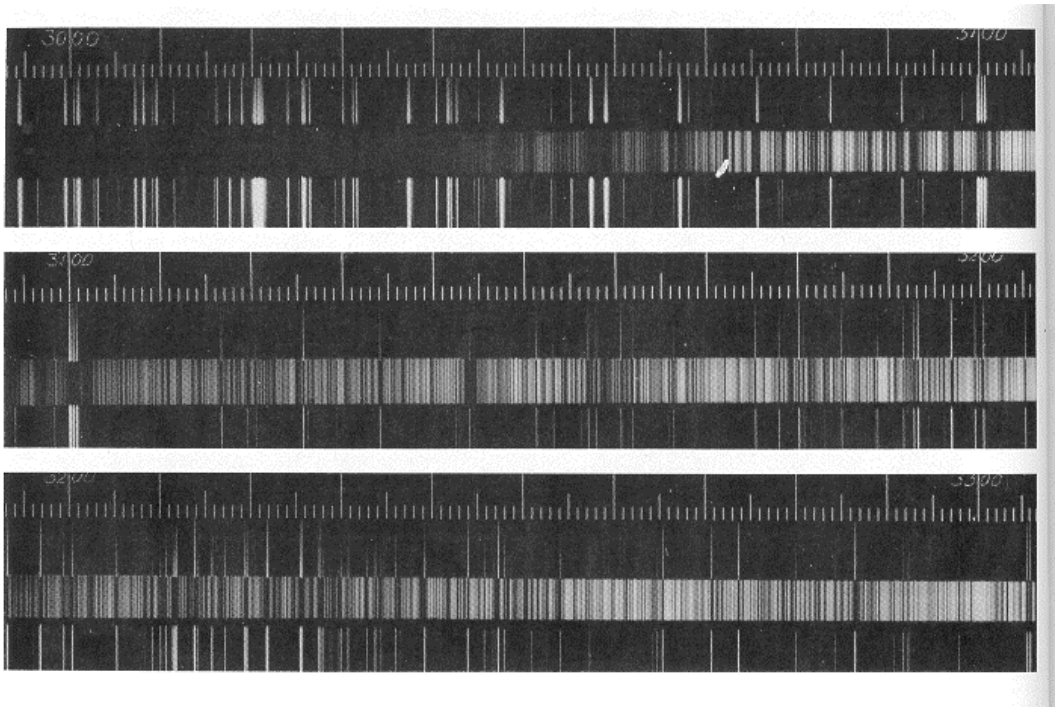

Fig. 8.1 The bright line spectrum of the vaporized element iron is shown with the spectrum of the sun. The wavelength regions are from 300 μm to 330 μm, in the ultraviolet. The solar spectrum is in the center of each strip, and the iron spectrum is above and below it. The bright lines of iron occur at the same wavelengths as some of the dark lines in the solar spectrum.

$$h\nu = E_2 - E_1 = \Delta E \tag{8.1}$$

- Thus absorption occurs when an electron jumps from level 1→2 (line absorption spectrum).
- Emission occurs when an electron falls from level 2→1 (emission spectrum).

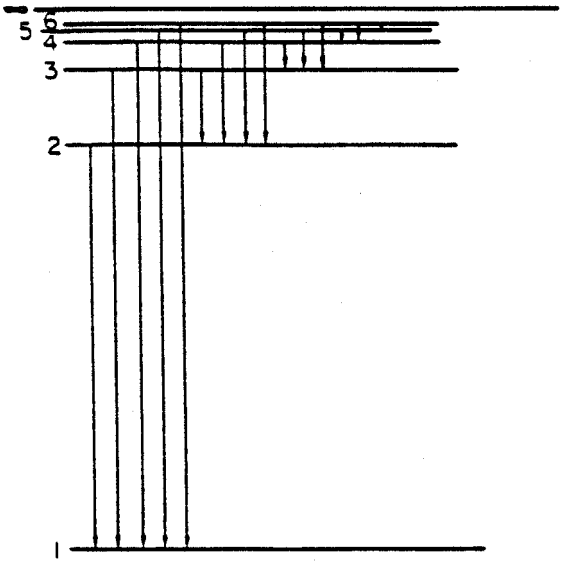

Fig. 8.2 *Energy levels of the hydrogen atoms according to the Bohr theory. The first six levels are shown and drawn to scale. Level 1 is the atoms' ground state. Light is emitted whenever the atoms make a transition from a higher state to a lower one, and the frequency of light is proportional to the energy difference. Higher levels are closer together. The line labeled infinity (∞) represents the energy the electron would have if it became barely free; that is, just able to escape from the nucleus.*

The atomic line spectrum is defined by internal energy states of atoms. The molecular line spectra are defined by the same plus the dynamic properties of the internal motions (such as vibrations and rotations). What determines whether a particular molecule absorbs radiation depends on, among other things, the way atoms are bonded and the geometry of the molecule.

The prevalent type of bonding is the covalent bond—viewed as a sharing of electrons. Certain molecules, like H_2O (Fig. 8.3) have a structure that naturally produces a dipole moment owing to the geometric configuration of the molecule that creates an asymmetry in the charge distribution that arises through this bonding. Molecules, like H_2O, that possess a permanent dipole moment are called polar molecules. Homonuclear molecules like N_2, O_2, and H_2 are homopolar as they do not possess a permanent $\vec{p}$. So too is CO_2. Homonuclear and homopolar molecules are not active absorbers in the IR region. An exception is pressure-induced absorption (e.g., in the atmosphere of Saturn). Polar molecules are radiatively active—the charge separation leads to oscillating charges, which according to EM theory produces an EM wave.

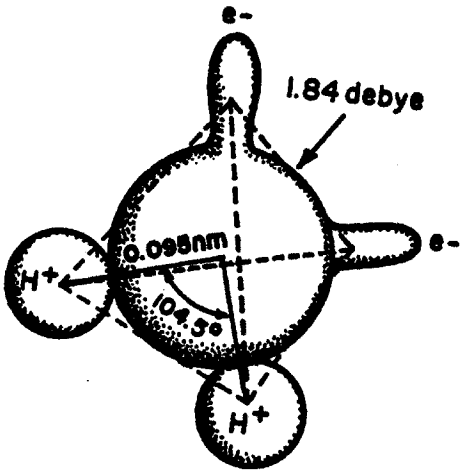

Molecule	p, m C
HCl	3.43×10^{-30}
HBr	2.60×10^{-30}
HI	1.26×10^{-30}
CO	0.40×10^{-30}
H_2O	6.20×10^{-30}
H_2S	5.30×10^{-30}
SO_2	5.30×10^{-30}
NH_3	5.00×10^{-30}
C_2H_3OH	3.66×10^{-30}

Molecules with sero dipole moment include: CO_2, H_2, CH_4 (methane), C_2H_4 (ethane), and CCl_4 (carbon tetrachloride).

Fig. 8.3 Schematic of atomic configuration and electronic orbitals for water molecule, with oxygen atom at center and hydrogen atoms at an angle of 105°. Dipolar character comes from protons at H^+ positions and unshared electrons at e^- locations; the direction of the dipole moment is along the symmetry axis. The atoms and the electronic orbitals have tetrahedral symmetry. The table to the right lists the dipole moment for selected molecules.

8.2 Molecular Absorption Spectra

The absorption spectrum of a molecule is substantially more complex than that of an atom. Not only are transitions possible between the energy states of the atoms that make up the molecule, but also transitions occur between energy states associated with movements of the atoms themselves.

Since the energy required to induce a transition from a lower to a higher state is inversely proportional to the wavelength of the photon, the types of mechanisms that induce absorption also depend on the wavelength of the absorbed photon. These mechanisms must induce either a magnetic or an electric effect, which can be influenced by electromagnetic radiation. Mechanisms responding fastest occur at the shortest wavelengths whereas the more sluggish mechanisms produce absorption at longer wavelengths. We can use this wavelength dependence as a convenient classification of the absorption mechanisms as shown in Fig. 8.4, although the dividing boundaries are by no means precise.

- In the radio frequency regime, the absorption is associated with the nucleons and electrons, which we consider to be tiny charged particles that spin, producing tiny magnetic dipoles. The reversal of this dipole due to spin reversal interacts with the magnetic field at frequencies in the range 3 x 10^6 to 3 x 10^{10} Hz.

- In the visible and ultraviolet region excitation of valence electrons results in moving electric charges in the molecule. Changes in the electric dipole give rise to a spectrum by its interaction with the oscillating electric field of radiation. These electronic transitions occur within the individual atoms of molecules and dominate the visible and ultraviolet portions of the electromagnetic spectrum. At even shorter wavelengths, photons can actually disrupt the absorbing molecule by *photodissociation* or even produce *photoionization* of individual atoms.

- Absorption by molecules in the mid and near infrared occur by vibration (although a mixture of vibrations and rotations are usually induced at these frequencies). Induction of vibrations requires

more energy than rotations and thus takes place at higher frequencies of infrared wavelengths between about 0.7 μm and about 20 μm.

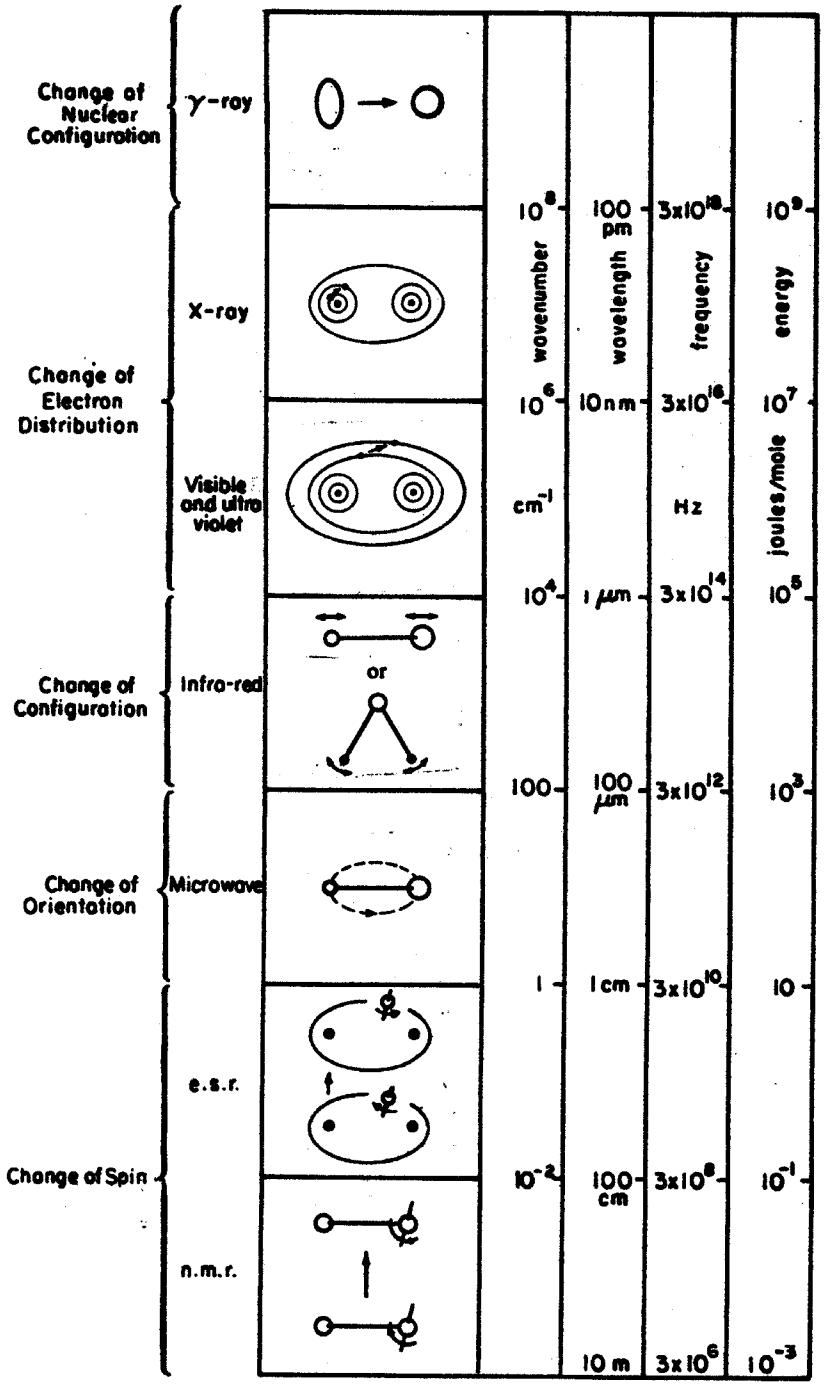

Fig. 8.4 The electromagnetic spectrum and the possible types of interactions between photons and a molecule or atom (Bandwell, 1983).

- In the microwave and far infrared, the molecule undergoes a rotation like that depicted in Fig. 8.5a and the component of the dipole in a given direction fluctuates in a regular fashion as shown in the lower part of Fig. 8.5a. These fluctuations are more sluggish than are the fluctuations associated with vibrations or the fluctuations associated with electronic transitions. Rotational lines generally occur in bands at the longer infrared wavelengths beyond about 20 μm extending into the microwave spectral region where individual rotational lines can be resolved.

As a consequence of the vibrational-rotational transitions, absorption lines are spread into bands containing many lines (as illustrated in Fig. 8.5b), which are used, either individually or as a group, to fingerprint molecules in the same way that atomic spectral lines fingerprint atoms. It is the vibrational-rotational absorption spectrum of molecules that is largely of interest to topics discussed in these notes.

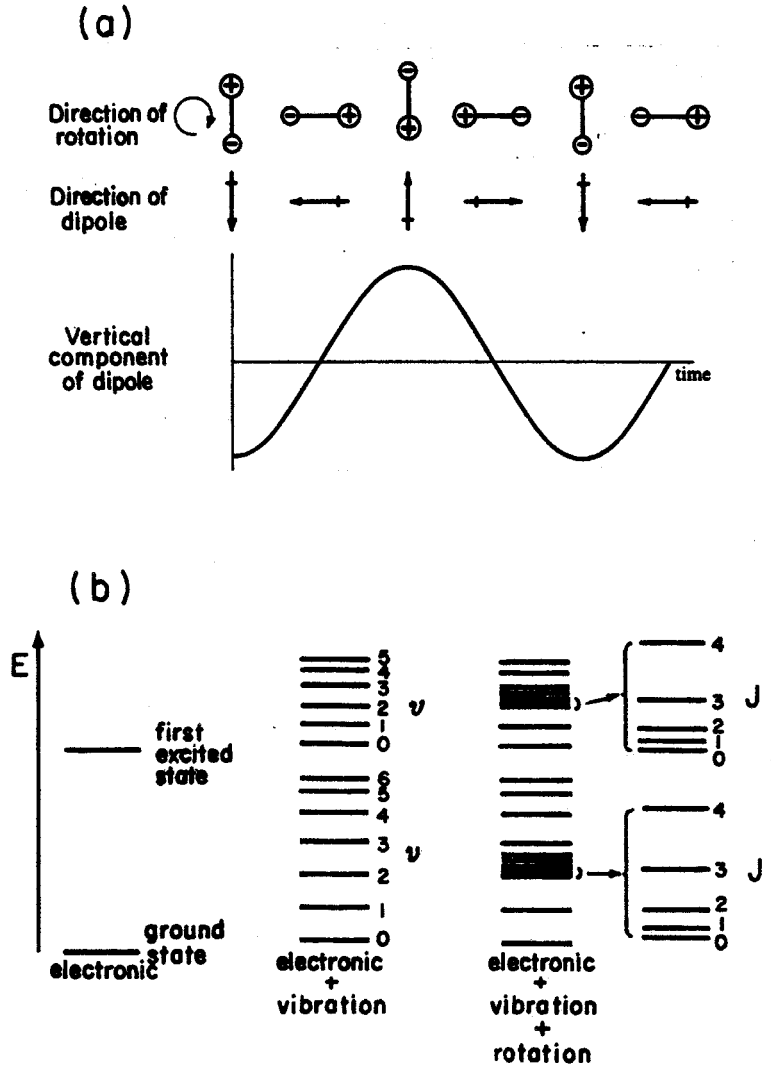

Fig. 8.5 *(a) The rotation of a simple diatomic molecule showing the fluctuation in the dipole moment measured in a particular direction (Bandwell, 1983). (b) Molecular absorption spectra actually consist of closely spaced lines due to rotational and vibrational transitions. J and v refer to the quantum numbers associated with the rotational and vibrational transitions, respectively. This diagram shows how these transitions are superimposed on electronic states.*

8.3 Simple Model Analogs of Vibrating and Rotating Molecules

Despite the complexity of the absorption processes within molecules, we can begin to understand their spectra by drawing on results from simple mechanical analogs to vibrating and rotating molecules.

(a) Simple Model of Rigid Rotators

Consider a simple diatomic molecule (Fig. 8.6), with the moment of inertia

$$I = m_1 r_1^2 + m_2 r_2^2 ,$$

and the center of mass

$$m_1 r_1 = m_2 r_2 .$$

Thus

$$I = \frac{m_1 m_2}{m_1 + m_2}(r_1 + r_2)^2$$

or

$$I = m' r^2$$

where m' is the reduced mass of the molecule and r is the distance between the two atoms. Quantum mechanics tells us that the angular momentum is $L = Iw = \sqrt{K(K+1)}\hbar$ where K is the rotational quantum number (K = 0,1,2,...). As noted above, only molecules with electric dipole moments (e.g., HCL) can interact with electromagnetic photons. The energy of a rigid rotator is

$$E = \frac{1}{2} I w^2 = \frac{L^2}{2I} = \frac{K(K+1)}{2I}\hbar^2 .$$

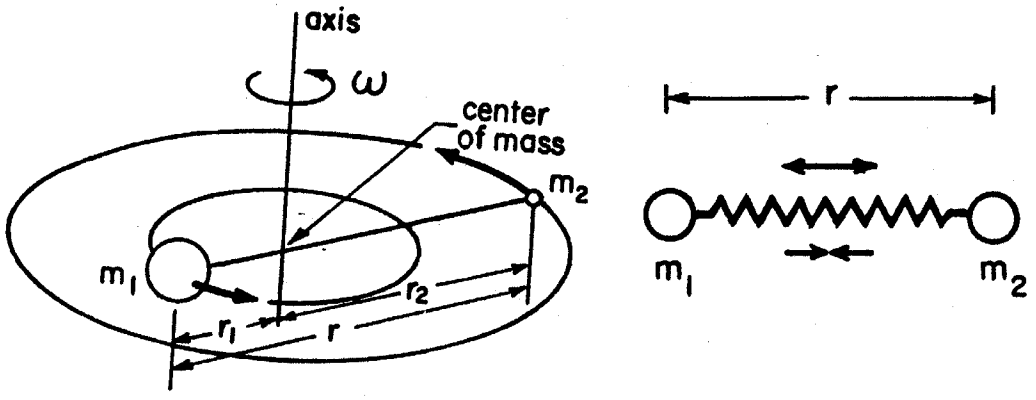

Fig. 8.6 A diatomic molecule that rotates and vibrates about its center of mass.

Thus, since

$$\Delta E = E_{K+1} - E_K = h\nu$$

$$\nu = \frac{\hbar}{2\pi I}(K+1) \tag{8.2}$$

$$\Delta\nu = \nu_K - \nu_{K-1} = \frac{\hbar}{2\pi I}(K+1-K)$$

Thus, the energy levels predicted for a diatomic molecule give rise to equally spaced absorption lines spaced $\Delta\nu \approx \frac{\hbar}{2\pi I}$ apart (Fig. 8.7). $B = \frac{\hbar}{2\pi I}$ is a basic quantity of the molecule known as the rotational constant.

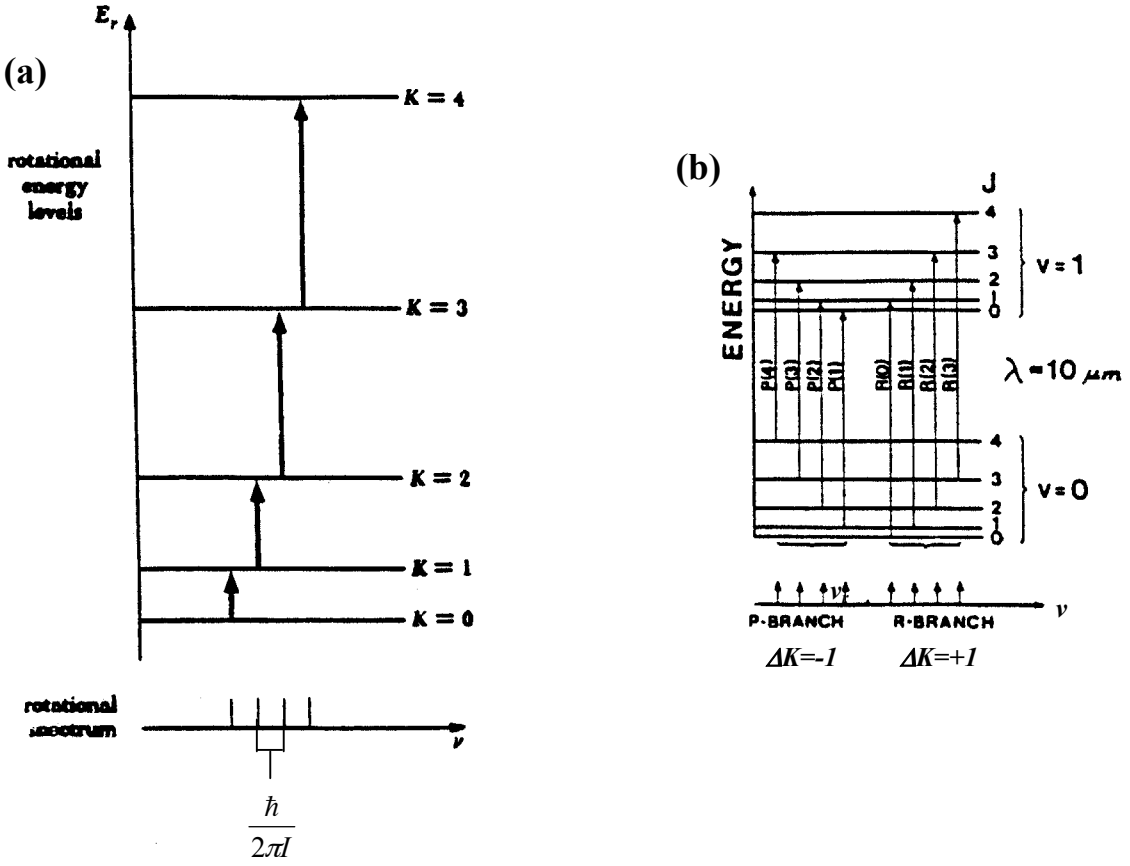

Fig. 8.7 (a) Energy levels and rotation spectrum of diatomic molecule. (b) Vibration-rotation spectra of a hypothetical diatomic molecule.

Note that:

- $\nu \rightarrow (I)^{-1}$. If we assume a value of r that is similar for all diatomic molecules, then the ν spectra is largely determined by the mass distribution within molecules. For typical molecules (H_2O), $\nu_{rotation} \geq 20$ μm.

From Eqn. (8.2) the moment of inertia of a molecule can be deduced from its rotational spectra and, since the masses of its constituent atoms are known, the interatomic separation *r* can be calculated.

Rotational molecules are generally specified in terms of its three principal moments of inertia

- Linear molecules: CO_2, N_2O, C_2H_2…
- Symmetric to *p* molecules: NH_3, CH_3Cl, CF_3C1, nonlinear with $I_1 = I_2$, I_3 different
- Spherical symmetric top: (methane) $I_1 = I_2 = I_3$
- Asymmetric top: H_2O, O_3 - all three moments of inertia are different. Absorption spectra defined by three rotational constants = $\frac{\hbar}{2\pi I}$ and three sets of rotational quantum numbers.

(b) Elementary Discussion of Vibrating Molecules

Excitation energy required to vibrate molecules is greater than that of rotation—so rotation always accompanies vibration. Vibration can be treated as a simple analogy to two masses attached to a spring, for which the restoring force related to some displacement about equilibrium is

$$F = -k(r - r_e)$$

For a harmonic oscillator, the frequency of the vibrating body is

$$v' = \frac{1}{2\pi}\sqrt{\frac{k}{m'}}$$

Quantum theory predicts that the frequency of a harmonic oscillator is quantized such that

$$v = \left(\nu_i + \frac{1}{2}\right)\frac{1}{2\pi}\sqrt{\frac{k}{m'}} = \left(\nu_i + \frac{1}{2}\right)v'$$

where *v* is the vibrational quantum number.

The energy required for a vibrational transition is larger than that required for a rotational transition. Vibrations, however, are typically accompanied by rotations so the rotating molecule is not exactly like a rigid rotator. We learn from quantum mechanics however, that only certain types of vibrations and rotations are permitted together. These are defined by selection rules, which for the diatomic molecule (or a longitudinal polyatomic molecule like the carbon dioxide molecule), the transition $\Delta\nu = \pm 1$ occurs simultaneously with a $\Delta K = \pm 1$ transition. This selection rule produces pairs of transitions of the form shown in Fig. 8.7b. As a rule, each vibrational transition frequency is split up into a series of spectral lines with mutual separations that approximately correspond to the respective rotational constant. In Fig. 8.7b, the vibrational transition from $\nu = 0$ to $\nu = 1$ is shown. Two branches of rotation lines result for this vibrational transition: one for $\Delta K = +1$, which is referred to as the *R branch* and the other for $\Delta K = -1$, the *P branch.*

(c) Triatomic Molecules

The rotational and vibrational absorption spectra of polyatomic molecules are much more complex than are the spectra of diatomic molecules owing to the higher degrees of freedom of both vibrational and rotational motions. The absorption spectra of the CO_2 molecule are highly relevant to atmospheric remote sensing. The CO_2 molecule vibrates in four different modes, two of which are energetically equivalent.

These modes are referred to as the *symmetric stretch mode,* the *asymmetric stretch mode,* and the *bending mode,* which has two equivalent modes of vibration. The dipole moment of the symmetric stretch mode is plainly zero throughout the whole motion (Fig. 8.8a) and this vibration is radiatively inactive. The asymmetric stretch produces a periodic alteration of the dipole moment and this mode is 'infrared active' as is the bending mode (Figs. 8.8b and c). The bending mode actually permits $\Delta v = \pm 1$, $\Delta K = 0$ transitions. These transitions then produce a large absorption peak centered on the fundamental frequency of the oscillator. The absorption is strong at these frequencies due to the superposition of all $\Delta v = 1$ transitions between all available J-levels. This absorption is referred to as the *Q branch.*

Another molecule of considerable importance to the study of the Earth's atmosphere is the H_2O molecule. Since this molecule is not linearly arranged like the CO_2 molecule, geometrically different modes of vibration and rotation occur. Figure 8.8d indicates the three modes of vibration of the water molecule. Superimposed on these three modes are the rotational modes around three axes of rotation. The spectra arising from the multiplicity of vibration-rotation transitions are accordingly complex producing absorption spectra that are more irregular in appearance.

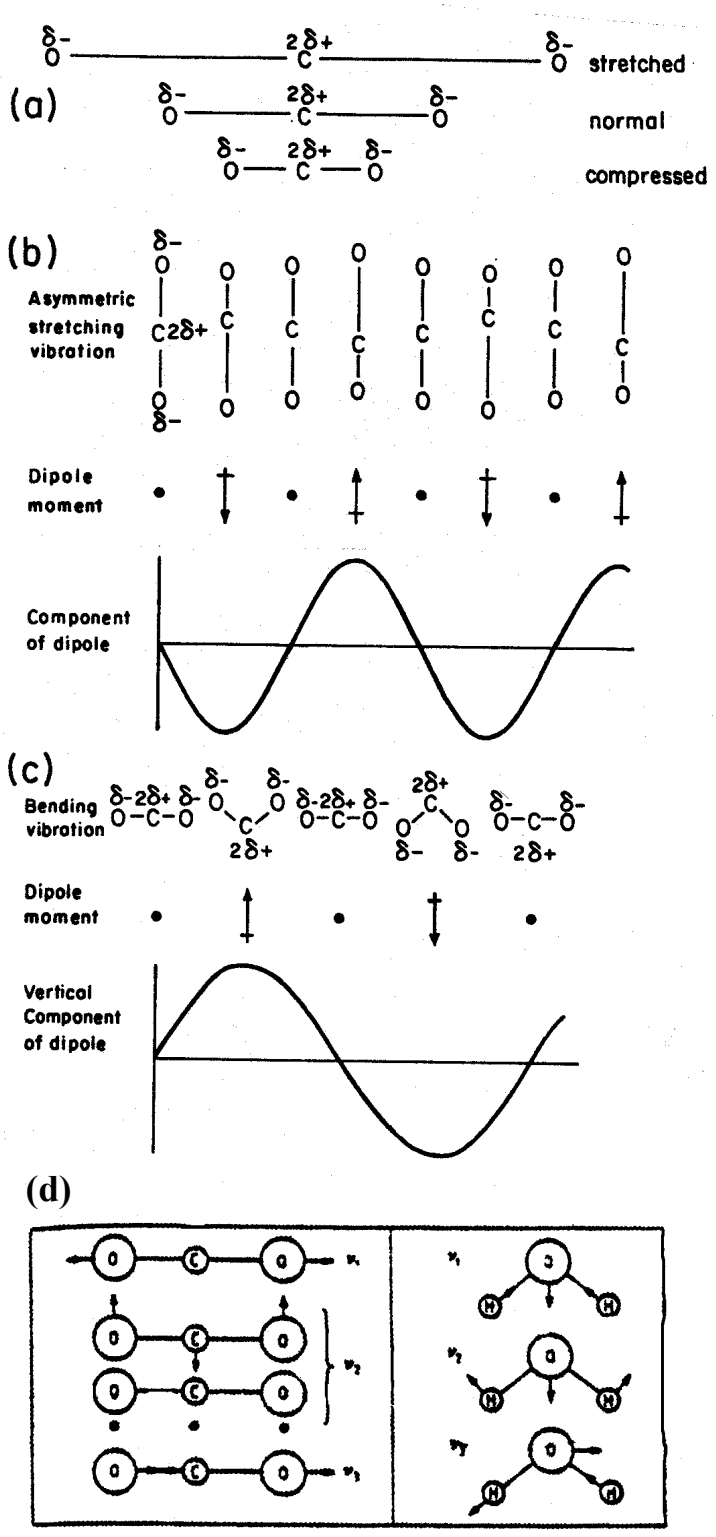

Fig. 8.8 *(a) The symmetric stretching of a vibrating CO_2 molecule. (b) The asymmetric stretching of the CO_2 molecule showing the fluctuating dipole moment. (c) The bending motion of the carbon dioxide molecules and its associated dipole fluctuation (Bandwell, 1983). (d) Vibrational modes of a water-vapor molecule.*

8.4 The Absorption Coefficient

Energy states of a molecule are more complicated in structure than of individual atoms. This arises from complicated motions of the atomic nuclei that make up the molecule. The electronic excitation to higher energy levels within the atoms of the molecule require much more energy and involve radiation in the shorter visible and UV. Superimposed on these electronic transitions are the vibration and rotation effects (Fig. 8.9 and Table 8.1).

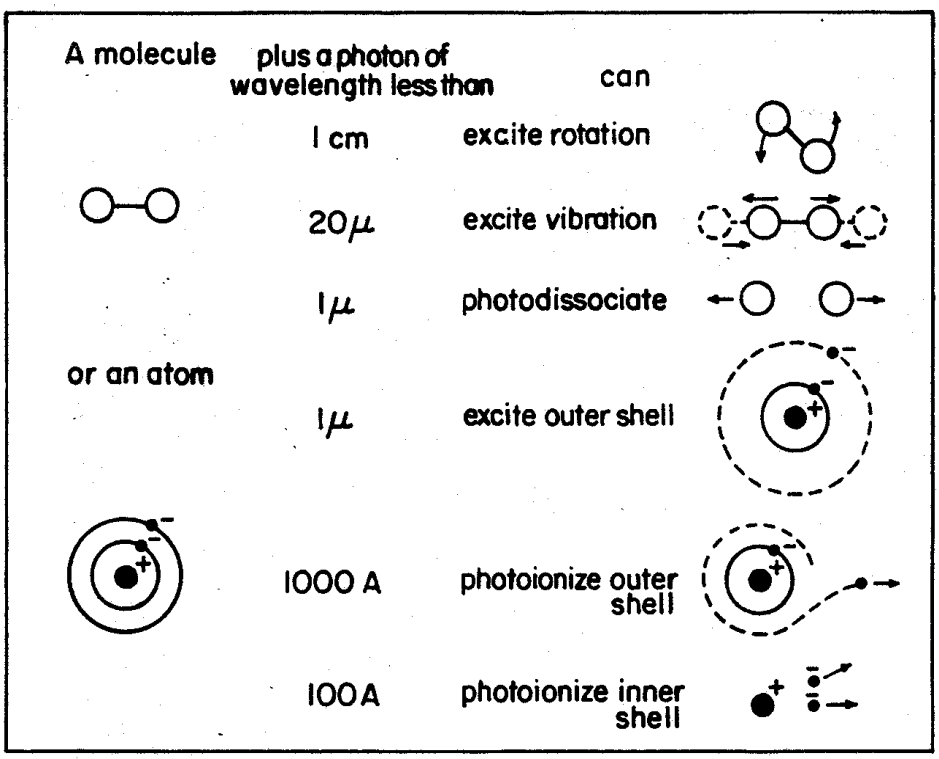

Fig. 8.9 *Possible interactions between a molecule of atom and a photon. The longer wavelength events, which involve less energy, are at the top. Bands in molecular spectra actually consist of closely spaced lines due to rotational and vibrational transitions.*

Table 8.1 *Typical energy differences and spectral ranges in electronic, vibrational, and rotational transitions.*

Transition	ΔW [eV]	$\nu = \Delta W/h$ [Hz]	Spectral range
Electronic	10	2.4×10^{15}	Ultraviolet and visible
Vibration	10^{-1}	2.4×10^{13}	Infrared
Rotation	10^{-3}	2.4×10^{11}	Millimeter waves

The absorption spectra are characterized in terms of the absorption coefficient k_ν . For an absorption line, k_ν is characterized by its

- spectral position ν_o, (and is determined by the factors already considered)

- strength S (or effectiveness of absorber)
- shape $f(v - v_o)$ (spectral "fine structure").

That is

$$k_v = Sf(v - v_o) \tag{8.3}$$

where the shape factor

$$\int_{-\infty}^{\infty} f(v - v_o)dv = 1$$

by definition. We now consider the latter two factors in more detail.

(a) Line Strength

This is a product of two distinct factors

- probability that a single isolated molecule in its lower state will absorb a photon (cross section σ)
- relative population of lower and upper states

Thus

$$S = \sigma\,(n - n_u)/n_{total}$$

The relative populations are determined by Boltzman's distribution (and hence are a function of temperature) according to $e^{-\Delta E/KT}$. (This is not true in the mesosphere where a "breakdown" of local thermodynamic equilibrium occurs). Here, ΔE *is* the energy associated with a particular v and K transition. The effect of this factor on the absorption spectrum occurs in the following way:

- Since ΔE *is* proportional to $K + 1$ for rotational lines, the line intensities are largest (i.e., absorption strongest) near the shortest wavelengths of each band. The important feature is the absorption line strength is temperature dependent owing to the temperature effects on population.

(b) Line Shape

Lines are not sharp but "fuzzy". Three main mechanisms for broadening lines are

- Natural broadening

  The energy level can only be defined within the uncertainty ΔE defined according to

$$\Delta E \Delta t \le h/2\pi$$

$$\frac{v}{2} = \frac{1}{4\pi\Delta t} = \sigma_N \tag{8.4a}$$

  If we take the mean lifetime in the upper state of molecules as indicative of Δt, then we can derive an estimate of σ_N typically ($\sim 3 \times 10^{-11}$ cm^{-1}), which is negligible for absorptions in the troposphere and stratosphere.

- Doppler broadening

Line broadening can occur through the motion of the molecules in the earth's atmosphere as they move about in random directions. The probability that molecules in a gas at temperature T possesses a velocity v is given by the Maxwellian distribution $\exp[-m_m v^2/2kT]$ where m_m is the molecular mass.

The shift in frequency due to such motion is

$$v - v_o = \Delta v = \pm \frac{v}{c} v_o$$

and the distribution of Doppler shifts follows as

$$f_D(v - v_o) = \frac{1}{\alpha_D \sqrt{\pi}} \exp(-(v - v_o)^2 / \alpha_D^2) \tag{8.4b}$$

where α_D is the Doppler half width $\left(\alpha_D = v_o \sqrt{\frac{2KT}{mc^2}} \right)$. This derivation assumes the distribution

$$p(v dv) = \left(\frac{m}{2\pi kT} \right)^{1/2} \exp\left(\frac{-mv^2}{2kT} \right) dv$$

$$f(v - v_o) = \int_{-\infty}^{\infty} p(v) \Delta v dv = \int_{-\infty}^{\infty} p(v) \frac{v v_o}{c} dv$$

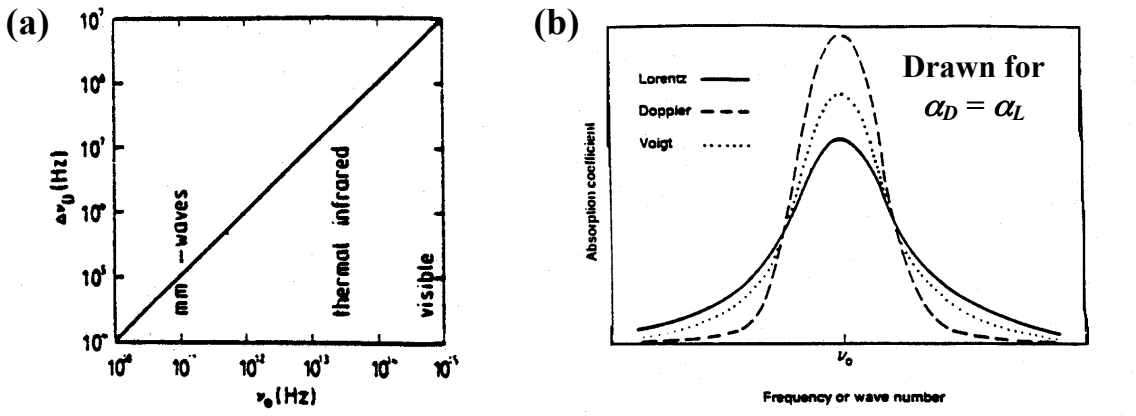

Fig. 8.10 (a) Typical width of Doppler broadened lines of light molecules at room temperature as a function of the respective center frequency. (b) Lorenz and Doppler line shapes from approximately equal half-widths and intensities. The corresponding Voigt profile is also shown.

For CO_2 and IR wavelengths, $\alpha_D \sim 7 \times 10^{-4}$ cm^{-1}. Doppler broadening is mainly important in the stratosphere and above. Accurate measurements of line width at low pressures allow deduction of T (through $T^{1/2}$ dependence).

- Pressure broadening

The third line broadening mechanism, and the one most relevant to our interests is through the effects of collisions (collision/pressure broadening). No precise model of this collision exists (the 'many' bodied problem). So simple conceptual models of collisions are employed. One model is to treat the collision as a discontinuity in the phase of the EM wave. These phase shifts are modeled as randomly occurring between 0, 2π and the period of collision is considered small compared to the period associated with passage of one wavelength.

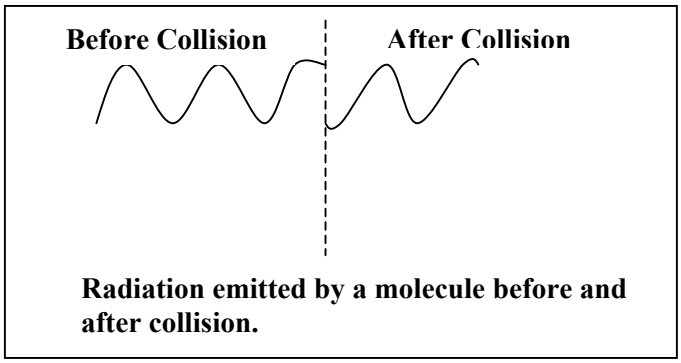

Radiation emitted by a molecule before and after collision.

The simplest and most successful treatment of this broadening is that of Lorenz

$$f_L(\nu - \nu_o) = \frac{\alpha_L / \pi}{(\nu - \nu_o)^2 + \alpha_L^2} \tag{8.4c}$$

for which $\alpha_L = \frac{1}{2}\pi\bar{t}$ ($\bar{t}$ = mean time between collisions, i.e., the more the collisions the broader the line). It follows that

$$\alpha_L \sim \alpha_{Lo}\left(\frac{P}{P_s}\right)\left(\frac{T_s}{T}\right)^{1/2} \approx 0.07\left(\frac{P}{P_s}\right)\left(\frac{T_s}{T}\right)^{1/2} \text{ cm}^{-1}$$

For example P_s = 1000 mb, T_s = 273, α_L ranges between 0.005 - 0.11 cm^{-1}.

Lorenz width is proportional to pressure (this is well confirmed by measurements). Dependence on T is less important and less well understood. Pressure dependence of absorption is of fundamental importance.

Some issues are:

- Line width is a function of type of colliding molecule (mostly N_2). Self-broadened lines (e.g., $H_2O \rightarrow H_2O$) are broader than foreign-broadened lines ($N_2 \rightarrow H_2O$)
- A fundamental problem is in the wings of Lorenz lines—extended wings are important to transparent regions of the spectrum (windows). Departures from Lorenz line shapes (super and sub Lorenzian) in the extended wings are virtually impossible to measure and a major source of uncertainty. In the far wings $\nu - \nu_o >> \alpha_L$ and

$$f_L(v - v_o) \approx \frac{\alpha_L \left(\frac{P}{P_s}\right)\left(\frac{T_s}{T}\right)^{1/2}}{(v - v_o)^2} \tag{8.5}$$

- Example of the significance of p effect on line shape: intuitive description of weighting functions that are relevant to topics of remote sensing profiles of temperature and certain species.

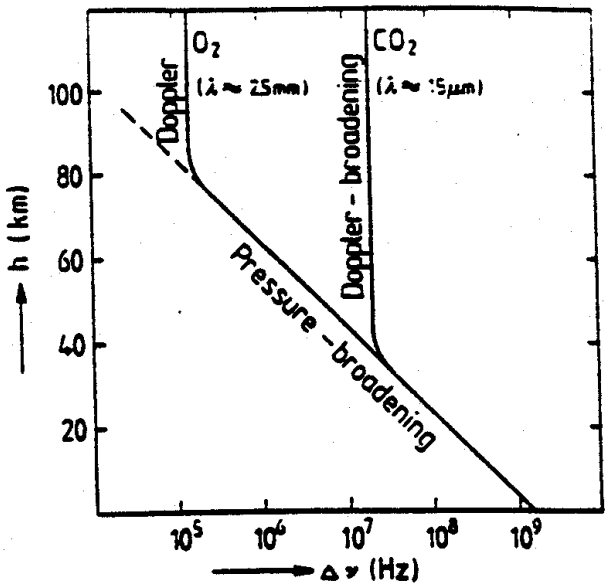

Fig. 8.11 Approximate relationship between atmospheric height h and line width for a microwave line of O_2 and an infrared line of CO_2 (idealized isothermal atmosphere and equal Δv_o values for O_2 and CO_2 are assumed).

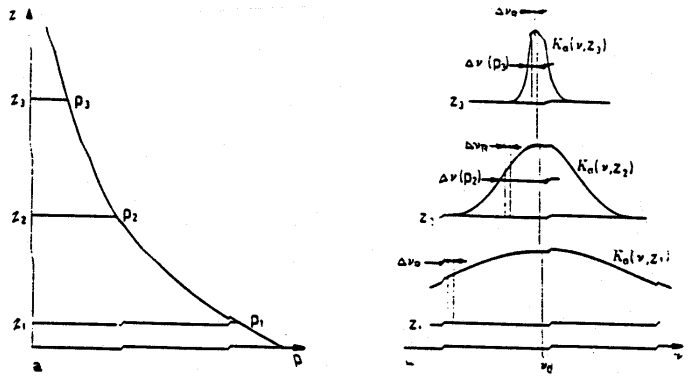

Fig. 8.12 (a) The atmospheric pressure as a function of the height. (b) The line shapes at three different height levels and filter positions.

8.5 Problems

Problem 8.1

The wavelength of radiation absorbed during a particular spectroscopic transition is observed to be 10 μm. Express this in frequency (Hz) and in wavenumber (cm^{-1}) and calculate the energy change during the transition in both joules per molecule and joules per mole. If the energy were twice as large, what would be the wavelength of the corresponding radiation? Hint: Planck's constant has the value $h = 6.63 \times 10^{-24}$ joules·s·molecule^{-1}. Avagadro's number $N = 6.02 \times 10^{23}$ mol^{-1}.

Problem 8.2

The rotational spectrum of $^{79}Br^{19}F$ shows a series of equidistant lines spaced 0.71433 cm^{-1} apart. Calculate the rotational constant B and hence the moment of inertia and the bond length of the molecule. Determine the wavenumber of the $J = 9 \rightarrow J = 10$ transition.

Problem 8.3

Using your answers to Problem 8.2, calculate the number of revolutions per second that a BrF molecule undergoes when in (a) the $J = 0$ state, (b) the $J = 1$ state. [Hint: Use (3.9) but remember that w is in radians per second.]

Problem 8.4

The masses of the H, Cl, C, and O atoms are 1.6×10^{-27} kg, 58.8×10^{-27} kg, 20×10^{-27} kg, and 26.5×10^{-27} kg, respectively.

(a) Calculate the reduced masses of the HCl and CO molecule.

(b) If the spring constants of the HCl and CO molecules are 4.78 and 1907 kgs^{-2}, respectively, determine the wavelength of the vibrational transition $0 \rightarrow 1$.

Problem 8.5

Derive a relationship between the central frequency ν_o of a line and the pressure (in atmospheres) at which the half-widths of a Lorenz line and a Doppler line are the same. Estimate this pressure for a CO_2 and O_2 molecule for the frequencies and temperature used to produce the curves shown in Fig. 8.11b. Assume the reference value of the Lorenz half-width at the ground is that given in Fig. 811b.

AT622 Section 9
Models of Transmission

The aim of this section is to introduce popular techniques used to model transmission through an absorbing layer of gas. We have already seen how the mathematical description of absorption by the gases of the atmosphere can be formulated in terms of transmission functions (Section 4). There are several types of transmission functions that must be learned and the connections to one another understood. The ultimate purpose, however is to be able to characterize the transmission averaged over many absorption lines (band transmission). Connections between different forms of transmission functions are shown in Fig. 9.1. There are transmission functions that apply to the transmission of intensity and the transmission of flux. Transmission can either be monochromatic (i.e., at a single wavelength) or broadband (i.e., an average over a band of several wavelengths), which is one of the goals of this section. These functions can either apply to homogeneous paths (i.e., applies to uniform path of fixed p and T such as encountered in the laboratory measurements) or to heterogeneous paths of varying p and T (such as in the atmosphere). We will see that the transformation from intensity to flux transmission is largely trivial and we will spend the most time discussing broadband transmission models and how we treat absorption along variable p and T paths.

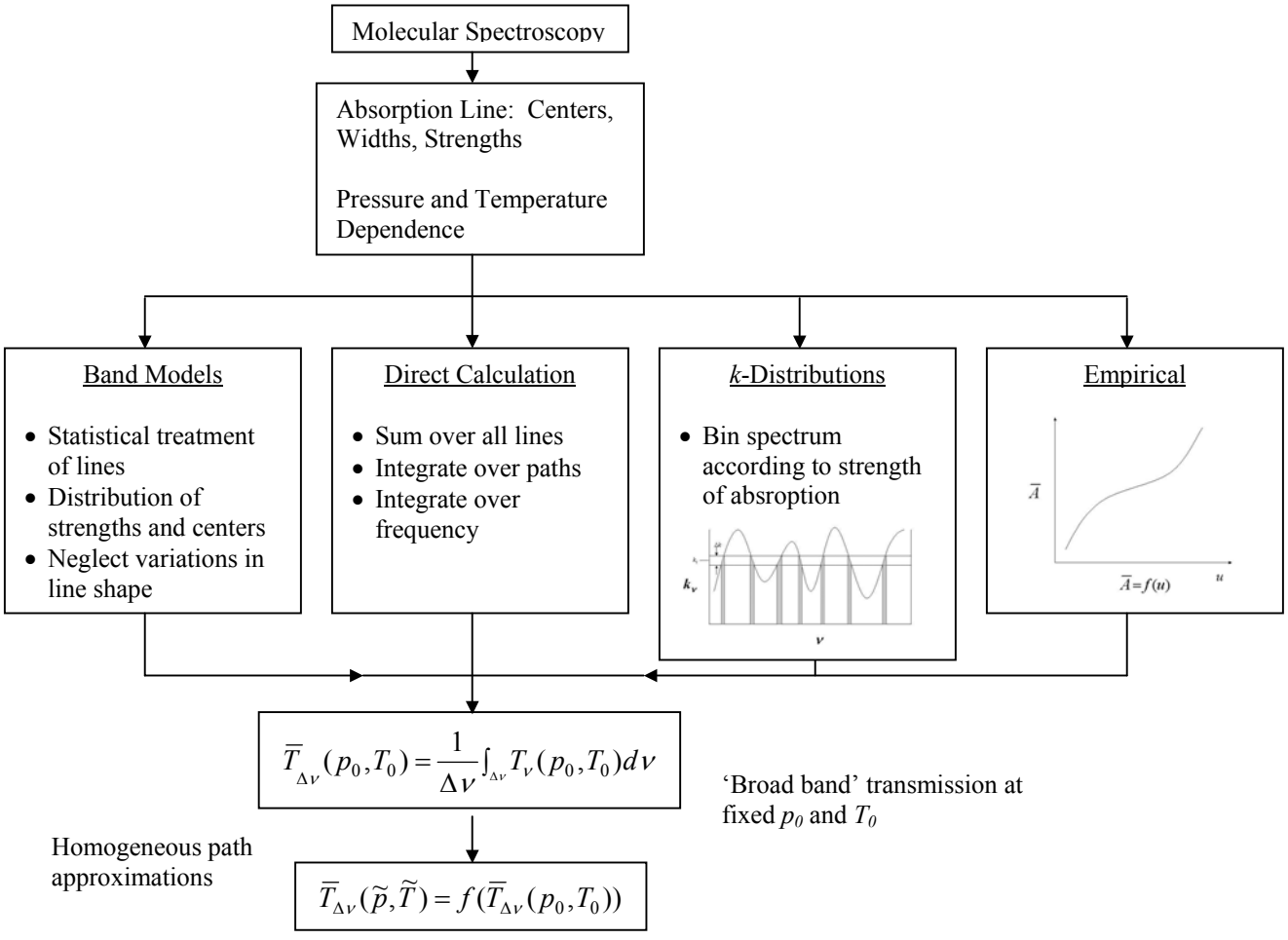

Fig. 9.1 Connections between different forms of transmission functions.

9.1 Basic Definition of Transmission Functions

The exchange of radiation with the gases of the atmosphere is described in terms of a transmission function. The concept of transmission follows directly from Lambert's law of extinction.

$$dI_\nu = -k_\nu I_\nu ds \tag{9.1}$$

where k_ν is the absorption coefficient (here we consider only absorption and ignore scattering), I_ν the intensity of the radiation field, and ds is some measure of path, defined such that the quantity

$$d\tau_\nu = k_\nu ds$$

is unitless. Solution of Eqn. (9.1) gives

$$I_\nu(\tau_\nu) = I_\nu(\tau_\nu = 0)e^{-\tau_\nu} \tag{9.2}$$

where

$$\mathcal{T}_\nu = e^{-\tau_\nu} = 1 - \mathcal{A}_\nu \tag{9.3}$$

is the monochromatic "transmission" function and A_ν *is* the monochromatic absorption. Since the relationship between absorption and transmission is trivial, we will develop our models in terms of either absorption or transmission.

The absorption coefficient (and for that matter the scattering coefficient) can be defined in a number of different ways according to how we measure the amount of matter along the path. Table 9.1 gives four more commonly used quantities together with the specification of the amount of matter. Note again that the product of extinction coefficient and amount of matter is unitless.

Table 9.1 provides the conversion factors between the different forms of extinction coefficient (read extinction here as absorption). With volume extinction, the computations use distance as the independent variable. This is generally only used in calculations involving particle absorption (and scattering). For gases, the path length is usually defined in a way that reflects gaseous density and it is more convenient to use one of the other forms. Of these, e_s *is* the most popular choice by many spectroscopists and thus we see the path lengths per centimeter at STP often used in empirical transmission formulas like those presented later.

Table 9.1 Dimensions and conversion factors for extinction coefficients[a].

Symbol	e_ν	e_m	e_n	e_s
Name	Volume e.c.	Mass e.c.	Molecular e.c.	e.c. per cm s.t.p.
Dimensions	cm^{-1}	$g^{-1}\ cm^2$	cm^2	cm^{-1}
e_σ	1	ρ^{-1}	n^{-1}	n_s/n
e_m	ρ	1	m	ρ_s
e_n	n	m^{-1}	1	n_s
e_s	n/n_s	ρ_s^{-1}	n_s^{-1}	1

[a] ρ = density of absorbing gas (g cm^{-3}) n_s = molecular no. density at s.t.p. (Loschmidt no., cm^{-3})
ρ_s = density of absorbing gas at s.t.p. (g cm^{-3}) m = molecular mass (g)
n = molecular number density (cm^{-3})

Example 9.1: Two specific examples of conversion highlight the advantage of e_n and the number of molecules per centimeter as the measure of attenuation gas over the other combinations. From Table 9.1 we deduce that

$$1\,\text{cm of gas at STP} = \frac{M}{2.24\times10^4}\,\text{gcm}^{-2},$$

where M is the molecular weight of the gas

$$1\text{ cm} - \text{STP} = 2.69 \times 10^{19}\text{ molecules cm}^{-2}.$$

The above expression is valid for all gases. It follows from these two examples that for water vapor

$$1\text{g cm}^{-2}\ (H_2O) = 3.34 \times 10^{22}\text{ molecules cm}^{-2}.$$

Thus, the unit "molecule cm^{-2}" is independent of the nature of the absorbing gas and basic to all gases and offers a way of unifying absorber concentration units for all atmospheric constituents.

Despite this benefit, absorption by gases is often expressed in terms of the mass absorption coefficient. For this case, the path element is expressed as

$$du = \rho_g ds$$

and in terms of the mixing ratio (mass)

$$r = \rho_g/\rho_{air}$$

$$du = r\rho_{air} ds$$

For vertical paths (together with the hydrostatic approximation), it follows that

$$u(z_1, z_2) = \int_{z_1}^{z_2} r\rho_{air}\, dz = \frac{1}{g}\int_{p_2}^{p_1} r\, dp \tag{9.4}$$

This is a formula that should be learned and its derivation understood.

Example 9.2: Water vapor and sea surface temperature. Develop a relationship between the vertically integrated water vapor path through the entire vertical extent of the atmosphere (precipitable water) and the sea surface temperature. Assume

(a) the vertical profile of specific humidity (expressed in terms of mass mixing ratio) has the following form $r(p) = r_s(p/p_s)^{\lambda}$ where r_s is the surface mixing ratio.

(b) the saturation vapor pressure at the surface is $e_s \approx be^{[a(T_s - T_o)]}$ such that $r_s \approx rh0.622e_s/p_s$.

Derive your answer in terms of the surface relative humidity, λ and the SST.

Answer: The column path follows from Eqn. (9.4) as

$$u = \frac{rh}{gp_s} be^{[a(T_s - T_o)]} \int_0^{p_s} (p / p_s)^{\lambda} dp$$

or

$$u = 0.622b\left(\frac{rh}{g(1+\lambda)}\right)e^{a(T_s - T_o)}$$

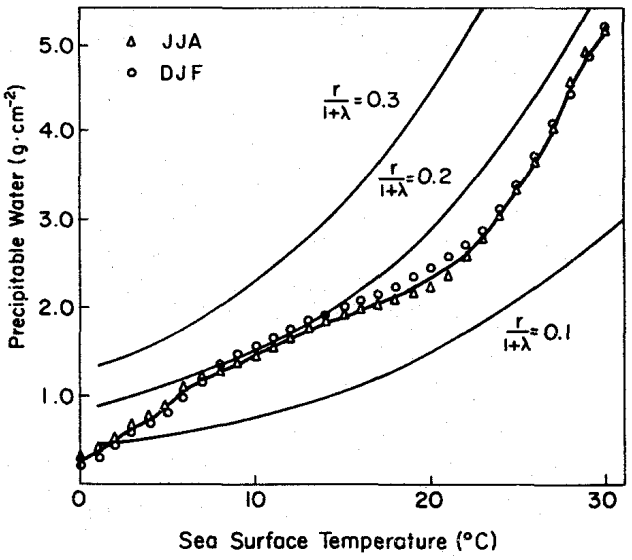

9.2 From Intensity (Beam) to Flux (Diffuse) Transmission

Transmission along a slant path $s_1 \rightarrow s_2$

$$\mathcal{T}(s_1, s_2) = e^{\int k_m dz/\mu} = \mathcal{T}(z_1, z_2, \mu)$$

$\mathcal{T}r(z_1, z_2, \mu)$ is referred to as the beam (or intensity) transmission function for the path defined by (z_1, z_2, μ).

The flux transmission function is defined as (assume azimuthal symmetry)

$$\mathcal{T}_f(z_1, z_2) = \int_0^1 \mu T(z_1, z_2, \mu) d\mu \Big/ \int_0^1 \mu d\mu \tag{9.5}$$

which is a μ-weighted transmission function characterizing the transmission of the irradiance (flux) through the slab $z_1 \rightarrow z_2$.

As noted previously in section 4, we can write Eqn. (9.5) in the following way

$$\mathcal{T}_f(z_1, z_2) = 2E_3[\tau(z_1, z_2)] \tag{9.6}$$

where $E_3(x)$ is the n^{th} exponential integral

$$E_n(x) = \int_1^\infty e^{-\eta x} d\eta / \eta^n$$

($\eta = 1/\mu, x = \tau$). To a high degree of accuracy,

$$2E_3(x) \approx e^{-\beta x} \tag{9.7}$$

where $\beta = 1.66$ (the so called diffusivity factor). Therefore,

$$\mathcal{T}_f(z_1, z_2) = e^{-\beta \int k du} \tag{9.8}$$

The important point here is that the flux transmission can be modeled using the transmission for intensity with the path merely increased by the diffusivity factor β. Thus in developing theories for broadband functions, we will consider intensity transmission and note that broadband flux transmission is given by this transmission function with the introduction of this diffusivity function.

9.3 Frequency Integrated Absorption of a Single Line

Most problems of interest require spectrally integrated transmission (or equivalently absorption) functions over a variety of spectral scales varying from the scale defined by the line half width to scales attached to broad spectral regions 10's-100's cm^{-1} wide. Before understanding how we can do this complicated integration, it is useful to study the heuristic properties of the integrated absorption of a single line.

The quantity of main interest is the monochromatic absorption as defined by the frequency integrated absorption, namely

$$W(u) = \int d\nu (1 - e^{-k_\nu u}) = \int d\nu \left(1 - e^{-Sf(\nu - \nu_o)u}\right) \tag{9.9a}$$

where u replaces s as a symbol of the measure of path. This absorption is called the equivalent width $W(u)$ since it measures the width of ν units of a hypothetical square shaped line that gives the equivalent

integrated absorption. It is crucial to recognize that for the developments here and in the next section, the absorption parameters (such as line half width α and intensity S) are constant and independent of path). This is obviously unrealistic and we will discuss later how the results below can be modified to treat this added complexity.

(a) Limits to the Integrated Absorption of a Single Line

There are two extremely useful asymptotic limits of $W(u)$ that occur repeatedly in discussion of molecular absorption.

- The weak line limit (linear limit)

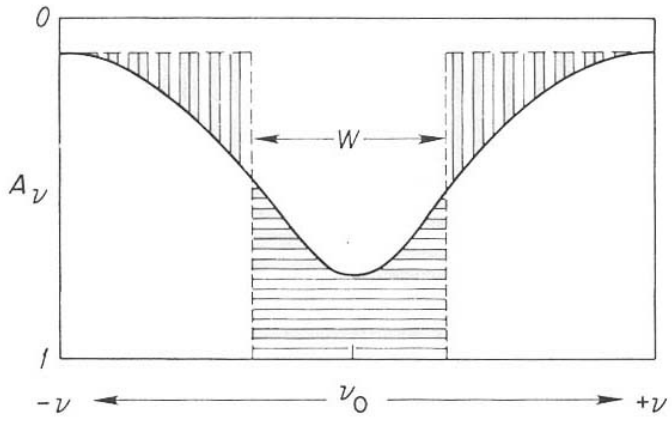

Fig. 9.2 Schematic interpretation of the equivalent width.

Suppose $u \to 0$, $Sf(\nu)u << 1$, then

$$e^{-Sf(\nu)u} \sim 1 - Sf(\nu)u \tag{9.9b}$$

and

$$W = Su\int f(\nu)d\nu = Su \tag{9.10}$$

which is valid no matter what the line shape.

- Strong line or square root limit:

For this limit we consider the Lorenz line shape

$$f(\nu - \nu_o) = \frac{\alpha_L / \pi}{(\nu - \nu_o)^2 + \alpha_L^2}$$

Suppose $|\ \nu - \nu_o\ | >> \alpha_L$ so that $\dfrac{1}{(\nu - \nu_o)^2 + \alpha_L^2} \to \dfrac{1}{(\nu - \nu_o^2)}$ then

$$\exp\left[-\frac{Su\alpha_L/\pi}{(\nu-\nu_o)^2+\alpha_L^2}\right]\rightarrow e^{-\frac{Su\alpha_L}{\pi(\nu-\nu_o)^2}}$$

and

$$W(u)=\int d\nu\left[1-e^{-\frac{Su\alpha_L}{\pi(\nu-\nu_o)^2}}\right]$$

and

$$W(u)=2\sqrt{Su\alpha_L}\,. \tag{9.11}$$

Conditions of strong absorption occur either as a result of abundant u absorber and/or high pressure (i.e., large α_L). Weak absorption is sensitive to abundance. A physical interpretation of these limits is afforded by reference to Fig. 9.3. In the linear region absorption occurs at the center of the line. A point is reached where all the energy is removed from the line center so that as u increases, the absorption increases through the wings (strong region).

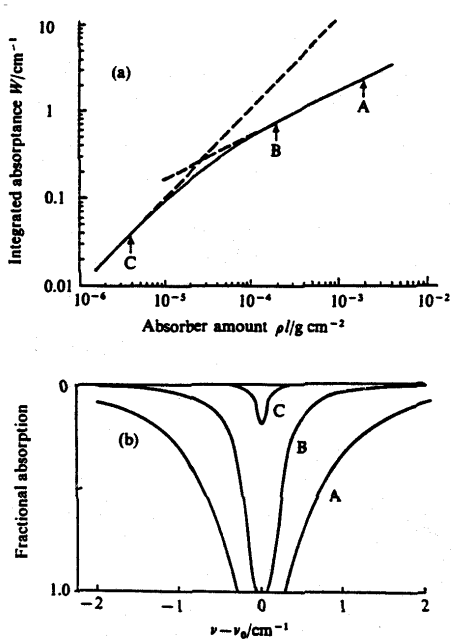

Fig. 9.3 The physical interpretation of strong and weak line absorption.

(b) Broadband Absorption by a Single Lorenz Line

The equivalent width of a single Lorenzian line is expressed by the Ladenburg-Reiche function,

$$W_{L-R}(u)=\int_{-\infty}^{\infty}\left[1-e^{-\frac{Su\alpha_L/\pi}{(\nu-\nu_o)^2+\alpha_L^2}}\right]d\nu=2\pi\alpha_L\left[\underbrace{ye^{-y}[I_o(y)+I_1(y)]}_{L-R\ \text{function}}\right] \tag{9.11a}$$

where $y = \dfrac{Su}{2\pi\alpha_L}$. This can be usefully approximated by

$$W_{L-R} \sim Su\left[1+\left(\frac{Su}{4\alpha_L}\right)^{5/4}\right]^{-2/5} \tag{9.11b}$$

within 1% for all values of Su/α_L.. Figure 9.3 (upper panel) provides a schematic demonstration of the strong and weak absorption and the *L-R* function. We call such plots 'the curve of growth' and these are fundamental to very important topics of atmospheric radiation.

(b) Absorption by Lines with Distributed Line Intensities

Here we consider the absorption averaged over lines that vary in intensities from line to line but not in their width and do not overlap in any way. Since the variation in line intensity over a band of thousands of lines is much more significant than is the variation of α_L, this is a reasonable approximation. Furthermore, we will see how certain models of bands of overlapping lines reduce to this simple distribution of single lines.

Figure 9.4 is a diagram of the line intensity distribution expressed as the function $p(S)$ where $p(S)dS$ is the fraction of lines having intensities between S and $S + dS$. There have been different models derived according to the assumed form of $p(S)dS$ and we will now consider two specific examples:

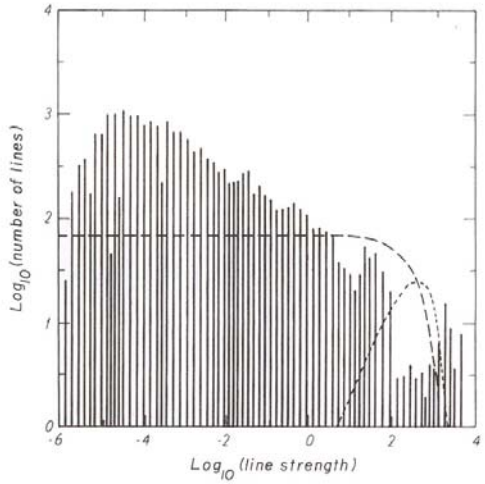

Fig. 9.4 A histogram (vertical bars) of all CO_2 lines at wave numbers between 450 and 900 cm^{-1}. Each bar represents the number of lines in a given line group. Lines with strengths within 20% of the mean strength of a given group are gathered into that group. Analytic line-strength distributions obtained with the Goody (dotted line) and Malkmus (long-dashed line) models are also shown (after Crisp et al., 1986, with modifications).

- Goody (1952)

$$P(S) = \frac{1}{\sigma}\exp\left[-\frac{S}{\sigma}\right]$$

- Malkmus (1967)

$$P(S) = \frac{1}{S}\exp\left[-\frac{S}{\sigma}\right]$$

where σ is the mean line intensity,

$$\sigma = \int_0^\infty Sp(S)dS\,.$$

if

$$k_\nu = f(\nu)S$$

then it follows that

$$\overline{W} = \int_0^\infty p(S)W(S)dS$$

and

$$\overline{W} = \int_0^\infty p(S)dS\int_{-\infty}^{+\infty} 1-\exp[-Sf(\nu)u]d\nu$$

Thus:

- Goody

$$W = \int_{-\infty}^{\infty} \sigma f(\nu)u/[1+Sf(\nu)u]d\nu$$
$$W_G = \sigma u\left[1+\frac{Su}{\pi\alpha_L}\right]^{-1/2} \qquad (9.12a)$$

- Malkmus

$$W = \int_{-\infty}^{\infty} \ln[1+uSf(\nu)]d\nu$$
$$W_M = \frac{\pi\alpha_L}{2}\left[\left(1+\frac{4Su}{\pi\alpha_L}\right)^{1/2}-1\right] \qquad (9.12b)$$

9.4 Overlapping Lines: Band Models

It is obvious that over some interval $\Delta\nu$, increasing the optical mass (u) cannot yield an increase in absorptance indefinitely if several overlapping lines are present in $\Delta\nu$. Thus the square root formula must fail. Attempts have been made to modify single line absorption theory to include line overlap—but these

on the whole are not fruitful. More successful are the approaches adopted based on treating the array of lines as a statistical entity rather than as a group of individual lines. Models of this type are referred to as *statistical band models.*

(a) Regular Model

Elsasser, *1938:* Mean absorption and equivalent absorption coefficient of a band spectrum. *Phys. Rev.,* **54**, 126-129. Goody and Yung, 4.5. This model is most closely met for $P + R$ branches of linear molecules.

$$f_E(\nu) = \frac{1}{\delta}\frac{\sin h(2\pi\alpha/\delta)}{\cos h(2\pi\alpha/\delta - \cos(2\pi\nu/\delta)} = \sum_{n=-\infty}^{n=+\infty}\frac{1}{\pi}\frac{\alpha_L}{(\nu - n\delta)^2 + \alpha_L^2} \tag{9.13}$$

The corresponding transmission for homogeneous paths is

$$\overline{\mathcal{T}}_E = \frac{1}{\Delta\nu}\int_{\Delta\nu}\exp[-Sf_E(\nu)u]d\nu$$

where $\Delta\nu = 6$. This integral cannot be solved in terms of elementary functions.

Consider two limits

- $\frac{\alpha_L}{\delta} \to \infty$, $\sin h 2\pi/\delta$, $\cos h 2\pi\alpha/\delta \to \infty$ and

$$\mathcal{T}_E = \exp[-Su/\delta]$$

  Here lines strongly overlap and there is no line structure. Further increase of α_L/δ (i.e., pressure) has no effect on the continuum. Transmission is independent of line shape.

- $\sin h 2\pi\alpha_L \sim 2\pi\alpha_L/\delta$, $\cos 2\pi\alpha_L/\delta \sim 1$ (small α_L/S)

$$\overline{\mathcal{T}}_E = 1 - \Phi\left(\sqrt{\pi S\alpha_L u/\delta}\right) = 1 - \Phi\left(\sqrt{\frac{\ell u}{2}}\right), \ell = \frac{2\pi\alpha S}{\delta^2} \tag{9.14}$$

  where

$$\Phi(x) = \frac{2}{\sqrt{\pi}}\int_0^x e^{-x}dx = \text{probability integral}$$

  The agreement with observation for this model is excellent when applied to an appropriate absorber (Fig. 9.5).

(b) Random Models (G + Y, p. 158)

Whereas the application of a regular band model to molecular absorption in the atmosphere has limited scope, use of random band models has been far more widely used and validated against

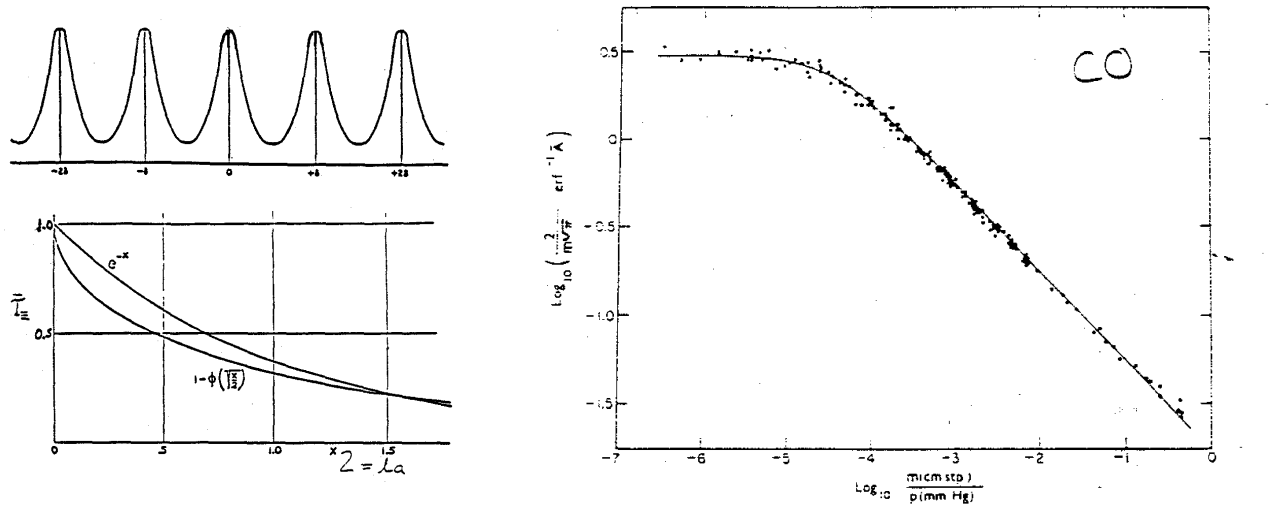

Fig. 9.5 *(a) Line shape for the Elsasser model (after Goody, 1964). (b) Comparison of transmission for purely exponential type (single line) and the Elsasser band model of regularly overlapping lines, (c) Measured and fitted transmissions for a CO absorption band.*

observations. One approach to the development of a random model is to take an infinite array (like the Elsasser model) and then combine a number of these arrays by multiplication. Consider for illustration a band of constant line intensity, then

$$k_\nu = \sum_{i=1}^{N} k_\nu^{(i)}$$

is the absorption coefficient at ν due to the superposition of N lines distributed randomly in the interval $-N\delta/2$ and $N\delta/2$ by lines located at ν_i. The transmission is

$$\mathcal{T}_\nu = \exp\left(-u\sum_{i=1}^{N} k_\nu^{(i)}\right) = \prod_{i=1}^{N} \exp(-uk_\nu^{(i)}) \tag{9.15}$$

If the probability that a single line lies in the interval $d\nu_i$ *is* $d\nu i/\delta$, then the joint probability that there are lines between ν_1 and $\nu_1 + d\nu_1$, ν_2 and $\nu_2 + d\nu_2$,, and so on is

$$\prod_{i=1}^{N} \frac{d\nu_i}{\delta} \tag{9.16}$$

For all possible arrangements of lines in the interval

$$\overline{\mathcal{T}} = \frac{\prod_{i=1}^{N} \int_{-N\delta/2}^{N\delta/2} \frac{d\nu_i}{\delta} \exp[-uk^{(i)}]}{\prod_{i=1}^{N} \int_{-N\delta/2}^{N\delta/2} d\nu_i/\delta} \tag{9.17}$$

with some approximation ($n \to \infty$)

$$\overline{\mathcal{T}} \to \exp\left[-\frac{1}{\delta}\int_{-\infty}^{\infty} 1-\exp[-uk_\nu]d\nu\right] = \exp[-W/\delta] \tag{9.18}$$

This states that the transmission through a random array of lines equals the exponential of the mean absorption (W/δ)

Consider now M such arrays of random lines superimposed on one spectral interval $M\delta$ wide, then

$$\overline{\mathcal{T}}_i = \exp[-W_i/M\delta] \tag{9.19}$$

where W_i is the equivalent width of one line in the *'i^{th}'* array. Since transmission is exponential,

$$\overline{\mathcal{T}} = \prod_{i=1}^{M}\overline{T}_i = \exp\left[-\frac{1}{M\delta}\sum_i W_i\right] = \exp[-\overline{W}/\delta] \tag{9.20}$$

Now the average absorption $\overline{W}$ was derived according to Eqns. (9.12a) and (9.12b) for Goody and Malkmus line intensity distribution. Thus:

$$\overline{\mathcal{T}}_{\text{Goody}} = \exp\left[\frac{-\bar{S}u/\delta}{(1+\bar{S}u/\pi\alpha_L)^{1/2}}\right]$$
$$\overline{\mathcal{T}}_{\text{Malkmus}} = \exp\left[\frac{-\pi\alpha_L}{2\delta}\left[\left(1+\frac{4\bar{S}u}{\pi\alpha_L}\right)^{1/2}-1\right]\right] \tag{9.21}$$

Clearly lines are not randomly distributed (they are predicted by quantum mechanical formula) and so a random band model is just an approximation to the actual transmission by a band of overlapping lines. The viability of the model, however, can be tested against laboratory data—with very good agreement (Fig. 9.6).

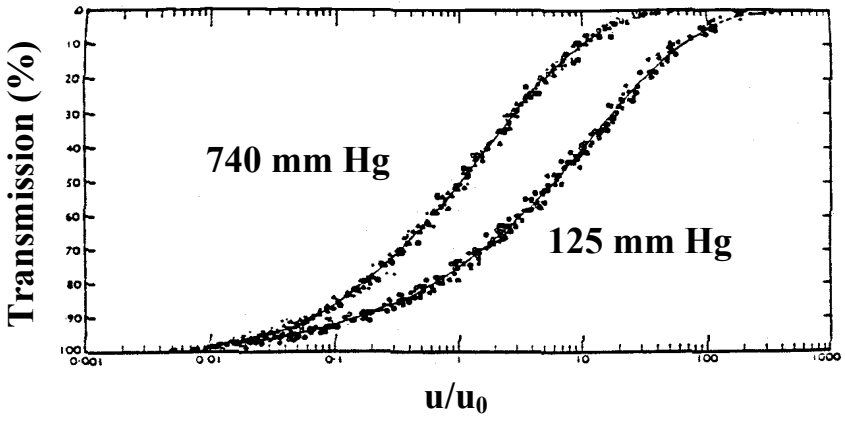

Fig. 9.6 Comparison between the random model (full line and observation (points) for sections of the 6.3 μm, 2.7 μm, 1.87 μm, 1.38 μm, and 1.1 μm band of water vapor. The different symbols represent absorptions by different bands.

(c) Band Parameter Fits (G + Y, p. 158)

The idea of a band model is to use Eqn. (9.21) to fit actual spectroscopic data to deduce the band parameters, namely α_L, δ, σ. We will not discuss the actual methods by which band models are matched to observations to provide these parameters. It suffices to state that this is done by fitting in the strong and weak limits of absorption, using Eqns. (9.18a) and (9.18b) in the form

$$\mathcal{T}_{\text{Goody}} = \exp\left[-(w^{-2} + s^{-2})^{1/2}\right]$$

$$\mathcal{T}_{\text{Malkmus}} = \exp\left(-\frac{s^2}{2w}\left[\left(1+\frac{4w^2}{s^2}\right)^{1/2} - 1\right]\right)$$

where we define the w (weak) and s (strong) parameters as

$$w = \frac{1}{\Delta\nu}\sum_i S_i u$$

$$s = \frac{1}{\Delta\nu}\sum_i \sqrt{S_i \alpha_i}$$

Table 9.2

Band	Interval (cm^{-1})	$\bar{S}/\delta$ ($cm^2\ g^{-1}$)	$\pi\alpha/\delta$
H_2O rotational	40-160	7210.30	0.182
	160-280	6024.80	0.094
	280-380	1614.10	0.081
	380-500	139.03	0.080
	500-600	21.64	0.068
	600-720	2.919	0.060
	720-800	0.386	0.059
	800-900	0.0715	0.067
CO_2 15 μm	582-752	718.7	0.448
O_3 9.6 μm	1000.0-1006.5	6.99×10^2	5.0
	1006.5-1013.0	1.40×10^2	5.0
	1013.0-1019.5	2.79×10^3	5.0
	1019.5-1026.0	4.66×10^3	5.5
	1026.0-1032.5	5.11×10^3	5.8
	1032.5-1039.0	3.72×10^3	8.0
	1039.0-1045.5	2.57×10^3	6.1
	1045.5-1052.0	6.05×10^3	8.4
	1052.0-1058.5	7.69×10^3	8.3
	1058.5-1065.0	2.79×10^3	6.7
H_2O 6.3 μm	1200-1350	12.65	0.089
	1350-1450	134.4	0.230
	1450-1550	632.9	0.320
	1550-1650	331.2	0.296
	1650-1750	434.1	0.452
	1750-1850	136.0	0.359
	1850-1950	35.65	0.165
	1950-2050	9.015	0.104
	2050-2200	1.529	0.116

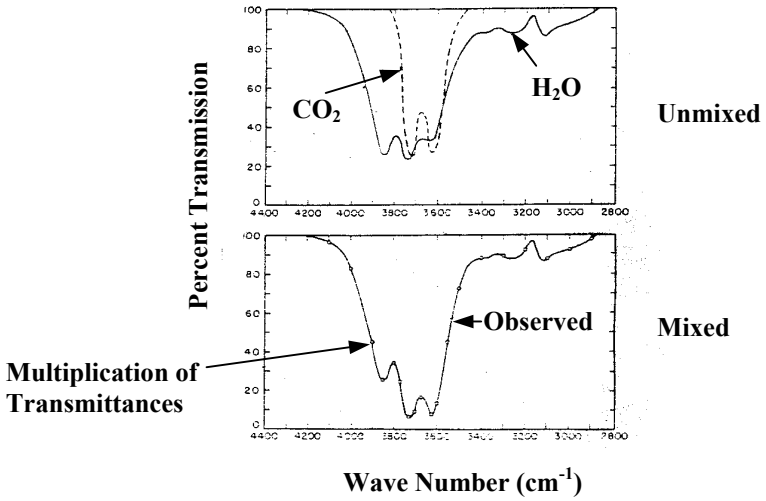

Fig. 9.7 Absorption in the spectral region from 4400-2800 cm^{-1} where CO_2 and H_2O overlap.

Example 9.3: Transmission in the CO_2-H_2O overlap band. In the 15 μm region, the transmission associated with two overlapped absorption bands has the form

$$\mathcal{T}_{H_2O+CO_2} = \mathcal{T}_{H_2O} \times \mathcal{T}_{CO_2}$$

From the band parameters listed in Table 9.2, we have

CO_2	$s/\delta = 718.7$	$\pi\alpha/\delta = 0.448$
H_2O	$s/\delta = 2.919$	$\pi\alpha/\delta = 0.06$

then

$$\mathcal{T}_{H_2O} = \exp\left[\frac{-2.919 \times \beta u_{H_2O}}{\left(1+\frac{2.919}{0.06}\times\beta u_{H_2O}\right)^{1/2}}\right]$$

$$\mathcal{T}_{CO_2} = \exp\left[\frac{-718.7 \times \beta u_{CO_2}}{\left(1+\frac{718.7}{0.448}\times\beta u_{CO_2}\right)^{1/2}}\right]$$

where u_{H2O} and u_{CO2} are the respective path lengths of water vapor and carbon dioxide under consideration. A typical column value of water vapor (see Example 9.2) is $u_{H2O} = 2.8$ gcm^{-2} and a typical value of the column carbon dioxide path is $u_{CO2} = r_s p_s/g \approx 44 \times 330 \times 101300/(980 \times 29) = 0.5$ gcm^{-2}. These values together with $\beta = 1.66$ lead to

$$\mathcal{T}_{H_2O+CO_2} = 0.406 \times 6.6 \times 10^{-8} = 2.68 \times 10^{-8}$$

and for double the amount of CO_2,

$$\mathcal{T}_{H_2O+CO_2} = 0.406 \times 7.0 \times 10^{-11} = 2.84 \times 10^{-11}$$

We conclude that the CO_2 portion of the band is highly opaque and increases in this absorber only marginally reduce the already small transmission.

9.5 The Method of *k* Distribution

The *k*-distribution method for transmission is based on grouping of the absorption coefficients k_ν in some spectral interval (or band) (Fig. 9.8). In a homogeneous atmosphere, the spectral transmittance is independent of the ordering of *k* for a given spectral interval. Hence, the wave number integration may be replaced by an integration over the *k* space. If the normalized probability distribution function for k_ν in the interval $\Delta\nu$ is given by $f(k)$ and its minimum and maximum values are k_{min} and k_{max} , respectively, then the spectral transmittance may be expressed by

$$\mathcal{T}(u) = \frac{1}{\Delta\nu}\int_{\Delta\nu} e^{-k_\nu u} d\nu = \int_0^\infty e^{-k_\nu u} f(k) dk$$

where $k_{min} \to 0$ and $k_{max} \to \infty$

$$\int_0^\infty f(k) dk = 1$$

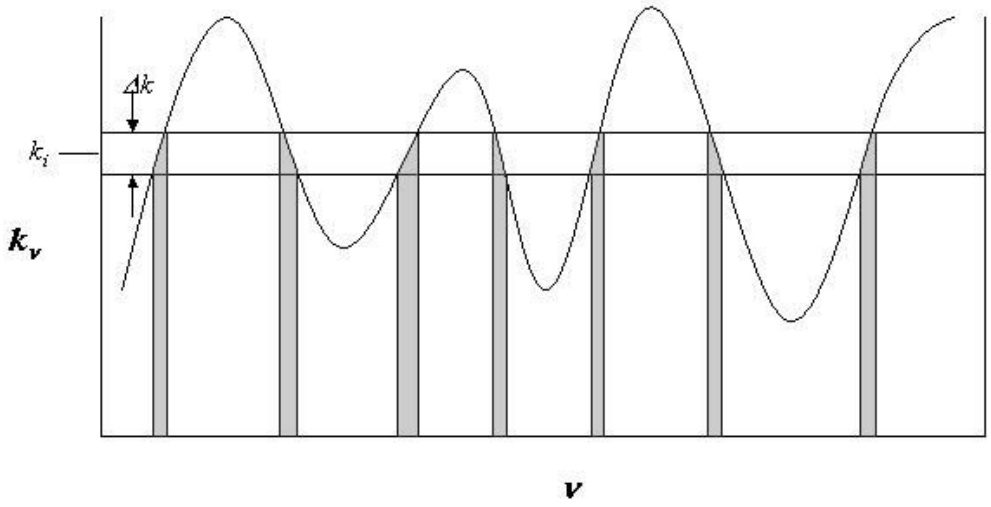

Fig. 9.8 *The concept of the k-distribution approach. Divide the plot into n horizontal slices, centered on values $k_1, k_2, \ldots, k_n$. F_i denotes the area of the ν axis covered by points where* $ki - \frac{\Delta k}{2} \le k_\nu \le k_i + \frac{\Delta k}{2}$.

Moreover, a cumulative probability function may be defined in the form

$$g(k) = \int_0^k f(k) dk \tag{9.22}$$

where $g(0) = 0$, $g(k \to \infty) = 1$, and $dg(k) = f(k)dk$. By definition, $g(k)$ is a monotonically increasing and smooth function in *k* space. By using the *g* function, the spectral transmittance can be written

$$\mathcal{T}(u) = \int_0^1 e^{-k(g)u} dg = \sum_{j=1}^{M} e^{-k(g_j)u} \Delta g_j \tag{9.23}$$

Since $g(k)$ is a smooth function in k space, the inverse will also be true here: that is, $k(g)$ is a smooth function in g space. Consequently, the integration in g space, which replaces the tedious wave-number integration, can be evaluated by a finite and relatively small number of exponential terms.

The steps to implementing the k-distribution approach are highlighted schematically in Fig. 9.9. Figure 9.9(a) shows the spectrum of k_ν in a portion of the 9.6 μm O_3 band at a pressure of 30 mb and a temperature of 220 K. Figure 9.9(b) shows the probability distribution $f(k)$ as a function of k derived from this spectrum (we will not discuss the details of how this is done although it is portrayed in Fig 9.8 and discussed further in G+Y). In Fig. 9.9(c) the cumulative probability function $g(k)$ is shown as a function of k. We may then compute $k(g)$ as a function of g from Eqn. (9.22). This curve is illustrated in Fig. 9.9(d). Since g is a smooth monotonic function, a few quadrature points suffice to achieve a high degree of accuracy in the transmittance computations.

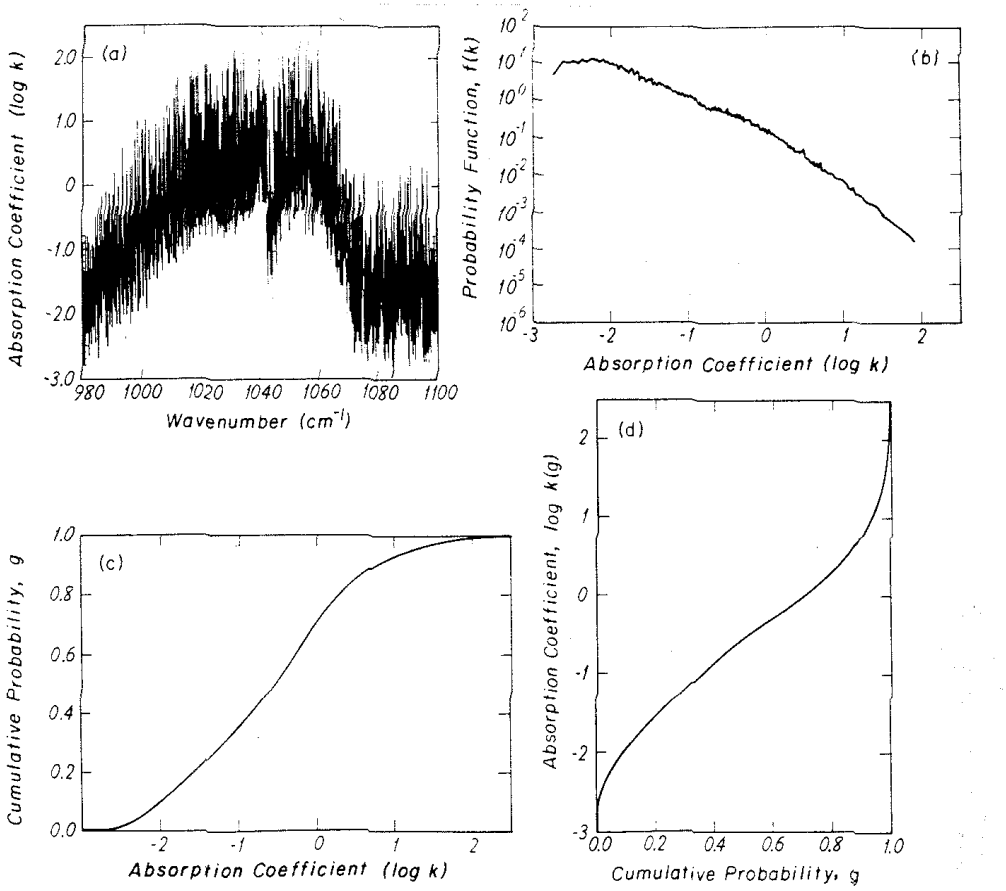

Fig. 9.9 *(a) Absorption coefficient k_ν in units of $cm^{-1}atm^{-1}$ as a function of wave number with a resolution of 0.05 cm^{-1} in the 9.6 μm O_3 band p = 30 mb* and *T = 220 K. (b) The probability function f(k) of the absorption coefficient. (c) The cumulative probability function of f(k) shown in (b), plotted as a function of k. (d) Same as (c), except that values of the absorption coefficient are expressed as a function of g.*

The physical foundation for the k distribution is quite simple, but it offers clear advantages in the computation of broadband transmission. It has also been discussed by Domoto (1974) on some aspects of the theoretical foundation and the Laplace transforms for a number of band models. The idea of

scrambling and ranking absorption lines was described in the work of Ambartsumian (1936) of stellar atmospheres.

There is a second way to approach the *k* distribution and it follows from a closer look at Eqn. (9.22). It follows by definition that the transmission can be expressed as

$$\mathcal{T}(u) = \mathcal{L}[f(k)]$$

where $\mathcal{L}$ *is* the Laplace transform. Thus the transmission is the Laplace transform of *f*(*k*) and this distribution is obtained as the inverse transform

$$f(k) = \mathcal{L}^{-1}[\mathcal{T}(u)]$$

For some functions, this provides a convenient way to obtain the spectral function *f*(*k*). As it turns out, the inverse Laplace transform of the Malkmus model is obtained analytically as

$$kf(k) = \frac{1}{2}\left(\frac{(\bar{k})y}{k}\right)^{1.2} \exp\left[\frac{\pi y}{4}\left(2 - \frac{k}{\bar{k}} - \frac{\bar{k}}{k}\right)\right]$$

where $\bar{k} = \sigma/\delta$ and $y = \alpha_L/\delta$.

9.6 Selected Empirical Transmission Functions

A wide variety of empirical transmission models based on laboratory measurements have been employed in the literature. For example:

$$\begin{aligned} W_{LAB} &= A\tilde{u} && W < W_o \\ &= B + C\log\tilde{u} && W > W_o \\ \tilde{u} &= \tilde{u}(p/p_{LAB})^n \end{aligned}$$

where *A. B, C, W_o,* and *n* are empirical constants. $\tilde{u}$ is absorber mass, *p* is pressure (subscript "LAB" refers to laboratory conditions). Most only involve single path parameter *u.* All empirical models should be used with caution: unless based on theory, applicable only to a range of parameters for which they are fitted.

Two widely used empirical approximations to the solar weighted broadband absorption function

$$\bar{A}(u) = \frac{\int F_{\odot,\lambda} A_\lambda(u)\, d\lambda}{Q_\odot}$$

for the path *u* were derived by Lacis and Hansen (1974) for UV and visible ozone absorption and near infrared water vapor absorption. (The transmission is just $1 - \bar{A}$). The formulae are:

$$A_{oz}^{vis}(\Omega) = \frac{0.02118X}{1 + 0.042X + 0.000323X^2} \qquad (9.24a)$$

$$A_{oz}^{uv}(\Omega) = \frac{1.082X}{(1+138.6X)^{0.805}} + \frac{0.0658X}{1+(103.6X)^3} \tag{9.24b}$$

where X is the ozone amount for the slant path expressed in cm STP and $X = \Omega m_r$ where Ω is the column ozone amount above some specified level

$$m_r = \frac{35\mu_o}{1224\mu_o^2 + 1}$$

and $\mu_\odot = \cos\,\theta_\odot$. This factor (referred to as the relative airmass) differs only from sec $\theta_\odot$ for $\theta_\odot$ near 90° due to refraction effects of the solar beam at these glancing angles.

The formula for water vapor is

$$A_{wv}(w) = \frac{2.9u}{[(1+141.5u)^{0.635} + 5.925u]} \tag{9.24c}$$

where $u = wm_r$ such that w is the column water vapor amount (precipitable water) in units of gcm^{-2} (this is equivalent to cm STP). The total broadband absorption with respect to the entire solar spectrum is

$$A \approx A_{wv}(u) + A_{oz}^{uv}(\Omega) + A_{oz}^{vis}(\Omega)$$

given that the three absorptions occur in three different portions of the solar spectrum such that they overlap in a simple additive way. Figure 9.10a presents comparisons of the two formulae against actual spectrally integrated ozone absorptions. Figure 9.10b shows the broadband water vapor absorption derived from a number of different sources of both absorption data and spectral solar flux. Much of the difference can be explained by the actual choice of $F_{\odot\lambda}$ for integrating the spectral absorption. These differences lead to significant differences in calculating the solar flux.

Example 9.4: Broadband transmission of the direct solar beam. Consider the following

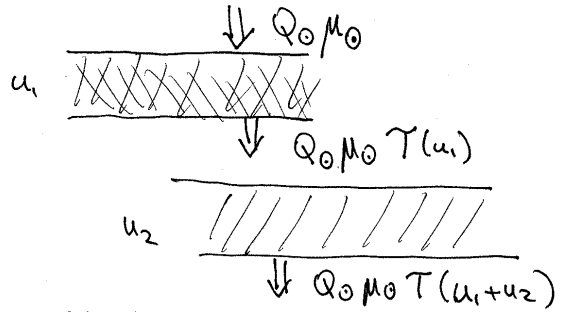

Two overlying absorbing layers of path u_1 and u_2. In the shaded upper layer, the absorbed flux is

$$\Delta F_1 = Q_\odot \mu_\odot \overline{A}(u_1 m_r)$$

where $m_r \approx 1/\cos\,\theta_\odot$ The absorption in the lower layer is then

$$\Delta F_2 = Q_\odot \mu_\odot [\overline{A}((u_1+u_2)m_r) - \overline{A}(u_1 m_r)]$$

The transmission through the two layers is $\mathcal{T} = 1 - \overline{A}((u_1+u_2)m_r)$

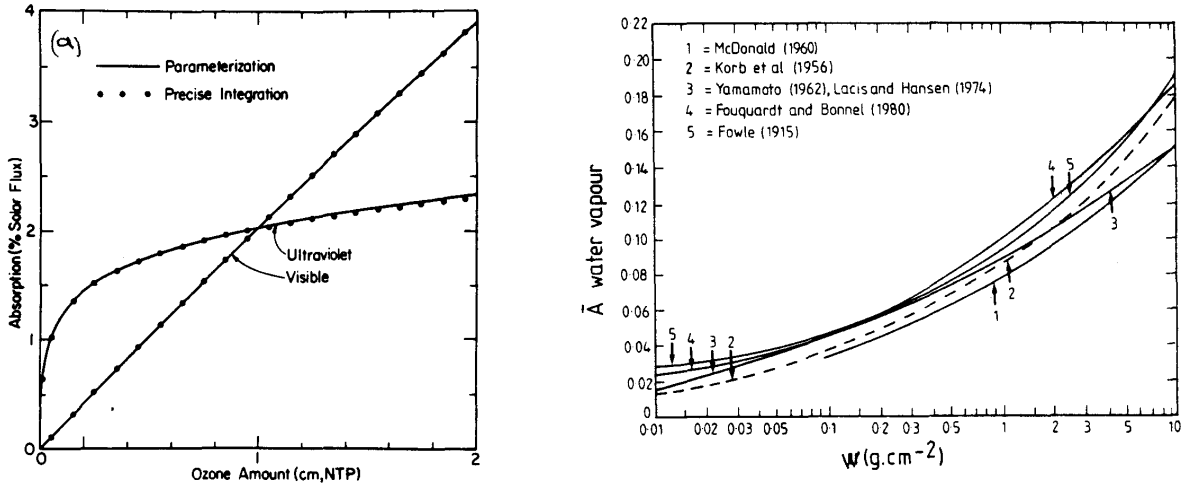

Fig. 9.10 (a) Percentage of the total solar flux absorbed as a function of ozone amount Ω. (b) Same as (a) but as a function of water vapor amount.

9.7 Transmission Along Inhomogeneous Paths (Section 6.4 Goody and Yung)

So far all our discussion of transmission applies to the case of homogeneous paths (i.e., paths over which temperature and pressure and hence $k(\nu)$ are constant) such as might arise in the laboratory. We now must modify this view as

- Most problems of transmission in the atmosphere apply to paths for which p and T vary.
- Laboratory data are obtained for fixed p and T, which might not be representative of atmospheric conditions and some adjustment is needed.

Figure 9.11 provides a schematic illustration of the consequence of transmission along a pressure varying path. The atmospheric line profile is no longer Lorenzian.

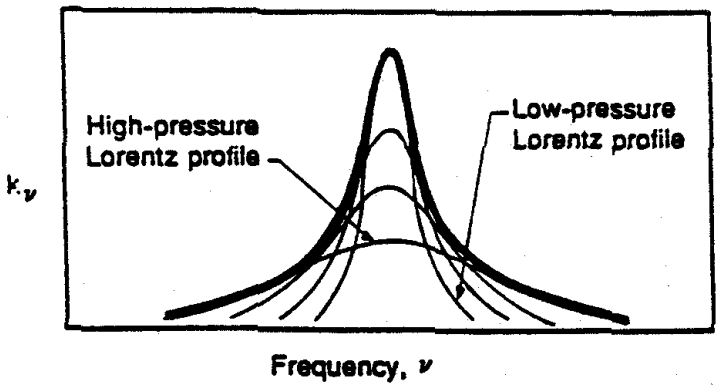

Fig. 9.11 Schematic composite showing how an actual line profile over a variable pressure path forms as a composite of the individual Lorenz profiles. The atmospheric line profile is not Lorenz in general: it is more sharply peaked because of low-pressure contributions, with broader wings due to high-pressure contributions.

In treating inhomogeneous effects, the assumption is made that the absorption for paths along which p and T vary can be approximated by absorption expressed in terms of a homogeneous path with the parameters scaled in some way. Two principal forms of scaling are used. Before discussing these, it is worthwhile considering one case for which an analytic solution exists.

(a) Constant Mixing Ratio, Isothermal Atmosphere—An Exact Solution

There is one hypothetical case for which the algebra can be done. Consider a line centered at $\nu_o = 0$ for convenience, then $\tau(\nu)$ has the form

$$\tau(\nu) = \int_{u_1}^{u_2} \frac{S(T)\alpha_0(p/p_0)}{\pi\nu^2 + [\alpha_0(p/p_0)]^2} du \tag{9.25}$$

$$du = \frac{r}{g} dp = m dp \quad (m = \text{absorber 'mass'})$$

Also, assume the property

$$rS = \text{constant} \tag{9.26}$$

such as occurs for an isothermal atmosphere (S constant) with a uniformly mixed absorber (r constant). Then

$$\tau(\nu) = \frac{Srp_s}{\pi\alpha_o g} \int_{p_2}^{p_1} \frac{\tilde{p}}{(\nu/\alpha_o)^2 + \tilde{p}^2} d\tilde{p} \tag{9.27}$$

where $\tilde{p} = p/p_o$ and

$$\tau(\nu) = \eta \left[\log_e \left\{ \left(\frac{\nu}{\alpha_o} \right)^2 + p^{-2} \right\} \right]_{\tilde{\mu}_2}^{\tilde{p}_1} \qquad \eta = Su/2\pi\alpha_o$$

$$\mathcal{T}_\nu = e^{-\tau(\nu)} = \left(\frac{\nu^2 + \alpha_1^2}{\nu^2 + \alpha_2^2} \right)^{-\eta} \tag{9.28}$$

for $\alpha_i = \alpha_o \tilde{p}_i$. Figure 9.12 in Example 9.5, shows the comparison between the transmission derived according to Eqn. (9.28) with -η = 1 and the transmission calculated assuming the mean pressure $\tilde{p} = (p_1 p_2)^{1/2}$ in the homogeneous path formula

$$\tau_\nu = \frac{S}{\pi} \frac{\alpha_o(\tilde{p}/p_o)u}{\nu^2 + [\alpha_o(\tilde{p}/p_o)]^2}.$$

(b) Scaling Approximation

The simplest and most common way of dealing with nonhomogeneous paths is the 'scaling' or one parameter approximation. Let us start with the assumption that pressure and temperature effects on the absorption are separable according to

$$ku(p,T) = \Psi(\nu)\Phi(p)\chi(T) \tag{9.29}$$

Example of factorization: $\nu - \nu_o > \alpha_L$ as occurs in line wings, then

$$k_\nu = \frac{S\alpha_L/\pi}{(\nu-\nu_o)^2}$$

$$\Rightarrow \Psi(\nu) \sim \left(\frac{1}{\nu-\nu_o}\right)^2, \quad \Phi(p) \sim \frac{p}{p_o}, \text{ and}$$

$$\chi \rightarrow \left(\frac{T_o}{T}\right)^{1/2}$$

Then

$$\tau_\nu = \int_{u_1(p_1,T_1)}^{u_2(p_2,T_2)} k_\nu(p,T)du(p,T)$$

approximates to

$$\tau_\nu = \overbrace{\Psi(\nu)\Phi(p_o)\chi(T_o)}^{k_\nu(p_o,T_o)} \int_{u_1}^{u_2} \frac{\Phi(p)}{\Phi(p_o)} \frac{\chi(T)du}{\chi(T_o)} \approx k_\nu(p_o,T_o)\tilde{u} \tag{9.30}$$

where

$$\tilde{u} = \int \frac{\Phi(p)}{\Phi(p_o)} \frac{\chi(T)}{\chi(T_o)} du$$

It is generally assumed that

$$\Phi(p) \sim p^n$$

and

$$\chi(T) \sim (T)^{-m}$$

thus

$$\tilde{u} = \int \left(\frac{p}{p_o}\right)^n \left(\frac{T_o}{T}\right)^m du \tag{9.31}$$

Table 9.3 provides some often used values of *n* and *m* for various absorbing gases.

Table 9.3: Generally accepted values of n and m for various absorbing species.

Gas	Spectral Region	*n*	*m*
Water vapor		0.9-1	0.45
Carbon dioxide	Shortwave	1.75	11-8
Ozone		0	0
Water vapor	Longwave	0.5-0.9	0.45
Carbon dioxide		1.75	11-8
Ozone		0.4	0.2

It is generally assumed that there is no foundation for Eqn. (9.25) other than it seems to work. While this statement is generally true, we see in the strong absorption limit that the absorption coefficient actually factors in this way with $n = 1$.

(c) Two Parameter Approximations: The Van de Hulst - Curtis - Godson (VCG) Approximation

The previous method relies only on a scaling of the absorber amount to correct for path inhomogeneities. In general n varies depending on the absorption regime ($n = 1$ strong, $n = 0$ weak) and so is poorly defined in general. Obviously, a better and more sophisticated approach would be to employ two disposable parameters to simulate the absorption (e.g., u and n in the scaling approximation). The most useful two-parameter method proposed is the Curtis-Godson approximation, which attempts to define a scaled absorber amount specified for a mean pressure. The approach was developed independently by Curtis (1952) and Godson (1954) and earlier by Van de Hulst (1945) in a rather intriguing article (unfortunately in French)—thus I prefer to call the approximation VCG. The aim of the VCG approximation is to provide such a fit of the transmission. To discuss this approximation, consider isothermal paths (for convenience only). The criteria adopted are to match the absorptions exactly in the strong and weak limits. To proceed, we start with

$$\begin{aligned} \overline{\mathcal{A}} &= \frac{W}{\Delta\nu} = \frac{1}{\Delta\nu}\int_{\Delta\nu} 1-\exp\left[\int -k_\nu du\right] d\nu \\ &= \frac{1}{\Delta\nu}\int_{\Delta\nu} 1-\exp\left[\int Sf(\nu)du\right] d\nu \end{aligned} \tag{9.32}$$

- Weak limit

  We obtain the weak-line limit directly by considering the exponent in Eqn. (9.32) as it approaches zero

$$\widetilde{\mathcal{T}} = \int e^{-\int Sf(\nu)du} d\nu \approx \frac{1}{\Delta\nu}\int \left[1-\int Sf(\nu)du\right] d\nu \approx 1-\int Sdu$$

  Since $\int f(\nu)d\nu = 1$ for regular band models, α_i and S_i are constant over the interval chosen and thus the VCG approximation in this context states.

$$S\widetilde{u} = \int Sdu \qquad \text{(weak limit)}$$

  or

$$\widetilde{u} = \int du \tag{9.33a}$$

- Strong limit

  The strong-line limit follows in an analogous way to the derivation of the strong limit for homogeneous paths. For the inhomogeneous case, in the strong limit where $|\nu - \nu_o| >> \alpha_L$ then for a single line

$$\widetilde{\mathcal{T}} = \frac{1}{\Delta\nu}\int_{\Delta\nu} \exp\left[-\int \frac{S\alpha_L/\pi}{(\widetilde{\nu})^2} du\right] d\widetilde{\nu}$$

  where $\widetilde{\nu} = \nu - \nu_o$. If

$$x = \widetilde{\nu}\left[\int \frac{S\alpha_L du}{\pi}\right]^{-1/2}$$

  then

$$\widetilde{\mathcal{T}} = \frac{1}{\Delta\nu}\left[\int_u S\alpha_L/\pi du\right]^{1/2} \int_{\Delta x} \exp\left(-\frac{1}{x^2}\right) dx$$

  and since $\Delta\nu >> \alpha_L$, the integral limits are effectively infinite. Thus

$$\widetilde{\mathcal{T}} \sim 1 - 2\left[\int (S\alpha_L du)\right]^{1/2}$$

  and by matching the equivalent homogeneous limit, we obtain

$$\begin{aligned} \widetilde{\alpha}\widetilde{u} &= \int \alpha du \qquad \text{(strong limit)} \\ \widetilde{p}\widetilde{u} &= \int \widetilde{p} d\widetilde{u}. \end{aligned} \tag{9.33b}$$

Example 9.5: Band model example revisited. Suppose that the vertical distribution of absorber has the form $r(p) = r_s \bar{p}^3$ where $\bar{p} = p / p_s$. Then under the VCG approximation,

$$\tilde{u} = \int du = \frac{r_s p_s}{g} \int_0^1 \bar{p}^3 d\bar{p} = \frac{r_s p_s}{4g}$$

and that

$$\tilde{p}\tilde{u} = \int p du = p_x \int_0^1 \bar{p} du$$

since *du = rdp/g,*

$$\tilde{p}\tilde{u} = \frac{p_s^2 r_s}{g} \int_0^1 \bar{p}^4 d\bar{p} = \frac{r_s p_s^2}{5g}$$

and thus $\tilde{p} = 0.8 p_s$. Now this may be simply applied to either the Goody or Malkmus band models in the following way. Consider the Goody band model: for a uniform path

$$\mathcal{T}_{\text{Goody}}(u) = \exp\left[\frac{(-\sigma/\delta)u}{(1+\sigma u/\pi\alpha_L)^{1/2}}\right]$$

where for a nonuniform path

$$\mathcal{T}_{\text{Goody}}(\tilde{u}) = \exp\left[\frac{(-\sigma/\delta)\tilde{u}}{(1+\sigma\tilde{u}/\pi\alpha_{L,s}\tilde{p})^{1/2}}\right]$$

where $\alpha_{L,s}$ is the band line half width defined at pressure p_s. Using the parameters from our earlier example, with $\tilde{u}$ = 2.8 gcm^{-2} then

$$\mathcal{T}_{Goody}(\tilde{u} = 2.8) = \exp\left[\frac{-2.919 \times 2.8}{(1+2.919 \times 2.8/0.06 \times 0.8)^{1/2}}\right] = 0.536$$

compared to the homogeneous path value of 0.498.

Example 9.6: A test of the VCG. The accuracy of this approach can be tested for the hypothetical case considered above. Consider the atmospheric layer as shown below, which extends between pressure $p_1 \rightarrow p_2$. Set

$$p_2 = f p_1$$

then according to Eqn. (9.28)

$$\tau_\nu^{exact}(1,2) = \eta \ln\left[\frac{\nu^2 + \alpha_L(1)^2}{\nu^2 + \alpha_L(2)^2}\right]$$

which can be written in the form

$$\tau_\nu^{exact}(1,2) = \eta \ln\left[\frac{(\nu/\overline{\alpha}_L)^2 + 1/f}{(\nu/\overline{\alpha}_L)^2 + f}\right]$$

where $\overline{\alpha}_L$ is the mean half width defined as $\overline{\alpha}_L[\alpha_L(1)\alpha_L(2)]^{1/2}$. The VCG approximation expresses the optical thickness in the form

$$\tau_\nu^{VCG}(1,2) = \frac{S\widetilde{u}}{2\pi\widetilde{\alpha}_L}\frac{2}{(\nu/\widetilde{\alpha}_L)^2 + 1}$$

where $\widetilde{u}$ and $\widetilde{\alpha}_L$ are defined by Eqns. (9.33a) and (9.33b). It is straightforward to show that

$$\widetilde{u} = \frac{rp_1}{g}(1 = f)$$

$$\widetilde{\alpha}_L = \left(\frac{1+f}{2}\right)\alpha_L(1)$$

for the case considered here. Thus the optical thickness of the layer predicted by the VCG approximation in terms of f and $\overline{\alpha}_L$ is

$$\tau_\nu^{VCG}(1,2) = 2\eta\frac{(1-f)}{(1+f)}\frac{2}{(\nu/\widetilde{\alpha}_L)^2 + 1}$$

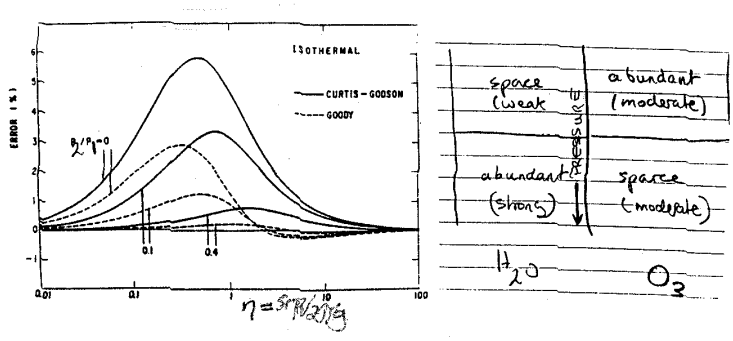

Fig. 9.12 Percentage error of the VCG for a single line and a constant mixing ratio for f = 0.

9.8 Problems

Problem 9.1

Briefly explain or interpret the following:

(a) Two sealed chambers contain the same amount of water vapor and are at the same temperature. One contains only water vapor, while the other holds a mixture of water vapor and air. Which has the smaller transmissivity averaged over a narrow spectral region containing a single water vapor absorption line?

(b) The two sealed cells of (a) now both contain some amount of water vapor mixed in air. The concentration of water vapor in one cell is adjusted so that the transmission of 10 μm radiation through one cell matches the transmission of 6.3 μm radiation through the other cell. Which cell contains the most water vapor?

(c) The temperature of both cells is now increased thus raising the pressure within the cell but assume no other changes occur. At which wavelength is the transmission a maximum (ignore any temperature effects on absorption)?

Problem 9.2

Develop a relationship between the vertically integrated water vapor path through the entire vertical extent of the atmosphere (precipitable water) and the sea surface temperature. Assume

(a) The vertical profile of specific humidity has the following form $q_s(p/p_s)^{\lambda}$ where q_s is the surface specific humidity.

(b) $e_s \approx b\exp[a(T_s - T_o)]$. Derive your answer in terms of the surface relative humidity, λ, and the SST T_S.

Problem 9.3

Compute the optical path for:

(a) Water vapor of a 100 mb thick homogeneous layer of mixing ratio r.

(b) Total atmospheric CO_2 if the mixing ratio is 330 ppm by volume.

Problem 9.4

The following function

$$r(\psi) = r_p \frac{4a\psi^2}{(1 + a\psi^2)^2}$$

reasonably resembles the vertical profile of ozone mixing ratio such that with a = 1600, the maximum occurs at $\psi = p/p_s = 0.025$. Assuming a value $r_p = 1 \times 10^{-5}$ kg/kg, derive the total column ozone and express your answer in Dobson units (the density of ozone at S.T.P. is 2.14 kgm^{-3}).

Problem 9.5

The rationale for the surface pressure measurement using two frequencies in the O_2 A band is discussed in Section 3.5. Given the definition of optical thickness, obtain an explicit form of the function $t(p_s)$ given in (3.41) assuming (1) a Lorenz line and frequencies at the line center ($\nu = \nu_o$), and (2) frequencies in the line wing $|(\nu - \nu_o)| >> \alpha_L$. Neglect the effects of atmospheric temperature on line intensity and half-width. Express your answers in terms of S, the line strength; α_o the line half width defined at some reference pressure p_o the mixing ratio r of the gas, p_{sat} the satellite pressure, and the acceleration by gravity g.

Problem 9.6

Absorption in the atmospheric window between 8 and 13 μm is represented by an absorption coefficient of the form $k_2 e$ where e is the water vapor pressure (in kPa), $k_2 \cong 10^{-1}$ (g cm^{-2})$^{-1}$ kPa^{-1}. If the water vapor pressure near the surface is 1 kPa, calculate (1) the transmission of a horizontal path 1 km long near the surface, and (2) the transmission of a vertical path of atmosphere assuming that the distribution of water vapor pressure is proportional to pressure units of atmospheres) raised to the fourth power.

Problem 9.7

The absorption coefficient in the continuum has the form

$$k_\nu \approx k_{2,\nu} e$$

where e is the water vapor partial pressure in units of atmosphere. Assuming a hydrostatic atmosphere

$$p = p_s e^{-z/H}$$

where p_s = 1013.13 mb, and assuming that the mixing ratio profile of water vapor is similarly exponential with

$$H_r = H/3$$

where H_r is the scale height of vapor

(a) Derive an expression for the optical mass u for the vertical path from $\tilde{p} = 0$ to $\tilde{p}$ where $\tilde{p} = p / p_s$ is the pressure in atmospheres. Express your answer in terms of r_s, the surface mixing ratio of water vapor, and $\tilde{p}$.

(b) Assume that the temperature dependence of the absorption parameter $k_{2,\nu}$ has the form

$$k_{2,\nu} = k_{2,\nu,s} / \tilde{p}$$

show that

$$\mathcal{T}_\nu = \exp[-\beta \tilde{p}^7]$$

where

$$\beta = \frac{p_s r_s^2 k_{2,\nu,s}}{4.354 g}$$

where $e = r\tilde{p} / 0.622$.

Problem 9.8

Assume the following profile for water vapor mixing ratio:

$$r = r_s e^{-3z/H}$$

Calculate the broadband water vapor absorption of solar radiation in 10 adjacent 100 mb thick layers from the top of the atmosphere (0 mb) to 1000 mb and plot this absorption as a function of the mean layer pressure.

(a) Contrast the vertical profiles of absorption assuming the following values of r_s: 5.4, 10.2 and 18.4 gkg^{-1}.

(b) Calculate the Planck weighted broadband flux absorption using a Goody band model and the parameters given in Table 4.4 (p. 11) for the rotation band and the vibration band. Calculate this transmission for a path extending through the column for the model atmosphere of 1 above (do only for r_s = 10.2 gkg^{-1}). Assume T = 270 K in calculating the Planck Function.

(b) Calculate the broadband transmission as in (2) above but for a path extending up from a reference level located at 800 mb to the top of the atmosphere and for a path extending downwards from this reference level to the surface. Plot these transmissions as a function of either pressure or altitude (your choice).

AT622 Section 10
The Atmospheric Absorption Spectrum

The aim of this section is introduce the characteristics of the atmospheric absorption spectrum as summarized in Fig. 10.1.

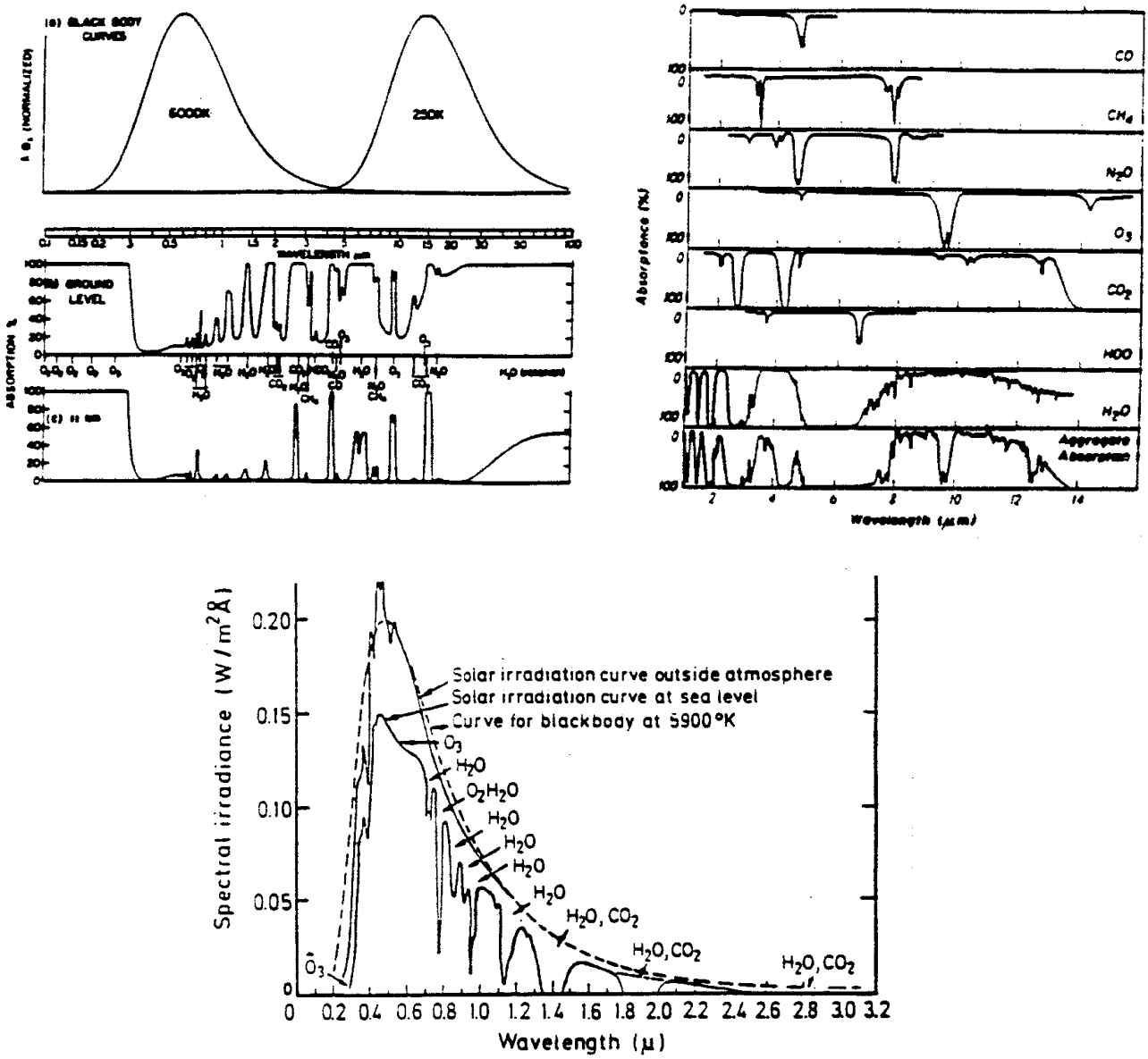

Fig. 10.1 (a) The broad characteristics of the atmospheric absorption spectrum. (b)The spectrum of solar flux between the ultraviolet and infrared with molecular absorption features indicated.

10.1 Visible - UV

Atmospheric absorption calculations in the visible and UV spectrum are commonly done on the basis of empirical data and at a level without requiring the degree of understanding applied to vibration-rotation

bands. Figure 10.2 shows the absorption by O_2 and O_3 by electronic transitions. It doesn't show the near UV Huggins bands of the visible Chappuis bands of O_3. Both of these electronic bands are of some importance to solar absorption but the absorption is weak.

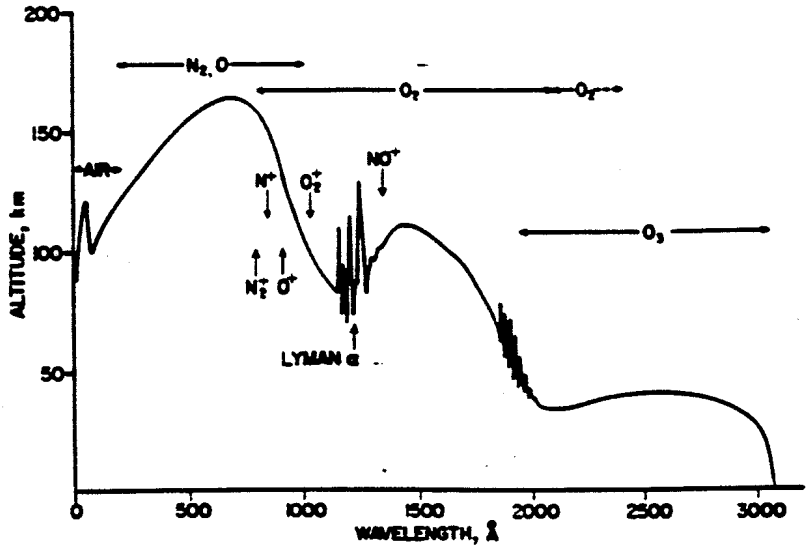

Fig. 10.2 Depth of penetration, defined as altitude at which $\tau = 1$ of solar radiation in the ultraviolet spectrum as a function of wavelength. The line shows the altitude of unit optical depth. The vertical arrows indicate ionization limits. The broken line represents predissociation for molecular oxygen. After Herzberg (1965).

10.2 The Near IR

The predominant absorption of near infrared wavelengths (0.7-4.0 μm) is by several vibrational-rotational H_2O absorption bands. CO_2 also contributes to near IR absorption by bands centered at 2.7 and 2.0 μm and weak bands at 1.6 and 1.4 μm. These features appear in Fig. 10.1b.

10.3 The Far IR

Again the most dominant absorption in the far IR is that of water vapor. Figure 10.3 shows the H_2O absorption spectra based on use of a theoretical line shape. Superimposed on this absorption is the absorption centered at 15 μm and at 4.4 μm by CO_2 and weaker bands at 10 and 5 μm. Ozone has a strong vibration-rotation band centered at 10.6 μm and a weaker band at 14 μm.

10.4 'Greenhouse Gases'

A variety of trace gases absorb in the far infrared and may be considered as greenhouse gases (e.g., CH4, ... etc.) and the prevalence of the absorption by these gases is highlighted in Fig. 10.4.

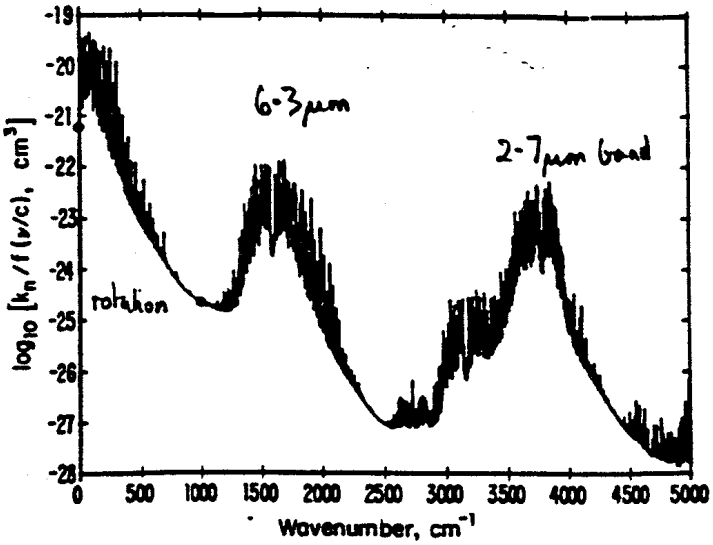

Fig. 10.3 Theoretical absorption coefficients of pure water vapor at 1 bar and 296 K. The vertical axis is the molecular absorption coefficient divided by a "radiation term", $f(v/c) = (v/c)\tanh(hv/2k\theta)$, which is approximately equal to v/c (the frequency in wave numbers) for v/c > 500 cm^{-1}. After Clough et al. (1980).

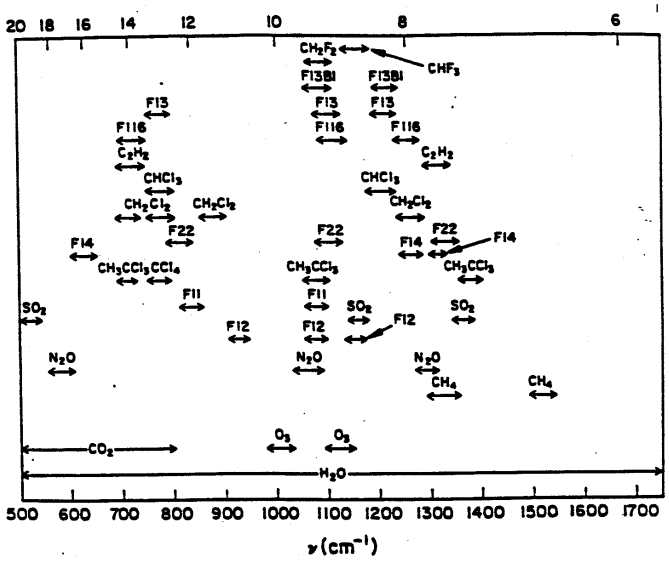

Fig. 10.4 Some general properties of absorption by greenhouse gases.

Molecule	Lifetime (years)	Concentration (ppbv)	Spectral Range (cm^{-1})	Band Strength ($cm^{-2}atm^{-1}$) at 296K
CO_2	2	3.39×10^3	550-800	220
O_3	0.1-0.3	variable	950-1200	312
N_2O	120	300	1200-1350	218
CH_4	5-10	1650	950-1650	134
$CFCl_3$ (CFC11)	65	0.18	800-900	1828
CF_2Cl_2 (CFC12)	110	0.28	875-950	1446
CF_3Cl (CFC13)	400	0.007	1075-1125	1758

10.5 Water Vapor Continuum Absorption

An especially important form of absorption for atmospheric problems is the more or less continuous absorption in regions where line absorption is weak. The continuum occurs at all frequencies (Fig. 10.3) but is most important in window regions in which continuum absorption exceeds line absorption.

The absorption in these windows has special properties such that

$$k_\nu = k_1 p + k_2 e$$

where p = atmospheric pressure, e = water vapor partial pressure, and $k_2 > k_1$. Thus,

$$k_\nu \sim k_2 e$$
$$\tau_\nu \sim \int k_2 e du$$

This is called "e-type"' absorption. The mechanism for this absorption is not decisively known at this time.

Mechanism?

- Overlapping foreign broadened lines, but

$$k_\nu \sim \frac{S\alpha_L^f / T}{(\nu - \nu_o)^2} \sim k_2 e$$

  in wings. This was the historical explanation. It was discovered however that continuum absorption was much stronger than this (especially in the tropics)

- Overlapping self broadened lines (water-water collisions)?

$$k_\nu \sim \frac{S\alpha_L^s / \pi}{(\nu - \nu_o)^2} \sim k_2 e$$

  since α_L^s proportional to e.

- Dimer absorption?

  Temperature variation is the reverse of line absorption and has the approximate form

$$\Phi(T) = \exp(1800 / T)$$

  Roberts provides a parameterization of k_ν such that

$$k_\nu(p,T) = \frac{\Phi(T)}{\Phi(T_o)} \Psi(\nu, T_o) e$$

where

$$\Psi = 4.18 + 5578\exp(-0.00787\nu)\mathrm{g}^{-1}\ \mathrm{cm}^{-2}$$

for T_o = 296 K with ν in crn^{-1}.

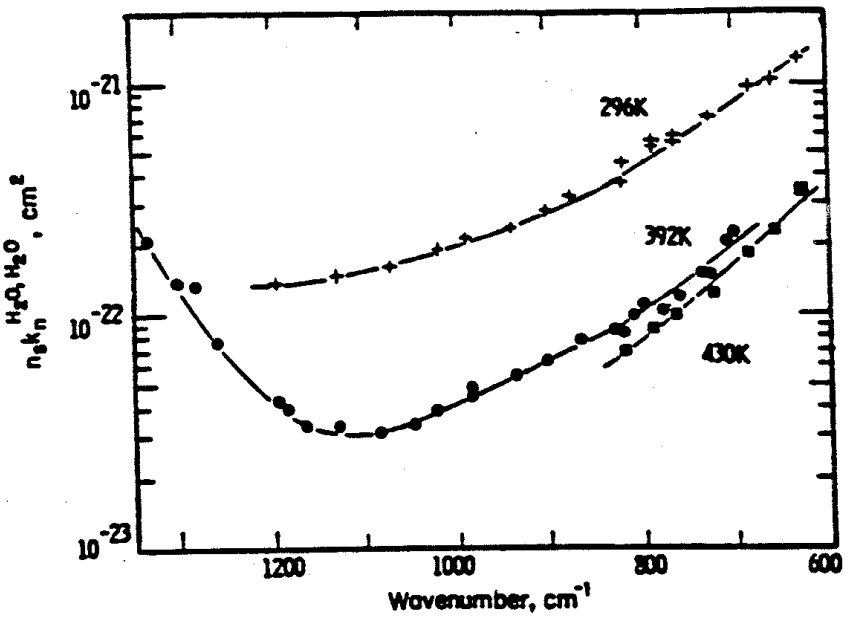

Fig. 10.5 Absorption coefficients for water-water collisions in the 1000 cm^{-1} window. n_s is Loschmidt's number.

AT622 Section 11
Broadband Infrared Fluxes

The aim of this section is to introduce the more common, approaches to solving broadband infrared radiative transfer. This will culminate in Section 11 in an understanding of the factors that define the long wave radiative heating and cooling in a cloud free atmosphere.

11.1 A Return to the Radiative Transfer Equation

Here we employ the radiative transfer equation developed previously in Section 4 for an absorbing and emitting horizontally stratified atmosphere

$$I(\tau,+\mu) = I(\tau^*,\mu)e^{-(\tau^*-\tau)/\mu} + \int_{\tau}^{\tau^*} B(t)e^{-(t-\tau)/\mu}\frac{dt}{\mu} \tag{11.1a}$$

for $0 < \mu < 1$ which defines radiation that upwells from the atmosphere, and

$$I(\tau,-\mu) = I(0,-\mu)e^{-\tau/|\mu|} + \int_{0}^{\tau^*} B(t)e^{-(\tau-t)/|\mu|)}\frac{dt}{|\mu|} \tag{11.1b}$$

for $0 > \mu > -1$ for downwelling radiation. We now develop this equation in flux form and seek to solve it when it is integrated spectrally.

11.2 Flux Equations and the Infrared Emissivity

It is trivial to transform Eqns. (11.1a) and (11.1b) from an equation of intensity into a radiative transfer equation for flux. First introduce

$$\mathcal{T}(t,\tau,\mu) = \exp[-(t-\tau)/\mu] \rightarrow T^f(t,\tau,\mu) = \exp[-\beta(t-\tau)]$$

where $\beta = 1.66$ is the diffusivity factor, then

$$F_\lambda(\tau) = F_\lambda(\tau^*)\mathcal{T}_\lambda^f(\tau,\tau^*) + \int_{\tau^*}^{\tau} \pi B(t)dT^f(t,\tau)$$

or equivalently

$$\begin{aligned} F_\lambda^+(z) &= F_\lambda^+(z=0)\mathcal{T}^f(0,z) + \int_0^z \pi B_\lambda(z')\frac{d\mathcal{T}^f}{dz'}(z',z)dz' \\ F_\lambda^-(z) &= \int_\infty^z \pi B_\lambda(z')\frac{d\mathcal{T}^f}{dz'}(z,z')dz' \end{aligned} \tag{11.2}$$

Broadband fluxes are then obtained by

$$F^{\pm}(z) = \int_0^{\infty} F_{\lambda}^{\pm}(z)d\lambda \tag{11.3a}$$

In evaluating the fluxes via the radiative transfer equation (11.2) and subsequently integrating these fluxes over the entire IR spectrum, four basic λ scales of dependence need to be resolved (Fig. 11.1)

- slow λ variation of B_{λ}
- the unresolved contour of absorption bands
- line structure, separation, etc.
- the finest scale on which Lambert's Law (and thus on which the RTE) applies.

The usual strategy to accommodate these variations is to:

1. Resolve Planck variation by dividing the spectrum into N discrete intervals (typically ranging from 4-20 intervals). Models at this resolution are referred to as coarse or wide band models).

2. Develop a model of the transmission function for each of these intervals. This can be done using a band model or the *k*-distribution model of transmission

3. The broadband fluxes are then obtained for example by summing over all N intervals, namely

$$F \approx \sum_{i}^{N} F_i \Delta\lambda_i \tag{11.3b}$$

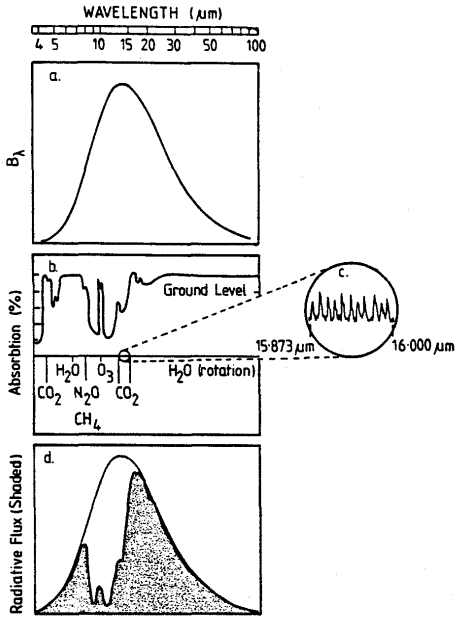

Fig. 11.1 Schematic of the various frequency scales encountered in the calculation of atmospheric longwave flux. These scales refer to (a) the Planck curve, (b) atmospheric gaseous absorption spectrum for longwave radiation reaching the ground, (c) higher resolution spectral absorption highlighting individual lines and line separations, and (d) the convolution of the absorption spectrum and the Planck function to give atmospheric flux (shaded area).

(a) Emissivity Approaches

Obviously the problem of calculating flux can be significantly simplified by keeping the number of spectral intervals to a minimum. An approach designed to do this is the emissivity method, which in principle seeks to reduce N → 1.

If we note that

$$\mathcal{T}_\lambda^f(z,z') = 1 - A_\lambda(z,z')$$

then

$$F^+(z) = \int_0^\infty \pi B_\lambda(z)[1 - A_\lambda(0,z)]d\lambda + \int_0^\infty d\lambda \int_z^0 \pi B_\lambda(z') \frac{dA_\lambda}{dz'}(z,z')dz'$$
$$F^-(z) = \int_0^\infty d\lambda \int_z^\infty \pi B_\lambda(z') \frac{dA_\lambda}{dz'}(z,z')dz'$$

Define

$$\varepsilon(z,z') = \frac{1}{\sigma T^4} \int_0^\infty A_\lambda(z,z')\pi B_\lambda(T)d\lambda$$

as the "emissivity" (note this is a function of temperature in principle), then

$$F^+(z) = \sigma T_g^4(1 - \varepsilon(0,z)) + \int_z^0 \sigma T^4(z') \frac{d\varepsilon}{dz'}(z',z)dz'$$
$$F^-(z) = \int_z^\infty \frac{d\varepsilon}{dz'}(z,z')\sigma T^4(z')dz' \qquad (11.4)$$

The approach is then to estimate the value of the absorption path u defined along the path (z, z') and deduce the value of ε from an *a priori* relationship between ε and u. Examples of such relationships are given in Figs. 11.2a and 11.2b. The latter shows the emissivity for three broad spectral regions and indicates how the temperature dependence reverses from one region to another to produce a much weaker dependence on the broadband emissivity.

(b) Illustrating the Emissivity Approach

Consider an n-layer atmosphere as shown in Fig. 11.3. Suppose we require to calculate the up- and downwelling broadband fluxes at some level between layer m and $m + 1$ (i.e., at level $m + 1$). For illustration, consider the contributions to the upwelling flux by the ℓ^{th} layer as illustrated. In calculating this contribution, we consider two basic approaches;

- Use Eqn. (11.1). The first step is to establish the path length. For example, the path length extending from level ℓ to level $m + 1$ is

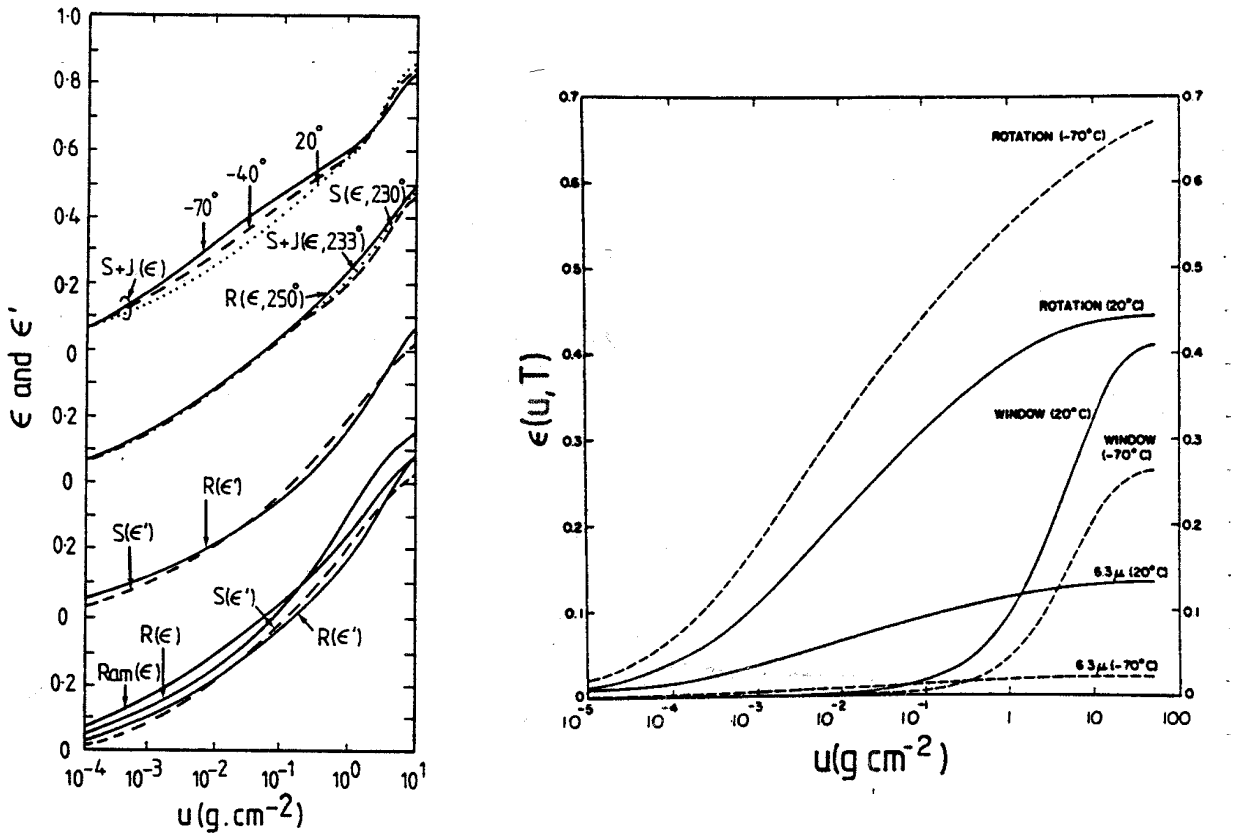

Fig. 11.2 (a) The emissivity ε and the modified emissivity ε′ as a function of water vapor path u. These relationships are taken from a variety of sources. R. Rodgers (1967), S. and J. Staley and Jurica (1970), RAM-Ramanathan et al. (1983), S. Sasamori (1969). The upper curves show ε for three different temperatures and the lower curves show comparisons of ε and ε′. (b) The contributions to the total water vapor gray body emissivity by three broad spectral regions, which include the water vapor rotation band, 6.3 μm band and the atmospheric window (excluding e-type absorption). These contributions are shown as a function of u (of $\bar{u}$ as the case may be) for two different temperatures (from Staley and Jurica, 1970).

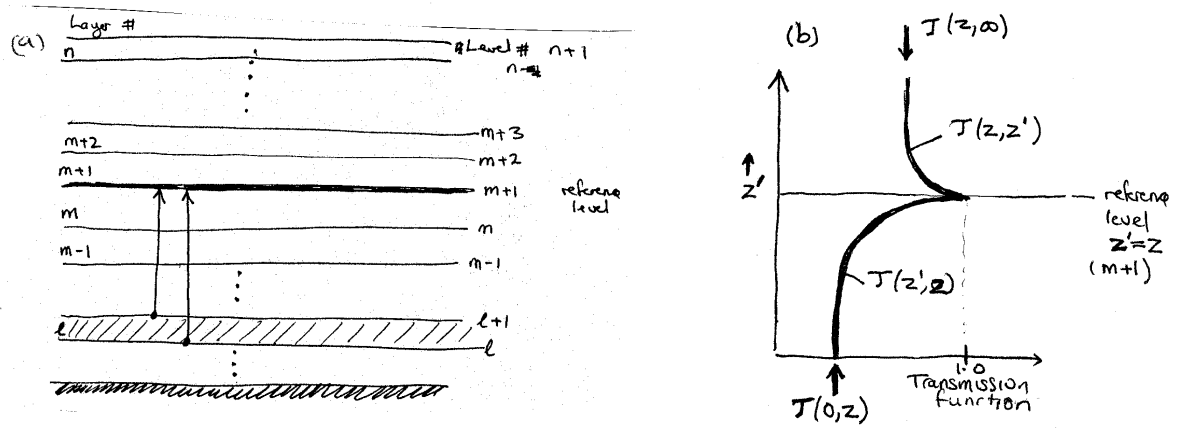

Fig. 11.3 (a) An illustration of an emissivity flux calculation. (b) The cusp in the transmission function with a discontinuity at level m + 1.

$$u_+ = u(\ell)\left(\frac{\bar{p}(\ell)}{p_o}\right)^n + u_-$$

where

$$u_- = u(\ell+1)\left(\frac{\bar{p}(\ell+1)}{p_o}\right)^n + \ldots + u(m)\left(\frac{\bar{p}(m)}{p_o}\right)^n$$

where the overbar on pressure denotes the layer average, and the power n is the scaling factor (note we again neglect temperature here for simplicity). The contribution to the broadband upwelling flux at $m + 1$ by the ℓ^{th} layer is

$$\Delta F^+(m+1,\ell) = \sigma\bar{T}^4(\ell)[\varepsilon(u_+) - \varepsilon(u_-)]$$

and the total flux follows as

$$F^+(m+1) = \sum_{\ell=1}^{m} \Delta F^\dagger(m+1,\ell)$$

- An alternative approach is to integrate Eqn. (11.1) by parts to obtain

$$\begin{aligned} F^+(z) &= \sigma T_g^4 + \varepsilon(0,z)(\sigma T_+^4 - \sigma T_g^4) + \int_0^z \varepsilon(z',z)\frac{d\sigma T^4(z')}{dz'}dz' \\ F^-(z) &= \sigma T_\infty^4(1-\varepsilon(z,\infty)) + \int_\infty^z e(z,z')\frac{d\sigma T^4(z')}{dz'}dz' \end{aligned} \qquad (11.5)$$

where T_∞ is usually set to zero and where T_+ is the air temperature just above the surface (and allows for a temperature jump there). The contribution to the flux at $m + 1$ is thus

$$\Delta F^\dagger(m+1,\ell) = \varepsilon(u)[\sigma T^4(\ell-1) - \sigma T^4(\ell)]$$

where u is the scaled path extending from the mid-point of the ℓ^{th} layer to the $m + 1$ level. This is usually the preferable way to evaluate the integral term as $\Delta\sigma T^4$ is known more accurately in principle than is $\Delta\varepsilon$ (i.e., this implies that the temperature variation with z is better known than is the variation of q with z).

There are two important issues to bear in mind in performing these calculations. First, calculation of the flux at each level requires the evaluation of the transmissivity/emissivity for all n levels. Thus the computation of the flux profile therefore goes as n^2. The second point is that no matter which approach is taken, the integration through the adjacent most layer (i.e., the m^{th} layer for the example considered here for upwelling radiation) should be performed by dividing the layer into sublayers to resolve the cusp (Fig. 11.3a) in the transmission function (note that $\mathcal{T}(z, z') = 1 - \varepsilon(z, z')$). Both issues pertain to band model schemes as well as emissivity schemes.

Example 11.1. The emissivity of the atmosphere. Consider a single isothermal layer atmosphere of temperature T_1 overlying a black surface radiating at a temperature T_g. The temperature of this surface is maintained through absorption of solar radiation by an amount $Q_o(1 - \alpha)/4$ and the atmosphere is transparent to this radiation. Assuming the atmosphere, planet, and surface are in radiative equilibrium, we seek to estimate the emissivity of the atmosphere and T_1 that give rise to the T_g = 288 K for Q_o = 1370 Wm^{-2} and α = 0.3.

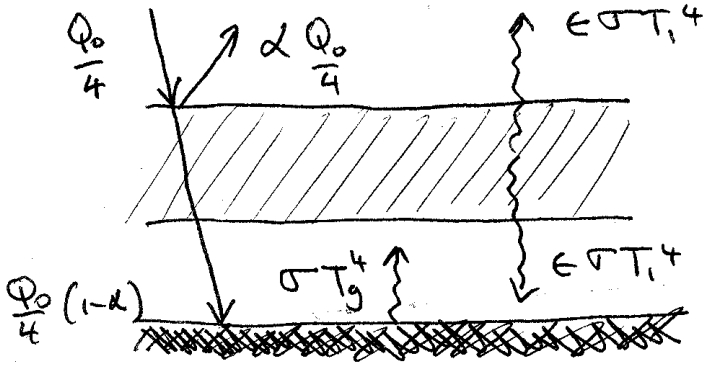

From Eqn. (11.1) it follows that the outgoing longwave radiation at the top of the atmosphere simplifies to

$$F^+(z=\infty) = \sigma T_g^4(1 - \varepsilon(0,\infty)) + \varepsilon(0,\infty)\sigma T_1^4$$

and the radiative equilibrium condition at the top of the atmosphere is

$$\frac{Q_\odot(1-\alpha)}{4} = \sigma T_g^4(1-\varepsilon) + \sigma T_1^4\varepsilon$$

where we simply write ε for $\varepsilon(0,\infty)$. The equilibrium condition for the atmosphere is

$$T_g^4 = 2T_1^4$$

and it follows that T_1 = 242 K for T_g = 288 K. The equilibrium at the surface is

$$\frac{Q_\odot(1-\alpha)}{4} + \varepsilon\sigma T_1^4 = \sigma T_g^4$$

where the second term of the left-hand side is the atmospheric emission to the surface. Rearrangement gives

$$\varepsilon = 2\left[1 - \frac{Q_\odot(1-\alpha)}{4\sigma T_g^4}\right]$$

and a value ε = 0.78 [Compare this with the value you estimate from Fig. 11.2 assuming 2.8 gm^{-2} for a global mean value of u.]

(a) Overlapping Gases in the Emissivity Approach

REF: Staley and Jurica, 1970: *J. Appl. Met.* When two overlapping gases, such as CO_2 and H_2O, absorb in the same spectral region, the combined transmission may be written as the product

$$\mathcal{T}_{over} = \mathcal{T}_{CO_2} \times \mathcal{T}_{H_2O}$$

provided the transmission function for each species is of a pure exponential form (as applies to the random band model). For broadband emissivity,

$$\mathcal{T} = 1 - \varepsilon$$

and, since ε is not a simple exponential function of path u (c.f., Fig. 11.2), the following is NOT true

$$T_{over} = [1 - \varepsilon(u_{H_2O})] \times [1 - \varepsilon(u_{CO_2})].$$

An approach to treat this type of overlap in the framework of emissivity models is to define the emissivity of the combined path

$$\varepsilon(u_{H_2O} + u_{CO_2}) = \varepsilon(u_{H_2O}) + \varepsilon(u_{CO_2}) - \Delta\varepsilon(u_{H_2O}, u_{CO_2})$$

where $\Delta\varepsilon$ is an overlap correction factor.

11.3 Intercomparison of Different Methods and Some Selected Results

Performances of both emissivity and coarse band models were tested as part of an international intercomparison program, the Intercomparison of Radiation Codes for Climate Models (ICRCCM). The results of these intercomparisons are summarized in a special issue of *J. Geophys. Res.,* **96**, D5, 1991.

(a) Features of the Clear-Sky Results (Ellingson, et al. 1991)

The range of in-model flux calculations and the manner by which these have changed over the course of ICRCCM is given in Fig. 11.4a through a comparison of the 1984 (open) and 1988 (shaded) distributions of downward fluxes at the surface relative to line-by-line calculations. The LBL calculations are from the Fels-Schwarzkopf (GFDL) model, and the MLS profile with all of the constituents (i.e., H_2O, O_3, and 300 ppmv CO_2) was used as input to all models. For this case, the 1988 data show nine more non-LBL models that agree to within ±2% of the GFDL LBL results, seven of these being from new participants. Of the 22 climate model type calculations for this case, 13 are within the ±2% range, and all but one fall within the ±6% range. On a percentage basis, 67% of the 1998 non-LBL model results agree to within ±2% of the LBL results as compared with 58% in 1984. Similar results hold for the net flux comparisons at the tropopause and the upward flux at the top of the atmosphere for this atmospheric profile.

The increase in the fraction of models agreeing closer with the LBL results also holds for the change of the net flux between the surface and tropopause (13 km), denoted ΔF_{net}, as illustrated in Figure. 11.4b. The 1988 data find more than twice the number of models agreeing with the LBL results to within ±2% than the 1984 data. About 82% of the 1988 and 75% of the 1984 model data agree with the LBL results when the range for agreement is increased to ±6%, or a rate of temperature change of about ±0.1 K/d.

However, only 60% of the climate model type calculations fall within this ±6% range. It should be noted that comparisons of vertical profiles of flux divergence have not been examined in detail, but our experience with the 1984 data suggest that much larger differences than those noted above will be found in some layers.

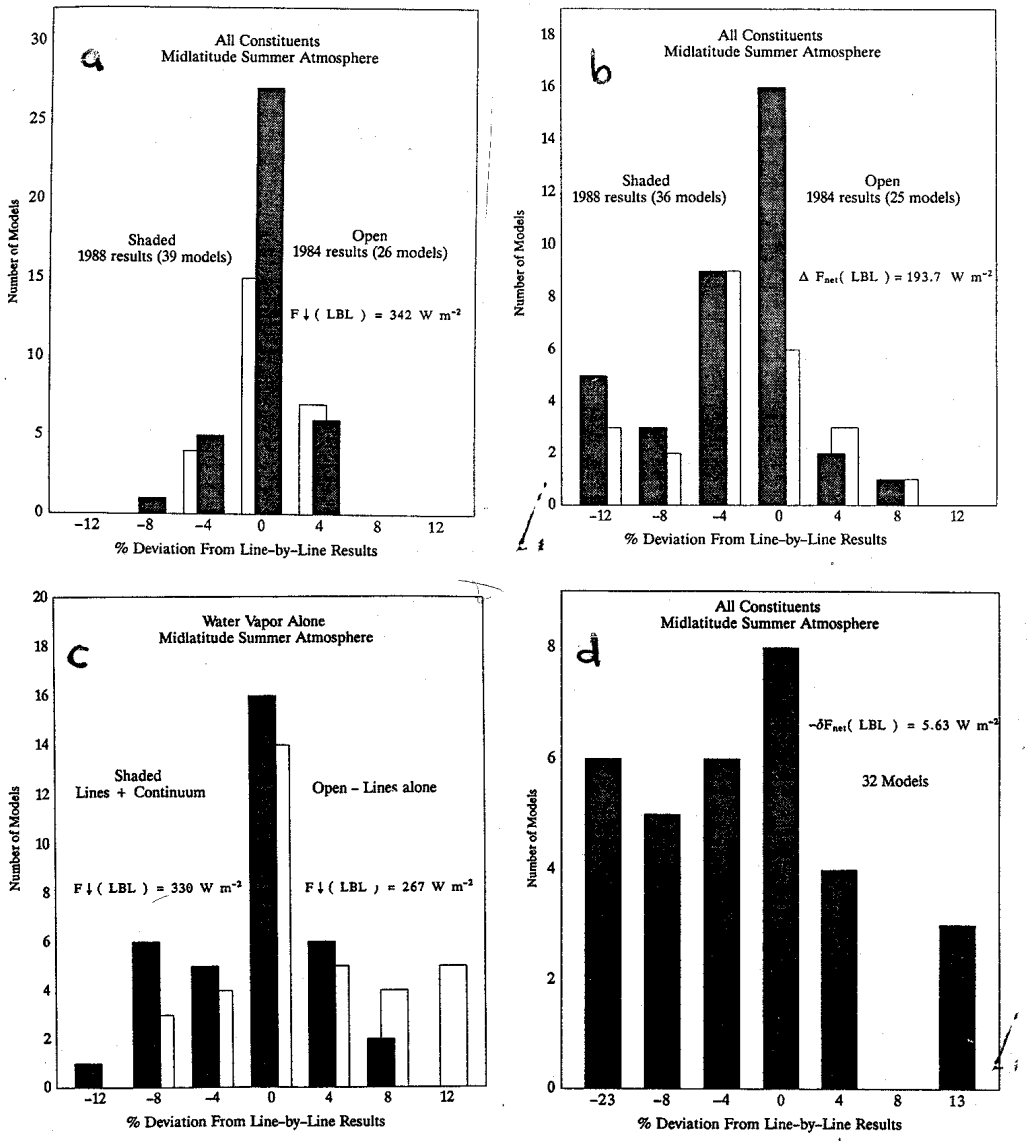

Fig. 11.4 (a) Comparison of 1984 (open) and 1988 (shaded) distributions of downward fluxes relative to a LBL calculation. (b) The flux divergence of the troposphere (0-13) km. (c) The 1988 distributions of downward flux differences relative to a LBL result with vaporlines only (open) and lines plus continuum (shaded). (d) Change in the net flux at the tropospause after doubling CO_2 from 300 ppmv relative to the LBL calculation.

Although Fig. 11.4a and b give some confidence in the general ability of the less detailed models to reproduce the gross features of the line-by-line results, this confidence is shaken somewhat when we examine the results when H_2O is the only absorbing gas as shown in Fig. 11.4c. When only the local lines of H_2O are included in the downward flux calculations more than half of the results are outside of the ±2% range, which was also seen in the 1984 data (not shown). The continuum masks many of the very

large positive differences, but it also amplifies many of the large negative ones. In general, the effect of the continuum and the overlap of different species tends to mask many of the large differences between absorption parameterizations of individual gases. Although this masking reduces the range of flux values expected from absorption differences alone, it also prohibits extending the range of agreement of this study to significantly different atmospheric conditions.

One of the major areas of study for ICRCCM was the sensitivity to changes in the concentration of the major absorbers, particularly CO_2. An important quantity calculated in CO_2 doubling studies is the change in the net flux at the tropopause as CO_2 doubles, denoted as δF_{net}. Figure 11.4d shows the distribution of δF_{net} relative to the LBL calculations clear-sky MLS conditions. The LBL models agree on this result to about ±1% of 5.6 Wm^{-2}. However, the various band model results differ by up to 50% of this value. Of the 17 codes actually used in climate models, six fall within ±5% of the LBL results, and one differs by more than 25%. The close agreement with LBL results for some of these models is not surprising because of tuning.

11.4 Flux Profiles

Figure 11.5a shows the vertical profile of the change in net upward longwave, net downward shortwave and total flux due to doubling the amount of CO_2. The solar flux change ΔS is negative due to enhanced absorption by CO_2, and the longwave flux change ΔF is positive indicating enhanced emission of approximately 1 Wm^{-2}.

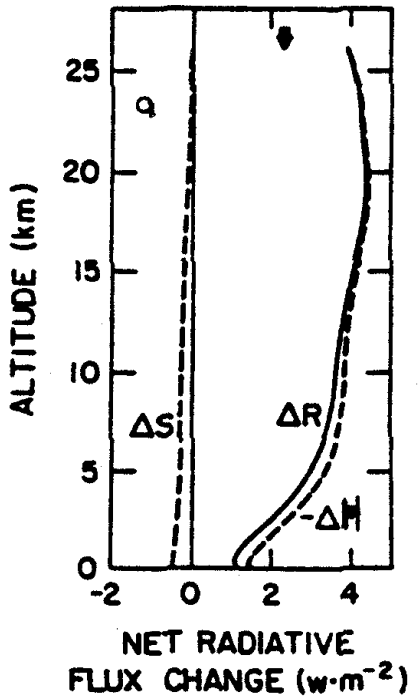

Fig. 11.5 Effect of CO_2 doubling on net radiative fluxes at 30°N. S is the net downward solar flux, F the net upward IR flux, and R = S – F is the net downward radiative flux. The symbol Δ preceding a quantity denotes a change in the flux due to doubling of CO_2. The arrow indicates the value at the top of the atmosphere for ΔR.

11.5 TOA Clear Sky Longwave Fluxes

Slingo and Webb (1992) apply a 10 cm^{-1} band model, together with data from the operational archive at the European Centre for Medium Range Weather Forecasts (ECMWF) to simulate the clear sky o1r. Temperature and specific humidity data on 19 model levels were directly incorporated into the simulations along with analyzed surface pressure. The radiation model is constructed around a high spectral resolution radiative transfer model (Shine, 1991) that incorporates the ECMWF analyses from the operational archive. The accuracy of the radiation model employed by SAMSON was checked using a single column version applied to ICRCCM test profiles (Ellingson et al., 1991). Calculations of clear sky outgoing longwave radiation (hereafter represented as F_∞) for five standard atmospheres with effects of water vapor, carbon dioxide, and ozone differed from line-by-line calculations of F_∞ by approximately 1 Wm^{-2} suggesting excellent agreement with these reference calculations (Slingo and Webb, 1992). Comparison of clear sky values of F_g depend to a small extent an the specific details of how the continuum absorption is dealt with in the model. The treatment of the continuum is described by Shine (1991) and is based on the far wing treatment of Clough et al., (1986). Variations of the treatment of this continuum can introduce uncertainties in calculations of the surface flux up to 10 Wm^{-2} (Ellingson et al., 1991). SAMSON simulations of F_g agreed with reference ICRCCM calculations of this flux within 3 Wm^{-2}.

Simulations of the monthly mean clear sky fluxes over the ice-free oceans were carried out for the period March 1989 to February 1989, which is also a period for which both ERBE and SSM/I observations are available. As in the original Study of Slingo and Webb (1992), these simulations apply to a horizontal resolution of 5 degrees. The radiation code applied to each daily analyses (a mean of four 6-hourly analyses for each day) and then averaged to produce the monthly mean flux distributions, which are used in the analyses described below. Both Slingo and Webb (1992) and Webb et al. (1993) discuss the differences between the simulated fluxes from SAMSON and the clear-sky values of F_∞ obtained from ERBE. Figure 11.6a presents examples of scatter diagrams of the SAMSON F_∞ versus the ERBE F_∞ for April, July and September 1988 and January 1989 to highlight some gross features of these comparisons. For instance, a slight positive bias of 3-5 Wm^{-2} exists between the SAMSON and ERBE fluxes, a bias similar in both sign and magnitude to that of the ERBE clear sky flux data (Harrison et al. 1988). As Webb et al. (1993) show, there are regions (not shown) where the differences between the simulated fluxes and ERBE derived fluxes exceed this small bias, such as over the areas of marine boundary layer clouds off the west coasts of the major continents where differences may be as large as 10 Wm^{-2} (Fig. 11.6b). These areas can be traced to biases in the ECMWF water vapor data (e.g. Liu et al., 1992; Stephens and Jackson, 1994) as highlighted in the difference between TOVS and SSMI column water vapor.

11.6 Longwave Fluxes at the Surface - A Satellite Retrieval

In Section 4, we derived a relationship between the longwave flux to the surface and the OLR (Eqn. (4.16c)). With arguments similar to those introduced in Section 6.2(b), we introduce the relationship (rearrangement of Eqn. (4.16c)),

$$\mathcal{F} = \frac{F_g}{F_\infty} = b\tau_s \tag{11.6}$$

and suppose that a simple relation exists between $\mathcal{F}$ and precipitable water w of the form

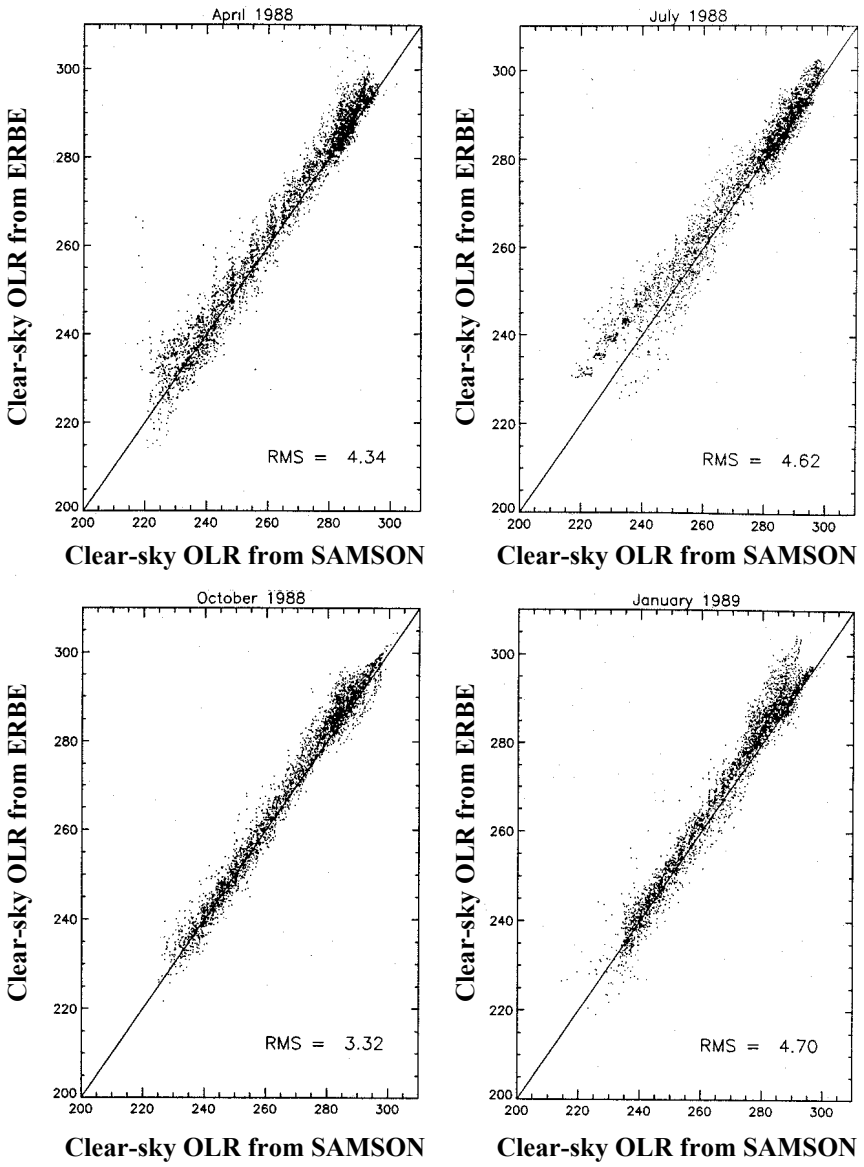

Fig. 11.6 (a) Scatter diagrams of SAMSON simulated F_∞ versus ERBE analyses of clear-sky longwave fluxes for April, July and September, 1988, and January 1989. (b) Comparison of the OLR difference between ERBE and the ECMWF simulation (upper) and the TOVS precipitable water and SSM/I precipitable water (lower).

$$\mathcal{F} = a_2 + c_2 w \tag{11.7}$$

in an entirely analogous way to Eqn. (6.5) where a_2 = 0.937 and c_2 = 0.0102 $kg^{-1}m^2$**.** Unfortunately, we do not have global observations of F_g and thus we cannot derive $\mathcal{F}$ solely from independent observations to test this relationship. The relationship between predicted fluxes and w is shown in Fig. 11.7

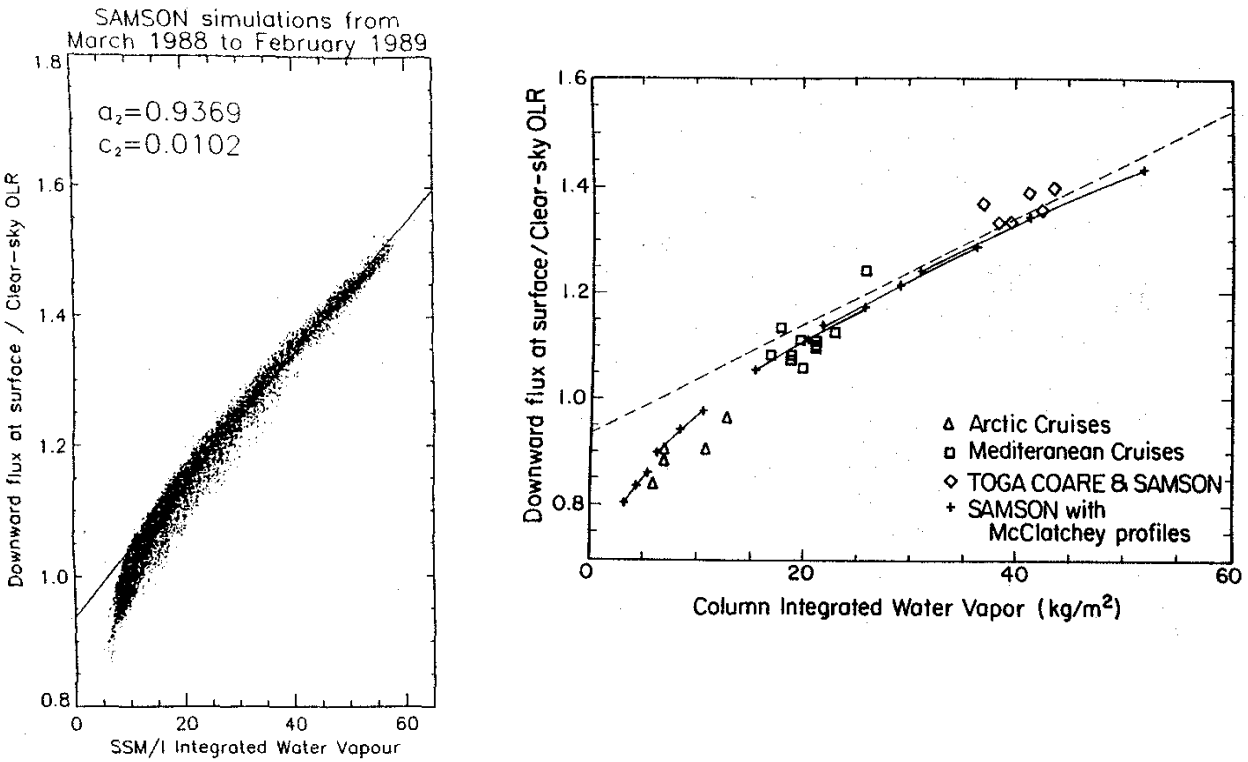

Fig. 11.7 The flux ratio $\mathcal{F}$ derived from combined simulations of January and July fluxes as a function of w.

Except for particular regions, the simulations of clear sky F_∞ from SAMSON generally agree with ERBE estimates of this flux to within 5-10 Wm^{-2}, which is considered to be of the same order of uncertainty as the latter. There are also no *a priori* reasons to expect the simulations of clear-sky F_g to be grossly in error although how the specific details of how the continuum absorption is modeled may introduce an uncertainty of the order of 10 Wm^{-2}. Bearing this possibility in mind, simulated distributions of F_g over the ice-free oceans are presented in Figs. 11.8a and b in the form of the surface net flux (i.e., $\sigma T_s^4 - F_g$ F,,). The distributions in Figs. 11.8c and d were derived from satellite distributions of *w* and OLR and the specified relationship that best fits the data in Fig. 11.7. The maps of the surface net flux derived by this approach and are presented here for comparison with actual model simulations shown in Figs. 11.8a, and b and match the simulations to ±6 Wm^{-2}.

The smallest net fluxes of around 40-50 Wm^{-2} occur in the tropical convergence zones over the Pacific and Indian Oceans and in the Northwest Pacific in July. A significant annual variation close to the northern continents also appears to exist which is associated with changes in the atmospheric circulation associated with the summer and winter monsoons.

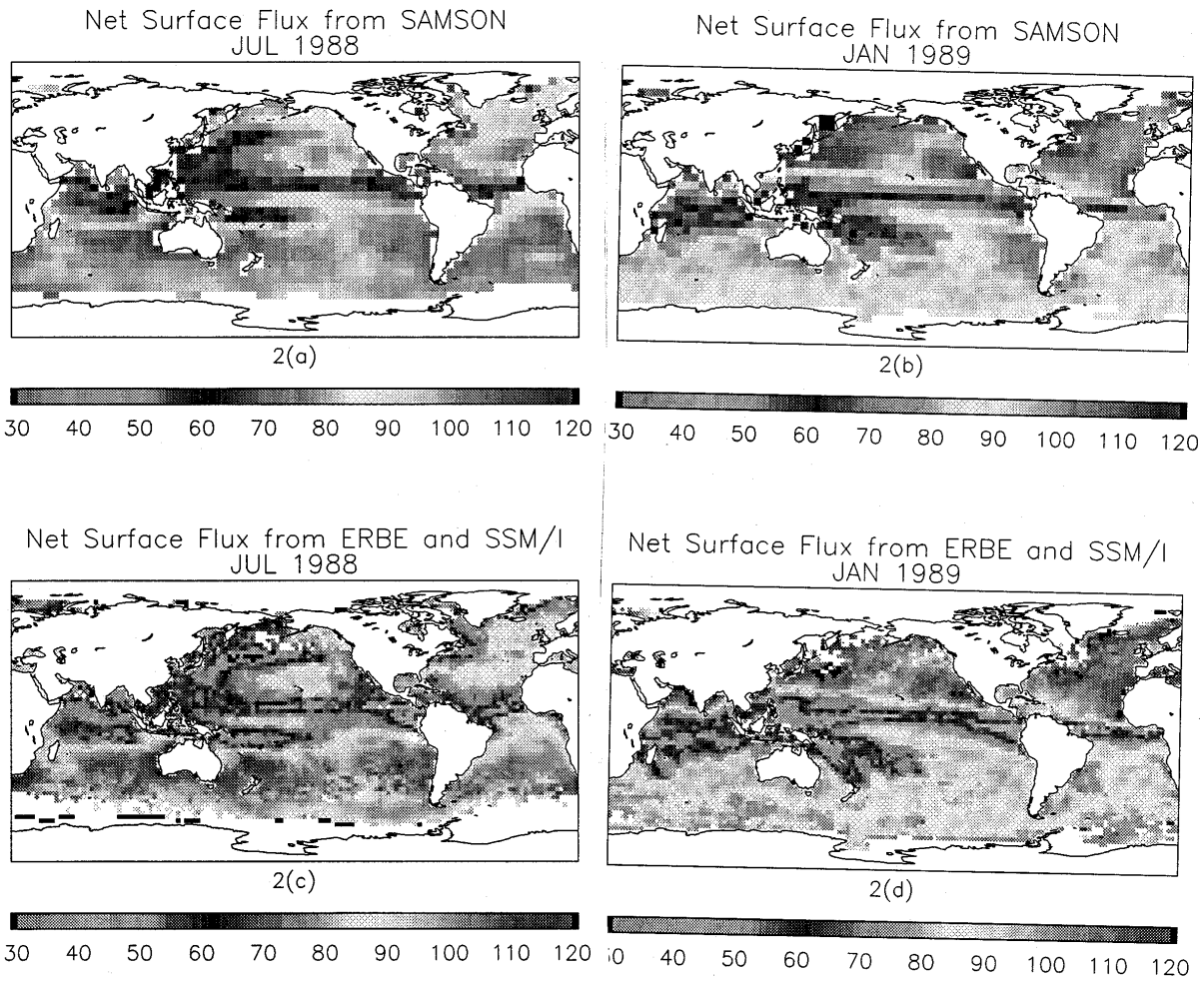

Fig. 11.8 (a) and (b) are distributions over the oceans of the July and January SAMSON simulations of surface net longwave flux. (c) and (d) are the same as (a) and (b) but the net flux is deduced using a linear regression of the flux ratio, ERBE air and SSM/I precipitable water.

AT622 Section 12
Heating

Figure 12.1 provides a perspective on the topic of radiative heating. For infrared radiation, a layer in the atmosphere emits radiation at a rate defined by its temperature and the emissivity of the layer. This layer also receives radiation from layers above and layers below. When it receives more than it emits, the layer radiatively heats and *vice versa.* We think of this as an exchange process: radiation is exchanged between the reference layer and the surrounding atmosphere and surface. The aim of this section is to consider the dominant exchanges and how they shape the radiative heating distribution in the atmosphere.

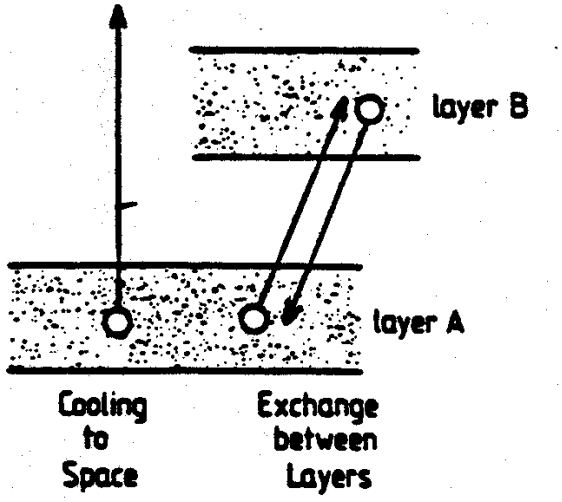

Fig. 12.1 A schematic of two different contributions to the radiative cooling by a layer. The first is by cooling to space (this occurs mainly in the transparent regions of the absorption spectrum in which contributions by surrounding layers are small). The second is by mutual exchange between layers; such as illustrated between layer A (reference) and layer B.

12.1 The Radiative Heating Rate

Consider a volume of atmosphere irradiated by a flux $F_x - \frac{\partial F_x}{\partial x}\delta x/2$ on one face and a flux $F_x + \frac{\partial F_x}{\partial x}\delta x/2$ exiting on the other face (Fig. 12.2). The net flow of energy into the volume along x is

$$net = -\frac{\partial F_x}{\partial x}\delta x \delta y \delta z$$

In three dimensions, the rate at which heat is added per unit volume of air is

$$\dot{Q} = -\nabla \cdot F = -\left[\frac{\partial F_x}{\partial x} + \frac{\partial F_y}{\partial y} + \frac{\partial F_z}{\partial z}\right] \cdot \delta V. \qquad (12.1)$$

For monochromatic, radiative equilibrium

$$\nabla \cdot F_\lambda = 0$$

where the wavelength dependence of the flux is brought to view.

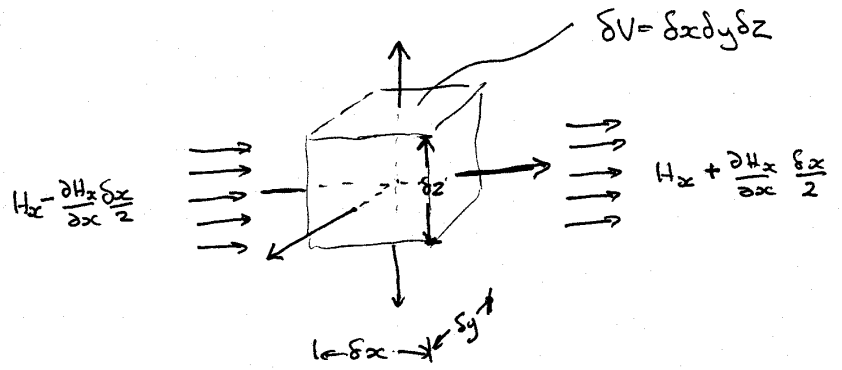

Fig. 12.2 Energy budget of a volume of atmosphere used to establish the heating rate equation.

From the first law of thermodynamics, the heat added to a volume per unit mass is

$$Q = C_p dT - V dp$$

from which it follows

$$\dot{Q} = C_p \frac{dT}{dt} - V \frac{dp}{dt} \tag{12.2}$$

Combining Eqns. (12.1) and (12.2), we obtain

$$C_p \frac{dT}{dt} = -(\nabla \cdot F)\delta V \approx -\frac{dF_{net}}{dz} \cdot \delta V \tag{12.3}$$

And, using the specific heat $c_p = \frac{C_p}{m}$ and assuming that heat is added at constant pressure, we derive

$$\frac{dT}{dt} = -\frac{1}{\rho c_p}\frac{dF_{net}}{dz} \tag{12.4a}$$

or for an atmosphere in hydrostatic equilibrium,

$$\frac{dT}{dt} = \frac{g}{c_p}\frac{dF_{net}}{dp} \tag{12.4b}$$

for a plane parallel atmosphere (for which x and y variability is neglected). This is the radiative heating rate and defines the **potential** of radiation for heating or cooling the atmosphere.

Heat added at constant temperature (e.g., tropics)

$$\frac{dz}{dt} = -\frac{1}{\rho g}\nabla \cdot F \approx \frac{1}{\rho g}\frac{dF}{dz} \tag{12.4c}$$

or

$$\frac{dz}{dt} = -\frac{dF_{net}}{dp} \tag{12.4d}$$

which defines the **potential** of radiation for inducing vertical motion.

Example 12.1: The heating rate of the atmosphere

Based on Fig. 6.13, we deduce that

$$\frac{dF_{net}}{dp} \approx \frac{-100}{1013 \times 100}$$

in which case it follows that

$$\frac{dT}{dt} = \frac{g}{c_p}\frac{dF_{net}}{dp} \approx -\frac{9.8}{1004} \times \frac{100}{1013 \times 100} \times 86400 = -0.83 \text{ Kday}^{-1}$$

or alternatively that

$$\frac{dz}{dt} = \frac{dF_{net}}{dp} = -\frac{-100}{1013 \times 100} \times 86400 = -85 \text{ mday}^{-1}$$

12.2 The IR Radiative Heating From Satellites

The rate of cooling of the atmospheric column follows from Eqn. (12.4b) as

$$\frac{dT}{dt} = -\frac{g}{c_p p_s}\Delta F_{net} \tag{12.5}$$

where the flux difference

$$\Delta F_{net} = -(\sigma T_s^4 - F_\infty - F_g)$$

which can be written as

$$\Delta F_{net} = -F_{\infty}\left(\frac{\sigma T_s^4}{F_{\infty}} - \frac{F_g}{F_{\infty}} - 1\right)$$

the column heating becomes

$$\frac{dT}{dt} = \frac{gF_{\infty}}{c_p p_s}[\mathcal{G} - \mathcal{F} - 1], \tag{12.6}$$

where we introduce the ratio terms defined earlier in Eqns. (6.5) and (11.7) and which vary in a systematic way with the PWC *w*. Furthermore, for a given *w*, the heating of the column varies proportionally with the clear-sky outgoing longwave radiation F_{∞}.

Using the retrieval strategy to estimate clear-sky values of F_g from satellite measurements of F_{∞} and *w* as described earlier and substituting a value of 1013 mb for p_s and use the monthly mean SST of Reynolds for T_s in Eqn. (12.6), we arrive at monthly mean distributions of the column averaged clear-sky heating rates shown in Figs. 12.3a and b (negative values represent cooling) for July 1988 and January 1989, respectively. A reasonable estimate of the uncertainty of the monthly averaged values of F_{∞} and F_g is ±10 Wm^{-2} based on published estimates in ERBE clear-sky flux uncertainties and in the uncertainties in F_g expressed by the rms differences discussed in relation to the comparisons shown previously in Fig. 10.8. These flux uncertainties in turn imply an uncertainty of approximately ±0.2 K/day in the column cooling rate. The SSM/I fields of *w* for July 1988 and January 1989, which are used to produce these heating rate distributions, are also shown in Figs. 12.3c and d for comparison. It is evident that the clear sky column heating rate distributions resemble the distributions of *w*, which is consistent with Eqn. (12.6) and the relationship between $\mathcal{G}$, $\mathcal{F}$ and *w*. The largest coolings occur in the moist equatorial regions and in the areas of moisture convergence over the northwest Pacific and Atlantic Oceans during July as well as in the South Pacific Convergence Zone.

The association between the column averaged heating rate and *w* is explored further in Figs. 12.4a and b, where the data displayed in Fig. 12.3a and c and Figs. 12.3b and d, respectively, are plotted against each other. Based on Eqn. (12.6) and the relationships assumed between the ratio quantities and *w*, we expect the cooling rate to increase in an approximate linear way with increasing *w* as confirmed in Figs. 12.4a and b. Linear fits of both $\mathcal{F}$ and $\mathcal{G}$ as a function of *w* yield the following slope coefficients: c_2 = 0.01015 $(kgm^{-2})^{-1}$ and c_1 = 0.00524 $(kgm^{-2})^{-1}$, respectively, which, according to Eqn. (12.6), implies a slope of -0.005 $(kgm^{-2})^{-1}$. An example of a relationship with this slope, defined using the global-mean value F_{∞} = 266 Wm^{-2}, is also given on each diagram for reference. The column cooling rate deviates from this simple linear dependence on *w* in such a way that the rate of increase of column cooling with increasing *w* above about 40 kgm^{-2} decreases.

When the column cooling rate is expressed as a function of SST rather than as a function of *w* as it is shown in Figs. 12.4c and d, a number of features emerge. The first is the general change in the cooling-SST slope for SST exceeding approximately 295 K due to the rapid increase in *w* as the SST increases beyond this value. The second feature that emerges from Figs. 12.4c and d are the winter-summer hemispheric branches in the column cooling similar to those noted in the $\mathcal{G}$-SST relationship. The characteristics of the relation between the column cooling rate and SST, especially the increased rate of cooling with increasing SST, may be better understood by reference to Fig. 12.5. This

diagram presents scatter diagrams of fluxes as a function of SST. The left panels are F_∞ and F_g derived from satellite data for July 1988 (left panels) as a function of SST and the matching fluxes derived from SAMSON are shown to the right. We can deduce that the enhanced rate of change of cooling for SSTs greater than about 295 K is a result of the enhanced emission from the atmosphere to the surface associated with the increasing water vapor with SST at these temperatures. The rate of increase of emission from the atmosphere as the SST increases exceeds the rate of change of the emission from the surface (i.e., σT_s^4). The latter is represented by the solid curve in the lower two panels of Fig. 12.4. For the SST > 290 K, we deduce that $\Delta F_g/\Delta\text{SST} \approx 15$ Wm^{-2} K^{-1} and that $\Delta\sigma T_s^4 / \Delta\text{SST} \approx$ Wm^{-2} K^{-1}.

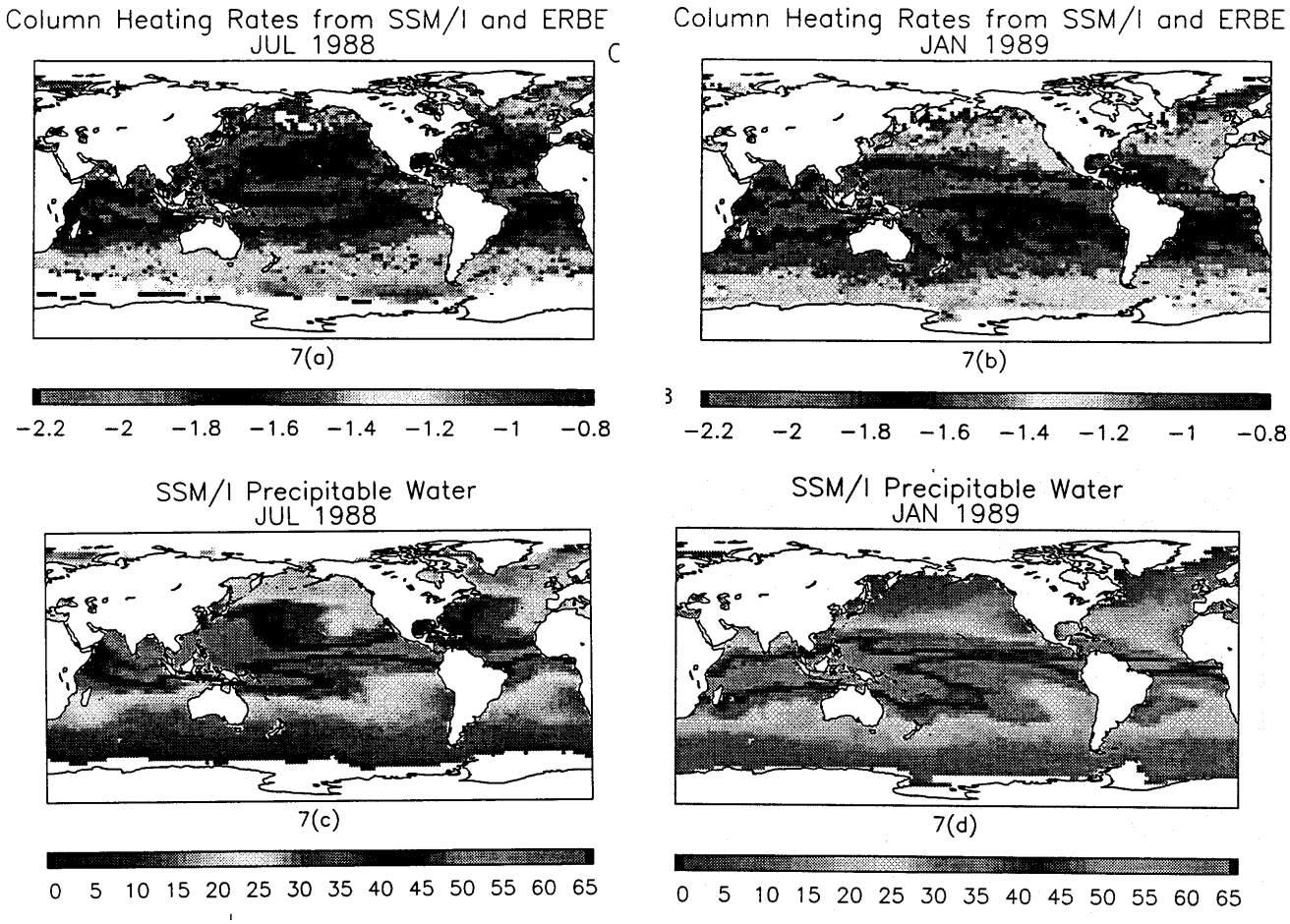

Fig. 12.3 (a) and (b) clear-sky column cooling rate distributions for July 1988 and January 1989 (in units of Kday^{-1}). (c) and (d) same as (a) and (b) except for vertically integrated water vapor (in units of kgm^{-2}).

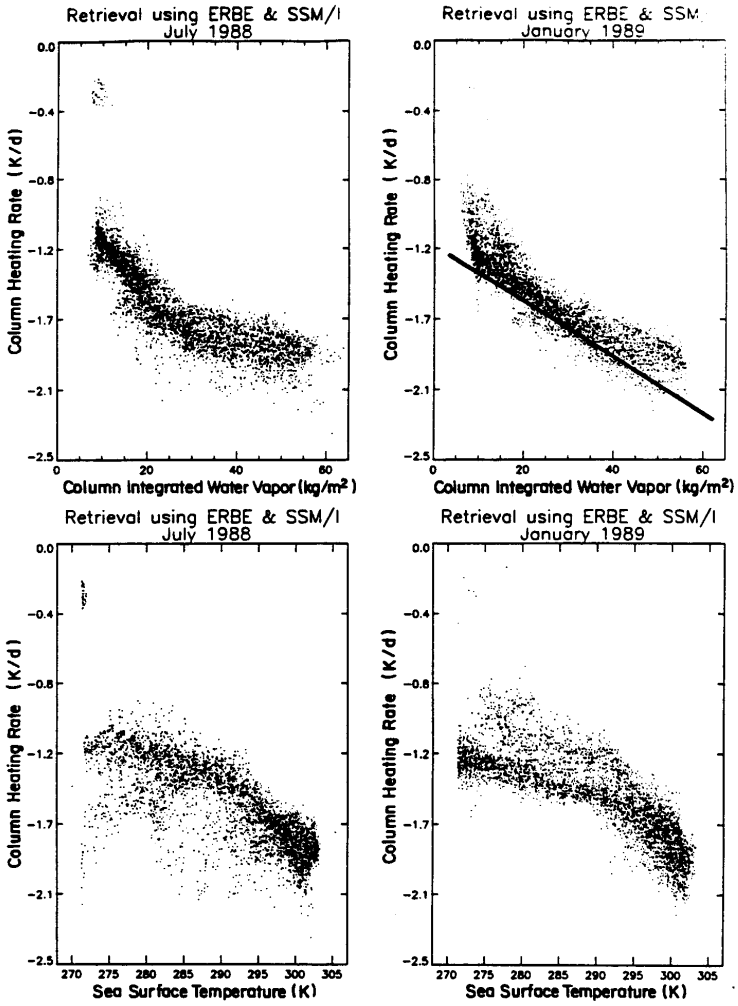

Fig. 12.4 The clear-sky column cooling rate correlated with the SSM/I derived column water vapor obtained from the data of (a) July 1988 and (b) January 1989. The solid lines are simple linear relationships implied by Eqn. (12.6), Fig. 1.3(a) and (b) and F_∞ = 266 Wm^{-2}. The clear-sky column cooling rate correlated with SST for (c) July 1988 and (d) January 1989.

12.3 The IR Radiative Heating Rate Exchange Equation

We start with the flux Eqns. (11.2) written as

$$F_i^+(z) = F_i^+(z=0)T_i^f(0,z) + \int_0^z \pi B_i(z')\frac{dT_i^f}{dz'}(z',z)dz'$$
$$F_i^-(z) = \int_z^\infty \pi B_i(z')\frac{dT^f}{dz'}(z,z')dz' \qquad (12.7)$$

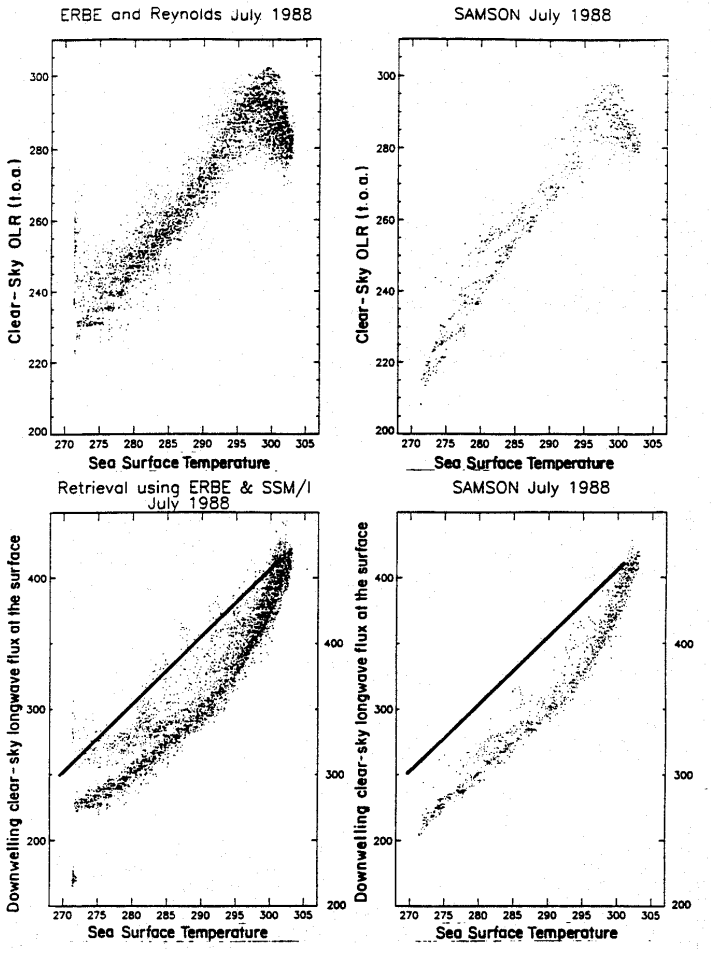

Fig. 12.5 *F_∞ as a function of SST (upper two panels) from ERBE (left) and SAMSON (right). F_g as a function of SST (bottom panels) derived from the retrieval method described in the text (left) and from SAMSON (right). The solid line on each of the bottom panels represents black body emission at the prescribed value of the SST and the scale on the left represents the scale of this blackbody flux.*

for the i^{th} spectral interval. The heating rate for this interval at level z is

$$h_i(z) = \frac{dT}{dt} = -\frac{1}{\rho c_p}\frac{dF_{net,i}}{dz}(z) \tag{12.8}$$

where the net flux at this level is

$$F_{net,i}(z) = F_i^+(z) - F_i^-(z). \tag{12.9}$$

Combining the above into Eqn. (12.8) and differentiating w.r.t. z yields

$$h_i(z) = -\frac{1}{\rho C_p}\left[\left[\pi B_i(0)\frac{d\mathcal{T}_i^f}{dz}(0,z) + \int_0^z \pi B_i(z')\frac{\partial^2 \mathcal{T}_i^f}{\partial z \partial z'}(z,z')dz' + \int_z^\infty \pi B_i(z')\frac{\partial^2 \mathcal{T}_i^f}{\partial z \partial z'}(z,z')dz'\right]\right. \tag{12.10}$$

where we suppose the surface emits as a blackbody such that $F_i^+(z=0) = \pi B(0)$. If we note that

$$\int_0^z \pi B\ (z')\frac{\partial^2 \mathcal{T}_i^f}{\partial z \partial z'}(z,z')dz' + \pi B(z)\frac{d\mathcal{T}_i^f}{dz}(z,0) = 0$$

and

$$\int_z^\infty \pi B_i(z')\frac{\partial^2 \mathcal{T}_i^f}{\partial z \partial z'}(z,z')dz' + \pi B(z)\frac{d\mathcal{T}_i^f}{dz}(z,\infty) = 0$$

then we can add each to Eqn. (12.10) to obtain

$$h_i(z) = \frac{1}{\rho C_p}\left[\begin{array}{l} \underbrace{-\pi B(z)\frac{d\mathcal{T}_i^f}{dz}(z,\infty)}_{A} \underbrace{-\pi[B_i(0) - B(z)]\frac{d\mathcal{T}_i^f}{dz}(z,0)}_{B} \\ \underbrace{-\pi\int_0^z [B_i(z') - B_i(z)]\frac{\partial^2 \mathcal{T}_i^f}{\partial z \partial z'}(z,z')dz'}_{C} \underbrace{-\pi\int_z^\infty [B_i(z') - B_i(z)]\frac{\partial^2 \mathcal{T}_i^f}{\partial z \partial z'}(z,z')dz'}_{D} \end{array}\right] \quad (12.11)$$

TERM A: is the exchange with z and space. Since $\frac{d\mathcal{T}_i^f}{dz}(z,\infty) > 0$, Term A < 0 and this term contributes to cooling at z. This is referred to as the cooling to "space" term and generally the most dominant term in the heating rate equation (Fig. 12.6b). It represents radiation escaping to space primarily through the more transparent regions of the spectrum at lower levels and through the more opaque spectral regions at higher levels. This is discussed in more detail below.

TERM B: this represents the exchange with the underlying surface. Since $B(0) > B(z)$ generally and since $\frac{d\mathcal{T}_i^f}{dz}(z,0) < 0$, this term is positive and contributes to **heating** at z.

TERM C+D: these represent the exchanges with the layers below z (C) and above z (D). For both terms $\frac{\partial^2 \mathcal{T}_i^f}{\partial z \partial z'}(z,z') < 0$ [1]so that these terms define a heating whenever $B(z') > B(z)$. This is usually the case for term C as z' refers to levels below z and thus are typically at a higher temperature. Since z' is above z in term D, this term usually contributes to cooling.

[1]It is relatively simple to demonstrate this. Suppose the transmission function has the form

$$\mathcal{T}_i^f(z,z') = \exp[-k(z-z')]$$

then it trivially follows that

$$\frac{\partial^2 \mathcal{T}_i^f}{\partial z \partial z'}(z,z') = -k^2 e^{-k(z-z')} < 0$$

since $k > 0$.

Figure 12.6a presents an example of the IR cooling rate profile from a radiative transfer model. This diagram shows the contribution to the net cooling by different spectral regions. In general, the troposphere cools at a rate of approximately 2-3 $Cday^{-1}$ primarily through emission by water vapor bands and by the continuum at lower levels although this contribution diminishes rapidly away from the moist tropics. The cooling in the stratosphere is dominated by emission from the 15 μm CO_2 band throughout and by water vapor in the lower stratosphere. Ozone emission gives rise to cooling in the stratosphere (in the vicinity of the ozone layer) and small warming below this. Figure 12.6b presents the profiles of longwave cooling separated into the exchange terms discussed above. The cooling to space term (A) dominates in the troposphere and exchange terms contribute in the stratosphere (B, C and D).

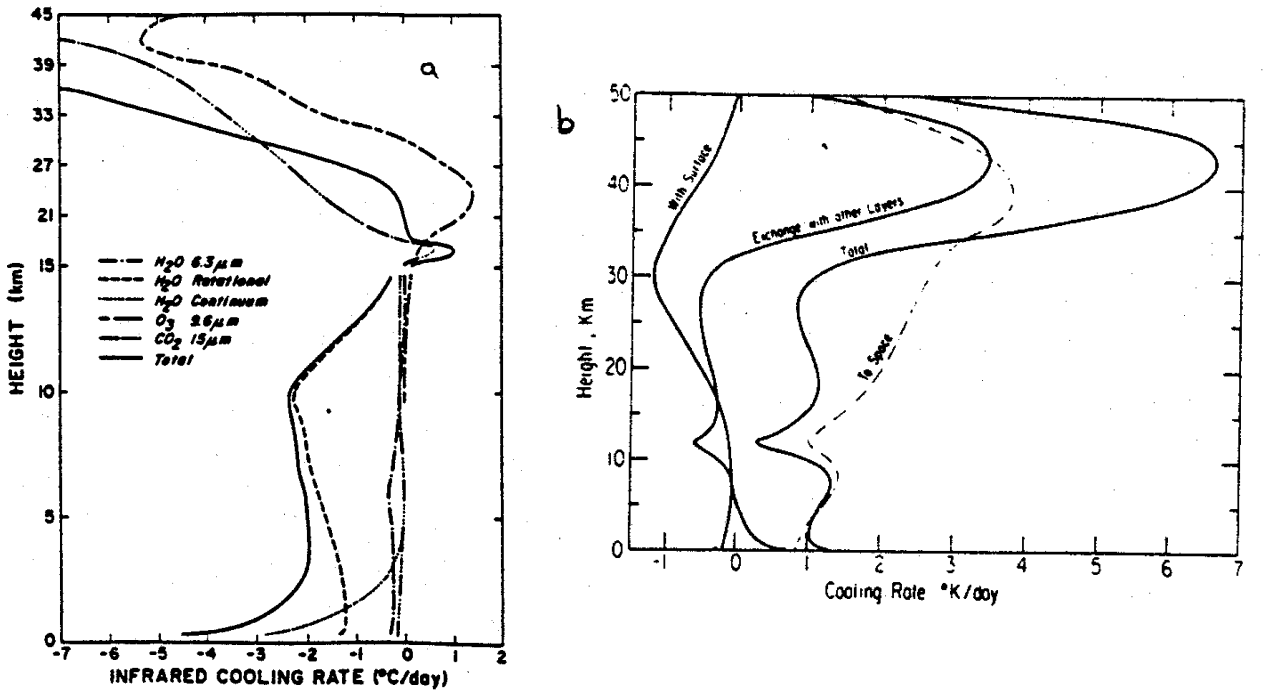

Fig. 12.6 (a) Total and spectral cooling rates in a clear tropical atmosphere (after Foewe and Liou). (b) Contributions of exchanges with surface, space and other layers to the total infrared cooling rate as functions of height.

(a) The Spectral Distribution of Longwave Cooling

The spectral distribution of the infrared cooling rate for selected layers in a model atmosphere is presented in Figs. 12.7a and b. These diagrams indicate how the cooling of layer shifts in its spectral properties from a maximum in the window (continuum absorption) low in atmosphere for the example of a tropical atmosphere shown to the stronger absorption regions of the rotation band higher up. The shaded bar in Fig. 12.7a is the cooling by the layer and the unshaded bars represent the heating of the layer by the surrounding atmosphere. Both this and Fig. 12.7b demonstrate how the net cooling of the layer is the residual of larger exchange terms. A clearer perspective of the spectral contribution to the cooling and how this contribution changes with pressure is presented in Fig. 12.8. The upper panel shows the cooling by a mid-latitude summer atmosphere by water vapor lines alone (no continuum) and the lower panel shows this cooling with the continuum added (both a foreign broadened continuum in the water vapor bands—especially the rotation band and the self broadened *e* continuum in the window). Note how the former enhances the cooling in the upper troposphere and the latter at lower levels.

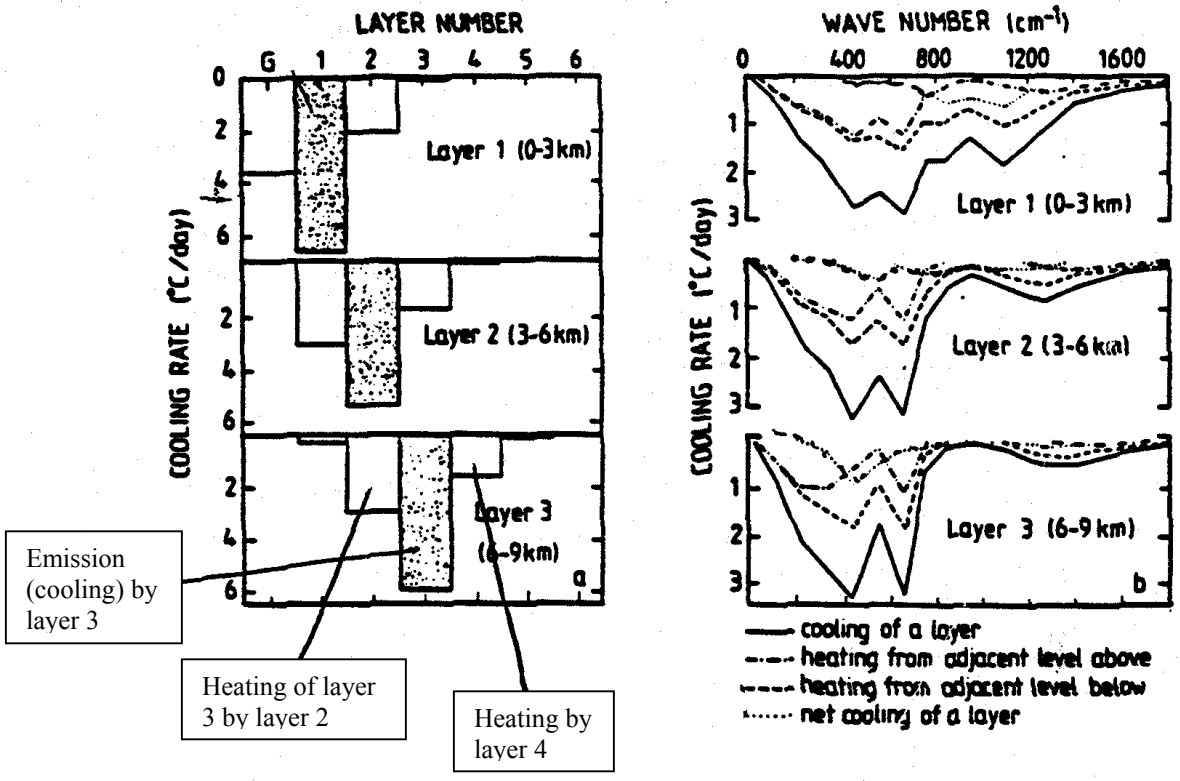

Fig. 12.7 (a) The contribution to the overall radiative cooling by emission from the layer itself (shaded area) and the absorption of radiation that originates from layers adjacent to the reference layer. The separation distance between the reference layer and the surrounding layers is shown on the upper horizontal axis. The total cooling by the reference layer is found from the sum of each individual contribution shown on (a). Note that the shaded area represents cooling, while the open areas define the heating by adjacent layers. (b) The spectral distribution of cooling for the three reference layers shown in (a). The contributions are separated into net cooling of the layer, heating from adjacent layers surrounding the reference layer and heating from all other layers (modified from Wu, 1980).

12.4 Curvature Effects on the IR Cooling

The dominance of the cooling to space term suggest that a convenient approximation to the IR cooling rule

$$\frac{dT}{dt}(z) \rightarrow \varepsilon\sigma T^4(z) \quad \text{(local emission at } z\text{)}.$$

However, the situation is more complicated than this as $\frac{dT}{dt}$ depends also in a complicated way on local curvature of temperature and moisture.

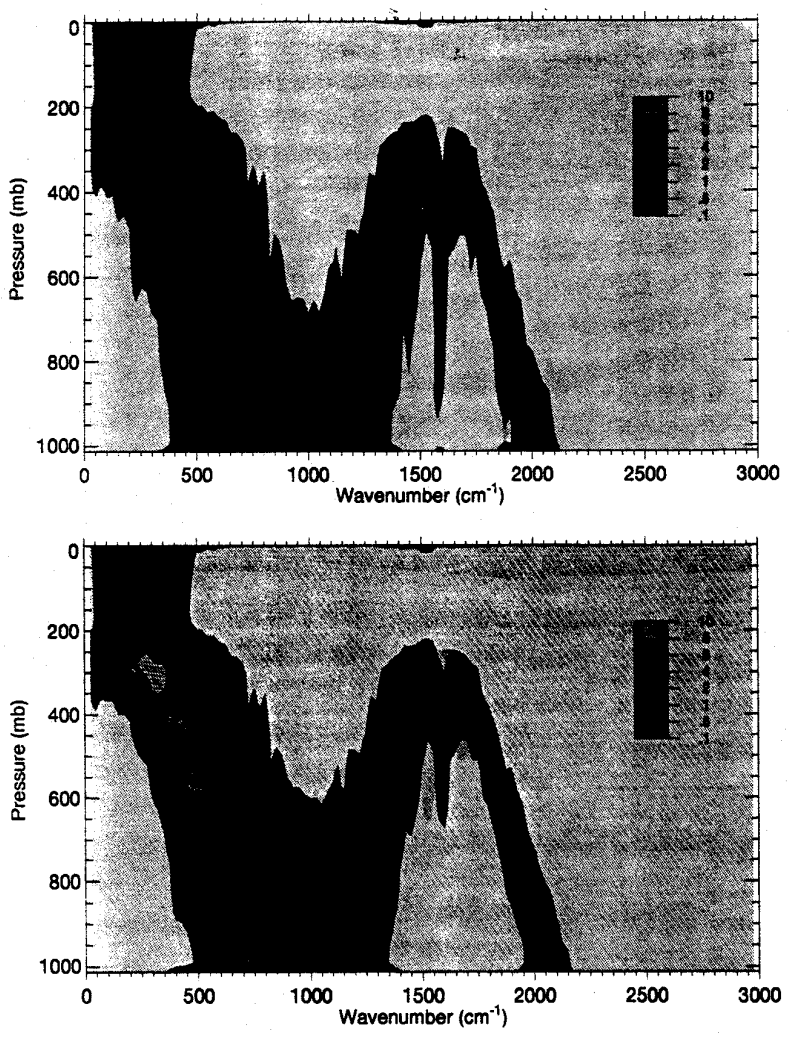

Fig. 12.8 Spectral cooling rate for water vapor for an mls atmosphere. Color scale is in units of Kday^{-1} (cm^{-1})$^{-1}$. The top panel is for no continuum and the bottom panel includes both a p and e continuum.

12.5 Climatology of Radiative Heating

- troposphere generally cools ~ 2° Cday^{-1} except at poles where the smaller water vapor decreased emission
- upper tropical troposphere, lower stratosphere - slight warming
- cooling increases with *z* in stratosphere.

(a) Solar and Net Heating Rates

We have not discussed solar heating rates in any detail. If we make some (reasonable) assumptions such as neglect Rayleigh scattering and multiple scattering, the clear-sky solar heating can be deduced by treating only absorption of the collimated solar beam, namely

$$F_n(\tau) = F_\odot \underbrace{e^{-\tau/\mu_o}}_{\mathcal{T}_r^f}$$

where we use empirical function for transmission (refer to Section 8). For example, water vapor absorption

$$\mathcal{T}_r^f = 1 - A = 1 - \frac{2.9\tilde{a}}{(1+141.5\tilde{u})^{0.645} + 0.5125\tilde{u}}$$

Scatter indicative of effects

- different absorption data
- different treatment of pressure scaling
- different solar flux data and others.
- O_3 heating increases systematically with z
- troposphere heating ~ 1° Cday^{-1} decreasing to winter pole
- combined heating-minimum in lower stratosphere

(b) Net Heating Rates

An example of the vertical profile of solar heating and IR cooling is shown in Fig. 12.9 derived from a climate model (after Manabe and Strickler, 1964). These profiles can be thought to be representative of globally averaged clear sky conditions. The net (solar+IR) profile highlights the radiative cooling of the troposphere of approximately 1 Kday^{-1} and a stratosphere that is in radiative equilibrium. Here, the solar heating by ozone absorption is balanced largely by CO_2 emission and to a lesser extent by water vapor emission.

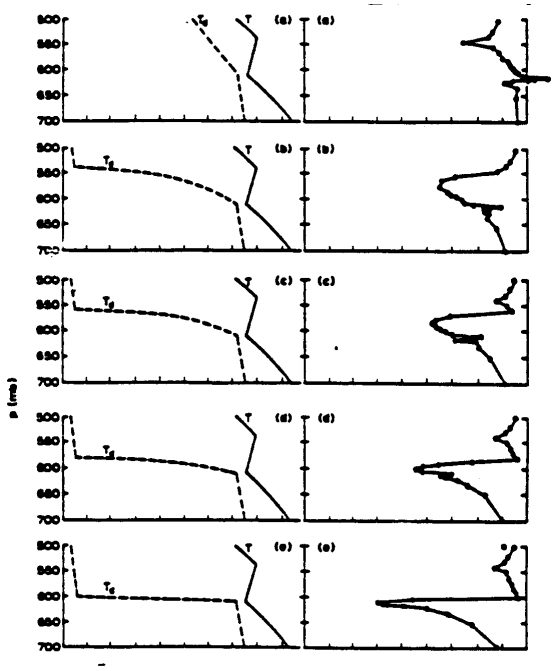

Fig. 12.9 Radiative cooling profiles associated with a temperature inversion and different degrees of "sharpness" in the water vapor profile. T and T_d are the dry and dewpoint temperatures, respectively (after Staley, 1965).

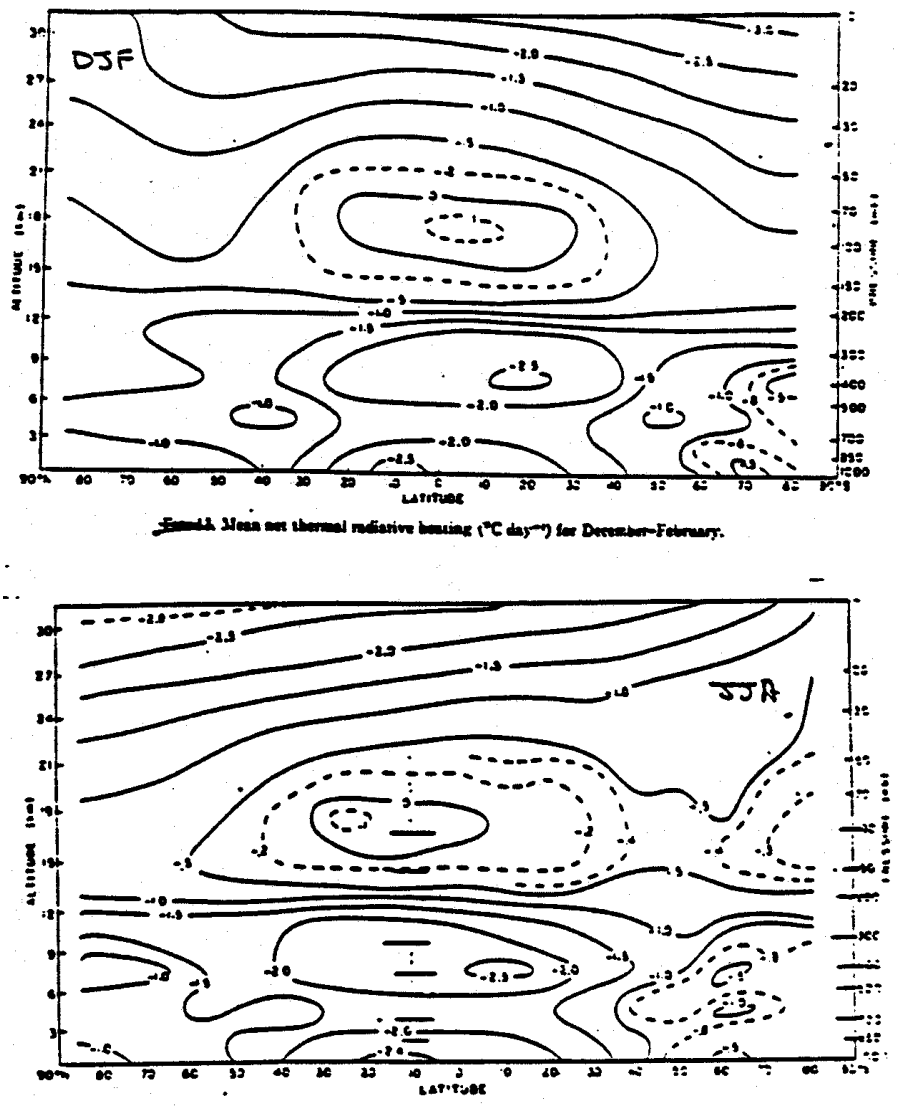

Fig. 12.10 (a) Mean net thermal radiative heating (°Cday^{-1}) for December-February. (b) Mean net thermal radiative heating (°Cday^{-1}) for June-August.

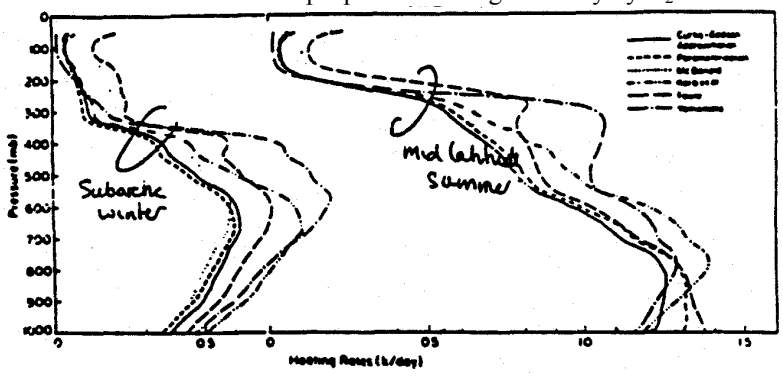

Fig. 12.11 Clear sky solar heating rate profiles due to water vapor absorption in model mid-latitude summer and subarctic winter atmospheres. The profiles were calculated for $\theta_o = 60°$ and $\alpha_g = 0.07$ for a variety of different absorption parameterizations that use either different absorption data and/or different extraterrestrial solar fluxes (refer Table 4 and discussion in text) (from Wang 1976).

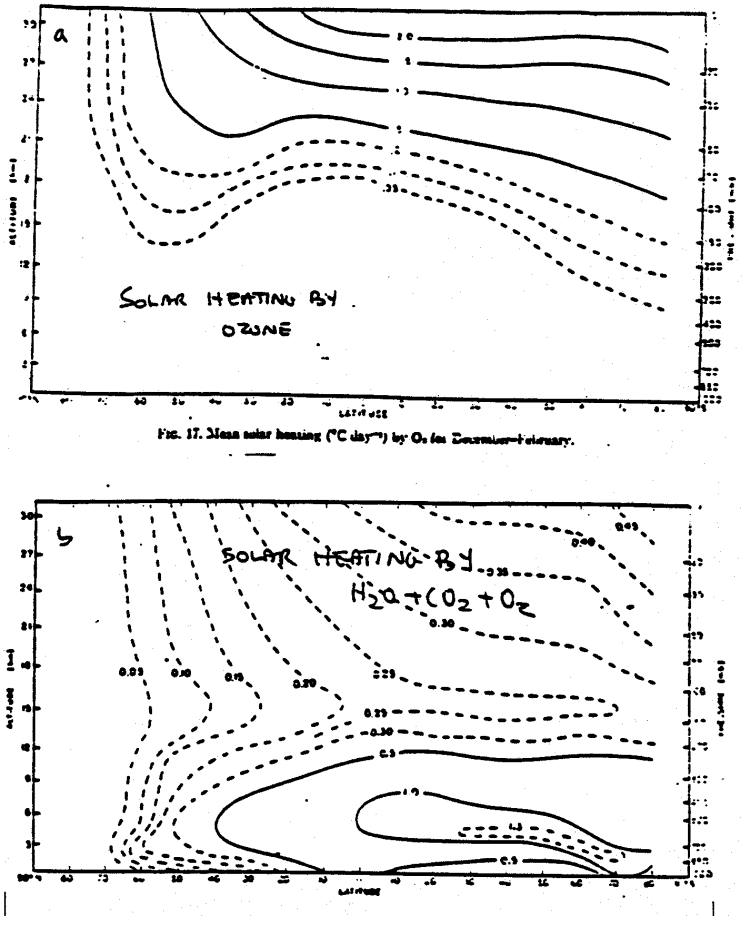

Fig. 12.12 (a) Mean solar heating (°Cday^{-1}) by O_3 for December-February. (b) Mean solar heating (°Cday^{-1}) by $H_2O + CO_2 + O_2$ for December-February.

AT622 Section 13
Elementary Dielectrics: Interaction with Condensed Matter

The object of this section is to introduce elementary properties of dielectric materials that shape the properties of scattering from homogeneous slabs and particles.

13.1 Polarization of Matter

The *polarization* of matter, in contrast to the polarization of radiation, is a property that relates to the ability of the material to form dipoles. This polarization occurs either by mechanisms that are induced (Fig. 13.1) or when molecules possess a permanent electric dipole moment so that they align themselves with the dipole moment parallel to the applied electric field. As a consequence of either induced or permanent dipoles, a piece of matter placed in an electric field becomes *electrically polarized* and the material polarized in this way is called a *dielectric*.

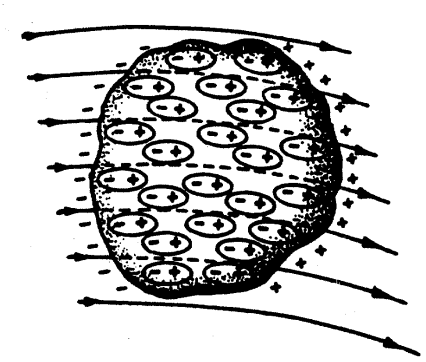

Fig. 13.1 Polarization of matter under the influence of an electric field.

The polarization per unit volume of matter is defined as

$$\vec{P} = (\varepsilon_r - 1)\varepsilon_o \vec{\mathcal{E}} \tag{13.1}$$

where ε_o is the electric permittivity in a vacuum. This macroscopic expression states that the electric field and polarization are directly related and the proportionality constant, ε_r, is referred to as the relative permittivity or alternatively as the optical or dielectric constant.

Various mechanisms cause displacement of charge in matter and therefore contribute to its polarizability. Under the influence of oscillatory fields of different frequency, the constituents of matter vibrate on different time scales and thus contribute to the observed properties in different portions of the electromagnetic spectrum. Figure 13.2 schematically depicts the three principal polarization mechanisms that are relevant to atmospheric radiation. Lightest parts (electrons) vibrate fastest (UV), the heavier parts (atoms and molecules) are more sluggish-IR and microwave. One of the mechanisms of interest involves oscillations and the other relaxation.

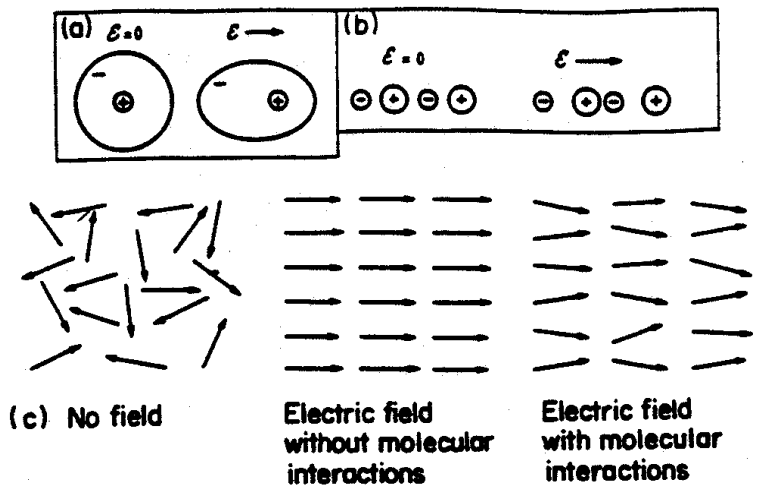

Fig. 13.2 The three main mechanisms of polarization under consideration are (a) electronic (b) atomic, and (c) orientation.

Let us now consider what happens to an individual dipole when an electric field is applied to it. The dipole moment of an individual atom or molecule $\vec{p}$ can be related to the locally active electric field $\mathcal{E}'$ by which α is the *polarizability*[*] of the material. If there are N of these molecules per unit volume of matter, then the polarization per unit volume of the material is $\vec{P} = N\vec{p}$.

$$\vec{p} = \alpha\vec{\mathcal{E}}' \tag{13.2}$$

We cannot yet combine Eqns. (13.1) and (13.2) to establish the link between the macroscopic parameter ε_r to the microscopic parameter α. The problem is that in condensed matter, where molecules are tightly packed, the field $\mathcal{E}'$ acting locally on the dipole is not the same as the external field $\mathcal{E}$ applied to the material. We will not discuss the way that we can express the local field in terms of the applied field here and references elaborating on this topic are given at the end of this chapter. Suffice to say that the field at the dipole may be derived by imagining that it sits in a spherical hole in a surrounding dielectric material. The field in such a hole is increased over a uniform static field $\mathcal{E}$ by an amount $P/3\varepsilon_o$. The same argument applies for an electric field in the form of a wave so long as the wavelength of the wave is much longer than the spacing between atoms and molecules. In this case, the field locally is increased by the fields associated with the neighboring dipoles such that

$$\mathcal{E}' = \mathcal{E} + \frac{P}{3\varepsilon_0} = \frac{\mathcal{E}}{3}(\varepsilon_r + 2). \tag{13.3}$$

Combining Eqns. (13.1) and (13.3) produces

[*]There are different forms of polarizability that can be defined. The polarizability introduced later is referred to as the atomic polarizability, the ratio of P to $\mathcal{E}$ defines the volume polarizabilty (i.e., $N\alpha$) and the quantity $N_o\alpha$ is the molar polarizability where N_o is Avocadro's number.

$$N\alpha = 3\varepsilon_0 \frac{\varepsilon_r - 1}{\varepsilon_r + 2} \quad , \tag{13.4}$$

which is known as the *Clausius-Mosotti* equation.

13.2 Classical Theories

The relative permittivity ε_r, a property relating the response of dense matter to the action of an electric field, is obviously related to the properties of atoms and molecules of the material as suggested by the discussion of Fig. 13.2. In this section, we provide a more quantitative, albeit phenomenological, account of how this quantity relates to these properties.

Actual calculation of ε_r reduces to the calculation of the polarizability of atoms or molecules. This amounts to determining the effects of an external field on the motion of charge in the material following the laws of quantum mechanics. For our purposes, simplified mechanical models suffice to approximate the permittivity.

(a) The Lorentz Model

We often picture in our minds a model of an atom represented by electrons whirling around a nucleus in a kind of fuzzy orbit. So far as problems involving nonresonant interaction with radiation, these electrons behave as though they are attached to springs producing a distortion of charge in response to an oscillating electric field. These electrons react to electromagnetic radiation in such a way that they vibrate just like a classical harmonic oscillator (Fig. 13.3). H.A. Lorentz introduced his model of electronic and atomic polarization around the beginning of the last century based on the principle of a classical harmonic oscillator.

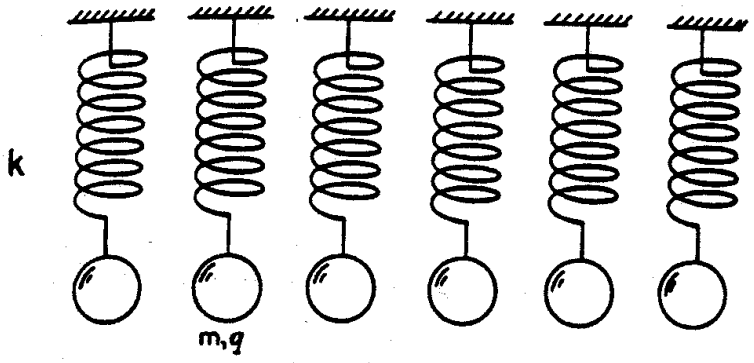

Fig. 13.3 The Lorentz model of matter.

The equation of motion of such an oscillator is

$$m\frac{d^2x}{dt^2} + \gamma\frac{dx}{dt} + kx = q\mathcal{E}' \, , \tag{13.5}$$

where m *is* the mass of the oscillator, $\gamma dx/dt$ *is* the damping force exerted by neighboring dipoles, and k is the 'spring' constant. In this expression, $q\mathcal{E}'$ *is* the driving force produced by the local electric field $\mathcal{E}'$, and x is the displacement of the mass from its equilibrium position. This is not really a legitimate model of an

atom but simple cases of correct quantum mechanical theory gives results equivalent to this model. In a crude sense, the effects of quantum theory are accounted for by the appropriate choice of the properties of oscillators.

If the electric field acting on the dipole vibrates with a frequency ω, the displacement x of the charge oscillates at the same frequency. Assuming that $x = x_0 e^{i\omega t}$, then x can be solved for in terms of $\mathcal{E}'$ producing

$$x = \frac{(q/m)\mathcal{E}'}{\omega_o^2 - \omega^2 - i\gamma\omega}, \tag{13.6}$$

where $\gamma = b/m$ and $\omega_o = \sqrt{k/m}$ *is* referred to as the resonant frequency of the oscillator. This displacement is complex and it is convenient to express it in the form $Ae^{i\Phi}(q/m)\mathcal{E}'$ where $A(q/m)\mathcal{E}'$ *is* the amplitude of the oscillation and Φ is its phase relative to the driving force of the electric field. Simple algebra provides us with

$$A = \frac{1}{[(\omega_o^2 - \omega^2)^2 + \gamma^2\omega^2]^{1/2}} \tag{13.7a}$$

$$\Phi = \tan^{-1}\frac{\gamma\omega}{\omega_o^2 - \omega^2} \tag{13.7b}$$

which follow from Eqn. (13.6). An interpretation of these results is provided in Fig. 13.4a and b where A and Φ are shown as a function of frequency ω. How these properties of the oscillator vary with frequency depends on the value of ω relative to the resonant frequency ω_o of the oscillator. For $\omega >> \omega_o$, the nonresonant oscillations are weak and out of phase with the driving force of the light. The amplitudes of the oscillation for this range of frequencies, according to Eqn. (13.7a), decreases at a rate proportional to $1/\omega^2$ (Fig. 13.4b). In the spectral range of low frequencies $\omega << \omega_o$, the nonresonant oscillations are again weak but, in this case, in phase with the driving force (Fig. 13.4a). In this spectral range, the amplitude approaches a constant value as ω is decreased from resonance. Only the resonance case ($\omega = \omega_o$ and $\Phi = 0$) corresponds to a transition from one quantum state to another.

Given the response of the single oscillator to a time-harmonic electric field, the relative permittivity can be derived using the definition of the dipole moment for a single oscillator as $p = qx$, and since $p = \alpha\mathcal{E}'$, then

$$\alpha = \frac{q^2/m}{\omega_o^2 - \omega^2 - i\gamma\omega}$$

and the polarization per unit volume, P for N oscillators in a unit volume follows as

$$P = \frac{\omega_p^2}{\omega_o^2 - \omega^2 - i\gamma\omega}\varepsilon_o\mathcal{E}' \tag{13.8}$$

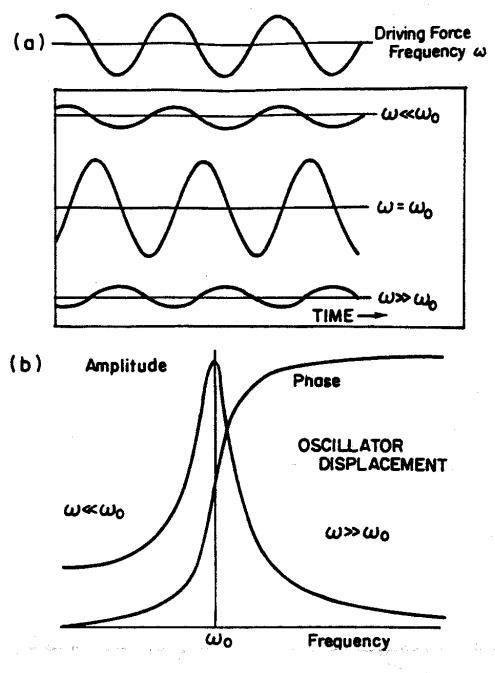

Fig. 13.4 (a) The response of an oscillator to a periodic driving force serves as a model of how charges in matter react to an electromagnetic driving force. The response of the oscillator depends on the frequency of the forcing ω to the oscillator's resonant frequency ω_o. (b) The oscillator amplitude and phase as a function of the ratio between the frequency ω and the resonant frequency ω_o. The amplitude approaches a constant value when the frequency of the driving force is much below resonance as in the case of N_2 and O_2 molecules exposed to visible light.

where $\omega_p^2 = Nq^2 / \varepsilon_o m$ is the *plasma frequency.* The difference between the local field and the external field is ignored since a proper treatment of local field effects only complicates matters without adding further insight. With this assumption, it follows by matching Eqn. (13.1) to Eqn. (13.8) that

$$\varepsilon_r = 1 + \frac{\omega_p^2}{\omega_o^2 - \omega^2 - i\gamma\omega} \tag{13.9}$$

which has the following real and imaginary parts

$$\varepsilon_r' = 1 + \frac{\omega_p^2(\omega_o^2 - \omega^2)}{(\omega_o^2 - \omega^2)^2 + \gamma^2\omega^2} \tag{13.10a}$$

$$\varepsilon_r'' = \frac{\omega_p^2\gamma\omega}{(\omega_o^2 - \omega^2)^2 + \gamma^2\omega^2} \tag{13.10b}$$

respectively. The frequency dependence of each of these components is schematically shown in Fig. 13.5a. The complex component provides the dampening of the oscillations and is a maximum at resonance and coincides with the most rapid change of the real part of the relative permittivity with frequency.

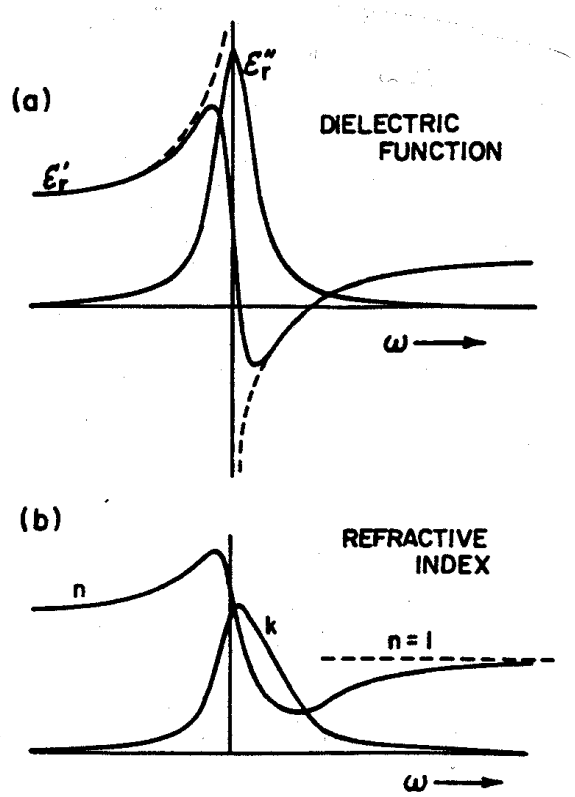

Fig. 13.5 *(a) The frequency dependence of the real and complex parts of the relative permittivity. Note that when the damping terms are neglected, $\gamma = 0$ and $\varepsilon_r'' = 0$ and the unphysical result occurs at the resonant frequency (dashed curve). Damping is not a result of the viscous movement of the oscillators but represents transitions from one state to another and therefore represents absorption processes. (b) The frequency dependence of the real and complex parts of the refractive index.*

Quantum mechanical solutions provide similar results but with the following modifications. Atoms and molecules have several natural frequencies and each has its own dissipation constant. The effective strength of each mode is also different and we represent this by the strength factor *f*. Summing over all modes leads to a modification of Eqn. (13.9) of the form

$$\varepsilon_r - 1 = \frac{Nq^2}{\varepsilon_o m} \sum_i \frac{f_i}{\omega_i^2 - \omega^2 - i\gamma_i \omega}. \tag{13.11}$$

(b) Orientational Polarization-Debye Relaxation

Lorentz's classical model describes polarization arising from the distortion of charge in nonpolar molecules. In solids and liquids composed of polar molecules, the orientation of the dipoles with respect to an electric field produces an additional low frequency contribution to the polarization. The ability of a molecule to reorient depends on its shape and its interactions with the environment. The nearer to sphericity and the lower the dipole moment, the more easily and faster the molecule reorients itself in a changing electric field. An asymmetrical molecule like H_2O has several stable orientations and changes direction relatively slowly from one stable orientation to another. The average time between these changes is the relaxation time.

The polarization that results via orientation of dipoles can be computed from methods of statistical mechanics. We consider only very simple aspects of these methods here. Consider a molecule with a permanent dipole moment p_o aligned at some angle θ to the electric field. The potential energy of the dipole is (e.g, Kittel, 1971)

$$U = -p_o \mathcal{E}' \cos\theta_o \, .$$

Statistical mechanics tells us that in a state of equilibrium, the relative number of molecules with a potential energy U is

$$e^{-U/KT}$$

and the number of molecules oriented at an angle θ_o

$$n(\theta_o) = n_o e^{p_o \mathcal{E}' \cos\theta_o / KT}$$

where K is Boltzmann's constant and T is temperature. For normal temperatures and $\mathcal{E}$ fields, this approximates to

$$n(\theta_o) = n_o \left(1 + \frac{p_o \mathcal{E} \cos\theta_o}{KT} \right)$$

where n_o is $N/4\pi$ (we find this by integrating $n(\theta_o)$ over θ_o and this should just be N, the total number of molecules). The net dipole moment per unit volume follows from the integration of the moment $p_o \cos\theta_o$ over solid angle $d\Omega = 2\pi \sin\theta_o d\theta_o$,

$$\overline{P} = 2\pi \int_0^{\pi} n(\theta_o) p_o \cos\theta_o \sin\theta_o d\theta_o \, ,$$

resulting in an average dipole moment

$$\overline{P} = \frac{N p_o^2}{3KT} \mathcal{E}' \tag{13.12}$$

and by combining Eqns. (13.4) and (13.12) leads to

$$\alpha_o = \frac{p_o^2}{3KT} \, .$$

Debye (1929) has given an elegant discussion of dielectric relaxation of polar molecules in liquids. He supposed that dipoles initially aligned themselves in the direction of a field only to relax their orientations back to an equilibrium state as defined by the average dipole moment above relevant to a static field. This relaxation occurs on a time scale τ. The central result of Debye's theory is that the orientational part of the polarizability depends on the applied frequency ω such that

$$\alpha = \frac{p_o^2}{3KT} \frac{1}{1 + i\omega\tau} \, . \tag{13.13}$$

Using the Mosotti field for $\mathcal{E}'$, then

$$\frac{N\alpha}{3\varepsilon_o} = \frac{N}{3\varepsilon_o}\left(\frac{p_o^2}{3KT}\frac{1}{1+i\omega\tau}\right) = \frac{\varepsilon_r - 1}{\varepsilon_r + 2}. \tag{13.14}$$

From this expression, the complex permittivity is given in terms of the permittivity defined at the limits $\omega \to 0$ (ε_{rs}, the static permittivity) and $\omega \to \infty$, the high frequency permittivity) and the effective relaxation time constant is,

$$\tau_e = \tau\frac{\varepsilon_{rs} + 2}{\varepsilon_{rh} + 2},$$

and it follows that

$$\varepsilon_r = \varepsilon_{rh} + \frac{\varepsilon_{rs} - \varepsilon_{rh}}{1 + i\omega\tau_e}. \tag{13.15}$$

This expression is the Debye relaxation formula for the permittivity of a friction-dominated medium in which the internal field is assumed to be the Clausius-Mosotti field. The relaxation time is lengthened from τ to τ_e due to the difference between the internal field and the applied field.

The real and imaginary parts of ε_r follow from Eqn. (13.15) as

$$\begin{aligned} \varepsilon' &= \varepsilon_{rh} + \frac{\Delta}{1 + \omega^2\tau_e^2} \\ \varepsilon'' &= \frac{\Delta\omega\tau_e}{1 + \omega^2\tau_e^2} \end{aligned} \tag{13.16}$$

where $\Delta = \varepsilon_{rs} - \varepsilon_{rh}$. The imaginary part of the dielectric function, according to Eqn. (13.16), is a maximum at $\omega = 1/\tau_e$, and its behavior with frequency is broadly similar to ε_r'' predicted for the Lorentz oscillator. The real part behaves quite differently: it has no maxima or minima but decreases monotonically with increasing frequency from a value of ε_{rs} at low frequencies to ε_{rh} at high frequencies. At low frequencies, permanent dipoles react to the more slowly oscillating electric field in enough time that they become aligned, producing a significant polarization and large values of . At higher frequencies, this part of the matter is unable to respond quickly enough to produce any polarization.

The Debye relaxation model has been successfully used to describe measured values of the dielectric function at microwave frequencies as demonstrated in Fig. 13.6. Both the real and complex parts of ε_r for water at microwave frequencies are compared to the Debye theory on this diagram. The parameters ε_{rs}, ε_{rh}, and τ are chosen to provide the best fit to the data. An especially relevant consequence of the relaxation spectrum of H_2O to remote sensing lies in the change of the spectrum of ε_r with the phase transition from liquid to solid water. To understand the differences in ε_r as this transition occurs it is helpful to consider the simple classical expression Debye derived for τ, namely

$$\tau = \frac{4\pi\eta a^3}{KT}, \tag{13.17}$$

for a sphere of radius a in a fluid of viscosity η. This time constant is a ratio of the viscous-restoring torque applied to the sphere that maintains alignment to the thermal forces that act to disrupt this alignment. When numerical values are substituted into Eqn. (13.17), the derived relaxation time corresponds approximately to that estimated from measurement. A naive interpretation of the phase transition from liquid water to ice is to consider a large discontinuous increase in viscosity that occurs when water freezes. Thus, the permanent electric dipoles that were free to rotate in the liquid are now immobilized. The relaxation time for ice is significantly larger than it is for water leading to smaller values of ε_r'' and a dramatic shift in the maximum of ε_r' to smaller frequencies. The consequences of such large changes in ε_r as ice melts are observed when microwave radiation transmitted by a radar system is backscattered by melting ice particles producing the "bright band" in vertical profiles of radar reflectivity.

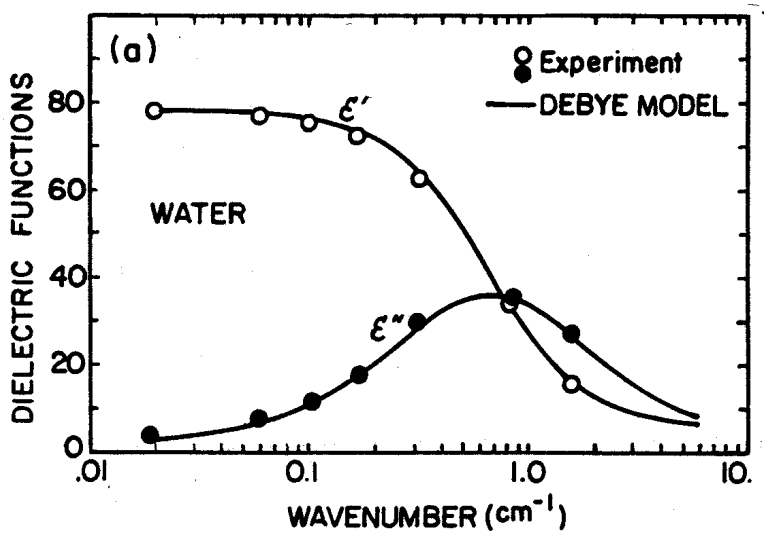

Fig. 13.6 The dielectric function of water at room temperature calculated from the Debye relaxation model with $\tau = 0.8 \times 10^{-11}$ sec, $\varepsilon_{rs} = 77.5$, $\varepsilon_{rh} = 5.27$. Data were obtained from three sources (after Bohren and Huffman 1993).

(c) Summary

We learn from both models that when a sunusoidal electric field acts on a dieletric material, there is an induced dipole moment that is proportional to the electric field. The proportionality constant $\varepsilon_r - 1$ depends on the frequency of the oscillating field and is a complex number, which means that the polarization does not follow the electric field but is shifted in phase. A schematic diagram summarizing the frequency dependence of ε_r' and ε_r'' for an ideal nonconducting substance is shown in Fig. 13.7. At the low frequency end, ε_r' is composed of contributions by all three mechanisms with the largest contributions resulting from dipole orientation processes. As the frequency increases, the dipoles are unable to respond fast enough, and this mechanism ceases to contribute to ε_r', instead the atomic polarization processes that produce vibrational motions contribute. For the water molecule, the resonances associated with these processes are found at infrared wavelengths. At even higher frequencies, inter-atomic vibrations cannot respond fast enough to the applied field. At these frequencies, the

electronic oscillations that are induced by the electric field now contribute to ε_r' and the resonant frequencies associated with these oscillators are typically found at UV wavelengths. Finally, as the frequency increases beyond the point where all electronic modes are exhausted, ε_r' approaches unity.

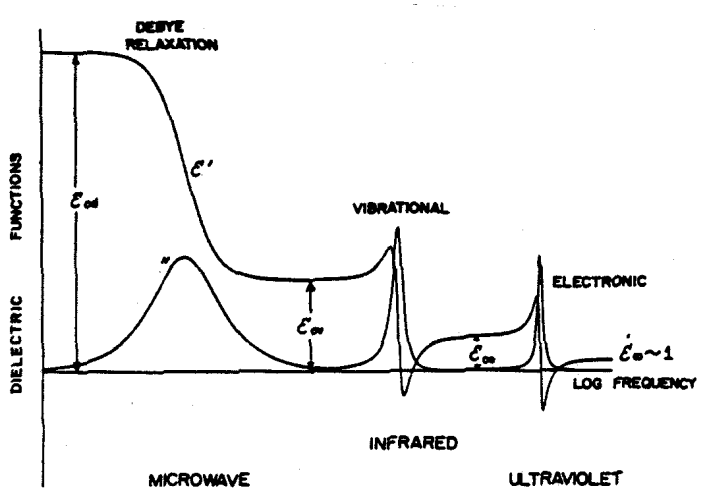

Fig. 13.7 Schematic diagram of the frequency variation of the dielectric function of an ideal nonconductor (Bohren and Huffman, 1983).

Where ε_r' changes most dramatically with frequency there is an associated peak in ε_r'', which characterizes the absorption of radiation by the substance. This absorption arises from the resonances associated with the vibrations of atoms and molecules of matter. In dense matter, the molecules are so tightly packed together that significant interactions exist between them. The internal modes of the oscillations are therefore modified and the natural frequencies of the atomic oscillations are spread out by the interactions producing a broadening of the absorption lines much in the same way as pressure broadening occurs in gases. In place of the precisely defined characteristic energy levels associated, for example, with the vibration and rotation states of the individual molecules, are energy bands composed of a continuum of levels. Thus the energy levels of the vibration and rotation states of, for instance, a water molecule, form a continuous absorption band resulting in a broad absorption spectrum as indicated in Fig. 13.7. Figure 13.8 provides a schematic illustration of the electron energy bands of two different types of material.

Since the energy bands in a solid form as a superposition of the energy levels of the individual molecules, the spectral positions of the more continuous absorption bands for solid matter more or less overlap the absorption spectrum of the individual molecules. Thus the infrared absorption spectra of liquid water and solid ice, for instance, occur at roughly the same wavelengths where absorption bands of water vapor lines are found.

There are features of the energy bands that have a significant bearing on the way radiation interacts with condensed matter and which are therefore important to our understanding of particle scattering. The energy bands of certain materials overlap, as depicted in Fig 4.8, and the electrons in such a material have a continuous distribution of energy within these overlapped bands. If one of the overlapping bands is partially empty, application of an electric field readily excites electrons into adjacent unoccupied states and an electric current results. The material is said to be a good conductor of electricity and its electrical behavior is determined by both the energy band structure and how the bands are normally filled by

electrons. This is the case for metals that can absorb radiation at any wavelength. When a photon is absorbed in a metal, the electron jumps to an excited state. A photon of the same energy is immediately re-emitted and the electron returns to its original state. Because of this rapid and efficient reradiation, the surface of the metal appears reflective rather than absorbant. Another type of material is the nonconductor, which possesses energy bands that are separated by intervals referred to as *forbidden bands;* absorption of radiation by such material is therefore only likely for photons possessing energies greater than this energy gap.

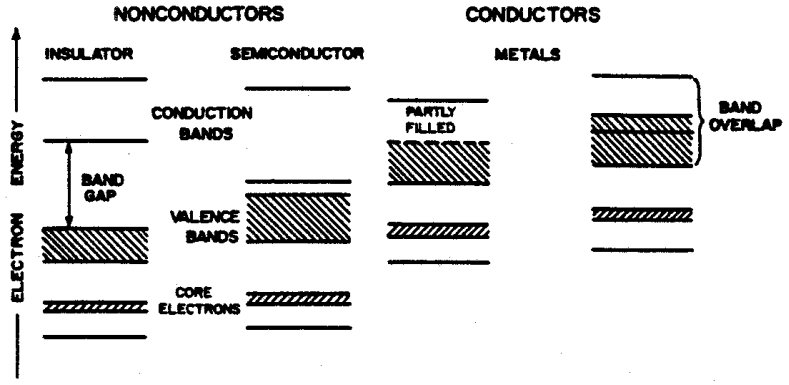

Fig. 13.8 Electron energy bands in nonconductors and conductors. The filled bands are shown hatched (Bohren and Huffman 1983).

13.3 The Refractive Index

The two sets of quantities that are often used to describe optical properties of matter are the relative permittivity ε_r and the refractive *index* m[†]. Both are related according to

$$\begin{aligned} \varepsilon_r' &= n^2 - \kappa^2 \\ \varepsilon_r'' &= 2n\kappa \end{aligned} \tag{13.18}$$

where n and κ are used here to denote the real and imaginary parts of the refractive index, respectively. The spectral variations of both n and κ from the near infrared to the microwave regions are depicted in Fig. 13.9. Certain features of the hypothetical spectra of ε_r' and ε_r'' shown in Fig. 13.7 can be identified in the refractive index spectra. Readily apparent are the relaxation spectra extending from about the millimeter wavelength range into the centimeter range. For water and ice, the values of κ lead to significant absorptions in clouds when wavelengths are greater than about about 1 μm. For ice, κ decreases again beyond wavelengths of about 100 μm. At microwave frequencies, ice particles in the atmosphere are more effective scatterers of radiation than absorbers, whereas the reverse is true of water drops. There are also significant differences between values of κ for water and ice in the near infrared especially around 1.6 and 3.7 μm, which also happen to be channels associated with radiometers flown (or to be flown) on meteorological satellites. The consequence of the different values of n to the transfer of solar radiation through clouds at these wavelengths has been proposed as a way discriminating ice clouds from water clouds.

[†] The refractive index is sometimes written as $m = n + i\kappa$ and other times as $m = n - i\kappa$.. The latter applies when the time dependence of factor of the wave is $\exp(i\omega t)$ rather than $\exp(-i\omega t)$. Both will be used in these notes.

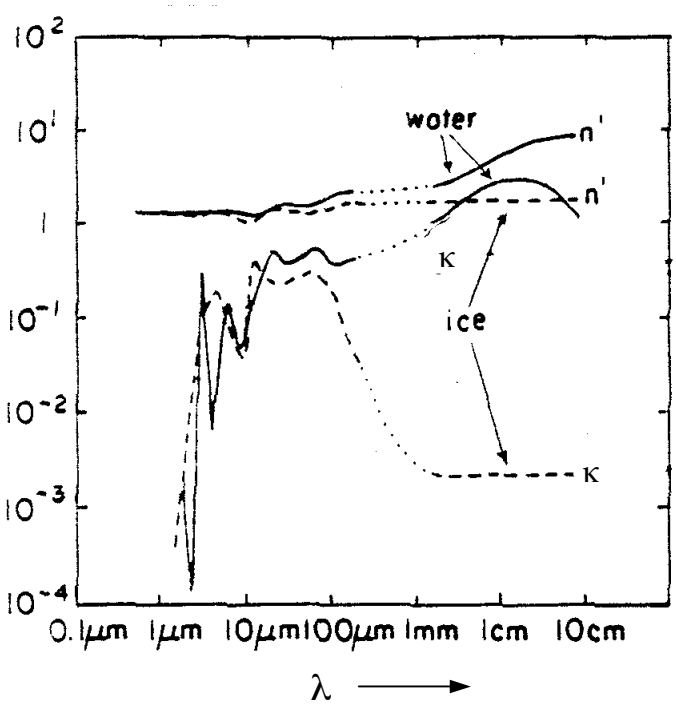

Fig. 13.9 Typical values of the refractive indices for water and ice.

Determining the refractive indices of atmospheric aerosol is quite a complex problem and a topic of apparent controversy. In Fig. 13.10, the spectra of the imaginary parts of the refractive index of several materials that exist in atmospheric particles are shown. Results are given for water, ammonium sulfate, crystalline quartz, sulfuric acid, carbon, sodium chloride, and hematite over selected spectral regions. As we have come to expect from our previous discussions, κ is large (around unity) in the infrared and ultraviolet spectral regions and small at visible wavelengths for all materials, except for carbon and hematite both of which significantly absorb visible light. To emphasize the transparency of the material in the visible region, the dashed line is the value of κ corresponding to a 1% transmission through a 1 cm thick homogeneous slab of material. Only carbon, which has metal-like overlapping electronic energy bands (e.g., Fig. 13.8), has high values of κ throughout most of the spectrum. The mineral hematite, although a very minor constituent of the atmospheric aerosol, is one of the few known materials that are also highly absorbing at visible wavelengths.

The hatched region in Fig. 13.10 shows the values of κ obtained from remote measurements using a retrieval scheme based on the particle scattering theories discussed in the following chapter. Clearly these derived values of κ do not seem to match those of any of the pure materials that make up the particle, and are presumably some kind of average of a mixture containing a small amount of a highly absorbing material. The meaning of such an average value and its direct application to theories of particle scattering must be treated with caution. Measurement of the refractive index of a substance in a pure homogeneous slab form is difficult enough, and these results highlight the complexity of estimating the refractive index when such material is broken up into small particles of heterogeneous material.

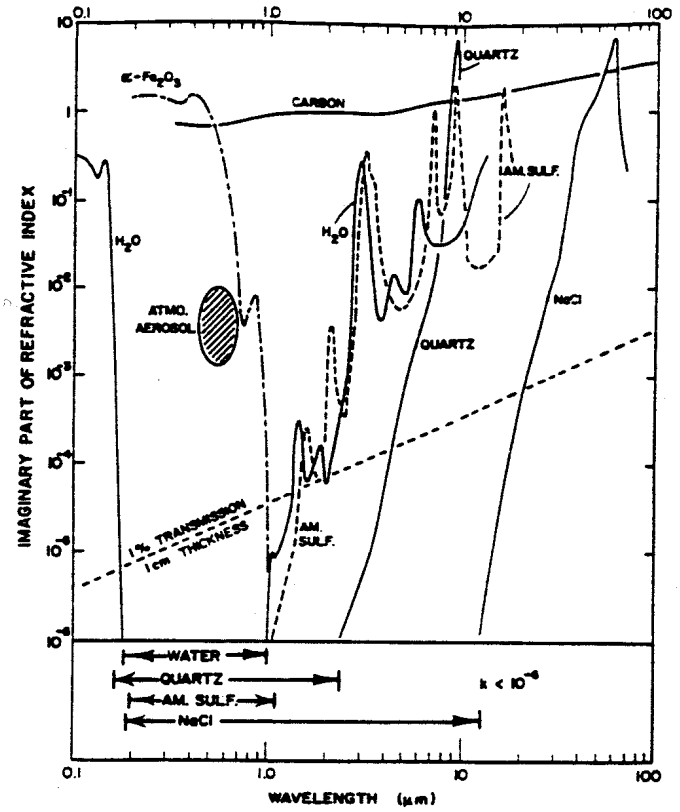

F ig. 13.10 The imaginary part of the refractive index of several solids and liquids that are found as atmospheric particles (Bohren and Huffman, 1983).

13.4 Dielectric Slab

The formal analogy between scattering by a particle and by a slab is shown in Fig. 13.11 in its most general aspect. The wave scattered by a particle is analogous to the waves reflected and transmitted by a slab. However, there are important differences between these two cases that need to be noted. We will learn that particles scatter in complicated ways depending on the direction of scatter, whereas the scattering by a slab occurs through interference effects such that radiation is concentrated in only two directions.

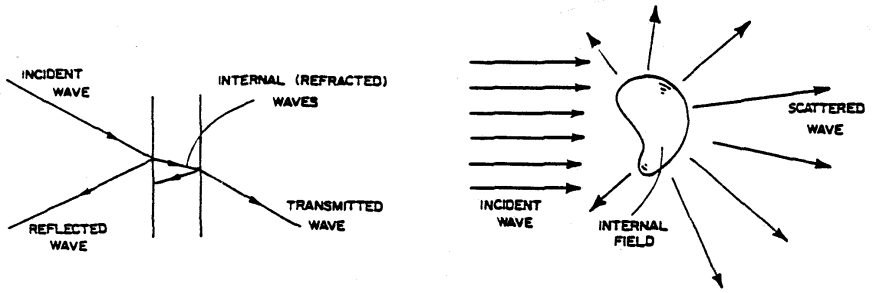

Fig. 13.11 A schematic depicting the analogy between scattering by a slab and by a particle. The scattered wave by a particle is analogous to the wave transmitted and reflected by the slab (from Bohren and Huffman, 1983).

General expression for a propagating plane wave along the z axis is

$$\mathcal{E} = \mathcal{E}_o e^{i(kz-\omega t)} \tag{13.19}$$

where, in a slab of condensed matter of refractive index m,

$$kz = mk_o z \tag{13.20}$$

which is defined relative to the wavenumber k_o in a vacuum. In an absorbing slab, m is complex and thus k is complex. For the simplest case of plane wave propagation along the z direction, and with $m = n + i$ in Eqn. (13.20), Eqn. (13.19) may be written as

$$\mathcal{E} = \mathcal{E}_o \left[e^{-2\pi k/\lambda_o} \right] e^{i(nk_o z-\omega t)}. \tag{13.21}$$

The first of the exponential factors describes the rate at which the radiation is attenuated in the slab. The second exponential factor represents the oscillatory part of the wave and we observe that the real part of the refractive index determines the phase speed of the wave. The attenuation factor can be written in terms of a bulk absorption coefficient $\beta = 4\pi k/\lambda_o$ such that the intensity of the radiation is attenuated according to the formula

$$I = Ie^{-\beta z}. \tag{13.22}$$

A useful and convenient way of interpreting this attenuation is in terms of the penetration depth $d_I = 1/\beta$, which is the depth to which the intensity is reduced by $1/e$ of its incident value.

Example 13.1: Depth of Penetration

Water and ice possess refractive indices that are strongly frequency dependent and thus have a penetration depth that varies significantly from wavelength to wavelength. Calculate the depth of penetration d_I in a water and ice slab for the following wavelengths and refractive indices. What inferences would you make about scattering versus absorption processes by water and ice particles at each wavelength?

Wavelength	Instrument	Refractive Index (n, κ)	
		water	ice
0.7 μm	AVHRR	(1.33, 0)	(1.31, 0)
1.6 μm	AVHRR	(1.317, 8 x 10^{-5})	(1.31, 0.0003)
3.7 μm	AVHRR	(1.374, 0.0036)	(1.40, 0.0092)
10.8 μm	AVHRR	(1.17, 0.086)	(1.087, 0.182)
0.8 cm	k-band radar	(8.18, 1.96)	(1.789, 0.0094)
10 cm	S-band radar	(5.55, 2.85)	(1.788, 0.00038)

The depths of penetration are listed on the table above. From these we can make a number of inferences about the difference between water and ice scattering at the wavelengths given. For example we expect that water surfaces and clouds will be relatively dark (relative to ice surfaces and clouds) at 3.7 μm, that ice particles are relatively transparent at 0.8 cm and more so at 10 cm, and that 1.6 μm may be useful in discriminating ice properties in clouds from water properties (glaciated clouds will be darker, all things equal, than water clouds).

AT622 Section 14
Particle Scattering

The aim here is to provide a conceptual grasp of particle scattering without inundating with complicated recipes.

Particle scattering is a complex topic—but we can simplify the view of particle scattering by visualizing the scattered radiation as composed of contributions of many waves generated by oscillating dipoles that make up the particle (Fig. 14.1). The complication is that each dipole affects the other such that the resulting field emitted by an oscillating dipole has a contribution that is due to stimulation by the incident field and a contribution due to stimulation by the fields of neighboring dipoles. Another complication is that the charge distribution in the particle forms higher order poles than dipoles and these multipoles also contribute to the scattered radiation.

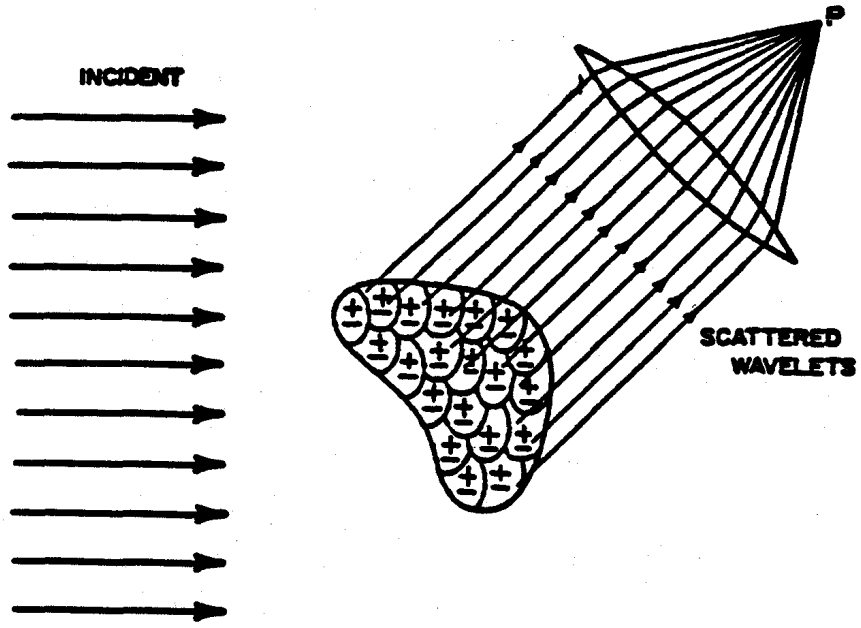

Fig. 14.1 The radiation scattered by a particle and observed at P results from the superposition of all wavelets scattered by the subparticle regions (dipoles)—from Bohren and Huffman (1983).

14.1 Scattering by a Single Dipole: Rayleigh Scattering

Assume that a spherical wave is emitted from a (spherical) dipole, i.e.,

$$\mathcal{E} \rightarrow \frac{\mathcal{E}_o}{kr} e^{-i\Phi}$$

where $\Phi = (kr - \omega t)$ is the phase of wave and k is the wavenumber. Based on arguments of geometry

$$\mathcal{E}_r = \mathcal{E}_{or}\left[\frac{e^{-ik(r-ct)}}{r}\right]k^2\alpha$$
$$\mathcal{E}_t = \mathcal{E}_{o\ell}\left[\frac{e^{-ik(r-ct)}}{r}\right]k^2\alpha\cos\theta \qquad (14.1)$$

where α is the polarizability (this is a parameter that is a 'measure' of how readily matter polarizes charges—refer to Section 4), and where radiation scattered by a single oscillating dipole is a spherical wave, which is represented by the factor in parentheses. In terms of intensities, the two components of polarized radiation therefore take the form

$$I_r = I_{or}k^4\,|\alpha|^2\,/\,r^2$$
$$I_\ell = I_{o\ell}k^4\,|\alpha|^2\cos^2\theta \qquad (14.2)$$

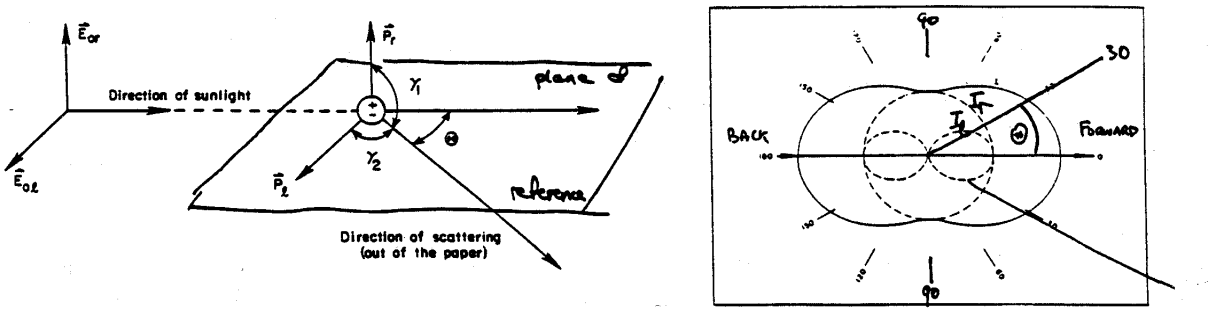

Fig. 14.2 (a) Geometry for scattering by a single dipole. Shown are the plane of reference and the orthogonal components of both the electric field and the dipole moment, which lie parallel and perpendicular to the plane. The scattering angle θ is defined on this plane. (b) Scattering pattern of a single dipole.

A special but nonetheless important case applies to an unpolarized beam of radiation, like sunlight, scattered by small particles. Unpolarized radiation can be viewed as a mixture of two independent linearly polarized beams of the same intensity. Therefore $I_{or} = I_{o\ell} = I_o/2$ and

$$I = \frac{1}{2}(I_\ell + I_r) = \frac{I_o}{2}[1+\cos^2\theta]k^4\,|\alpha|^2\,/\,r^2 \qquad (14.3)$$

describes the scattered intensity of unpolarized radiation by small particles. The scattering pattern predicted by Eqn. (14.3) is also shown in Fig. 14.3 for unpolarized incident radiation.

There are a number of consequences of Eqn. (14.3) including:

- under pure Rayleigh scattering as much radiation is scattered forward as backwards
- at $\theta = 90$, Rayleigh scattering completely polarizes unpolarized incident light (such as from the sun).
- the amount (i.e., intensity) of light scattered varies as k^4 or as λ^{-4}. Consequently, the blue portions of white light are preferentially scattered whereas the red portions of white light are preferentially transmitted.

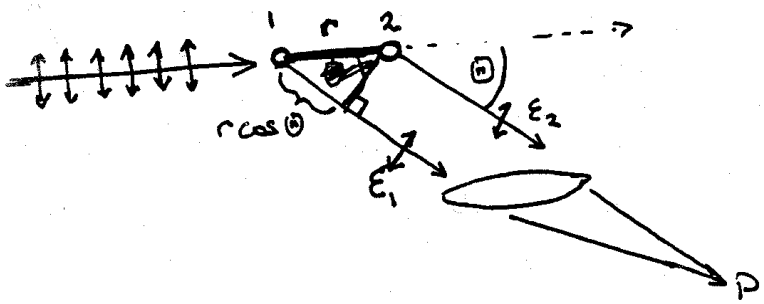

Fig. 14.3 Two isolated dipoles emit waves in all directions. At some point P far from the 'particle', these waves superimpose to create the scattered wave along the direction θ. These waves either constructively or destructively interfere depending on their relative phase difference ΔΦ, which is defined in terms of the extra distance the incident wave travels first to the second dipole (r) less the extra distance from the first dipole to P(r cos θ).

14.2 Radiation From Multiple Dipoles: Towards Understanding Scattering by Large Particles

Phase difference between waves 1 and 2 (simply proportional to the difference in path length)

$$\Delta\Phi = \frac{2\pi r}{\lambda}(1 - \cos\theta)$$

The EM waves from dipoles 1 and 2 superimpose (i.e., they add)

$$\mathcal{E}_{1+2} = \mathcal{E}_1 e^{i\Phi} + \mathcal{E}_2 e^{i\Phi+\Delta\Phi} \tag{14.4}$$

and in terms of intensity (= radiance, which is proportional to $|\mathcal{E}|^2$)

$$I(=N)_{1+2} = \text{constant}[\mathcal{E}_1^2 + \mathcal{E}_2^2 + 2\mathcal{E}_1\mathcal{E}_2\cos\Delta\Phi] \tag{14.5}$$

(Assume $\mathcal{E}_1 = \mathcal{E}_2$). Now for certain phase conditions, such as $\Delta\Phi = \pi, 3\pi, \ldots$ the fields cancel (are out of phase). For other conditions, $\Delta\Phi = 0, 2\pi, \ldots$ and the fields reinforce (Fig. 14.4a). The latter condition is always met in the forward direction, -*M* radiating dipoles (Fig. 14.4b) each radiating with an intensity *I* at $\theta = 0$ produces an intensity which *is* M^2 times the intensity of a single dipole in the forward direction. Some other general inferences are

- The larger the particle, more radiation is scattered forward
- The larger the ratio $2\pi r/\lambda$ (size parameter) the more convoluted is the scattering (i.e., more maxima and minima are expected as θ is varied, e.g., Fig. 14.5).

Although the simple discussion of multiple dipoles given above ignores the complicating effects of dipole-dipole interactions, the broad behavior predicted carries over to the more complete calculation of particle scattering illustrated, for example, in Fig. 14.5.

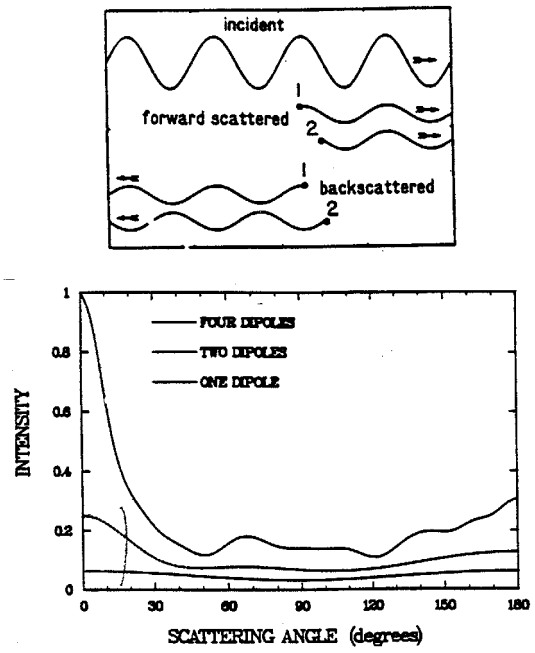

Fig. 14.4 (a) Excited by an incident wave, two dipoles scattering all directions. In the forward direction, the two waves are exactly in phase regardless of the separation of dipoles. (b) The greater the number of dipoles in the particle array, the more they collectively scatter toward the forward direction, For the example shown here, all dipoles lie on the same line, are separated by one wavelength, and interact with each other. The scattered intensity is obtained as an average over all orientations of the line of dipoles (from Bohreu, 1988).

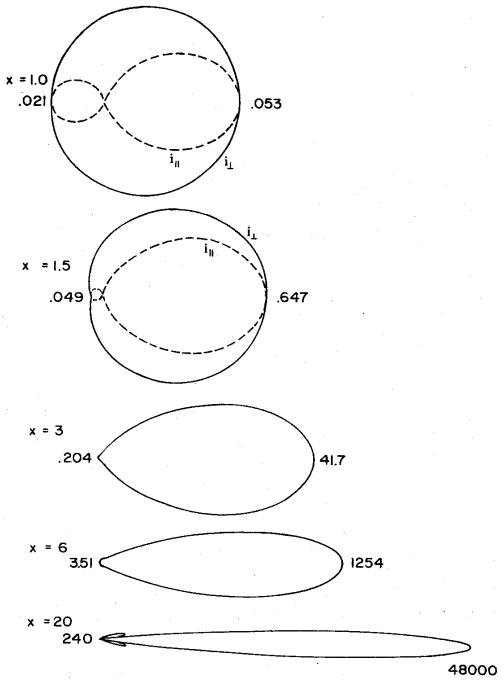

Fig. 14.5 Polar plots of the scattered intensity for the values of size parameter stated derived from Lorentz-Mie theory. The numbers indicate magnitudes in the forward and backward directions (note the scale change) - from Bohren and Huffman (1983).

14.3 Particle Extinction

Forward scattering is a special measure of the totality of the interaction. Depletion of forward propagating radiation is referred to as extinction, BUT we cannot distinguish scattering from absorption along this direction. So in addition to a measure of extinction (this is measured by the extinction coefficient), we also need a parameter that defines the ratio of extinction by scattering to extinction by absorption. This ratio defines the single scatter albedo

$$\tilde{\omega}_o = \frac{\text{amount of scattering}}{\text{total extinction}} = \text{single scattering albedo}$$

$$\tilde{\omega}_o = 1 \text{ all scattering (conservative)}$$

$$\tilde{\omega}_o = 0 \text{ all absorption (absorptive).}$$

Some idea of the general properties of $\tilde{\omega}_o$ for spherical particles of a size that is typically found in clouds is provided in Figs. 14.6a and b. Example spectra of $\tilde{\omega}_o$ for 5 and 50 μm water and ice spheres are shown for wavelengths between 0.3 and 50 μm. The spectra presented in these diagrams illustrate a number of important properties of $\tilde{\omega}_o$:

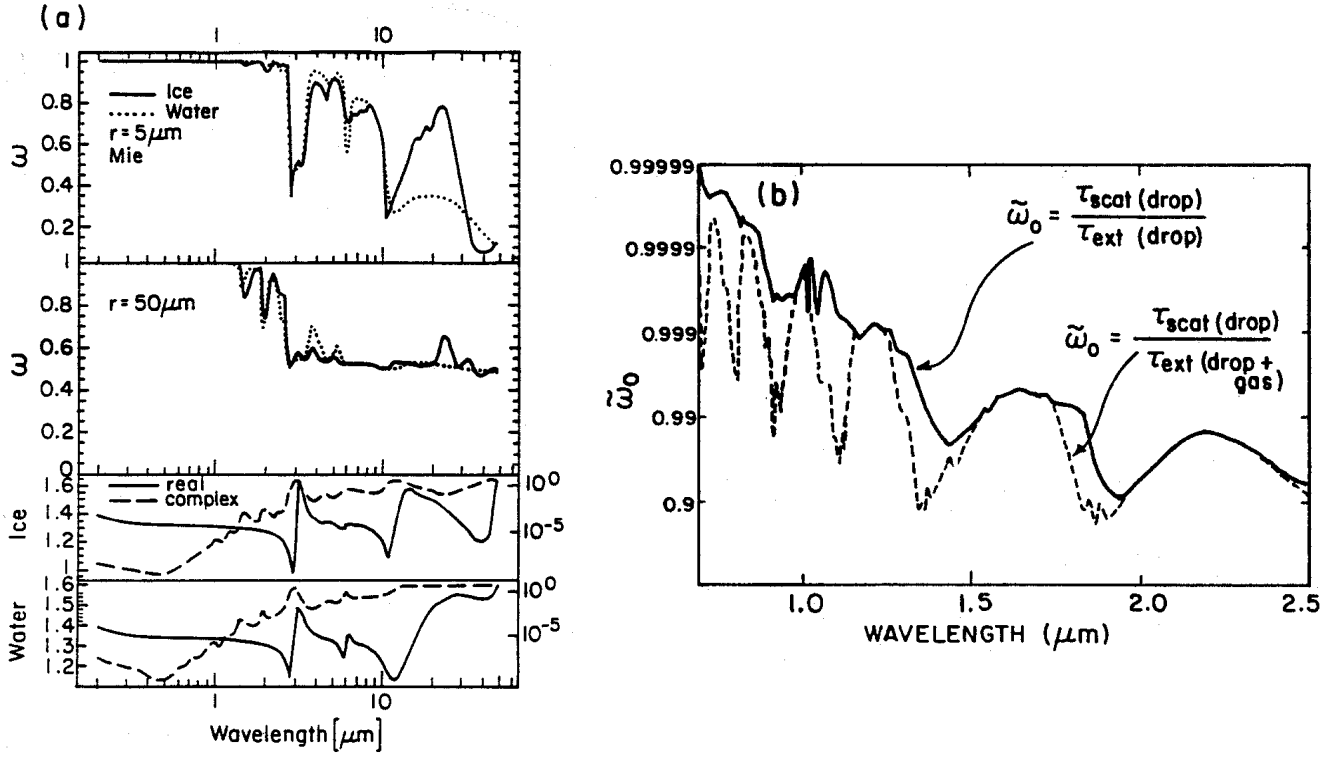

Fig. 14.6 (a) The single scatter albedo as a function of λ for 5 μm water and ice spheres. (b) The single scatter albedo of a model cloud as a function of wavelength. The solid line refers to droplet absorption alone, whereas the dashed line to droplet plus vapor absorption (from Twomey and Seton, 1980).

- values of $\tilde{\omega}_o \geq 0.99$ are typical of wavelengths less than about 1.5 μm (this is made clear in Fig. 14.6b). The spectra of $\tilde{\omega}_o$ in the visible and near infrared region is actually complex.

- The minima in $\tilde{\omega}_o$ represent absorption features by ice and water and these align with the corresponding maxima of the complex part of the refractive index κ. This is consistent with our expectations from the simple theories described below.

    - Particle absorption (to the extent it is defined by the co-albedo 1-$\tilde{\omega}_o$) is dependent on particle radius.
    - There are a number of spectral regions where the differences in $\tilde{\omega}_o$ between ice and water spheres are large. Differences that exist in the near infrared region (such as near 1.6 μm) cannot be seen but others can.

    - The single scatter $\tilde{\omega}_o$ is a volumetric quantity defined as the ratio of the scattering properties of the volume to the properties that define the total extinction by the volume. For most wavelengths of interest, this extinction is a result of both absorption and scattering by cloud particles as well as absorption by the minor gases in the volume, especially water vapor. An example of the effects of water vapor absorption on $\tilde{\omega}_o$ over the wavelength range 0.5 to 2.5 μm is presented in Fig 14.6b. What makes the problem of multiple scattering particularly troublesome at these wavelengths is the fact that both liquid water and bands containing thousands of water vapor lines overlap in the same spectral region.

(a) Cross Sections and Efficiencies

Particle extinction is conveniently defined in terms of a quantity called the extinction efficiency Q_{ext} way of visualizing this quantity (but not an entirely correct way) is provided by reference to Fig 14.7. In this simplistic view, we consider radiation as a stream of photons that flow into a volume containing the scattering particles. Each particle within the volume blocks a certain amount of radiation resulting in a reduction of the amount of radiation directly transmitted through the volume. The reduction in the radiation as it passes through a volume of spheres can be expressed in terms of a cross-sectional area C_{ext}, which is generally different from the geometric cross-sectional area of the particle. For spherical particles of radius r, the definition of Q_{ext} then follows as

$$Q_{ext} = \frac{C_{ext}}{\pi r^2}. \tag{14.6}$$

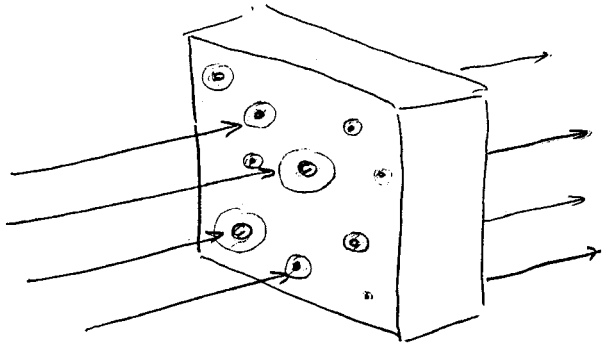

Fig. 14.7 An approximate view of particle extinction. Particles 'block' a certain amount of radiation from penetrating through the slab. The reduced transmission can be described in terms of a cross-sectional area C_{ext} shown as the shaded area around the particle. While this view of extinction is a simple one, to visualize it is not entirely correct as extinction occurs through subtle interference effects.

When C_{ext} exceeds the value of the geometrical cross-sectional area of the particle, $Q_{ext} > 1$ and more radiation is attenuated by the particle than is actually intercepted by its physical cross-sectional area. Since this extinction occurs by absorption or by scattering or by a combination of both, it follows that

$$Q_{ext} = Q_{abs} + Q_{sca} . \tag{14.7}$$

We expect that Q_{ext} depends on the refractive index of the material, the wavelength of radiation and the size of the particle. Figure 14.8 shows a plot of Q_{ext}, calculated from Lorentz-Mie theory, as a function of the size parameter x for water sphere illuminated by light of a wavelength of 0.5 μm. Somewhat obvious are the large maxima and minima with a superposition of finer scale variations (referred to as ripples). Another familiar phenomenon that follows from consideration of Fig. 14.8 *is* the *reddening* of white light as it passes through a collection of small particles. This is depicted by the rapid rise in extinction as x increases (i.e., toward shorter wavelengths) and is a general characteristic of nonabsorbing particles that are smaller than the incident wavelength. Thus, blue light is extinguished (scattered) more than red light, leaving the transmitted light reddened in comparison to the incident light. This reddening is a phenomenon that is not only limited to sunlight in the Earth's atmosphere but also for starlight reddened by interstellar dust particles. It is obvious from Fig. 14.8 that extinction is highly dependent on the size of the particle.

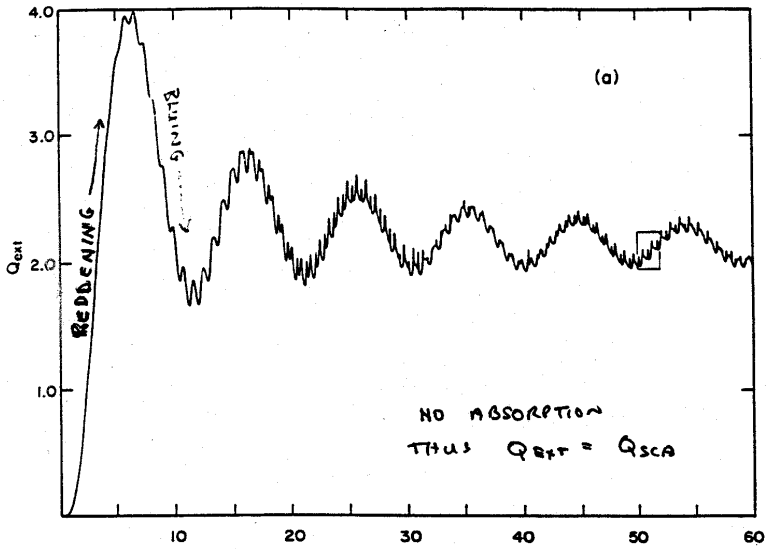

Fig. 14.8 Extinction efficiency for water droplet in air calculated for $\lambda = 0.51$ μm as a function of size parameter x. There are two ways of presenting results of this type. For the example shown, the size parameter can also be varied by changing the wavelength, while fixing the size of the particle. The results are not the same because as wavelength varies so does the refractive index and extinction depends not only on the size parameter but also on the refractive index (adapted from Bohren and Huffman, 1983).

(b) Extinction by a Cloud of Many Particles

The opposite spectral effect of reddening is the blueing of transmitted white light that occurs as the extinction decreases with increasing x on the high x side of the extinction peaks shown in Fig. 14.8. Unlike reddening, this blueing phenomenon is highly dependent on the character of the particle size distribution and occurs rarely: "once in a blue moon." In fact, this extinction feature and others that depend on particle size are obscured, if not totally obliterated, when the extinction is determined from observations of light scattered by a small volume of air containing particles of a variety of sizes. Under

atmospheric conditions, the intensity of radiation scattered by such a volume of particles may be simply obtained as the addition of the intensities of light scattered by individual particles.

Suppose

$$n(r) = \text{constant}\, r^{(1-3b)/b} e^{-r/r_m}, \tag{14.8}$$

represents the size distribution of (say) water droplets in a given volume of cloud. Some basic properties of this distribution are:

- $r_{mode} = (b - 1)r_m$
- $r_{mean} = br_m$
- $r_e = \dfrac{V}{A} = \dfrac{\int n(r) r^3 dr}{\int n(r) r^2 dr} = (b + 2)r_m$
- $LWC = \dfrac{4}{3}\pi\rho_{water} N_o r_m^3 f(3); \qquad f(\ell) = \dfrac{\Gamma(b + \ell)}{\Gamma(b)}$
- $A = \pi \int n(r) r^2 dr = \pi N_o r_m^2 f(2)$

The parameter *b is* a measure of the distribution variance and thus the width of the distribution. When the scattered fields from all particles in the volume are added, we see a general smoothing of the extinction spectrum as *b* increases. The very fine ripple structure in extinction for the monodispersed cloud (i.e., $b = 0$) disappears as *b* is systematically increased from zero and the interference structure (i.e., the broad maxima and minima) eventually fades away as the distribution widens. For the widest distributions chosen for this illustration ($b = 0.5$), the only remaining features are reddening at small size parameters, and, the asymptotic approach to the limiting value 2.

(c) The Extinction Paradox

Another important feature of the $Q_{ext} - x$ spectrum is the tendency for the extinction Q_{ext} either to oscillate around the value of 2 as $x \rightarrow \infty$ as illustrated in Fig. 14.8 or to converge to the value of 2 as in the cases of Fig. 14.9. This behavior of particle extinction is referred to as the *extinction paradox.* Why a paradox? Intuition suggests that if we consider extinction as just the radiation that is blocked by the particle, like that illustrated in Fig. 4.7, then the extinction cross section is just the shadow projected by the very large particle. This geometrical view of extinction predicts that the limiting value of Q_{ext} is 1 and not 2. However, no matter how large the particle, it still has an edge, and in the vicinity of the edge rays do not behave the way our simple geometrical arguments say they should. The energy removed from the forward direction can be thought of as being made up of a part that represents the amount blocked by the cross-sectional area of the particle and a part diffracted around the particle's edge. The diffracted amount eventually fills in the shadow area when viewed far enough from the particle. The total amount removed from the incident beam by diffraction is therefore also characterized by the particle cross-sectional area. The net result is that an amount twice the cross-sectional area of the particle is scattered out of the incident beam. We learn from this, and further discussion below, that particle extinction is not just a process of blocking light, but is actually a result of more subtle interference effects (Fig. 14.10).

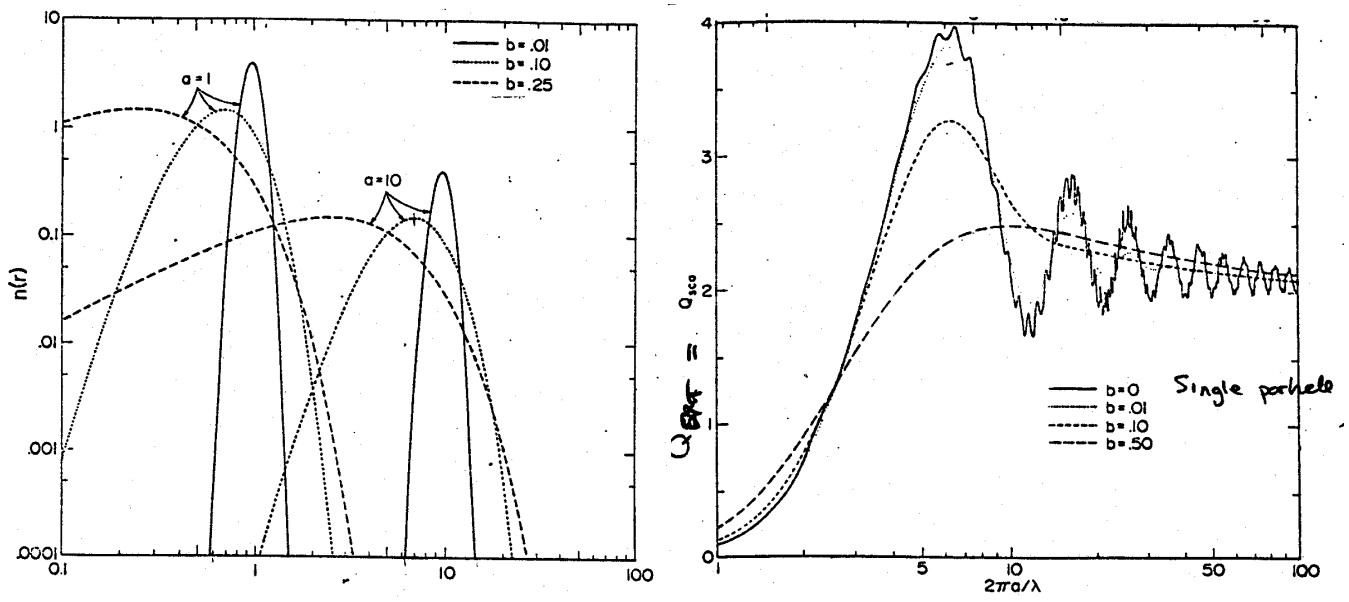

Fig. 14.9 (a) Standard size distribution (14.8) for 2 values of a and three values of b. The size distribution is normalized so that the integral over all sizes is N = 1. (b) The extinction efficiency, Q_{ext}, as a function of the effective size parameter $x = 2\pi a/\lambda$ for the values of effective variance b given. Mie theory was used with a refractive index $n' = 1.33$, $\kappa = 0$ (after Hansen and Travis 1974).

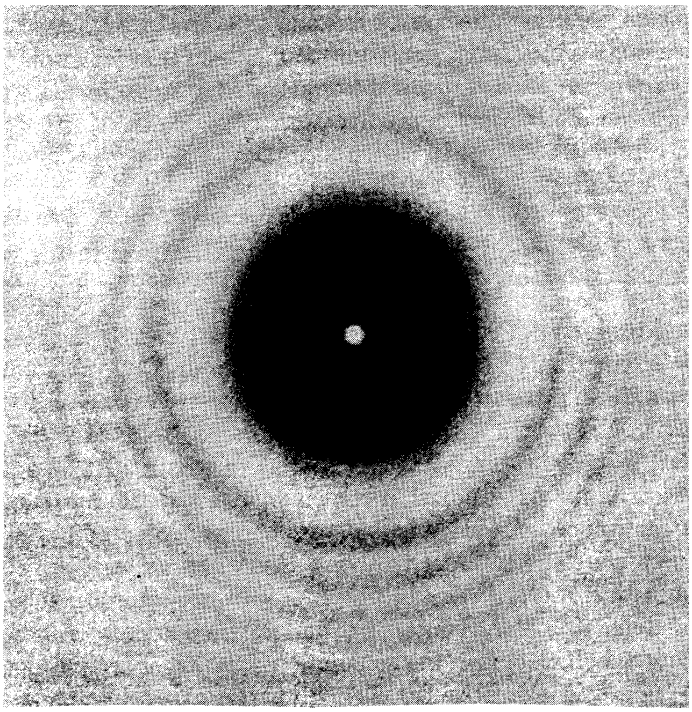

Fig. 14.10 An illustration of the extinction paradox. The photograph shows the diffraction pattern produced by a round stop. In the middle is the Poisson spot. The image is created by observing a light source obscured at some distance by a ball bearing of 10 mm diameter. The telescope is located several meters behind this obstacle.

14.4 A Simple Model of Particle Extinction

General references:

Van deHulst, 1957: Chapts. 3 and 11

Stephens, 1984: *Appl. Opt*., **23**, 954-959.

Ackerman S. and G.L. Stephens, 1987 *J. Atmos. Sci.,*

G.L. Stephens, 1994: *Remote Sensing.,*

(a) Fundamental Extinction Formula

Consider a plane wave incident on a particle that we choose to write as

$$\mathcal{E}_o = e^{-ikz+iwt} \tag{14.9}$$

where we conveniently assume the wave has a unitary amplitude.

Suppose the scattered wave at O' in Fig. 14.11 is a spherical wave of the form[1]

$$\mathcal{E}_{sca} = S(\theta)\frac{e^{-ikr+iwt}}{ikr} \tag{14.10}$$

that introduces the function $S(\theta)$, which we hereafter refer to as the amplitude function. This function accounts for the fact that the intensity of the scattered radiation varies with scattering angle θ. Now extinction is defined at $\theta = 0$ and C_{ext} can be derived in terms of $S(\theta)$—this relation is known as the fundamental extinction formula. In deriving this relation, consider points near $\theta = 0$ such that[2]

$$r \approx z + \frac{x^2 + y^2}{2z}$$

provided $x, y << z$. The resultant wave is

$$\begin{aligned}\mathcal{E}_{sca} + \mathcal{E}_o &= \frac{S(\theta=0)}{ikz}e^{-ik(z+(x^2+y^2)/2z)+iwt} + e^{-ikz+iwt} \\ &= \mathcal{E}_o\left[1 + \frac{S(\theta=0)}{ikz}e^{-ik(x^2+y^2)/2z}\right]\end{aligned}$$

[1] In the derivation of Van deHulst (1957, p.29), the complex factor i appears in the denominator for reasons that become evident in his derivation of cross sections. We will not outline these derivations here and choose to omit this factor in our discussion.

[2]
$$\left[r = (z^2 + x^2 + y^2)^{1/2} = z\left(1 + \frac{x^2 + y^2}{z^2}\right)^{1/2} \approx z\left(1 + \frac{x^2 + y^2}{2z^2}\right)\right]$$

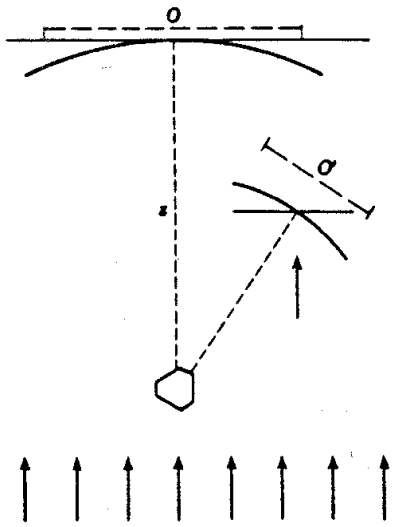

Fig. 14.11 An arbitrary particle that scatters a plane wave to the point O'.

The intensity is obtained by squaring the modulus of this expression

$$I(x,y) \approx |\, E + E_o \,|^2 = |\, E_o \,|^2 \left[1 + \frac{2}{kz} \Re e \left\{ \frac{S(\theta = 0)}{i} e^{-ik(x^2+y^2)/2z} \right\} \right]$$

Now, the total intensity is

$$\int_{area} \int I(x,y)dxdy \Rightarrow I_o \iint dxdy + \frac{2I_o}{kz} \iint \Re \left[\frac{S(\theta = 0)}{i} e^{-ik(x^2+y^2)/2z} \right] dxdy \qquad (14.11)$$
$$\approx O - C$$

where O is the integral of the first term and corresponds to the geometric area projected by the particle on a distant screen and C is the integral of the second term and can be interpreted as the amount of light reduced by the presence of the particle (due to extinction). This integral reduces to

$$C_{ext} = \frac{4\pi}{k^2} \Re e[S(\theta = 0)]; \quad \text{thus, } Q_{ext} = \frac{4}{x^2} \Re e[S(\theta = 0)]. \qquad (14.12)$$

(b) Anomalous Diffraction Theory

One may gain the false impression, both from Fig. 14.7 and from the arguments leading to Eqn. (14.12) that extinction occurs through blocking an amount of incident light of magnitude C_{ext}. In fact, extinction is a subtle interference phenomenon and not one of merely a blocking of light as the extinction paradox reminds us. In discussing this paradox, we learn that the particle not only 'blocks' an amount of light that is defined by the geometric cross section but also removes some of the energy of the original wave via interference. A relatively simple, but nonetheless useful model of extinction is provided by the anomalous diffraction theory of Van de Hulst (1957, Ch. 11), which seeks to model these interferences.

In the ADT of van de Hulst, we are interested in defining the characteristics of the wave on a reference "screen" V far removed from the particle (Fig. 14.12). We argue that the characteristics of this

wave at V are governed only by diffraction resulting from interference between the ray just outside the particle to one that passes through the particle. A difference in phase between these rays creates this interference. The basis that we claim these can interfere results from considering that V is infinitely far from the particle and that the particle is both large (such that we can trace rays through it and 'soft' so that refraction at the surface interface is negligible).

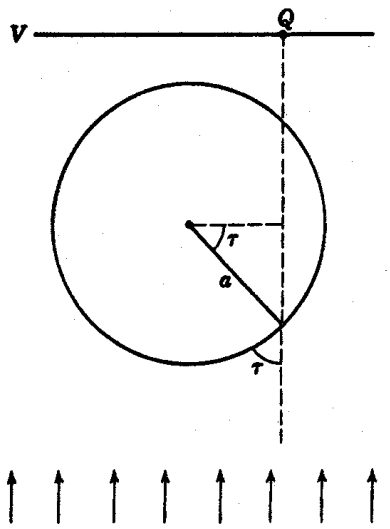

Fig. 14.12 Ray passing through sphere.

We begin by noting that the extinction paradox predicts

$$C_{ext} = 2G \tag{14.13}$$

where G is the geometric cross section leading to a value of $Q_{ext} = 2$ when $r \to \infty$. From this and Eqn. (14.12) it follows that

$$S(\theta = 0) = \frac{k^2}{2\pi} G \tag{14.14}$$

Now consider a transparent particle with a ray traversing it along the direction drawn in Fig. 14.12. The phase difference between the ray outside the particle to the ray that penetrates the particle at an angle φ as shown in Fig. 14.12 is

$$\Delta\phi = 2x(m-1)\sin\varphi = \rho\sin\varphi$$

where ρ defines the phase shift of the central ray. At point Q the amplitude $\mathcal{E}_Q$ is

$$\mathcal{E}_Q = e^{-\Delta\phi} = e^{-i\rho\sin\varphi}$$

for an amplitude of the incident wave $\mathcal{E}_o$. Thus the net attenuation is

$$S(\theta = 0) = \frac{k^2}{2\pi} \iint [1 - e^{-i\rho \sin \varphi}] dx dy$$

where the integral is taken over the geometric shadow area of the particle. With substitution and change of coordinates, the above integral can be evaluated (refer Van de Hulst, p175) to yield

$$S(\theta = 0^\circ) = x^2 K(i\rho) \tag{14.15}$$

where

$$K(w) = \frac{1}{2} + \frac{e^{-w}}{w} + \frac{e^{-w} - 1}{w^2},$$

and thus

$$Q_{ext} = 4\Re e(K(i\rho)). \tag{14.16}$$

Figure 14.13 shows examples of Q_{ext} calculated using this simple formula and compares it to the Lorentz-Mie formula. Clearly the approximate formula has some shortcomings (no ripple structure) but the overall characteristics of the Q_{ext} curves are well represented (especially as $m \rightarrow 1$). The simple theory also allows us to interpret the larger maxima and minima as interference features. The approach is very simple and readily adapted to non-spherical particles. It may prove to be a desirable way of incorporating scattering parameters into atmospheric circulation models for example.

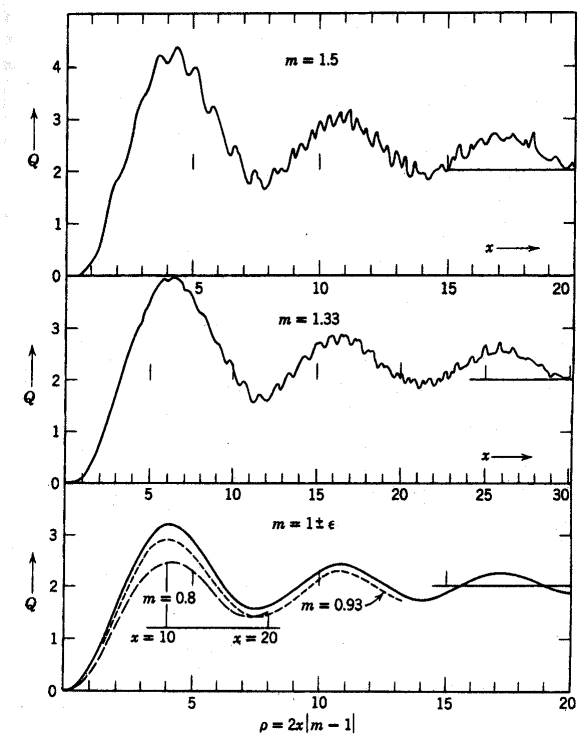

Fig. 14.13 Extinction curves computed from Mie's formulas for m = 1.5, 1.33, 0.93, and 0.8. The scales of x have been chosen in such a manner that the scale of $\rho = 2x \mid m - 1 \mid$ is common to these four curves and to the extinction curve for $m - 1 = \pm\varepsilon$.

Absorbing particles can also be simply handled in the ADT approach. If $m = n - i\kappa$, then we can define the quantity

$$\tan\beta = \frac{\kappa}{n-1}$$

and note that β is very small for most solar wavelengths (see Fig. 14.14).

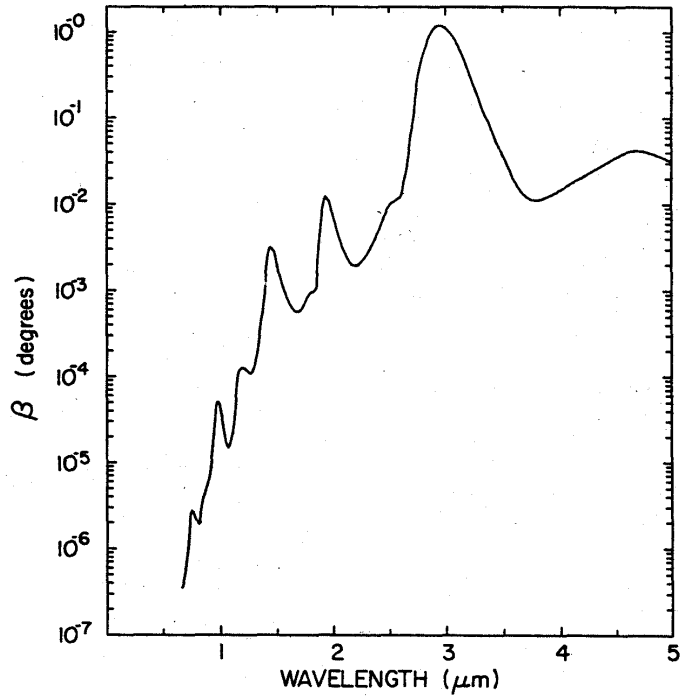

Fig. 14.14 The angle as a function of wavelength for water

The phase shift of the central ray is then

$$\rho^* = 2x(m-1) = \rho(1 - i\tan\beta) \tag{14.17}$$

where $\rho = 2x(n - 1)$ and from Eqn. (14.16)

$$Q_{ext} = 4\Re e[K(i\rho + \rho\tan\beta)] \tag{14.18}$$

The energy absorbed inside the sphere is simply calculated by considering the dampening factor of the wave in the particle. The waveform is

$$\exp(-i\rho^*\sin\tau) \rightarrow \exp[-2x\kappa\sin\tau] \quad \exp[-i\rho\sin\tau].$$

The decrease in **intensity** on passage through the particle is therefore

$$1 - e^{-4x\kappa\sin\varphi}$$

which is due to absorption. Thus

$$Q_{abs} \cong \frac{1}{\pi r^2}\iint [1 - e^{-4x\kappa \sin\varphi}]dxdy$$

and

$$Q_{abs}\, 2K(4x\kappa) \tag{14.20}$$

where $v = 4x\kappa$ serves as a particle absorption similarity parameter—i.e., absorption by two particles one of radius a_1 and composition κ_1, and the other of radius a_2 and composition κ_2, are identical (self similar) when $v_1 = v_2$. Figure 14.15 presents a plot of Q_{abs} as a function of v from Eqn. (14.20) and contrasts this with efficiencies derived from Lorentz-Mie theory, assuming ice spheres. The ADT results match those of Lorentz-Mie when v is small (which is the range of validity of the ADT). Spectra of Q_{abs}, also indicate reasonable agreement and serve to remind us that this absorption is sensitive to particle size.

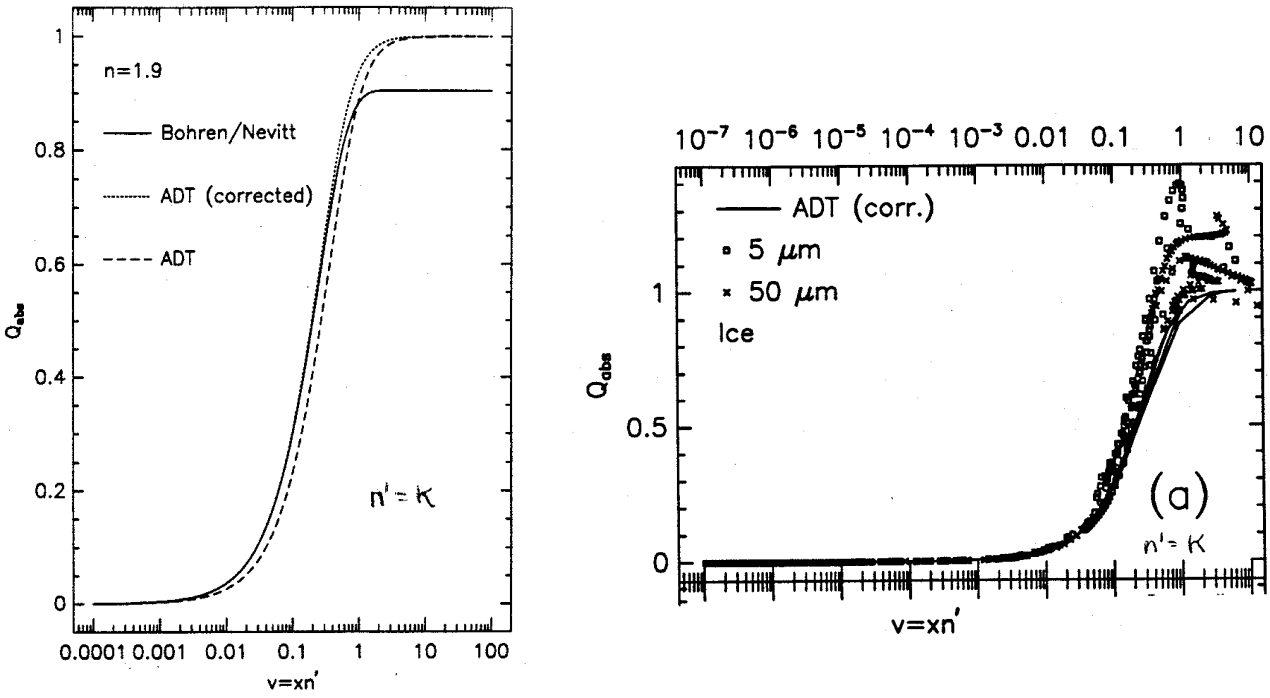

Fig. 14.15 The absorption efficiency as a function of v. Spectra of Q_{abs} and v as a function of wavelength for 5 μm and 10 μm water spheres.

14.5 Extinction Coefficients and Optical Depths

The extinction coefficient (in this case, volume extinction coefficient) is defined as

$$\sigma_{ext} = \pi \int n(r) Q_{ext} r^2 dr \tag{14.21}$$

for spherical particles. Similar expressions apply to scattering and absorption. Based on dimensional arguments, $n(r) \rightarrow L^{-4}$, $r^2 \rightarrow L^2$, and $dr \rightarrow L$ and $\sigma \rightarrow L^{-1}$. *By* definition, the optical **depth** is

$$d\tau = \sigma_{ext} dz$$

(a) Rayleigh Scatter (Liou, p76-79)

$$\tau_{RAY}(p) = \int_p^0 \sigma_{ext}(p) \frac{dz}{dp'} dp'$$

O_2 and N_2 are conservative scatterers and the scattering cross section per unit molecule is

$$\sigma_{sca} = \frac{8\pi^3 (m^2 - 1)^2}{3\lambda^4 N_s^2} f(\delta),$$

where $f(\delta)$ accounts for depolarization effects induced by the nonsphericity of the molecule [$f(\delta) = (6 + 3\delta)/(6 - 7\delta)$], $\delta = 0.035$. The optical depth is thus

$$\tau(\lambda) = \sigma_{sca} \int N(z')dz'$$

where $N(z)$ is the number concentration of molecules as a function of height. Since this is proportional to pressure,

$$\tau(p, \lambda) = \tau_o(\lambda) p / p_o$$

A convenient parameterization of the Rayleigh optical depth is

$$\tau_{RAY}(z) = 0.0088\lambda^{-4.15+0.2\lambda} \exp[-0.1188z - 0.0016z^2]$$

where z is expressed in km. The variation different than λ^{-4} arises through the slight dependence of a (polarizability) on λ.

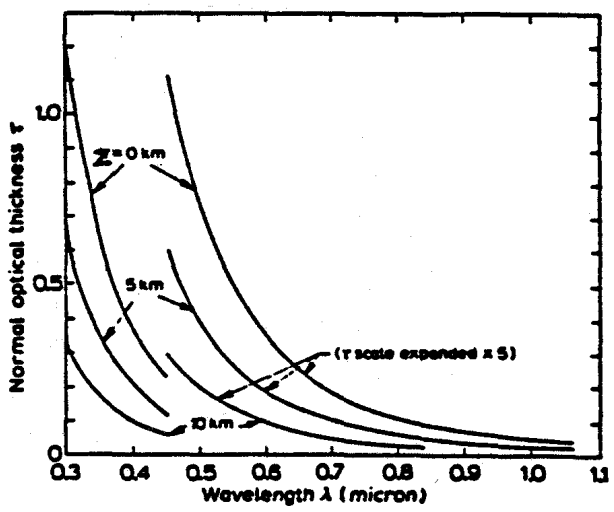

Fig. 14.16 Rayleigh normal optical thickness between the top of the atmosphere and the altitudes given on the figure. (From Marggraf and Griggs, 1969).

(b) Cloud Optical Depth (at Solar Wavelengths)

$$\tau_{cloud} = \int \sigma_{ext} dz$$

where

$$\sigma_{ext} = \int n(r) Q_{ext} \pi r^2 dr$$

At these wavelengths and for tropical cloud droplet sizes, $x >> 1$ so that

$$Q_{ext} \to 2$$

(the extinction paradox). Thus

$$\tau_{cloud} \cong 2 \iint n(r) \pi r^2 dr dz$$

With the following definitions

$$w = \frac{4}{3} \pi \rho \int n(r) \pi r^3 dr \qquad \text{(liquid water content)}$$

$$r_e = \int n(r) \pi r^3 dr \Big/ \int n(r) \pi r^2 dr \qquad \text{(effective radius)}$$

it follows that

$$\tau \sim \frac{3}{2} \frac{W}{r_e} \tag{14.22}$$

where $W = \int w(z') dz'$ = liquid water path. Thus extinction is inversely proportional to r_e –this is important as it says that clouds composed of high concentrations of small droplets are optically thicker than clouds composed of fewer but larger droplets.

(c) Cloud Optical Depth (IR)

Let's suppose that only the absorption of IR radiation by cloud particle is important. Then the optical thickness is

$$\tau \sim \tau_{abs} \sim \int_0^{\Delta z} \int_0^{\infty} n(r) \pi r^2 Q_{abs} dr dz \tag{14.23a}$$

0 0

For IR wavelengths and cloud droplets ~ few microns, the size parameter is small and Q_{abs} is approximately a linear function of x and thus r (e.g., Fig. 14.17).

To some limit, we can approximate Q_{abs} by

$$Q_{abs} \sim \text{constant} \cdot r, \quad r < r_m$$

where r_m is the characteristic radius of the distribution $n(r)$. On substitution

$$\tau_{abs} \sim \int_0^{\Delta z} \quad \text{constant} \quad \left\{ \int n(r) \pi r^3 dr \right\} dz$$

the terms in brackets is proportional to the cloud liquid water, therefore

$$\tau_{abs} \cong \text{constant} \cdot W \tag{14.23b}$$

where W is cloud liquid water path.

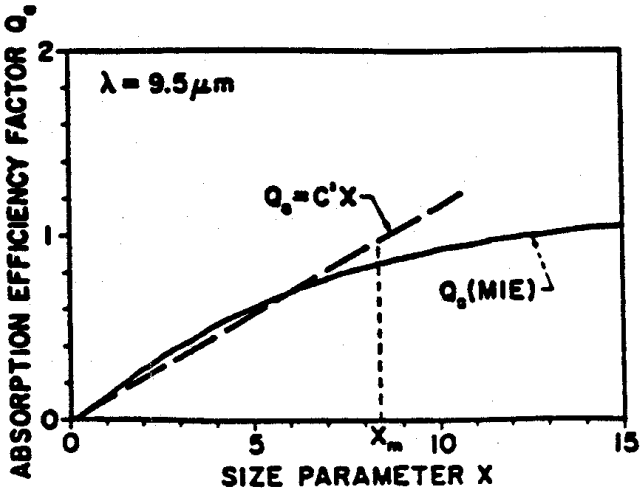

Fig. 14.17 The Mie absorption efficiency Q_s as a function of size parameter $x = (2\pi r/\lambda)$ and thus, of particle size for $\lambda = 9.5$ μm, x_m corresponds to $2\pi r_m/\lambda$ where r_m is referred to in the text (from Pinnick et al., 1979).

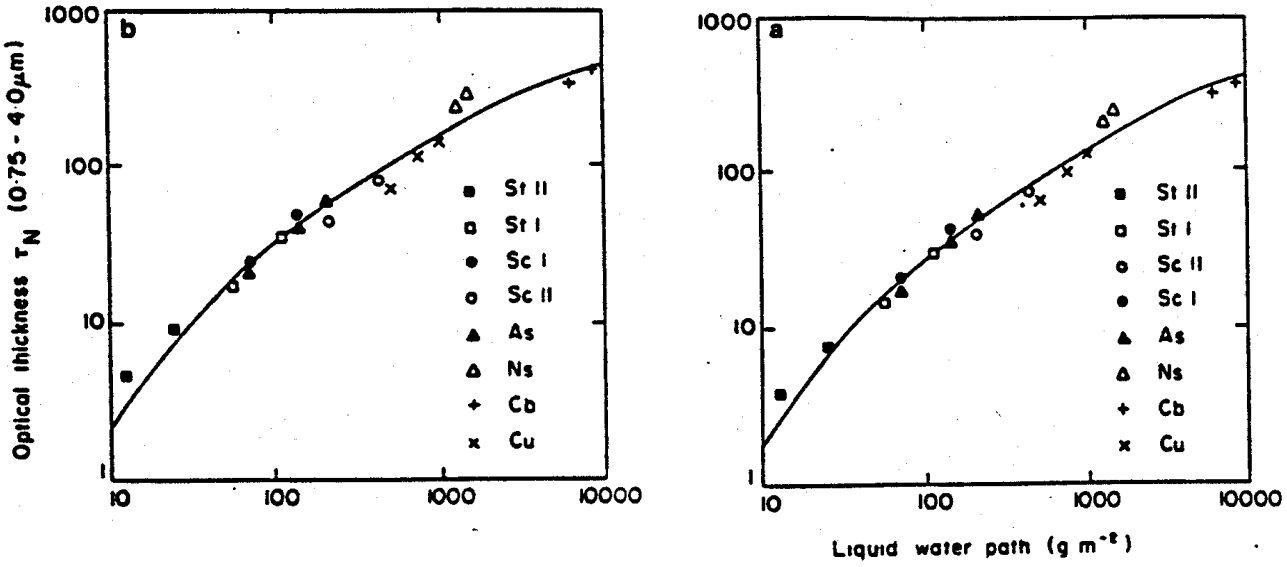

Fig. 14.18 The broadband optical thickness for the 0.3—0.75 μm (a) and 0.75—4.0 μm (b) regions as a function of liquid water path and for several cloud types.

14.6 Scattering Phase Function

The scattering pattern is described in terms of the amplitude function $S(\theta)$. We can gain a better grasp of this function by considering the following experiment. In this experiment, a particle of arbitrary shape is illuminated by a plane wave traveling from the negative z direction as shown in Fig. 14.11. A detector is placed at O' some distance R from the particle and is moved around the particle at this distance. The field incident on the particle is

$$\mathcal{E}_{inc} = \mathcal{E}_o e^{-ikz+iwt}. \tag{14.24}$$

and the field measured at O' is (refer to Eqn. (14.7))

$$\mathcal{E}_{sca} = S(\theta)\frac{e^{-ikR+iwt}}{kR}. \tag{14.25}$$

This field can be expressed in terms of the incident field at the particle by combining Eqns. (14.24) and (14.25)

$$\mathcal{E}_{sca} = S(\theta)\frac{e^{-ikr+ikz}}{kr}\mathcal{E}_o,$$

and in terms of intensities it follows that

$$I_{sca} = \frac{|S(\theta)|^2 I_o}{k^2 R^2}. \tag{14.26}$$

It is more usual to describe the angular patterns of scattered light in terms of a quantity referred to as the scattering phase function.[3] We can consider the relation of the phase function to the amplitude function in the following way. Consider an instrument located at the position at O'. If the area of the detector is dA, then the amount of radiation received by the detector is contained in the set of directions confined to a small solid angle element $d\Omega = dA/r^2$. Therefore the total energy per unit time at a given wavelength that is received by a detector capable of measuring the scattered radiation over the entire range of solid angles is

$$dw = I_{sca} dA \approx R^2 \int_{\Xi} I_{sca} d\Omega = \frac{I_o}{k^2}\int_{\Xi} |S(\theta)|^2 \, d\Omega \tag{14.27}$$

where Ξ is used to denote the entire sphere of directions over which the integration is taken. Now we mentioned that the total amount of radiation scattered by a particle can be defined in terms of its scattering cross-sectional area C_{sca}. By definition,

$$I_o C_{sca} = R^2 \int_{\Xi} I_{sca} d\Omega, \tag{14.28}$$

[3] The use of the word phase to name this function has no relation to the phase of the wave but originates from the astronomical literature where it refers to lunar phases.

and

$$C_{sca} = \frac{1}{k^2}\int_{\Xi} |S(\theta)|^2 \, d\Omega \,. \tag{14.29}$$

These relationships provide us with the definition of the scattering phase function $P(\theta)$

$$\frac{P(\theta)}{r\pi} = \frac{|S(\theta)|^2}{k^2 C_{sca}} \tag{14.30}$$

which is a unitless quantity and when integrated over solid angle obeys the following condition

$$\frac{1}{4\pi}\int_{\Xi} P(\theta) d\Omega = 1. \tag{14.31}$$

This is an energy conservation condition, which simply states that in the absence of absorption the energy scattered in all directions around the particle must be just that amount that has been decreased from the original direction of propagation of the incident field.

Figure 14.19 presents plots of the phase function derived from Lorentz-Mie theory for spheres of varying size.

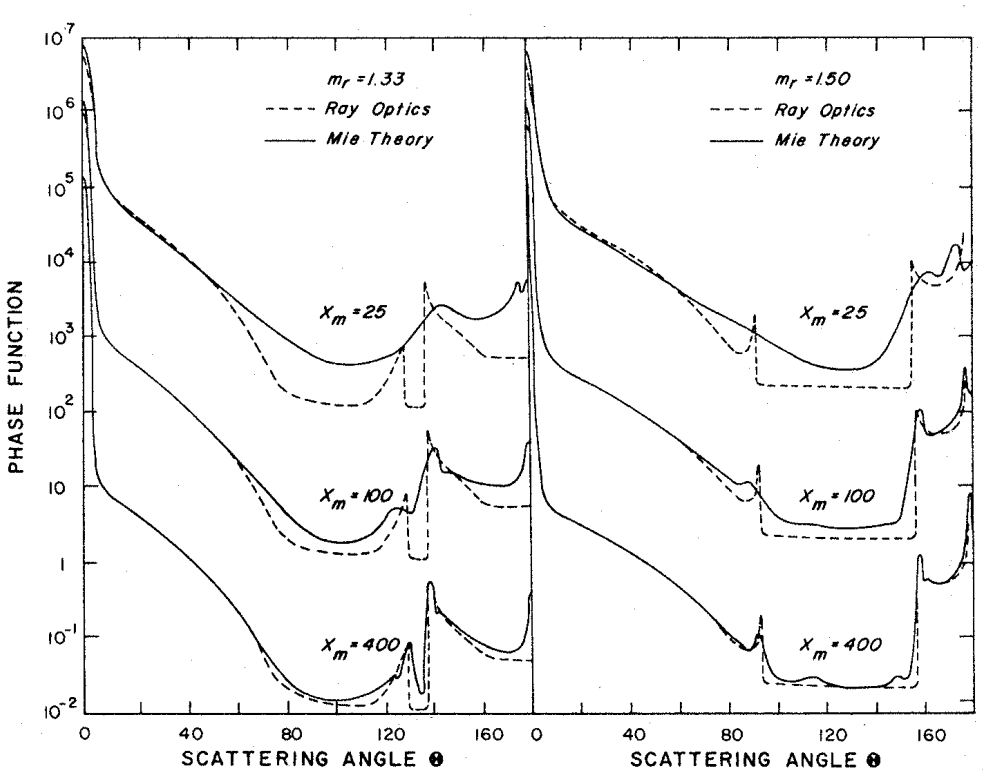

Fig. 14.19 Comparison ray optics and Lorentz-Mie theory for phase functions derived from three size distributions ($x_m = 2\pi r_m/\lambda$) and two values of refractive index.

(a) Parameters of the Scattering Phase Function

One parameter that usefully characterizes the asymmetry of particle scatter is the asymmetry parameter. It is defined as

$$g = \frac{1}{2}\int_{-1}^{+1} P(\cos\theta)\cos\theta d\cos\theta \,. \tag{14.32}$$

Note that $g = 1$ is complete forward scatter and $g = 0$ is isotropic and symmetric scatter (e.g., Rayleigh scatter).

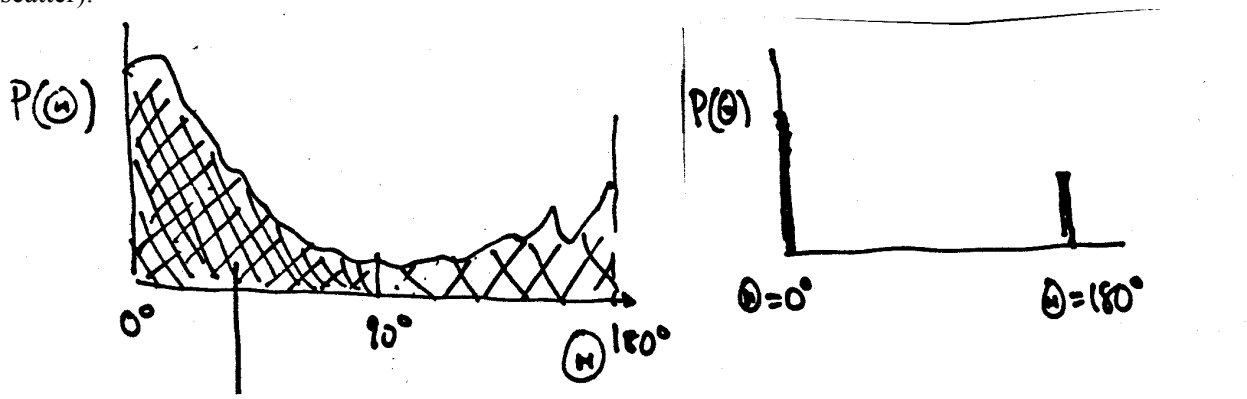

Consider as an example, the simplistic phase function shown below.

Forward scatter:

$$f = \frac{1}{4\pi}\int_0^{2\pi}\int_0^{1} P(\cos\theta)\sin\theta d\theta d\Phi$$

Backscatter:

$$b = \frac{1}{4\pi}\int_0^{2\pi}\int_{-1}^{0} P(\cos\theta)\sin\theta d\theta d\Phi$$

Normalization:

$$f + b = 1$$

For the simple phase function illustrated, it follows that

$$g = (+1)f + (-1)b$$

and

$$b = (1 - g)/2$$

$$f = (1 + g)/2$$

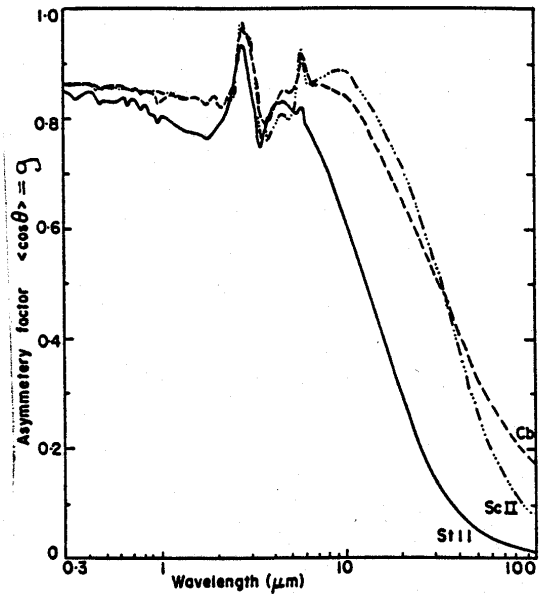

Fig. 14.20 The asymmetry factor as a function of wavelength for the three cloud models.

(b) Simple Parameterization of the Scattering Phase Function

We find it convenient to present the phase function by

$$P(\cos\theta) = \sum_{\ell=0}^{N} \chi_\ell P_\ell(\cos\theta)$$

where P_ℓ is the ℓ^{th} order Legendre polynomial and χ_ℓ are the associated expansion coefficients. (Refer to exercise 14 (summer lecture course), for further discussion of phase function expansions.) A general rule of thumb is, the larger the particle the more terms are required to represent the phase function (Fig. 14.21).

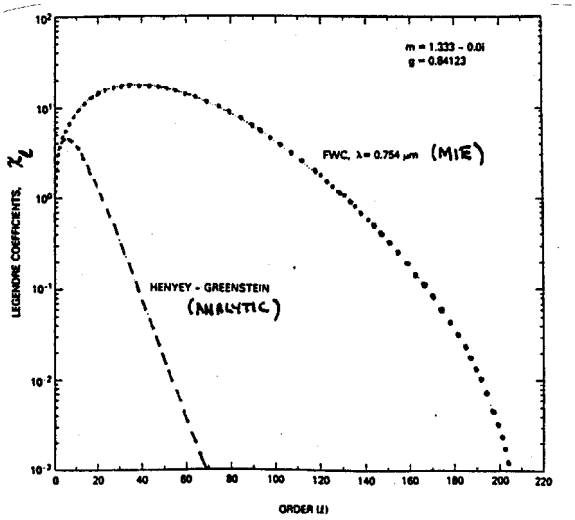

Fig. 14.21 Coefficients of the Legendre polynomial expansion for a hypothetical cloud model derived for both Lorentz-Mie and Henyey-Greenstein phase functions.

A specific form of phase functions useful in cloud calculations is the Henyey-Greenstein phase function. The H-C function decays monotonically with θ unlike real functions that possess glories, rainbows, and other optical phenomena (Fig. 14.22). It can be expressed in terms of g as

$$P_{HG}(\cos\theta) = \frac{1 - g^2}{(1 + g^2 + 2g\cos\theta)^{3/2}}$$

which has a very convenient expansion

$$P_{HG}(\cos\theta) = \sum_{\ell} (2\ell + 1) g^{\ell} P_{\ell}(\cos\theta)$$

Combinations of H-G functions have been proposed to model the scattering in the back-hemisphere more realistically. An example is the double H-G function

$$\begin{aligned} P_{DHG} &= bP_{HG}(g_1) + (1-b)P_{HG}(g_2) \\ \overline{g} &= \text{effective asym. parameter} \\ &= bg_1 + (1-b)g_2 \end{aligned}$$

which is also graphically illustrated in Fig. 14.22c

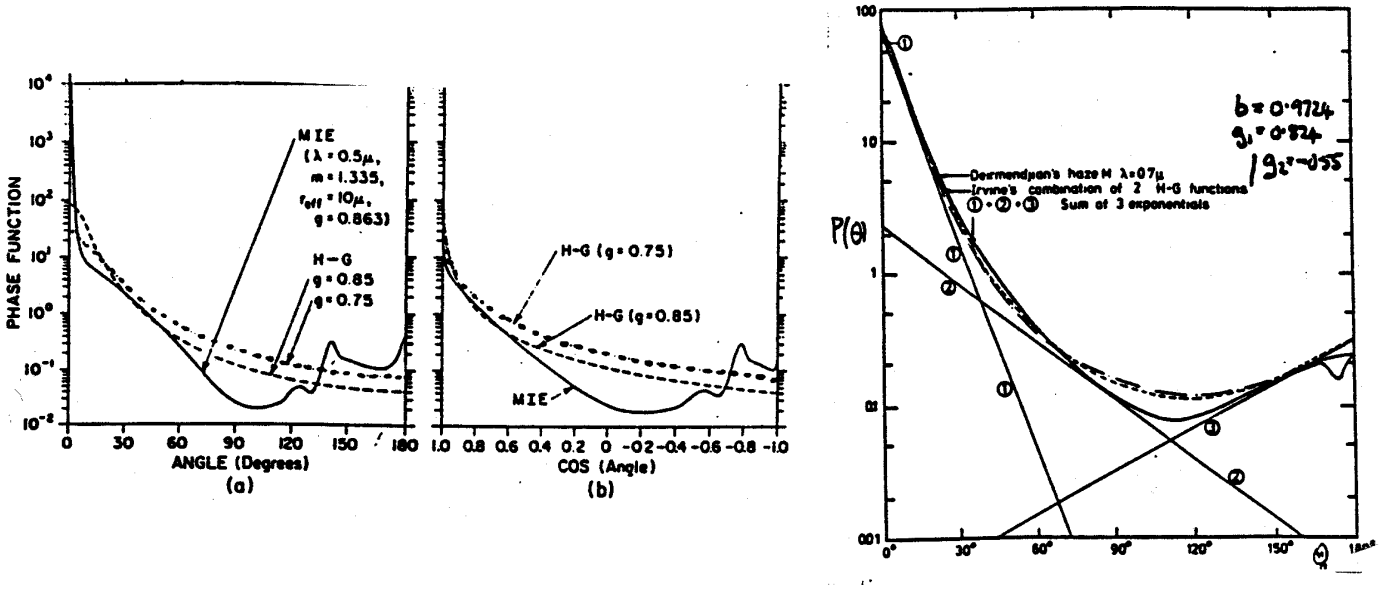

Fig. 14.22 Comparison of three different phase functions plotted as functions of (a) θ and (b) cos θ. Two are Henyey-Greenstein functions with g = 0.75 and 0.85 and with values at θ = 0 of 28 and 86, respectively. The third is a Lorentz-Mie case for a polydisperse water cloud of effective radius 10 μm, with a value of 9.7 x 10^3 at θ = 0. (c) Example of a double H-G function with the values of b, g_1 and g_2 as indicated.

14.7 Scattering by Spheres: A Brief Outline of Lorentz-Mie Theory

The theory for scattering by dielectric spheres was developed independently by Lorentz in 1890 and Gustav Mie in 1908 (refer to the discussion of these developments in the bibliographical discussions at

the end of this chapter). The derivation of the solution is a straightforward application of classical electromagnetic theory so only the resulting formulae are given here.

(a) General Formulae

Mie's solutions for scattering by a dielectric sphere are infinite series whose rates of convergence depend on the value of the size parameter x. The two scattering amplitude functions have the form

$$S_1(\theta) = \sum_{n=1}^{\infty} \frac{2n+1}{n(n+1)} [a_n \pi_n(\cos\theta) + b_n \tau_n(\cos\theta)], \tag{14.33a}$$

$$S_2(\theta) = \sum_{n=1}^{\infty} \frac{2n+1}{n(n+1)} [a_n \tau_n(\cos\theta) + b_n \pi_n(\cos\theta)], \tag{14.33b}$$

where

$$\begin{aligned} \pi_n(\cos\theta) &= \frac{1}{\sin\theta} P_n^1(\cos\theta) \\ \tau_n(\cos\theta) &= \frac{d}{d\theta} P_n^1(\cos\theta), \end{aligned} \tag{14.34}$$

and where P_n^1 is the associated Legendre polynomial (e.g., Abromowitz and Stegun 1971). The coefficients a_n and b_n are referred to as Mie scattering coefficients and are functions of refractive index m and size parameter x. The mathematical forms of these coefficients are given as ratios of Ricatti-Bessel functions. The extinction and scattering efficiencies are also series

$$Q_{ext} = \frac{2}{x^2} \sum_{n=1}^{\infty} (2n+1) \operatorname{Re}(a_n + b_n) \tag{14.35a}$$

$$Q_{sca} = \frac{2}{x} \sum_{n=1}^{\infty} (2n+1)(|a_n|^2 + |b_n|^2). \tag{14.35b}$$

AT622 Section 15
Radiative Transfer Revisited: Two-Stream Models

The goal of this section is to introduce some elementary concepts of radiative transfer that accounts for scattering, absorption and emission and introduce simple ways of solving multiple scattering problems. We introduce simple models to solve the relevant radiative transfer equation and demonstrate how they offer a glimpse at the intricate way in which the radiance field depends on the properties of the scattering and absorbing medium.

15.1 Scattering as a Source of Radiation

Photons flowing along a given direction are removed by single scattering as Beer's law predicts. However, these photons can actually reappear again along that same direction when scattered a multiple number of times. In fact, many of the scattering media of interest to studies of the atmosphere are multiple scattering media, that is media containing a sufficient number of scatterers that photons traversing it are likely to be scattered more than once. Multiple scattering of sunlight, for instance, gives rise to many observable phenomena that cannot be explained from single scattering arguments alone. For example, single scattering predicts a sky that is of uniform brightness and color contrary to what we observe. The whiteness and brightness of clouds is also a result of multiple scattering. Reflection of visible and microwave radiation from various surfaces is largely influenced by multiple scattering. Multiple scattering is thus relevant to many topics and we need to develop a mathematical description of how these photons reappear along the reference direction in order to account for it.

Consider a beam of monochromatic radiation flowing along a direction defined by the vector $\vec{\xi}'$ illuminating a small volume located at $\vec{r}$ and of length *ds* containing scattering particles (Fig. 15.1). The volume is taken to be small enough that only single scattered photons emerge from it. The incremental

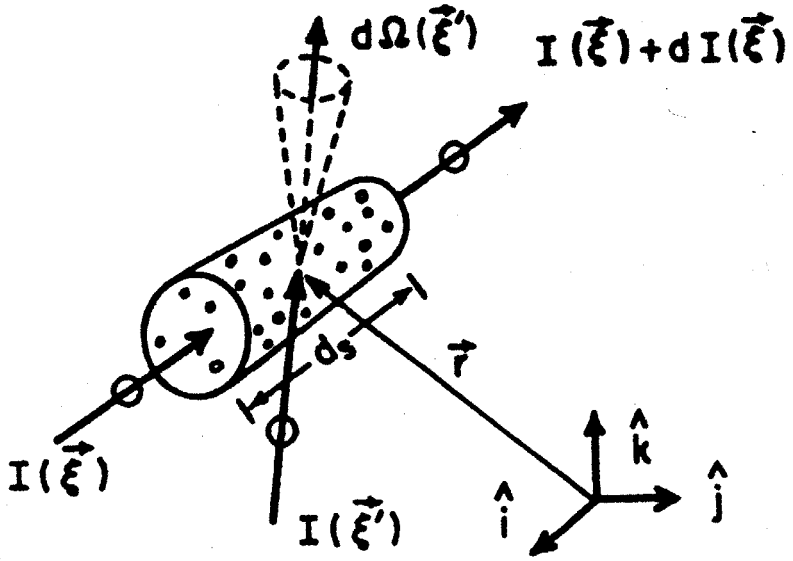

Fig. 15.1 Geometry for scattering of diffuse light. $\vec{\xi}'$ is the unit vector that defines the direction of the flow and $\vec{r}$ is the vector that specifies the position of the volume element relative to an origin point.

increase in intensity along the direction specified by $\vec{\xi}$ due to the scattering of this incident beam is, by virtue of the definition of the phase function[1] given in Section 13,

$$\delta I(\vec{r},\vec{\xi}) = \sigma_{sca} ds \frac{P(\vec{r},\vec{\xi},\vec{\xi}')}{4\pi} I(\vec{r},\vec{\xi}') d\Omega(\vec{\xi}') , \tag{15.1}$$

where σ_{sca} is the volume scattering coefficient given earlier and the wavelength dependence on all quantities is understood. The total contribution to $I(\vec{r},\vec{\xi})$ by scattering of the complete diffuse field surrounding the volume is given by the integral of Eqn. (15.1), namely

$$dI(\vec{r},\vec{\xi}) = \sigma_{sca} ds \int_{4\pi} \frac{P(\vec{r},\vec{\xi},\vec{\xi}')}{4\pi} I(\vec{r},\vec{\xi}') d\Omega(\vec{\xi}') , \tag{15.2}$$

which leads to the following definition

$$J(\vec{r},\vec{\xi}) = \tilde{\omega}_o \int_{4\pi} \frac{P(\vec{r},\vec{\xi},\vec{\xi}')}{4\pi} I(\vec{r},\vec{\xi}') d\Omega(\vec{\xi}')$$

such that

$$dI(\vec{r},\vec{\xi}) = \sigma_{sca} ds\, J(\vec{r},\vec{\xi}) . \tag{15.4}$$

The quantity $J(\vec{r},\vec{\xi})$ is the source of radiation due to scattering of diffuse light (sometimes this source is referred to as *virtual emission)* and $\tilde{\omega}_o$ is the single scatter albedo defined as

$$\tilde{\omega}_o = \frac{\sigma_{sca}}{\sigma_{ext}}$$

and varies between zero for pure absorption and unity for pure scattering (the latter condition is known as conservative scattering) such that the quantity 1 - $\tilde{\omega}_o$ is the fraction of the incident radiation that is absorbed by the small volume element under consideration.

The monochromatic radiative transfer equation defines the net change in intensity of a beam as it traverses the path element *ds* through a small volume. The change in intensity as the beam traverses a volume of atmosphere that both absorbs and scatters {and emits} radiation is

$$dI = dI(extinction) + dI(scattering) + \{dI(emission)\}, \tag{15.5}$$

or

$$\frac{dI(\vec{r},\xi)}{ds} = -\sigma_{ext}[I(\vec{r},\xi) - J(\vec{r},\xi)] + \{dI(emision)\} , \tag{15.6a}$$

[1] The phase function is a bidirectional scattering function that is entirely analogous to the bidirectional functions.

after collecting the extinction term and Eqn. (15.4) for scattering. It is relevant to note the similarity of this equation to Eqn. (4.8a,b) except that the scattering source in Eqn. (15.6a) is replaced by the Planck function in (4.8b).[2]

The radiative transfer equation relevant to a horizontally stratified atmosphere is

$$\mu \frac{dI(z,\theta,\phi)}{dz} = -\sigma_{ext} I(z,\theta,\phi) + \frac{\sigma_{sca}}{4\pi} \int_{4\pi} P(z,\theta,\phi,\theta'\phi') I(r,\theta'\phi') d\Omega' + \sigma_{abs} B(T) . \qquad (15.6b)$$

where if it were not for the presence of the integral term, this equation would be a mere differential equation and the theory of multiple scattering would have been worked out and forgotten long ago.

Example 15.1: Virtual Sources?

The problem of solar radiation multiply scattered by cloud or aerosol is more conveniently posed in terms of a source of collimated light that enters the cloud and by scattering creates a virtual source of *diffuse* radiation. This leads to an additional source term in the equation of transfer, which may be derived as follows. Consider Eqn. (15.6b), and suppose that the *global* intensity $I(z, \theta, \phi)$ may be expressed as two components:

$$I(z,\theta,\phi) = I_*(z,\theta,\phi) + I_o(z,\theta,\phi)$$

one for the diffuse field I_* and the second

$$I_0(z,\theta,\phi) = I_\odot(z)\delta(\theta - \theta_\odot)\delta(\phi - \phi_\odot)$$

for a collimated beam of intensity $I_\odot$ along the solar direction $\theta = \theta_\odot$, $\phi = \phi_\odot$. Substitution leads to

$$\mu \frac{d}{dz} I_* + I_o = -\sigma_{ext}(I_* + I_o) + \frac{\sigma_{sca}}{4\pi} \int P(I_* + I_o) d\Omega'$$

or

$$\mu \frac{dI_*}{dz} = -\sigma_{ext} I_* + \frac{\sigma_{sca}}{4\pi} \int P I_* d\Omega + I_\odot P(\theta,\phi,\theta_\odot,\phi_\odot)$$

and

$$\mu_\odot \frac{dI_0}{dz} = -\sigma_{ext} I_\odot, \text{ where } I_\odot(z) = I_\odot(z_r) e^{-\sigma_{ext}(z_r - z)/\mu_\odot}$$

[2] We can also follow the procedure of Section 4.3 to obtain an integral equation of transfer that is analogous to Eqn. (4.10). However, there is a fundamental difference between this and the equivalent integral equation that follows in this way. In Eqn. (4.10) the source function appearing in the integrand is known as *a priori* (assuming that the temperature distribution along the path is known) and the solution requires a straightforward integration of known functions. For scattering, the source function appearing in the integrand unfortunately contains the desired intensity and cannot be evaluated *a priori* unless some approximation is made. The presence of the intensity in the definition of J is what complicates the problem of multiple scattering and why a host of different approaches exist to overcome it.

15.2 Multiple Scattering: A Natural Method of Solution

A natural solution to problems of multiply scattered light in the atmosphere is one that decomposes the light field into components that can be identified with the number of times a photon has been scattered. This is termed the method of *orders of of scattering* and Fig. 15.2 provides the general geometric setting for discussing this approach. Suppose light of intensity I_o enters the medium along the direction $\vec{\xi}$ at the point $\vec{r}_o$. The amount of radiation leaving the distant point $\vec{r}_o$ along $\vec{\xi}$ is

$$I^0(\vec{r},\vec{\xi}) = I_o(\vec{r}_o,\vec{\xi})T(\vec{r}_o,\vec{r},\vec{\xi}) \tag{15.7}$$

where $t(\vec{r}_o,\vec{r},\vec{\xi})$ is the transmission function defined by the path $\vec{r}_o \rightarrow \vec{r}$ along $\vec{\xi}$ as shown in Fig. 15.2. We refer to I^0 as the *reduced* or *unscattered* intensity. When some light $I^o(\vec{r}',\vec{\xi}')$ at an intermediate point $\vec{r}'$ undergoes a scattering event, a first order or primary scattered intensity is generated at that point by an amount defined by Eqn. (15.3). This amount of intensity per unit length of path is

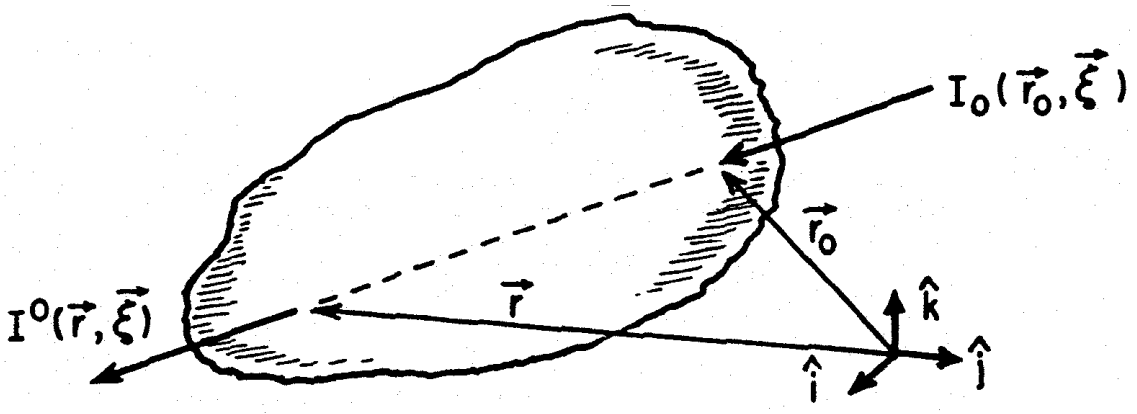

Fig. 15.2 Geometry for orders of scattering and geometry of a plane parallel atmosphere for computing the primary scattered intensity induced by a collimated source of solar radiation of intensity I_o.

$$I_*^1(\vec{r}',\vec{\xi}) = J^1(\vec{r}',\vec{\xi})\sigma_{ext}$$

where, according to Eqn. (15.3), J^1 may be considered as the source associated with the primary scattering of I^0. It therefore follows that the radiation from primary scattering of light from all directions is

$$I_*^1(\vec{r}',\vec{\xi}) = \sigma_{sca}\int_{4\pi}\frac{P(\vec{r}',\vec{\xi},\vec{\xi}')}{4\pi}I^0(\vec{r}',\vec{\xi}')d\Omega(\vec{\xi}')\,. \tag{15.8}$$

The amount of this primary scattered radiation that is accumulated along the path from $\vec{r}_o \rightarrow \vec{r}$ is

$$I^1(\vec{r},\vec{\xi}) = \int_{\vec{r}_o}^{\vec{r}} I_*^1(\vec{r}',\vec{\xi})T(\vec{r}_o,\vec{r}',\vec{\xi})d\vec{r}'\,. \tag{15.9}$$

It is a simple and somewhat intuitive matter to show that construction of the intensities associated with higher order scattering then follows from the repeated application of Eqns. (15.8) and (15.9) such that

$$I_*^{n+1}(\vec{r}',\vec{\xi}) = \sigma_{sca}\int_{4\pi}\frac{P(\vec{r}',\vec{\xi},\vec{\xi}')}{4\pi}I^n(\vec{r}',\vec{\xi}')d\Omega(\vec{\xi}')\,, \tag{15.10a}$$

$$I^{n+1}(\vec{r},\xi) = \int_{\vec{r}_o}^{\vec{r}} I_*^{n+1}(\vec{r}',\xi)T(\vec{r}_o,\vec{r}',\xi)d\vec{r}' \tag{15.10b}$$

for each integer order $n = 0, 1,\ldots$ of scattering. The total intensity is therefore the sum of all orders of scattering, namely

$$I = I^0 + I^1 + I^2 + \ldots + I^n + \ldots = \sum_n I^n\,, \tag{15.11a}$$

which is conveniently written as

$$I = I^0 + I^* \tag{15.11b}$$

where I^* in this case is the total diffuse intensity $I^* = \sum_{n=1} I_n$.

An obvious question to ask is how many orders of scattering are required to approximate the diffuse field to some given accuracy? The general answer to this question depends on how many particles there are in the volume and on how efficiently the particles scatter the radiation. A rough idea of the effect of the single scatter albedo on scattering is given by the following arguments. Suppose $\overline{I}^0$ is an upper bound on I^0. Then from Eqn. (15.8)

$$I_*^1(\vec{r}',\vec{\xi}) \le \overline{I}^0\sigma_{sca}\frac{1}{4\pi}\int P(\vec{r}',\vec{\xi},\vec{\xi}')d\Omega(\vec{\xi}') = \overline{I}^0\sigma_{sca} \tag{15.12}$$

by virtue of the phase function renormalization condition Eqn. (15.9) then becomes

$$I^1(\vec{r},\vec{\xi}) = \int I_*^1(\vec{r}',\vec{\xi})e^{-\sigma_{ext}|\vec{r}-\vec{r}'|}d\vec{r}'$$

where the exponential factor is the transmission function for the path of length $d = |\vec{r} - \vec{r}'|$. From the condition on I_*^1 it follows that

$$I^1(\vec{r},\vec{\xi}) \le \overline{I}^0\omega_o(1 - e^{-\sigma_{ext}d}) \le \overline{I}^0\tilde{\omega}_o\,.$$

Repeating this procedure for the next order of scattering leads to

$$I^2(\vec{r},\vec{\xi}) \le \overline{I}^0\tilde{\omega}_o$$

and

$$I^n(\vec{r},\vec{\xi}) \le \overline{I}^0\tilde{\omega}_o^n \tag{15.13}$$

for every scattering order *n*. With the following notation

$$I^{(k)}(\vec{r},\vec{\xi}) \quad \text{for} \quad \sum_{n=0}^{k} I^{n}(\vec{r},\vec{\xi}),$$

it follows that the difference $\Delta = I(\vec{r},\vec{\xi}) - I^{(k)}(\vec{r},\vec{\xi})$ is

$$\Delta = \sum_{j=k+1} I^{j}(\vec{r},\vec{\xi}) \le \overline{I}^{0} \sum_{j=k+1} \tilde{\omega}_o$$

or

$$\Delta \le \overline{I}_o \tilde{\omega}_o^{j+1} \sum_{j=0} \tilde{\omega}_o^{j} = \overline{I}^{0} \frac{\tilde{\omega}_o^{j+1}}{(1-\tilde{\omega}_o)}. \tag{15.14}$$

Example 15.2: How many times does a photon get scattered?

Consider the example with $\tilde{\omega}_o$ = 0.5 and suppose that we require I^k to differ from the actual intensity by an amount no larger than 1% of $\overline{I}^{0}$. It follows that $\Delta / \overline{I}^{0} \le$ 0.01 and that

$$0.01 \le \frac{0.5^{j+1}}{0.5}$$

or j = 7 for the nearest integer value. Thus only 7 orders of scattering are required to model the diffuse intensity with a 1% accuracy when $\tilde{\omega}_o$ = 0.5. This simple exercise offers a clear illustration of the significance of $\tilde{\omega}_o$ to multiple scattering. We infer that the number of scatterings required to represent the total intensity decreases as the absorption by the particle increases (or as $\tilde{\omega}_o \to 0$). For example, many orders of scattering contribute to the total radiation field in clouds at solar wavelengths where $\tilde{\omega}_o$ > 0.9 but relatively few scatterings contribute at the infrared wavelengths where $\tilde{\omega}_o$ < 0.5

15.3 The Two-Stream Approximation

On examination of the equation of transfer, which includes scattering in either its interodifferential or its integral form, one is confronted with the complicating presence of the integral term that involves an integration over the direction variable. In fact if it weren't for this term, the equation of transfer would be but a mere differential equation and the theory of multiple scattering would have been worked out and forgotten long ago. Thus the essence of the simplification that is introduced by the class of simple models discussed here is to approximate, in some way, the angular shape of the radiance field so as to introduce some approximation to this integral term. To this end there is a property of the radiance field that is utilized to great benefit by these approximate methods although it is not often explicitly realized. This

property is illustrated in Figs. 15.3a and b in which the zenith radiance distribution is shown on descent into the sea (Fig. 15.3a) and deep in a thick cloud (Fig. 15.3b). It is apparent that this radiance structure approaches some sort of asymptotic form with increasing depth into the "medium". Eventually some steady distribution is reached and all radiances decrease at the same exponential rate with increasing depth ultimately shrinking down in size but preserving its shape. It is also apparent that this *asymptotic distribution* can be described as some simple function of zenith angle (this is the basis of the diffusion approximations, which we will not discuss here).

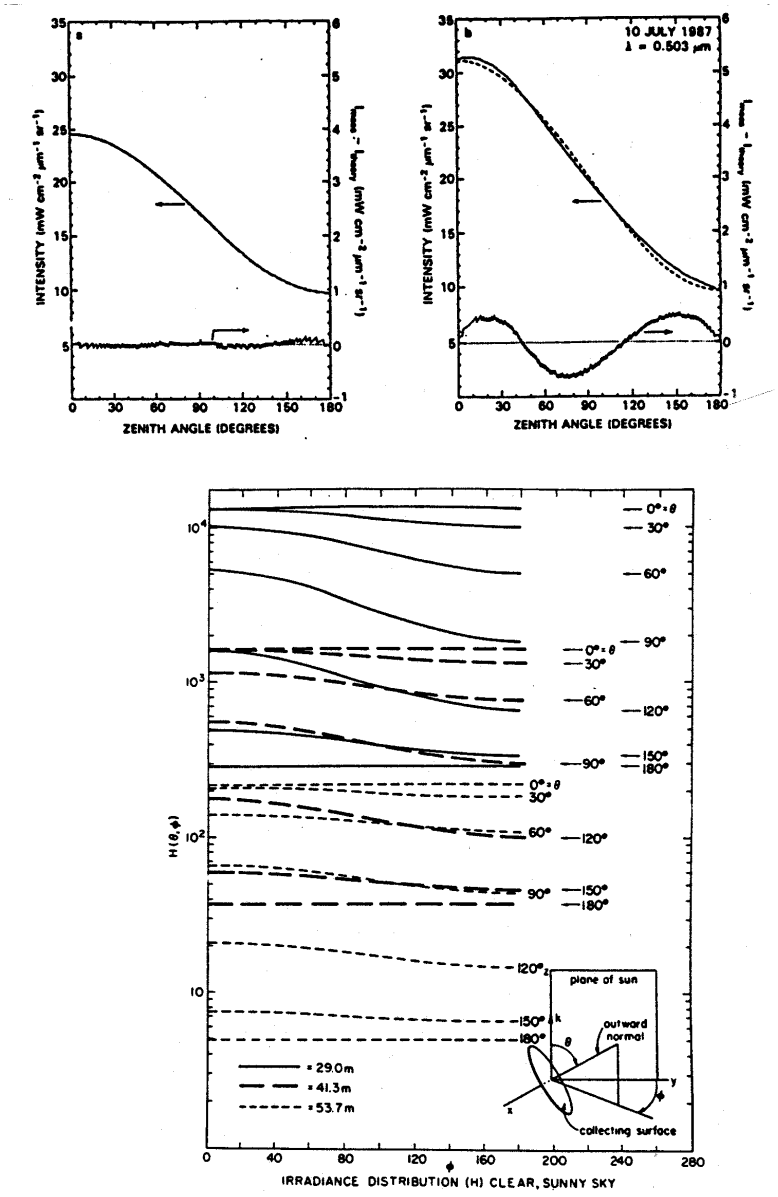

Fig. 15.3 (a) The flux distribution on a clear sunny day at three indicated depths in Lake Pend Orielle, Idaho (adapted from Preisendorfer, 1976). These fluxes are defined for a collecting surface inclined at an angle θ as shown in the inset. (b) Measured intensity as a function of zenith angle obtained from a scanning radiometer on an aircraft as it flew through the center of a deep stratiform cloud. The lower curve is the difference between measurement and a simple cosine of zenith angle variation (King et al., 1990).

While we can approach the development of the two-stream equations in a number of different ways, the end result is always the same, namely that we arrive at equations of the form

$$\frac{d}{dt}\begin{pmatrix} F^+ \\ F^- \end{pmatrix} = \begin{pmatrix} t & -r \\ r & -t \end{pmatrix}\begin{pmatrix} F^+ \\ F^- \end{pmatrix} + \begin{pmatrix} Q^+ \\ Q^- \end{pmatrix} \tag{15.15}$$

(a) The Two-Stream Equations—The Conceptual Approach

The arguments formulated here are similar to those used in the pioneering work on radiative transfer by Schuster in 1905. Consider a parallel, horizontally uniform slab of cloud and consider the fluxes flowing in two opposing directions.[3] We will use the + superscript to refer to quantities associated with flow in the upward direction and a – superscript on quantities relevant to downward flow. The two-stream equations define the energy balance of this thin slab of thickness Δz in exactly the same way as Eqn. (15.6b) describes an energy balance of a small volume of cloud. In order to express the radiative energy budget of a layer Δz thick, it is necessary to define the following optical properties:

- The proportion of the incident flux lost by absorption as the radiation flows through the layer of unit thickness is $k_{abs}D^{\pm}$ where $D^{\pm}$ is a measure of the 'diffuseness' of the radiation field. This parameter more or less represents the mean extension of the path, relative to the vertical, that a diffuse radiation field travels as it penetrates the layer. It is a function of the angular properties of the intensity field among other parameters and represents one of the simplifications mentioned above. If we suppose that the angular distribution of radiation that produces the flux is the same in both directions (the magnitudes might be different), then

  $$D^+ = D^- .$$

  Although this assumption is questionable, it tends to be universally used in two-stream models.

- The proportional loss of flux by scattering is $s_{sca}b^{\pm}$ per unit thickness. Here we note that the process of absorption is treated differently from scattering in that a measure of the path length is needed for estimating absorption but this measure is not needed for scattering. We will further suppose that this scattering is the same whether the radiation flows upward or downward, and thus

  $$b^+ = b^- .$$

Another parameter of relevance is the fraction of radiation f that is scattered in the forward direction. This fraction is defined such that

$$f + b = 1 \tag{15.16}$$

For a change in flux ΔF defined as positive upwards, then the change in flux on transfer through the layer Δz is

$$\Delta F^{\pm} = \mp(Dk_{abs} + s_{sca}b)F^{\pm}\Delta z \pm s_{sca}bF^{\mp}\Delta z(\pm Q^{\pm}\Delta z) \tag{15.17}$$

[3] The relationship between radiative flux and intensity is explored in the Appendix. The derivation of the two-stream equations given here follows the more conceptual arguments of Schuster. The same equations can be derived directly from Eqn. (15.6b) given some assumption about the intensity field. This alternative derivation is left for later.

where the last term in parentheses represents internal sources of $F^{\pm}$ in the layer Δz[4]. The first two terms on the right hand side and enclosed by parentheses describe the losses of radiation through the processes of absorption and scatter, respectively, while the middle terms represent the increase of flux by backscatter of the opposing stream. Introducing the definition of optical thickness as

$$\Delta\tau = -(k_{abs} + s_{sca})\Delta z$$

where the minus sign defines τ as increasing downwards from cloud base opposite to the change in z. On taking the limit $\Delta z \to 0$, we obtain the two-flow radiative transfer equation

$$\mp\frac{dF^{\pm}}{d\tau} = -[D(1-\tilde{\omega}_o) + \tilde{\omega}_o b]F^{\pm} + \tilde{\omega}_o b F^{\mp}(+Q^{\pm}) \tag{15.18}$$

where $\tilde{\omega}_o = s_{sca}/(s_{sca} + k_{abs})$. All two-stream methods described in the literature essentially reduce down to this equation. The only difference between the various methods lies in how D, b, and $S^{\pm}$ are specified. One example is to consider the simple phase function introduced in Section 13.7a, then it follows that

$$b = (1 - g)/2$$

where g is the phase function asymmetry. The radiative transfer equation then becomes

$$\mp\frac{dF^{\pm}}{d\tau} = -\left[D(1-\tilde{\omega}_o) + \frac{\tilde{\omega}_o}{2}(1-g)\right]F^{\pm} + \frac{\tilde{\omega}_o}{2}(1-g)F^{\mp}(+Q^{\pm}). \tag{15.19}$$

The general solution to Eqn. (15.19) for given sources can be complicated. Here we neglect this term and consider only solar radiation incident on cloud top assuming this incident flux is purely diffuse (as opposed to the more realistic case of a purely collimated incident flux). While the details of the solutions described below change with the addition of the source term for solar radiation, notably by introducing a solar zenith angle dependence to the solutions, the gross relationships between the optical properties of clouds (τ^*, $\tilde{\omega}_o$, and g) and the diffuse reflectance and transmittance does not change.

[4]Two main sources of flux are usually considered in these models. One is the source of radiation due to thermal emission, which according to Kirchoffs law takes the form

$$Q^{\pm} = k_{abs}\pi B(T)$$

for emitting cloud particles of temperature T. The second is the source of diffuse radiation that results from the single scattering of a collimated flux $F_{\odot}$ of sunlight. This source has the form

$$Q^{\pm} = F_{\odot} e^{-\tau/\mu_{\odot}} s_{sca} \begin{pmatrix} b_{\odot} \\ f_{\odot} \end{pmatrix}$$

where $f_{\odot}$ and $b_{\odot}$ are the forward and backward scattering fractions of the incident flux $F_{\odot}$ and these fractions are functions of the cosine of the solar zenith angle $\mu_{\odot}$

Example 15.3: Solution for sourceless atmosphere, pure scattering

Consider the example of a single layer of 'cloud' with $S = 0$. For pure scattering, $\tilde{\omega}_o = 1$, $k_{abs} = 0$

$$F^{\pm} = m_{+} \mp m_{-}(1 + \tilde{\tau})$$

where m_+ and m_- are constants determined by boundary conditions and

$$\tilde{\tau} = (1 - g)\tau^{*}$$

is the optical depth of the entire slab, τ^*, scaled by the factor $(1 - g)$. The relevance of this scaled parameter becomes apparent by considering an isolated scattering and absorbing layer illuminated from above by flux $F_{\odot}$ overlying a dark surface. Under these conditions, the albedo of the cloud layer is

$$R = \frac{F^{+}(0)}{F_{\odot}} = \frac{\tilde{\tau}}{2 + \tilde{\tau}} \qquad (15.20a)$$

and the transmittance

$$T = \frac{F^{-}(\tau^{*})}{F_{\odot}} = 1 - R = \frac{2}{2 + \tilde{\tau}} \qquad (15.20b)$$

This result implies that two non-absorbing cloud layers with different optical thicknesses τ^* and g reflect the same amount of radiation when the respective values of $\tilde{\tau}$ are the same. This is referred to as a similarity condition and implies that it is not possible to infer τ^* from a single reflection or a single transmission measurement without information about g. One of the problems associated with the remote sensing of ice crystal clouds is that g is neither well known nor well understood in how it varies with different crystal habits. This parameter is well known for water droplet clouds and is quasi-constant with a typical value in the range 0.8-0.85.

Example 15.4: Solution for sourceless atmosphere, nonconservative scattering

For this case, $\tilde{\omega}_o < 1$, $k_{abs} > 0$: The solution to Eqn. (15.19) for a sourceless, uniform medium has the form

$$F^{\pm}(\tau) = m_+ \gamma_{\pm} e^{kt} + m_- \gamma_{\mp} e^{-kt} \tag{15.21a}$$

where

$$k = \{(1-\tilde{\omega}_o)D[(1-\tilde{\omega}_o)D + 2\tilde{\omega}_o b]\}^{1/2} \tag{15.21b}$$

and

$$\gamma_{\pm} = 1 \pm (1-\tilde{\omega}_o)D/k \tag{15.21c}$$

where as above the coefficients $m\pm$ are determined from appropriate boundary conditions. Consider the same conditions applied to Eqns. (15.21a,b)

$$F^{+}(\tau^*) = 0$$

$$F^{-}(0) = F_{\odot}$$

for an isolated layer of optical thickness τ^*. With some manipulation of Eqn. (15.21a), the albedo and transmittance of the layer can be written as

$$R = \gamma_+ \gamma_- [e^{-k\tau^*} - e^{-k\tau^*}]/\Delta(\tau^*) \tag{15.22a}$$

$$T = (\gamma_+^2 - \gamma_-^2)/\Delta(\tau^*) \tag{15.22b}$$

where

$$\Delta(\tau^*) = \gamma_+^2 e^{k\tau^*} - \gamma_-^2 e^{-k\tau^*} \tag{15.22c}$$

As $\tau^* \to \infty$, $R \to R_\infty = \gamma_-/\gamma_+$ and this is referred to as the albedo of a semi-infinite cloud. This represents the upper limit to the albedo of a cloud and since $T = 0$ and $A = 1 - R$, this is also the upper limit to the absorption A_∞ within the cloud. These upper limits are determined entirely by the optical properties $\tilde{\omega}_o$, k, g, and D of the cloud. From the substitution of Eqn. (15.22b) in Eqn. (15.22c) together with the definition of R_∞, it follows that

$$R_\infty = \frac{[1+1/s^2]^{1/2} - \sqrt{2}}{[1+1/s^2]^{1/2} + \sqrt{2}} \tag{15.23}$$

where

$$s = \left(\frac{1-\tilde{\omega}_o}{1-\tilde{\omega}_o g}\right)^{1/2}$$

is another similarity parameter (Fig. 15.4b). Equation (15.23) states that the reflection by two different optically thick clouds are equivalent when the similarity parameter s is equivalent.

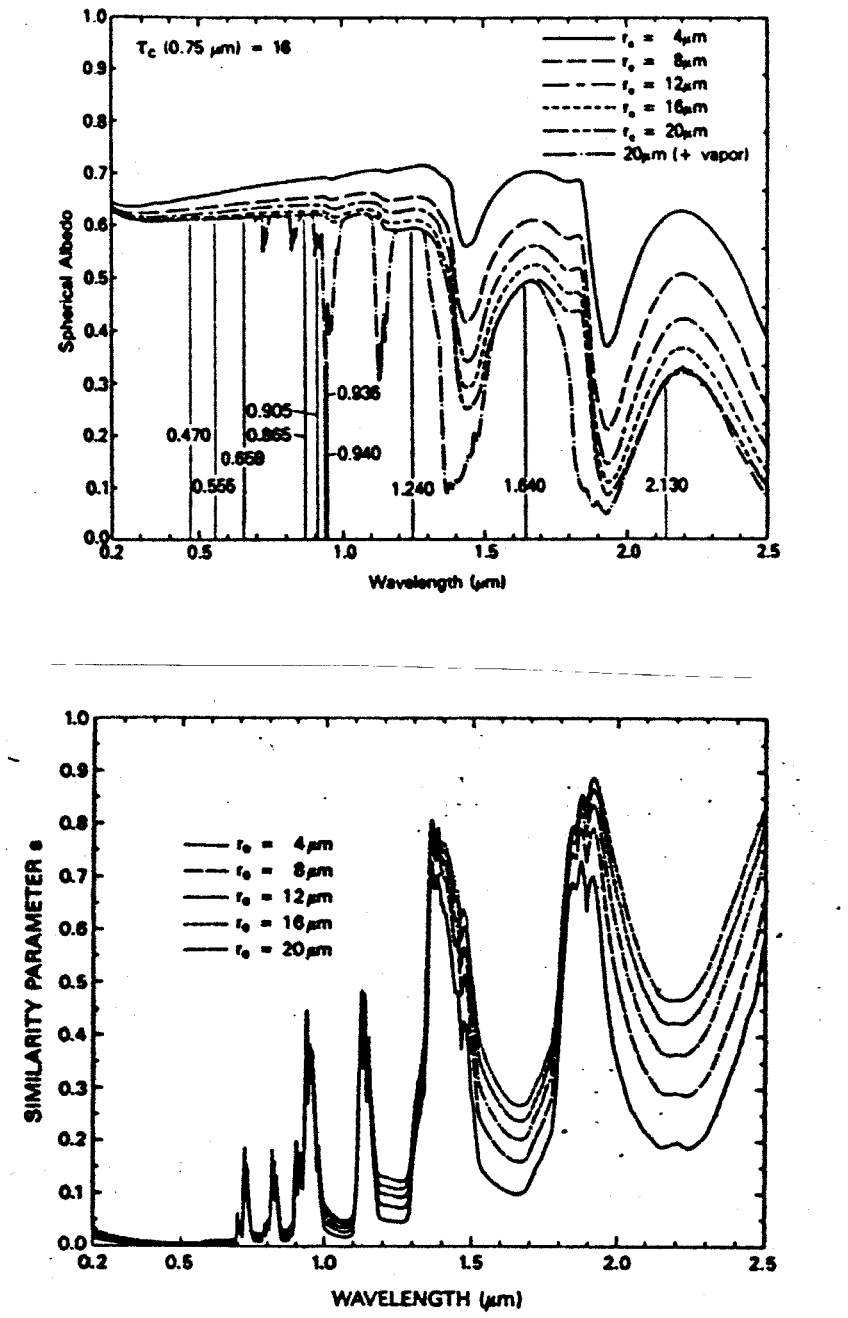

Fig. 15.4 *(a) The spectral reflectance from modeled clouds as a function of their particle size. (b) The similarity parameter as a function of wavelength for different assumed values of the cloud droplet effective radious r_e.*

Example 15.5: Pollution Susceptible Clouds

The effect of ship stack effluents on cloud optical depth and cloud albedo is a topic of intensive interest. The simple two-stream model introduced previously now serves to emphasize how the scaled optical depth is the direct controlling parameter on the albedo of clouds. We can deduce that optical depth of clouds is

$$\tau^* \approx 2\pi N_o \bar{r}^2 h$$

for a cloud of depth h composed of N_o particles of a size $\bar{r}$ that exceeds the wavelength of radiation. Increased water content (occurring largely as an increase in $\bar{r}$), for instance, can increase the optical depth of clouds. An increase in number concentration N_o can also increase τ^* and the sensitivity of optical thickness τ^* to N_o, for constant liquid-water content, is given by

$$\frac{\Delta\tau^*}{\tau^*} = \frac{1}{3}\frac{\Delta N_o}{N_o}.$$

For cloud droplets under solar illumination, g is quasi-constant and ≈ 0.85. Using this value in Eqn. (15.20a), one obtains the following simple approximate expression

$$R \cong \frac{\tau}{13+\tau}.$$

for the albedo of a cloud. We can readily derive the sensitivity of R to droplet number N_o from this relation and express it in terms of N_o and R. The result for fixed liquid water content w is

$$\left(\frac{dR}{dN_o}\right)_w = \frac{R(1-R)}{3N_o}.$$

Thus, for a given N_o, the most susceptible clouds are those with $R \approx 1/2$, but the maximum of R is rather flat - for R = 1/4 or 3/4, dR/dN_o is still three-fourths of its maximum value. For fixed R, $(dR/dN_o)_w$ is inversely related to N_o, which in the real present atmosphere, can vary by more than two orders of magnitude. The susceptibility $dRldN_o$ (graphed in Fig. 15.5) reveals a considerable sensitivity for clean conditions—e.g., in oceanic and remote areas (where N_o is low). There $(dR/dN_o)_w$ *is* seen to approach 1% (per cm^{-3}), that value would mean a reflectance change *of* 0.01 for a concentration change of just 1 cm^{-3}.

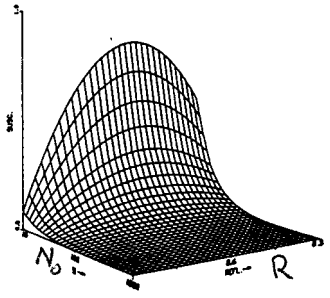

Fig. 15.5 Susceptibility for different conditions of N_o and R.

b) The Two-Stream Equations—Analytic Approach: Eddington's Approximation as an Example

Suppose we consider azimuthally averaged quantities $\overline{I}$,

$$F = 2\pi \int_0^1 \overline{I}\,\mu d\mu$$

then

$$\mu d\frac{\overline{I}}{d\tau} = \overline{I} - \frac{\tilde{\omega}_o}{2}\int_{-1}^{+1} \overline{p}(\mu,\mu')\overline{I}(\mu')d\mu'$$

- If we assume that

$$\overline{I} \approx I_o + I_1\mu$$

which resembles the form used in our diffusion approximation, then

$$F^+ = 2\pi\int_0^1 I\,\mu d\mu = 2\pi\left[\frac{I_o}{2} + \frac{1}{3}I_1\right]$$
$$F^- = 2\pi\int_0^{-1} I\,\mu d\mu = 2\pi\left[-\frac{1}{3}I_1 + \frac{I_o}{2}\right]$$

and

$$F_{net} = F^+ - F^- = 2\pi\int_{-1}^{+1} I\,\mu d\mu = \left(\frac{2}{3}I_1\right)2\pi$$
$$I_1 = \frac{3}{4\pi}(F^+ - F^-)$$
$$F^+ + F^- = 2\pi I_o$$
$$I_o = \frac{F^+ + F^-}{2\pi}$$

- The second approximation we introduce is the following

$$\overline{P}(\mu,\mu') = 1 + 3g\mu\mu'$$

for the phase function expansion. If we consider our radiative transfer equation and integrate over each respective hemisphere, then we obtain the following two equations (ignoring sources for the moment):

$$2\pi\int_0^1 \mu\underbrace{\frac{dI}{d\tau}(\mu)}_{A}d\mu = 2\pi\int_0^1 \underbrace{I(\mu)}_{B}d\mu - \frac{\tilde{\omega}_o}{2}\int_0^1\int_{-1}^{+1}\underbrace{p(\mu,\mu')I(\mu')}_{C}d\mu' d\mu$$

$$2\pi\int_0^{-1} \mu\underbrace{\frac{dI}{d\tau}(\mu)}_{A'}d\mu = 2\pi\int_0^{-1} \underbrace{I(\mu)}_{B'}d\mu - \frac{\tilde{\omega}_o}{2}\int_0^{-1}\int_{-1}^{+1}\underbrace{p(\mu,\mu')I(\mu')}_{C'}d\mu' d\mu$$

Consider the first equation:

Term $A = 2\pi\int_0^1 \mu\frac{dI}{d\tau}d\mu = 2\pi\frac{d}{d\tau}\int_0^1 \mu[I_o + I_1\mu]d\mu = \frac{d}{d\tau}F^+$

Term $A' = \frac{d}{d\tau}F^-$

Term $B = 2\pi\int_0^1 (I_o + I_1\mu)d\mu = (I_o + \frac{1}{2}I_1)2\pi$

Term $B' = 2\pi\int_0^{-1} (I_o + I_1\mu)d\mu = (\frac{1}{2}I_1 - I_o)2\pi$

Term $\frac{C}{2\pi} = \frac{\tilde{\omega}_o}{2}\int_0^1 d\mu\int_{-1}^{+1}(I_o + I_1\mu') + 3g\mu(I_o\mu' + I_1\mu'^2)d\mu'$

$$= \frac{\tilde{\omega}_o}{2}\int_0^1 d\mu[I_o\mu' + \frac{1}{2}I_1\mu'^2 + \frac{3}{2}g\mu I_o\mu'^2 + g\mu I_1\mu'^3]_{-1}^{+1}$$

$$= \frac{\tilde{\omega}_o}{2}\int d\mu[2I_o + 2g\mu I_1]$$

Term $\frac{C(C')}{2\pi} = \tilde{\omega}_o\int_0^{1(-1)} d\mu(I_o + g\mu I_1)$

$$= \tilde{\omega}_o[I_o + \frac{1}{2}gI_1](\tilde{\omega}_o[\frac{1}{2}gI_1 - I_o])$$

After collecting terms, we obtain

$$\frac{dF^+}{d\tau} = 2\pi\left(I_o + \frac{1}{2}I_1\right) - 2\pi\tilde{\omega}_o\left[I_o + \frac{1}{2}gI_1\right]$$

$$= F^+ + F^- + \frac{3}{4}(F^+ - F^-) - \tilde{\omega}_o\left[F^+ + F^- + \frac{3}{4}g(F^+ - F^-)\right]$$

$$= \frac{7}{4}F^+ - \frac{\tilde{\omega}_o}{4}(4+3g)F^+ + \frac{1}{4}F^- - \frac{\tilde{\omega}_o}{4}(4-3g)F^-$$

or

$$\frac{dF^+}{d\tau} = \left\{\frac{7}{4} - \frac{\tilde{\omega}_o}{4}(4+3g)\right\}F^+ + \left\{\frac{1}{4} - \frac{\tilde{\omega}_o}{4}(4-3g)\right\}F^-$$

Similarly

$$\frac{dF^-}{d\tau} = 2\pi\left[-I_o + \frac{1}{2}I_1\right] = 2\pi\tilde{\omega}_o\left[\frac{1}{2}gI_1 - I_o\right]$$

$$= \left[-F^+ - F^- + \frac{3}{4}(F^+ - F^-)\right] - \tilde{\omega}_o\left[-F^+ - F^- + \frac{3}{4}g(F^+ - F^-)\right]$$

$$= -\frac{7}{4}F^- + \frac{\tilde{\omega}_o}{4}(4+3g)F^- - \frac{1}{4}F^+ + \frac{\tilde{\omega}_o}{4}(4-3g)F^+$$

or

$$\frac{dF^-}{d\tau} = -\left\{\frac{7}{4} - \frac{\tilde{\omega}_o}{4}(4+3g)\right\}F^- - \left\{\frac{1}{4} - \frac{\tilde{\omega}_o}{4}(4-3g)\right\}F^+$$

where we can readily identify

$$\begin{aligned} t &= \frac{7}{4} - \frac{\tilde{\omega}_o}{4}(4+3g) \\ r &= -\frac{\tilde{\omega}_o}{4}(4-3g) \end{aligned} \tag{15.24}$$

(c) Delta-Two Stream Models

We have already remarked on the scaling associated with phase functions of the form

$$p(\mu,\mu') = 2f\delta(\mu'-\mu) + (1-f)(1+3g\mu\mu')$$

which reduces to the formal two-stream solutions when

$$\begin{aligned} g' &= \frac{g-f}{1-f} \\ \tau' &= (1-\tilde{\omega}_o f)\tau \\ \tilde{\omega}_o' &= \frac{(1-f)\tilde{\omega}_o}{1-f\tilde{\omega}_o} \end{aligned}$$

are used directly in the solutions. It is usual to employ the second moment of the expansion, namely

$$f = \chi/5 = g^2$$

for the scaling factor.

15.4 General Solutions

The two-stream model and its general solution are briefly introduced here. We will consider two kinds of source functions to represent those described in footnote 2. In developing these solutions, it is useful to introduce two-stream equations (Eqn. (15.15)) as follows

$$L_F F = Q \tag{15.25a}$$

where F is a flux vector

$$F = \begin{pmatrix} F^+ \\ F^- \end{pmatrix}$$

of upwelling (F^+) and downwelling (F^-) flux at level z'. The dependence of each factor in Eqn. (15.25a) on z' is taken to be understood. The source function vector,

$$Q = \begin{pmatrix} Q^+ \\ Q^- \end{pmatrix}$$

too depends on z'. The two-stream transport operator is

$$L_F = \frac{d}{dz'} - \sigma_{ext} \begin{pmatrix} -t & r \\ -r & t \end{pmatrix} \tag{15.25b}$$

where we note the streaming term is defined relative to z rather than τ as in Eqn. (15.15), which means that the coefficients t and r differ from those of Eqn. (15.24) only by a factor of σ_{ext}. Although these define the flux equations, the form of this equation is generic in the sense that they also equally apply to radiance and the 'n stream' problem (e.g., Flatau and Stephens, 1988).

The different forms of the equation coefficients in Eqn. (15.15), namely t and r, define different version of a two-stream model. The 2 x 2 matrix of coefficients defines the attenuation matrix

$$\mathbf{A} = \sigma_{ext} \begin{pmatrix} -t & r \\ -r & t \end{pmatrix} \tag{15.26}$$

and the 'solution' to the sourceless equation (i.e., $Q = 0$) can be expressed in terms of the matrix exponential

$$\mathbf{M}(z, y) = e^{-\mathbf{A}(z-y)} \tag{15.27}$$

where **M** is a mapping function. By virtue of the block structure of **A**, this mapping matrix has a similar form

$$\mathbf{M}(z, y) = \begin{pmatrix} m_{++}(z, y) & m_{+-}(z, y) \\ m_{-+}(z, y) & m_{--}(z, y) \end{pmatrix} \tag{15.28}$$

For the 2 x 2 matrix **A** of the two-stream equations, Eqn. (15.27) follows as

$$m_{++}(z, y) = \frac{e^{\kappa(z-y)}}{2} f_+ + \frac{e^{-\kappa(z-y)}}{2} f_-$$

$$m_{+-}(z, y) = \frac{r}{\kappa} \left[\frac{e^{-\kappa(z-y)}}{2} - \frac{e^{\kappa(z-y)}}{2} \right]$$

$$m_{-+}(z,y) = \frac{r}{\kappa}\left[\frac{e^{\kappa(z-y)}}{2} - \frac{e^{-\kappa(z-y)}}{2}\right]$$
$$m_{--}(z,y) = \frac{e^{\kappa(z-y)}}{2} f_- + \frac{e^{-\kappa(z-y)}}{2} f_+ \qquad (15.29)$$

where

$$f_+ = (1 + t/\kappa)$$
$$f_- = (1 - t/\kappa)$$

(a) The Interaction Principle

Consider the two types of radiative transfer problem as posed in Fig. 15.6. The goal of the first is to deduce the fluxes at the upper boundary of an isolated layer at z_T in terms of the fluxes at the lower boundary z. Stated, this way the radiative transfer problem is an initial value problem. Its solution is as follows. First consider the sourceless equations for which the solution (assuming constant coefficients) is

$$\begin{pmatrix} F^+ \\ F^- \end{pmatrix}(z) = \begin{pmatrix} m_{++}(z,y) & m_{+-}(z,y) \\ m_{-+}(z,y) & m_{--}(z,y) \end{pmatrix}\begin{pmatrix} F^+ \\ F^- \end{pmatrix}(y) \qquad (15.30)$$

Unfortunately, most problems of radiative transfer are posed as follows. Given fluxes incident on the boundaries, what are the emergent fluxes (Fig. 15.6). These are two point boundary value problems, which can be solved through rearrangement of Eqn. (15.30). The relationship between fluxes out in terms of fluxes in (and internal sources) is referred to as the interaction principle. In rearranging Eqn. (15.30) in the form of the interaction principle, we obtain the relation between the mapping functions above and the more classical properties of reflection and transmission.

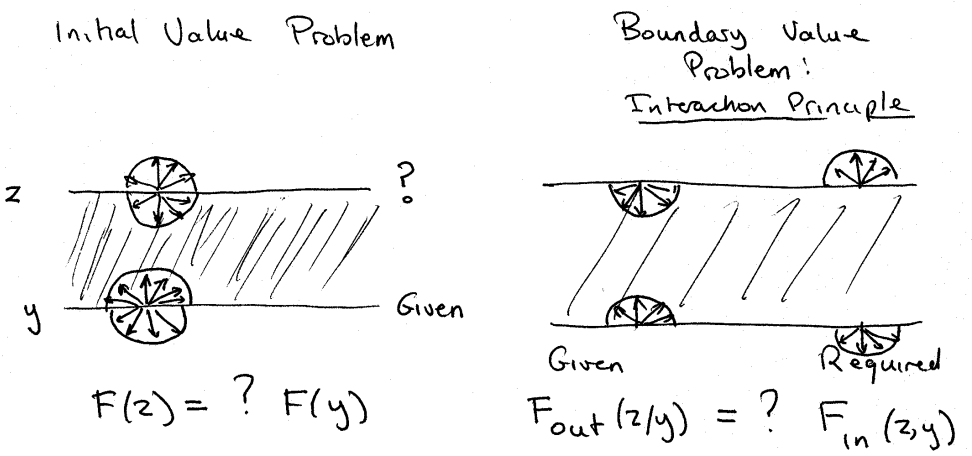

Fig. 15.6 Two types of transfer problems, the initial value problem at left and the more traditional two-point boundary value problem defining the interaction principle.

Simple reorganization of Eqn. (15.30) in its interaction form gives the desired emergent fluxes $F^{+}(z_T)$ and $F^{-}(z)$ in terms of input fluxes

$$\begin{pmatrix} F^{+}(z_T) \\ F^{-}(z) \end{pmatrix} = \begin{pmatrix} 1/m_{++} & -m_{+-}/m_{++} \\ m_{-+}/m_{++} & m_{--} - m_{-+}m_{+-}/m_{++} \end{pmatrix} \begin{pmatrix} F^{+}(z) \\ F^{-}(z_T) \end{pmatrix}. \tag{15.31}$$

where the notation indicating the mapping factors are defined for the layer (z_T,z) is dropped for convenience. This identifies the layer diffuse reflection and transmission functions as

$$R(z_T,z) = \frac{-m_{+-}(z_T,z)}{m_{++}(z_T,z)} \tag{15.32a}$$

$$T(z_T,z) = \frac{1}{m_{++}(z_T,z)} \tag{15.32b}$$

which are those of Eqn. (15.22).

(b) Adding Sources - General Solution

We proceed with Eqn. (15.25b) in Eqn. (15.25a) and multiplying both sides by the exponential of the matrix

$$e^{-Az'}\frac{dF}{dz'} - e^{-Az'}AF(z') = e^{-Az'}Q(z') \tag{15.33}$$

where we assume that the attenuation matrix (i.e., the optical properties r and t) is independent of z'. Integration of Eqn. (15.33) from $(z \rightarrow z_T)$ yields

$$F(z) = e^{-A(z_t - z)}F(z_T) + S(z_T,z) \tag{15.34}$$

by virtue of the property of the matrix exponential

$$[e^{-Az}]^{-1} = e^{Az}$$

and where the vector

$$S(z_T,z) = -\int_z^{z_T} e^{-A(z_t - z)}Q(z')dz' \tag{15.35}$$

These resemble the more traditional integral form of the radiative transfer equation (Sections 4 and 10). However, it contains the desired emergent fluxes (i.e., the solution) on both sides of the equation as seen more clearly in the expanded form

$$\begin{pmatrix} F^{+}(z) \\ F^{-}(z) \end{pmatrix} = \begin{pmatrix} m_{++}(z_T,z) & m_{+-}(z_T,z) \\ m_{-+}(z_T,z) & m_{--}(z_T,z) \end{pmatrix} \begin{pmatrix} F^{+}(z_T) \\ F^{-}(z_T) \end{pmatrix} + \begin{pmatrix} S^{+}(z_T,z) \\ S^{-}(z_T,z) \end{pmatrix}. \tag{5.36}$$

A special solution arises for problems in which the medium is illuminated with zero incident fluxes (known as vacuum boundary conditions). Then we obtain

$$\begin{pmatrix} F^+(z_T) \\ F^-(z) \end{pmatrix} = \begin{pmatrix} -S(z_T,z)/m_{++}(z_T,z) \\ -m_{-+}(z_T,z)S^+(z_T,z)/m_{++}(z_T,z) + S^-(z_T,z) \end{pmatrix} \tag{15.37}$$

which are the particular solutions to Eqn. (15.25a) for general solutions.

AT622 Section 16
Radiative Properties of Clouds

Here we provide an overview of the properties of clouds that define how much radiation is absorbed in the atmosphere and how much radiation escapes through the boundaries of the atmosphere. The properties of relevance include:

(1) The three dimensional distribution of the cloud. This influence is usually thought of in terms of separate vertical and horizontal effects. Vertical variability is dealt with in models by introducing cloud overlap assumptions (e.g., Geleyn and Hollingworth, 1979). Horizontal variability is dealt with using assumptions involving cloud amount (Stephens, 1988). Either is empirical and a critical assessment of the uncertainties associated, with assumptions of each, is lacking. Research is now beginning to demonstrate how the 3D nature of clouds is perhaps the most significant factor determining the radiative transfer. Hereafter the macroscopic cloud properties that determine this influence are referred to as *extrinsic optical properties* (EOP). We will consider only the most basic aspects of the effects of these properties on radiation.

(2) The internal optical properties of the cloud. These properties are intrinsically defined by cloud microphysics (such as size and shape of particles). In the case of ice clouds, our understanding of the relationship between optical properties to ice particle microphysics is qualitative. Global climate models and most cloud resolving models do not predict the relevant microphysical properties even of water clouds. Most parameterizations are then carried out in terms of the predictable water or ice mass and a specified microphysical parameter (such as effective particle size). The optical properties of clouds defined by the intrinsic microphysics of clouds will hereafter be referred to as *intrinsic optical properties* (IOP). The single scatter albedo is an example of an IOP. As shown below, cloud optical depth is defined both by macroscopic properties (e.g., cloud depth) and microphysical properties (such as particle size) and thus is a combination of both.

16.1 Intrinsic IR Optical Properties—Cloud Emissivity

The effect of IOPs on IR radiative properties of clouds is generally thought to be negligible as it is commonly assumed that scattering by cloud particles at infrared wavelengths is negligibly small (despite the fact that $\tilde{\omega}_o \approx 0.5$). Some support of this assumption is given in Fig. 16.1, which suggests that the longwave reflectivity of the thickest of clouds is only a few percent. However, even a relatively small amount of scattering has effects both on the emissivity of high clouds (Stephens, 1980) and subsequently IR heating rates of these clouds (discussed below).

Ignoring at first the effects of scattering, we might deduce from Fig. 16.1 that the gray-body assumption is reasonable (i.e., the properties of reflection and absorption are spectrally flat). If we work on the assumption that absorption is dominant, then

$$\tau \approx \tau_{abs}$$

and

$$\tau_{abs} \approx kW$$

where k is an 'absorption' coefficient. We introduce the following for the cloud emissivity

$$\varepsilon = 1 - \exp(-\beta k W) \tag{16.1}$$

where β is the diffusivity ($\beta \approx 1.66$). [Note how W for clouds is entirely analogous to u for gases.]

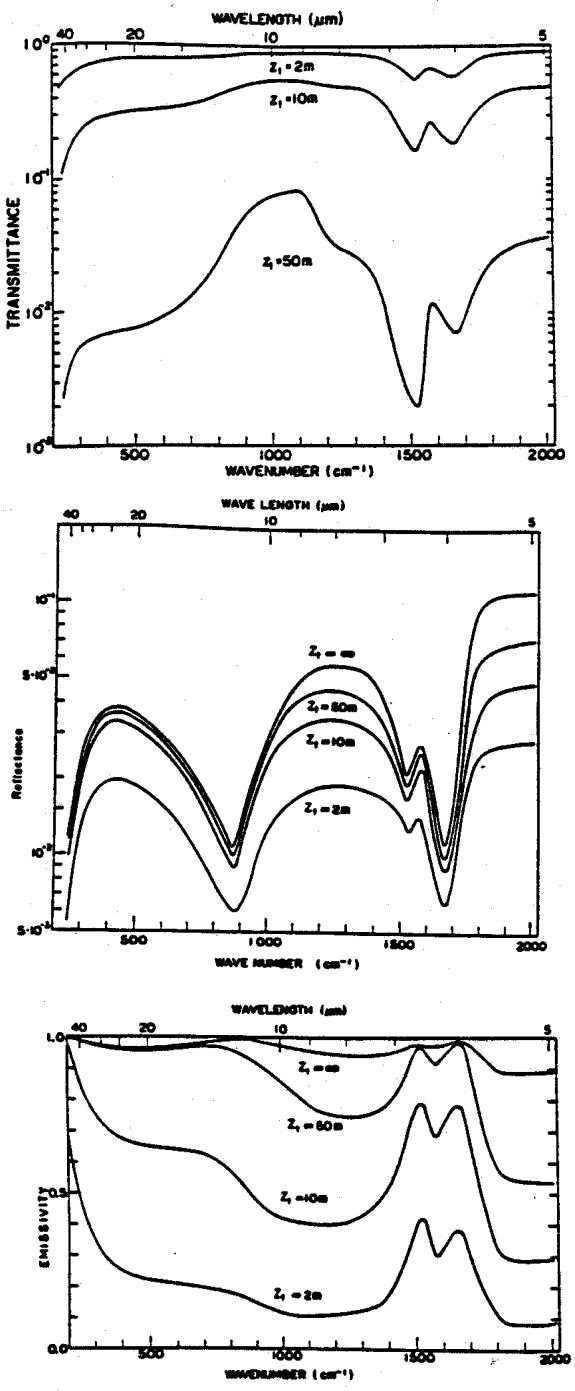

Fig. 16.1 (a) Spectral transmittance of a cloud of various thickness. Altostratus cloud with a liquid water content of 0.28 gm^{-3} (Yamamoto et al., 1970). (b) Spectral reflectance of a cloud. Same characteristics as (a) (Yamamoto et al., 1970). (c) Spectral emissivity of a cloud. Same characteristics as (a) (Yamamoto et al., 1970).

In this context, k is an inherent optical property and it is derived, or estimated, in the following way. Consider the emissivity form of flux equations

$$F^{\uparrow}(z) = F^{\uparrow}(z_b)(1-\varepsilon^{\uparrow}) + \varepsilon^{\uparrow}\sigma T_c^4$$
$$F^{\downarrow}(z) = F^{\downarrow}(z_t)(1-\varepsilon^{\downarrow}) + \varepsilon^{\downarrow}\sigma T_c^4 \qquad (16.2)$$

applicable to a single cloud layer from which

$$\varepsilon^{\uparrow}(z) = \frac{F^{\uparrow}(z_b) - F^{\uparrow}(z)}{F^{\uparrow}(z_b) - \sigma T_c^4}$$
$$\varepsilon^{\downarrow}(z) = \frac{F^{\downarrow}(z_t) - F^{\downarrow}(z)}{F^{\downarrow}(z_t) - \sigma T_c^4} \qquad (16.3)$$

follows as an inversion. Observations of $F^{\uparrow,\downarrow}$, T_c (as best estimated) and W are used to derive $\varepsilon^{\uparrow,\downarrow}$ and hence $k^{\uparrow,\downarrow}$ from Eqn. (16.3). Table 16.1 summarizes various estimates of k published in the literature. Figures 16.2a,b show examples of longwave intensities and fluxes obtained from aircraft measurements in clouds and shows how Eqn. (16.3) fits these data. Figure 16.2c shows this relationship fitted against model simulations of broadband longwave fluxes.

Table. 16.1 Summary of the cloud mass absorption coefficients [mainly ($k^{\uparrow,\downarrow}$)] in m^2g^{-1} for low-level water cloud and upper level cirrus cloud

βk^c	Source	Type of measurement
Boundary layer cloud		
0.13-0.16	Stephens (1978)	Theoretical
0.13	Platt (1976)	Vertical narrowband (10-12 μm) radiance
0.11-0.15	Schmetz, et al. (1981)	Vertical narrowband (11 μm) radiance
0.13	Bonnel, et al. (1980)	Vertical narrowband (8-14 μm) radiance
0.08	Stephens, et al. (1978)	Broadband hemispheric irradiance
Cirrus cloud		
0.08	Paltridge and Platt (1981)	Vertical narrowband (10-12 μm) radiance
0.056	Ibid	Broadband hemispheric irradiance
0.076-0.096	Griffith, et al. (1980)	Broadband hemispheric irradiance

Given a simple expression for cloud emissivity and the profile of cloud liquid (or ice) water content, it is a simple matter to derive the longwave flux profiles through a cloud layer using Eqn. (16.2). Examples of this kind of calculation are presented in Fig. 16.3a for $F^{\uparrow,\downarrow}$ at 10 μm and in Figs. 16.3b,c for F_{net}. The downward fluxes increase rapidly from cloud top (depending on the growth of ε) and the upward flux, which at cloud base exceeds the black body flux, decreases into the cloud. Both $F^{\downarrow}$ and $F^{\uparrow}$ approach the equivalent black body fluxes at the respective cloud boundaries where $\varepsilon^{\uparrow,\downarrow} \approx 1$.

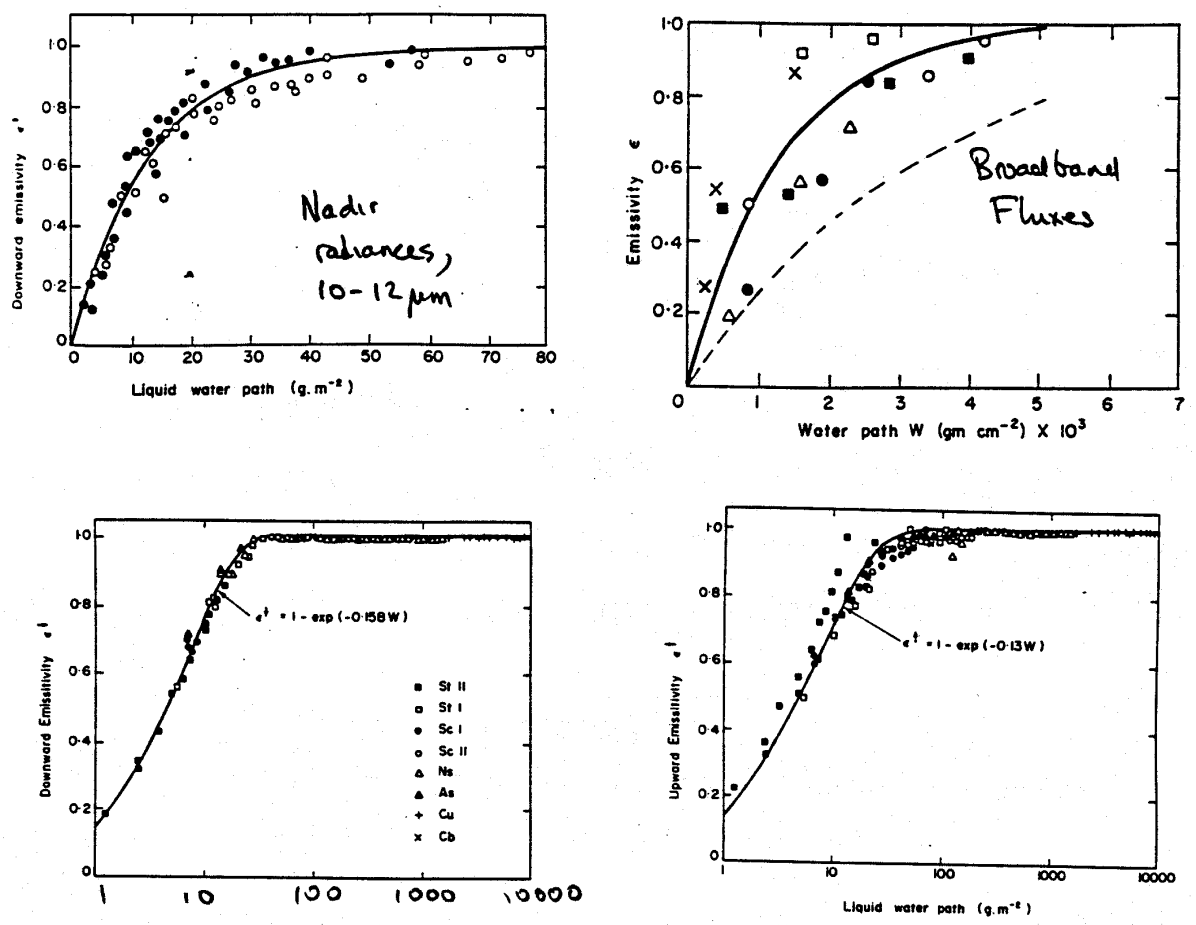

Fig. 16.2 Experimental values of 10-12 μm emissivity determined from nadir radiance measurements as a function of liquid water path. The solid and open points are the measured values. (b) Mean cloud emissivity versus total water path W to cloud top. (c) Empirical presentation of downward (a) and upward (b) emissivity as a function of liquid water path. The solid line is the least-squares best fit through the given points using the analytic form described in the text.

The net flux profiles presented in Figs. 16.3b,c show how the changing $F^{\downarrow}$ at cloud top influences F_{net} there and how the changing $F^{\uparrow}$ at cloud base governs the profile of the F_{net} in the lower portions of the cloud. The contribution of both depends on the optical thickness (Fig. 16.3b) and the temperature difference between cloud and ground (Fig. 16.3c). These dependencies vary with wavelength. The results shown in Fig. 16.3 apply to a cloud overlying a surface with no atmosphere above or below it. Figures 16.4a,b presents longwave flux profiles actually observed in clouds and features similar to those illustrated in Fig. 16.3 and are easily recognized.

16.2 Intrinsic Solar Optical Properties

The influence of cloud IOP on solar radiative transfer is complex and germane to a number of current cloud-radiation issues thought to be important to topics of climate and global change (e.g., the so-called Twomey effect).

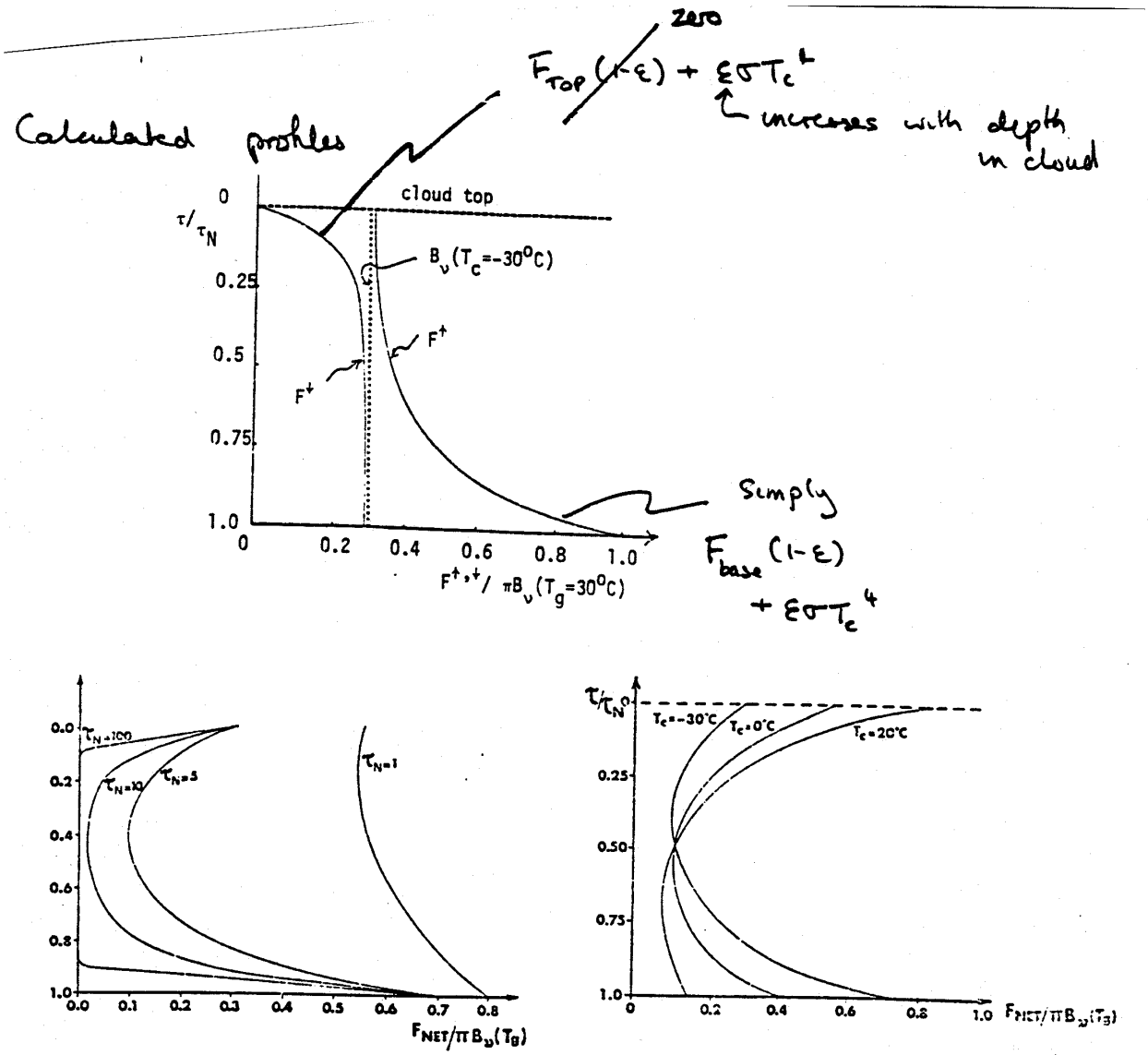

Fig. 16.3 (a) The 10 μm flux profiles for an Sc cloud layer of optical thickness $\tau_N = 5$. (b) The 10 μm net flux profiles as a function of optical thickness, $T_g = 30°$. (c) The 10 μm net flux profiles for an Sc cloud layer possessing three different cloud temperatures, $T_g = 30°C$ and $\tau_N = 5$.

The relation between IOPs and solar transfer may be explored in the context of our simple two stream model solutions in the limit as $\tau^* \to 0$ and $\tau^* \to \infty$. For optically thick, we deduce from Eqn. (15.22) that the albedo (and hence absorption) depends as follows

$$R_\infty = R(\tilde{\omega}_o, b(g), D, \mu_o) \tag{16.4a}$$

$$A_\infty = 1 - R_\infty \tag{16.4b}$$

where R_∞ and A_∞ are respectively the albedo and absorption of this 'semi-infinite' cloud. According to these simple relationships both the albedo and absorption approach fixed asymptotic limits as τ^* increases. It is relatively straightforward to show that these limits may largely be considered to depend on $\tilde{\omega}_o$ using Eqns. (15.22) and (15.21) as a guide. Stephens and Tsay showed that

$$A_\infty \approx \text{constant} \times (1 - \tilde{\omega}_o)^{0.4} \tag{16.5}$$

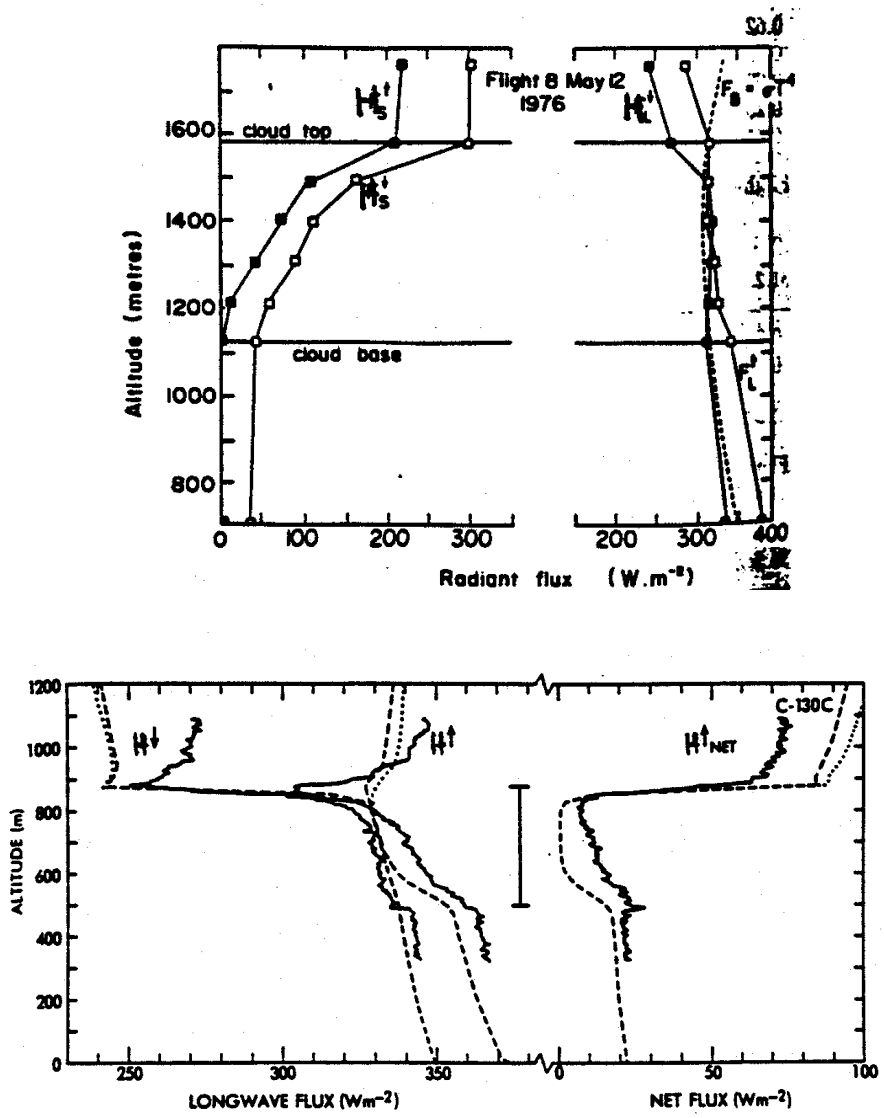

Fig. 16.4 The total longwave and shortwave flux profiles measured in three Sc cloud layers $F_s^{\uparrow,\downarrow}$, $F_L^{\uparrow,\downarrow}$ and F_B are the shortwave and longwave fluxes, and black body flux, respectively. Each point is a 4 min average value. (b) Comparison of the observed upward $F^{\uparrow}$, downward $F_{\downarrow}$ and the net F_{net} longwave fluxes measured by the C-130 on profile C with the theoretical fluxes from the radiation scheme of Schmetz and Raschke (1981), shown as the dashed lines. The fluxes from the scheme of Roach and Slingo (1979) are within about 2 Wm^{-2} of these values, except above the cloud top where they are shown by the dotted lines. Slingo et al, 1982: QJRMS, ***108****, 833-838.*

For optically thin clouds with $\tau^* \to 0$, it can also be shown (e.g., from Eqn. (15.22) and Stephens and Tsay, 1990)

$$R_o = \frac{\tau^*}{\mu_o}\tilde{\omega}_o b_o \tag{16.6.a}$$

$$T_o = 1 - \frac{\tau^*}{\mu_o}(1 - \tilde{\omega}_o f_o) \tag{16.6b}$$

and

$$A_o = \frac{\tau^*}{\mu_o}(1 - \tilde{\omega}_o) \tag{16.6c}$$

Thus both the albedo and absorption of thin clouds vary linearly with optical thickness and, as expected, respectively depend on the backscatter and absorption properties of the individual cloud particles.

These relations provide us with a way of deducing the effects of particle size on the albedo and absorption of solar radiation. Two factors that are important are:

- The first is a reciprocal dependence of optical depth on particle size

$$\tau = \frac{3W}{2\rho_{water} r_e} \tag{16.7a}$$

  where W is the liquid water path (LWP), r_e is the effective radius (the ratio of volume to area of the distribution) and ρ_{water} is the density of water. The same sort of reciprocal relationship follows for ice clouds (e.g., Fu and Liou, 1993). An alternative relation is

$$\tau = 2\pi h N_o^{1/3} \ell^{2/3} \tag{16.7b}$$

  where h is the cloud thickness, N_o is the number density of particles and ℓ is the liquid water content ($W \approx \ell h$). Both relationships predict that for fixed liquid water content or path, the optical depth increases through increases in N_o or equivalently through decreases in r_e. Such an increase in optical depth implies increased albedo of clouds through Eqn. (16.6a) but not necessarily an increase in the albedo of thick clouds since the reflection of these clouds is largely insensitive to any changes in optical depth if deep enough.

- The second factor involves the relationship between $1 - \tilde{\omega}_o$ and r_e, which Ackerman and Stephens (1987) simplify to

$$1 - \tilde{\omega}_o \approx \text{constant} \times \kappa r_e^p \tag{16.8}$$

  where κ is the bulk absorption by water and $p \leq 1$.

From the relationships in Eqns. (16.7a) and (16.8), and the expressions for albedo in Eqns. (16.6a), (16.4b), and (16.5), it follows that the albedo of clouds increases as particle size decreases (Fig. 16.5a) through a combination of both decreasing in absorption (predicted from Eqn. (16.8)) and associated increases of optical depth, Eqn. (16.7a). The relationship between absorption and particle size as

highlighted in Fig. 16.5b is complex. The dependence on particle size is such that the absorption of thin clouds (i.e., small LWP) actually increases with decreasing particle size, while the reverse applies for thick clouds (or large LWP). This thick cloud dependence has been mistakenly interpreted to imply that indiscriminant increases of particle size enhances absorption in clouds explains discrepancies with observations. Marine boundary layer clouds typified by intermediate values of LWP (and optical depth) are characterized by a weak dependence on r_e.

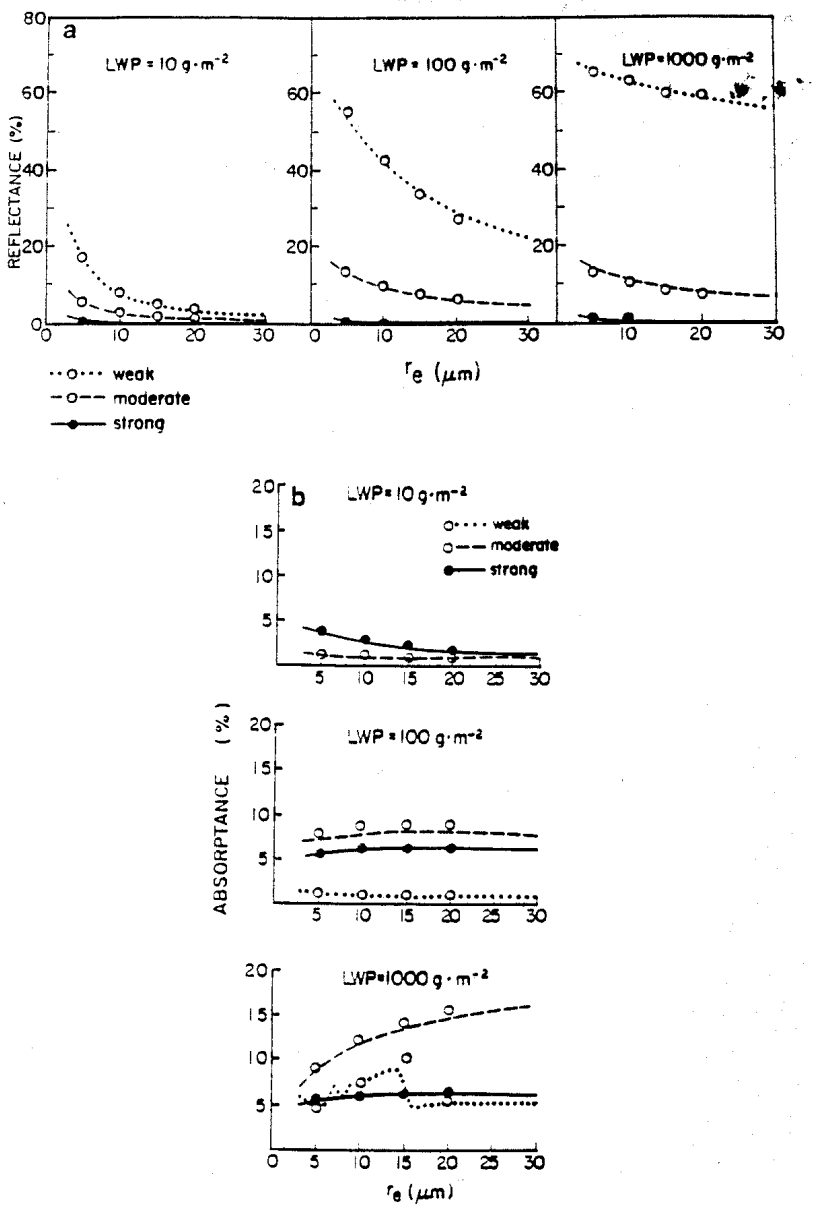

Fig. 16.5 Contributions to the (a) albedo and (b) absorptance by the three spectral absorption regimes introduced by Ackerman and Stephens (1987) as a function of r_e for specified values of LWP. The symbols refer to calculations using scattering properties from Lorenz-Mie theory (ignore differences between symbols and curves).

In summary, we deduce that the albedo of clouds is sensitive to both particle size and LWP (or IWP) and varies in a systematic way with changes in these parameters. By contrast, the solar absorption depends on these parameters in a complex way.

A series of aircraft experiments that seek to confirm the relation between r_e and cloud albedo are those of the Southern Ocean Cloud Experiments (SOCEX) described by Boers et al. (1995). They find significant seasonal variations in r_e characteristic of marine layered cloud between summer and winter (Fig. 16.6a) with composite mean values of r_e = 19 μm in winter and r_e = 13 μm in summer. Since these measurements were carried out in baseline air (free of continental effects), these results are consistent with the seasonal variations of DMS and the subsequent influence of DMS on CCNs and thus cloud microphysics. These large measured seasonal changes in r_e translate to significant percentage changes in cloud albedo (refer to Fig. 16.5a). In Fig. 16.6b the profile of effect radius is shown when the measured drizzle component is added to the measured profiles of Fig. 16.6a. This drizzle contributes significantly to the particle size at cloud base but its direct effect on the albedo of clouds has not yet been determined. The indirect effects of drizzle on albedo, through its effect on cloud evolution, are thought to be significant (Stephens, 1994).

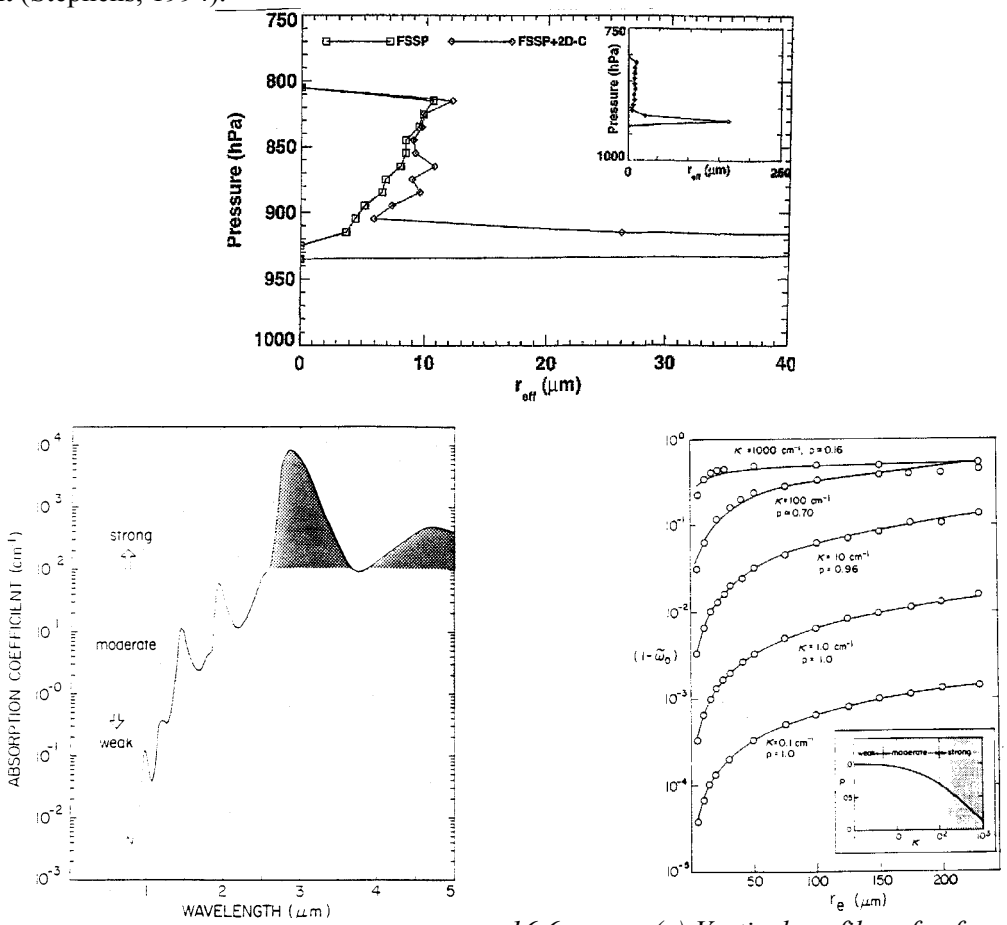

Fig. 16.6 (a) Vertical profiles of r_e from aircraft measurements of c

effective radius for selected values of ?? The solid curves represent the relationship described by Eqn. (??) for the values of p indicated and the open circles apply to the MADT theory. The insert depicts the breakdown of the weak, moderate, and strong absorption regimes.

16.3 Extrinsic Cloud Optical Properties

The most dominant control on the infrared radiative transfer through clouds is the contrast between radiation emitted from the atmosphere to the cloud from above and below and the radiation emitted from the cloud. This influence is visible in the results shown in Figs. 16.2 and 16.3. Unlike for the clear sky, the net LW radiative energy budget is largely dominated by those spectral regions that are most

transparent to gas absorption—that is in the atmospheric window. The net LW budget of a cloud is one of a balance between emission from top (cooling) and absorption from the large flux below the cloud (warming). This balance changes sign as the altitude of the cloud layer changes—net warming by high cirrus in a tropical environment is expected, net cooling for lower cloud. This variation is evident in Fig. 16.8, which shows the net longwave radiation budget of a 1 km blackbody cloud located at different levels in a standard atmosphere. This budget is defined as

$$\Delta F = F_{net}\,(\text{base}) - F_{net}\,(\text{top})$$

and this budget is more to be positive. Examples of the spectral disposition of ΔH for cirrus clouds of different thicknesses located in the tropical atmosphere and in the subarctic winter atmosphere are shown in Fig. 16.7.

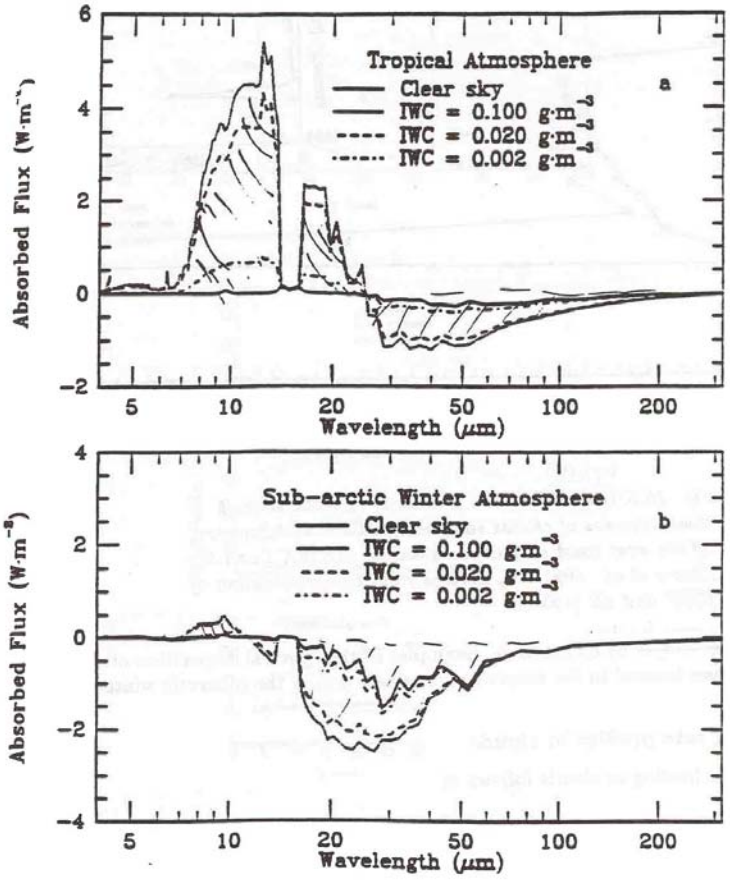

Fig. 16.7 Spectral distribution of ΔF for various cirrus clouds in (a) a tropical atmosphere and (b) a subarctic winter atmosphere.

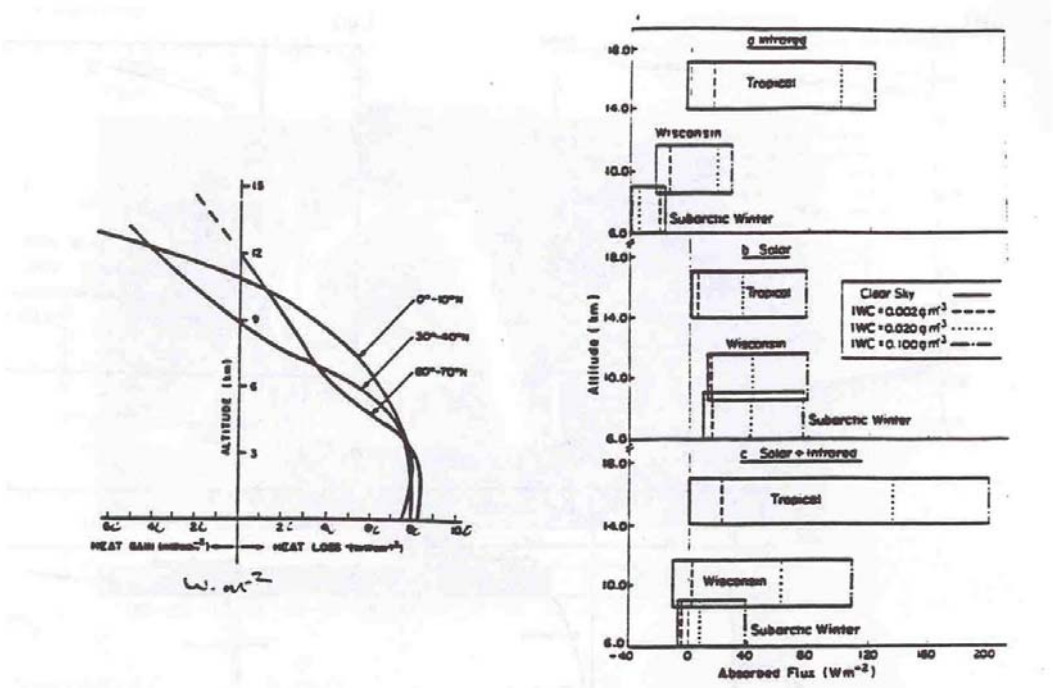

Fig. 16.8 Net radiative loss from a thin "black" cloud inserted at various heights in the mean atmospheres of three latitude zones. (After Paltridge, 1974d)

16.4 Heating Rate Profiles in Clouds

The radiative heating in clouds follows as

$$\frac{dT}{dt} = -\frac{1}{\rho C_p}\frac{dF_{net}}{dz}$$

and depends on the optical depth, cloud temperature, wavelength and all parameters that affect the fluxes (we get some sense of the effect of particle size from the above discussion). Examples of the longwave heating are given in Figs. 16.9a,b. Figure 16.9c presents the first measured profiles of solar heating and IR cooling. Generally, these profiles are characterized by radiative cooling at cloud top and warming at cloud base, although the latter is strongly dependent on the temperature differential of the radiation incident from below and the cloud temperature.

The spectral infrared heating of a cloud located in a tropical and subarctic winter atmosphere, respectively, is given in Fig. 16.10. High tropical clouds predominantly heat because the difference between emission at cloud base and absorption of radiation from below leads to a gain in radiative energy and thus a heating of high tropical clouds. This heating occurs principally in the more transparent regions of the spectrum where these differences are largest. The details of this heating and how it penetrates into the cloud also depend on the optical depth of the cloud, which under the Rayleigh assumptions, depends on the ice water path. For the lower cloud in the subarctic atmosphere, the lack of a distinct contrast between the emission from cloud base and the upwelling radiation from below leads to a much reduced heating at cloud base. These lower clouds predominantly cool at cloud top at most wavelengths.

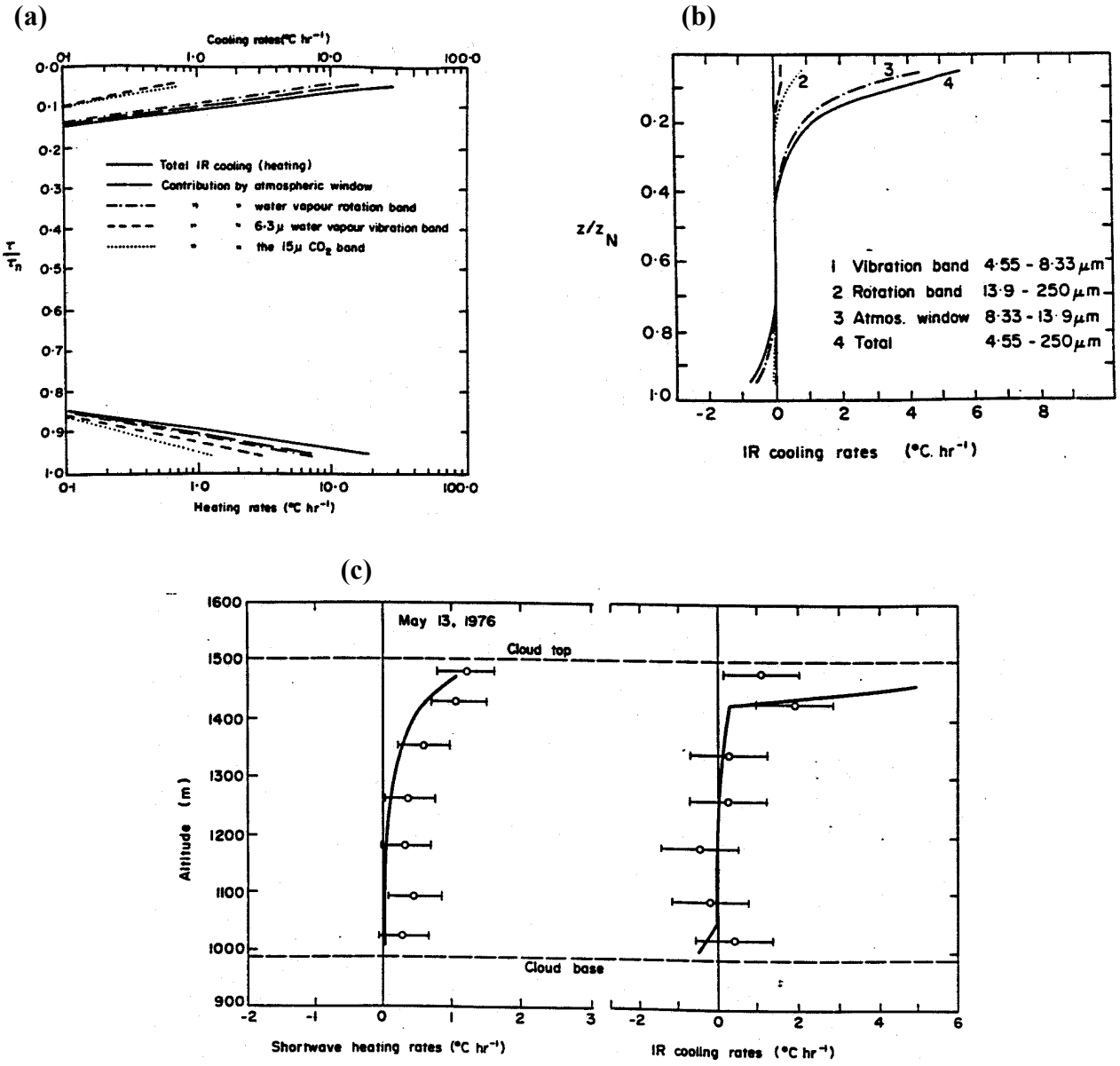

Fig. 16.9 (a) Cooling profiles for various spectral regions through an isotropic cloud at approximately 4 km altitude for a standard atmosphere with surface temepature equal to 22°C. Cloud thickenss = 1.6 km, extinction coefficient (10 μm) = 27 km^{-1}, $\tilde{\omega}_o$(10 μm) = 0.57. (b) The IR cooling rate profile in a SC I cloud layer 500 m thick positioned at 1.5 km in the tropical atmosphere model. The contributions by the three main spectral regions are displayed. (c) The shortwave and longwave heating and cooling rate profiles measured in the cloud layer sampled on 13 May 1976. The extent of the rms experimatnal error is shown by the horizontal lines. The solid curve is the theoretically calculated profile.

The important point to be drawn from this diagram is that the IR radiative properties of clouds, specifically the extent and magnitude of IR heating, is strongly dependent on the properties of the environment around the cloud (such as the temperature contrast and the amount of water vapor above and below the cloud). What is not emphasized in these diagrams but is of equal importance is the effect of optical depth (or IWP) on the radiative heating of the cloud.

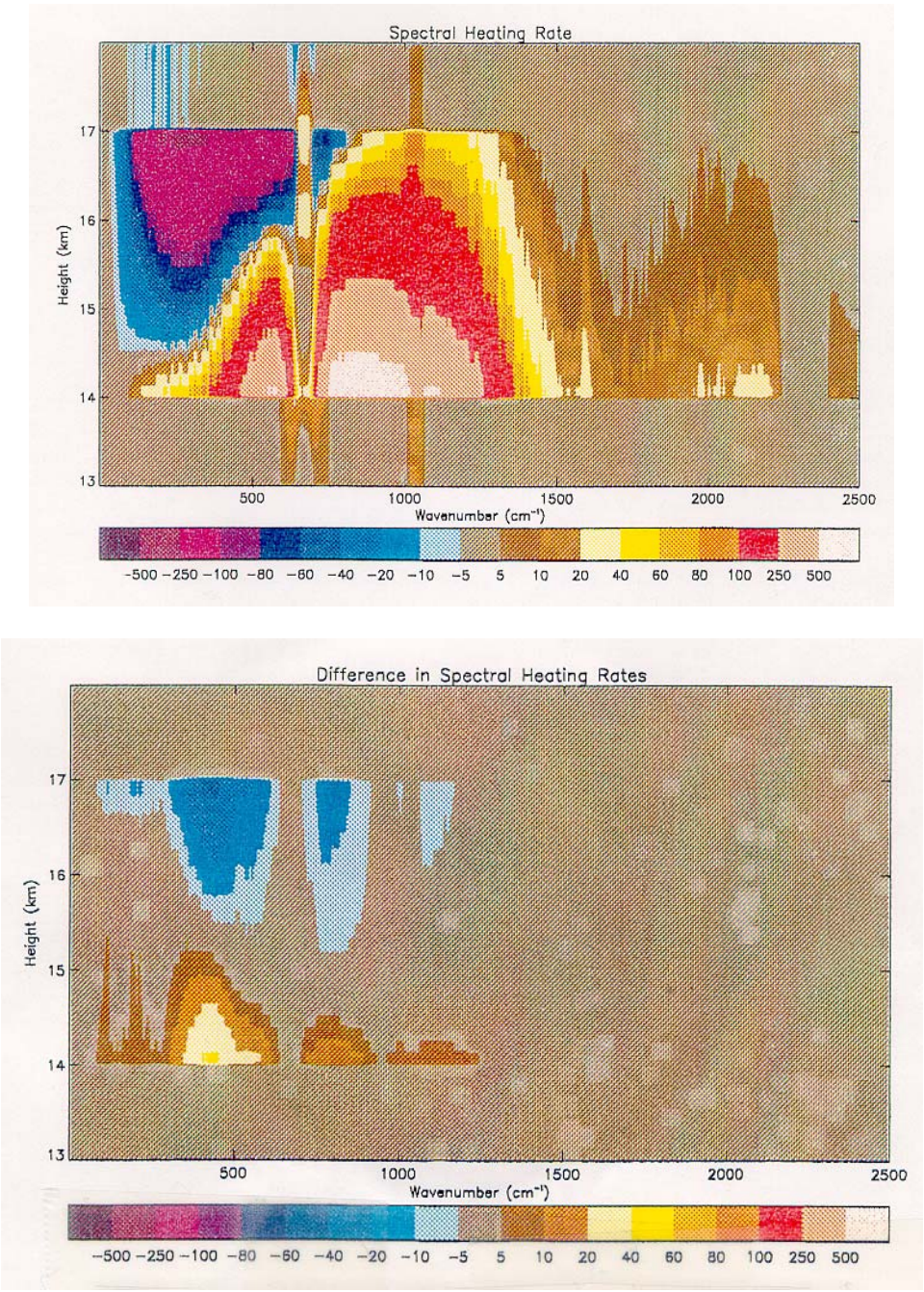

Fig. 16.10 The vertical profile of the spectral IR cooling rate for (a) an ice cloud located in a model tropical atmosphere and (b) for the same in a subarctic winter atmosphere (Edwards and Slingo, 1995).